Characterization of Novel Pyroelectrics: From Bulk GaN to Thin Film HfO$_2$

By the Faculty of Chemistry and Physics
of the Technische Universität Bergakademie Freiberg

approved

Thesis

to attain the academic degree of

doctor rerum naturalium
(Dr. rer. nat)

submitted by **M. Sc. Sven Jachalke**

born on the November 13, 1988 in Riesa

Assessor: Prof. Dr. Dirk C. Meyer
          Prof. Dr. Thomas Mikolajick

Date of the award: Freiberg, May 6, 2019

Abstract

The change of the spontaneous polarization due to a change of temperature is known as the pyroelectric effect and is restricted to crystalline, non-centrosymmetric and polar matter. Its main application is the utilization in infrared radiation sensors, but usage for waste heat energy harvesting or chemical catalysis is also possible. A precise quantification, i.e. the measurement of the pyroelectric coefficient p, is inevitable to assess the performance of a material. Hence, a comprehensive overview is provided in this work, which summarizes and evaluates the available techniques to characterize p. A setup allowing the fully automated measurement of p by utilizing the SHARP-GARN method and the measurement of ferroelectric hysteresis loops is described. It was used to characterize and discuss the behavior of p with respect to the temperature of the doped bulk III-V compound semiconductors gallium nitride and aluminum nitride and thin films of doped hafnium oxide, as reliable data for these materials is still missing in the literature. Here, the nitride-based semiconductors show a comparable small p and temperature dependency, which is only slightly affected by the incorporated dopant, compared to traditional ferroelectric oxides. In contrast, p of HfO_2 thin films is about an order of magnitude larger and seems to be affected by the present dopant and its concentrations, as it is considered to be responsible for the formation of the polar orthorhombic phase.

Kurzdarstellung

Die Änderung der spontanen Polarisation durch eine Änderung der Temperatur ist bekannt als der pyroelektrische Effekt, welcher auf kristalline, nicht-zentrosymmetrische und polare Materie beschränkt ist. Er findet vor allem Anwendung in Infrarot-Strahlungsdetektoren, bietet aber weitere Anwendungsfelder wie die Niedertemperatur-Abwärmenutzung oder die chemische Katalyse. Eine präzise Quantifizierung, d. h. die Messung des pyroelektrischen Koeffizienten p, ist unabdingbar, um die Leistungsfähigkeit eines Materials zu bewerten. Daher bietet diese Arbeit u. a. einen umfassenden Überblick und eine Bewertung der verfügbaren Messmethoden zur Charakterisierung von p. Weiterhin wird ein Messaufbau beschrieben, welcher die voll automatisierte Messung von p mit Hilfe der SHARP-GARN Methode und auch die Charakterisierung der ferroelektrischen Hystereseschleife ermöglicht. Aufgrund fehlender Literaturdaten wurde dieser Aufbau anschließend genutzt, um den temperaturabhängigen pyroelektrischen Koeffizienten der dotierten III-V-Verbindungshalbleiter Gallium- und Aluminiumnitrid sowie dünner Schichten bestehend aus dotiertem Hafniumoxid zu messen und zu diskutieren. Im Vergleich zu klassischen ferroelektrischen Oxiden zeigen dabei die nitridbasierten Halbleiter einen geringen pyroelektrischen Koeffizienten und eine kleine Temperaturabhängigkeit, welche auch nur leicht durch den vorhandenen Dotanden beeinflusst werden kann. Dagegen zeigen dünne Hafniumoxidschichten einen um eine Größenordnung größeren pyroelektrischen Koeffizienten, welcher durch den anwesenden Dotanden und seine Konzentration beeinflusst wird, da dieser verantwortlich für die Ausbildung der polaren, orthorhombischen Phase gemacht wird.

Contents

List of Figures

List of Tables

1. Motivation and Introduction

Pyroelectric materials can generally be described as a subclass of dielectric matter, in which a spontaneous polarization prevails without an externally applied electric field. Its magnitude can be altered due to a change in temperature. This so-called pyroelectric effect already enabled a lot of commercially available applications such as fast infrared detection, i.e. in IR cameras or motion and temperature sensors [160, 161, 163, 362]. Furthermore, great potential for waste heat harvesting [152, 166, 205, 230, 235, 240], X-ray generation [31], pyroelectrocatalytic disinfection [103], radical [18] and hydrogen production [9, 135] as well as electrocaloric cooling [158] can be provided by such materials. Detailed fundamentals of the phenomenon pyroelectricity as well as the related ferroelectricity are given in Chapter 2.

As every application needs a precise knowledge of the physical properties of the active material, an accurate determination of these is inevitable. Beside common dielectric and thermal properties, such as relative dielectric permittivity, loss tangent, heat capacity, thermal conductance and so on, the quantification of the change in spontaneous polarization due to a change in temperature, known as the pyroelectric coefficient p, lies at the heart of the characterization of a pyroelectric material. Of course, the literature provides a variety of possibilities for the quantification of p, but a comprehensive and almost complete summary, revealing and comparing the capabilities and restrictions of different measurement methods, is missing. Thus, Chapter 3 is dedicated to the summary of almost 20 different measurement techniques combined with considerations on the suitability of a chosen method.

As it turns out, the electric-current-based SHARP-GARN method is the most versatile technique. Thus, Chapter 4 presents the setup, originally developed by ERIK MEHNER [207], for the determination of the pyroelectric coefficient using this method. Here, the focus lies on the automated evaluation of p and its temperature dependency $p(T)$. Furthermore, the determination of the remanent polarization P_R of a ferroelectric from a polarization versus electric electric field (P-E) hysteresis measurement, as well as the reconstruction of its temperature dependency $P_R(T)$, was established.

The setup and method were further used to characterize p of novel pyroelectrics, such as bulk III-V compound semiconductors GaN and AlN and thin films of HfO_2, as there are only few published values (see Chapter 5). Here, special attention is paid to the impact of the different doping atoms and their influence on the polar properties of the materials.

Reliable data of the pyroelectric coefficient of the non-ferroelectric, but pyroelectric gallium nitride (GaN) and aluminum nitride (AlN), especially in form of thick bulk single crystals, is still missing in the literature. A characterization of such weak polar materials with a current-measuring method is quite challenging due to the very low currents, which have to be detected. Furthermore, an increased electrical conductivity mediated by growth-induced defects in these wide-band gap semiconductors typically prevents such a measurement. The intentional doping used to suppress the electrical conductivity simultaneously affects the polar properties, as outlined in Chapter 6.1.

Another challenge for the Sharp-Garn method is its application to thin films, i.e. the measurement of the pyroelectric coefficients of layers with a thickness of only few tens of nanometers. The discovery of ferroelectricity in the high-k material HfO_2 in 2011 led to a revived scientific interest, especially due to its potential application in ferroelectric random access memory (FRAM) to fill the gap between fast volatile DRAM and slow non-volatile FLASH memory. While the number of publications dealing with the stabilization and enhancement of ferroelectricity by doping the material with different elements is steadily growing, investigations on its pyro- and piezoelectric properties are comparably rare. As a first starting point in this sector, the influence of differently doped HfO_2 with silicon (HfO_2:Si) and several other dopants was of particular interest. The results allow evaluating the usability of the material in potential applications, e.g. sensor or energy harvesting, beyond the memory technology, as shown in Chapter 6.2.

2. Fundamentals

2.1. Dielectrics and their Classification

The phenomena of piezo-, pyro- and ferroelectricity require crystalline matter, typically with a large band gap and a low electrical conductivity. The latter and the crystallinity, i.e. the spatial periodic arrangement of atoms, are prerequisites for the considered coupling phenomena. For their theoretical description three sets of intensive and extensive state variables, i.e. electrical, thermal and mechanical, are used. They are mathematically represented by tensors of different rank and summarized in the HECKMANN diagram, which is shown in Fig. 2.1. Here, special focus lies on the pyroelectric coupling, as it is the main topic of this work. Thus, magnetic fields are neglected here, so their properties are omitted in the following (for magnetic coupling effects see Ref. [252, 332]).

The direct and cross-coupling between these fields is described by specific material properties, which in turn are also represented by tensors. Based on MAXWELL's equations, the dielectric displacement field $\vec{D}$ is given by

$$\vec{D} = \varepsilon_0 \vec{E} + \vec{P}, \tag{2.1}$$
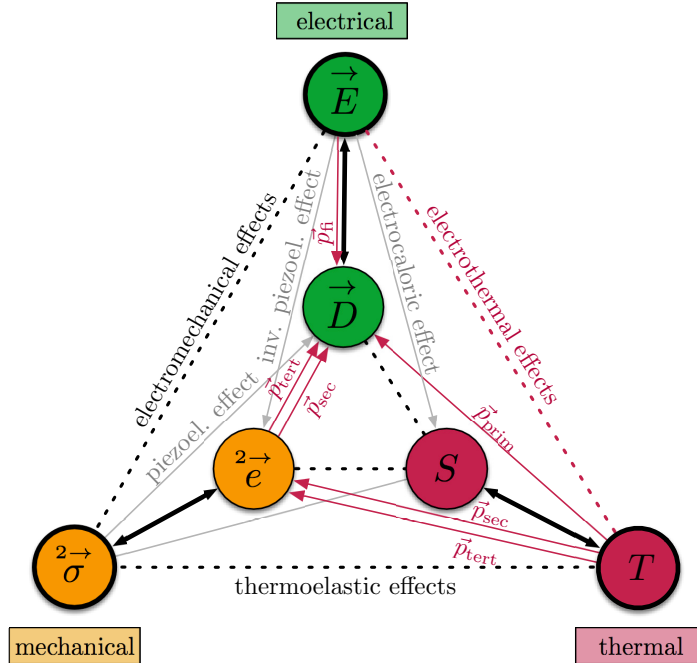
Fig. 2.1.: The HECKMANN diagram, describing direct and cross-coupling phenomena between thermal, electrical, and mechanical state variables. Bold and non-bold circles represent intensive and extensive state variables, respectively. Also $\vec{p}_{\mathrm{prim}}$, $\vec{p}_{\mathrm{sec}}$, $\vec{p}_{\mathrm{tert}}$ and $\vec{p}_{\mathrm{fi}}$ denote the path of primary, secondary, tertiary and field-induced pyroelectricity, respectively (see Sec. 2.3). For reasons of simplicity magnetic properties are omitted. Redrawn after Ref. [161].

in which ε_0 is the permittivity of free space, and $\vec{E}$ and $\vec{P}$ are the vector of the electric and polarization field, respectively. The polarization caused by the presence of an electric field is called "induced" polarization and linear approximated by $\vec{P}_{\mathrm{ind}} = \varepsilon_0 \overset{2\to}{\chi} \vec{E}$, which gives an equivalent expression for $\vec{D}$ by:

$$\vec{D} = \varepsilon_0 (1 + \overset{2\to}{\chi}) \vec{E}. \tag{2.2}$$

Here, $\overset{2\to}{\chi}$ is the electrical susceptibility, which characterizes the degree of polarizability of a material and is closely related to the relative dielectric permittivity $\overset{2\to}{\varepsilon_{\mathrm{r}}}$ by:

$$\overset{2\to}{\chi} = \overset{2\to}{\varepsilon_{\mathrm{r}}} - 1. \tag{2.3}$$

Taking into account the symmetry of the crystal lattice, several point groups allow a "spontaneous polarization" $\vec{P}_{\mathrm{S}}$, which exists independent of the application of an external electric field $\vec{E}$. The total polarization is then represented by induced (under applied electric field) and spontaneous (without applied electric field) polarization [55]:

$$\vec{P} = \vec{P}_{\mathrm{ind}} + \vec{P}_{\mathrm{S}}. \tag{2.4}$$

Hence, the dielectric displacement field is given by:

$$\vec{D} = \varepsilon_0 \overset{2\to}{\varepsilon_{\mathrm{r}}} \vec{E} + \vec{P}_{\mathrm{S}}. \tag{2.5}$$

Thus, in the absence of an external electric field, $\vec{D} = \vec{P}_{\mathrm{S}}$, since $\vec{P}_{\mathrm{ind}} = 0$.

As mentioned above, the reason for $\vec{P}_{\mathrm{S}}$ lies in the symmetry of the crystal structure, allowing a classification of dielectric matter [252] as provided in Fig. 2.2. From the 32 point groups (39 when including continuous point groups), 20 (23) exhibit no center of inversion symmetry and, thus, piezoelectricity, i.e. the stress-induced change of $\vec{D}$. From these non-centrosymmetric, only 10 (12) have one polar axis, the requirement for pyroelectricity. It exists in point groups with a rotation axis, with mirror planes parallel to the rotation axis, in point group 1 and two continuous point groups [145, 161, 252]:

$$1, 2, 3, 4, 6, m, mm2, 3m, 4mm, 6mm \text{ (and } \infty, \infty m). \tag{2.6}$$

The corresponding space groups are given in Tab 2.1. Whereas point group 1 and m have three and two components of the polar axes, respectively, all other point groups allow only one component (2 in y-, all other in z-direction [145, 252]). Hence, the spontaneous polarization vector (as well as the pyroelectric coefficient vector, see below) is usually treated as a scalar quantity.

From Fig. 2.2 it is obvious that all ferroelectrics are pyroelectric, but the reverse is not always true. This difference is also present in the investigated material systems of this work (see Sec. 6): Gallium nitride (GaN) is a non-ferroelectric pyroelectric, while hafnium oxide (HfO$_2$) is a ferroelectric pyroelectric.

2.2. Polarization

The macroscopic polarization $\vec{P}$, including both $\vec{P}_{\mathrm{ind}}$ and $\vec{P}_{\mathrm{S}}$, is of great fundamental and technological importance for dielectrics, since it is the quantity defining piezo-, pyro- and ferroelectricity. Polarization $\vec{P}$ is an extensive vector quantity, which is defined as an electric

Tab. 2.1.: Pyroelectric point and corresponding space groups.

Crystal Class	Point Group	Space Group	No.
Triclinic	1	$P1$	1
Monoclinic	2	$P2$, $P2_1$	3–4
		$C2$	5
	m	Pm, Pc	6–7
		Cm, Cc	8–9
Orthorhombic	$mm2$	$Pmm2$, $Pmc2_1$, $Pcc2$, $Pma2$, $Pca2_1$, $Pnc2$, $Pmn2_1$, $Pba2$, $Pna21$, $Pnn2$	25–34
		$Cmm2$, $Cmc2_1$, $Ccc2$, $Amm2$, $Aem2$, $Ama2$, $Aea2$	35–41
		$Fmm2$, $Fdd2$	42–43
		$Imm2$, $Iba2$, $Ima2$	44–46
Tetragonal	4	$P4$, $P4_1$, $P4_2$, $P4_3$, $I4$, $I4_1$	75–80
	$4mm$	$P4mm$, $P4bm$, $P4_2cm$, $P4_2nm$, $P4cc$, $P4nc$, $P4_2mc$, $P4_2bc$	99–106
		$I4mm$, $I4cm$, $I4_1md$, $I4_1cd$	107–110
Trigonal	3	$P3$, $P3_1$, $P3_2$	143–145
		$R3$	146
	$3m$	$P3m1$, $P31m$, $P3c1$, $P31c$	156–159
		$R3m$, $R3c$	160–161
Hexagonal	6	$P6$, $P6_1$, $P6_5$, $P6_2$, $P6_4$, $P6_3$	168–173
	$6mm$	$P6mm$, $P6cc$, $P6_3cm$, $P6_3mc$	183–186
Cubic	–	–	–
Total	10	68	–
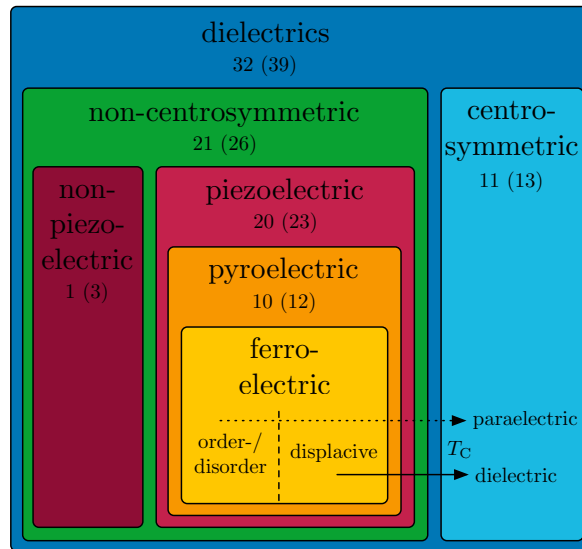
Fig. 2.2.: Classification of dielectric matter. Closed areas represent real subsets with their corresponding number of possible points groups. The number in parenthesis include the continuous point groups. The arrows mark the phase transformation at the CURIE temperature T_C, depending on the predominant type of polarization (see 2.4).
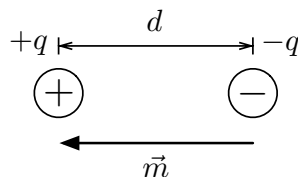
Fig. 2.3.: Definition of an electric dipole.

dipole moment $\vec{m}$ per unit volume V (dipole density) and, thus, is measured in units[1] of $C\,m^{-2}$ and can be interpreted as a surface charge density in a material. Generally, an electric dipole is mathematically described by

$$\vec{m} = q \cdot \vec{d}, \tag{2.7}$$

representing two point charges, of elementary charge $+q$ and $-q$, separated by a distance d and, thus, given in units of $C\,m$. As shown in Fig. 2.3, the dipole or vector direction of $\vec{m}$ is defined from negative to positive charge[2].

As it turned out, the fusion of this microscopic dipole picture with a measurable macroscopic polarization is not straightforward. Unfortunately, an adequate microscopic description is quite difficult, which prevented e.g. first-principle approaches to understand and predict material behavior until the 1990s. The achievements of the "modern theory of polarization" in recent years are shortly outlined below, following the didactics of RESTA and VANDERBILT in Ref. [275].

---

[1] Dipole moment $\vec{m}$ $(C\,m)$ per unit volume V (m^3) yields $C\,m^{-2}$

[2] In a material with applied electric field $\vec{E}$ the direction of $\vec{P}_{ind}$ is of opposite direction to electric field lines due to its role as counterforce to $\vec{E}$

The simplest model after CLAUSIUS and MOSOTTI describes the induced (and spontaneous) macroscopic polarization of a material as the sum of all electric dipole moments divided by the respective cell or sample volume:

$$\vec{P} = \frac{\sum_i \vec{m}_i}{V_{\mathrm{Samp}}}. \tag{2.8}$$

Unfortunately, this is a highly idealized picture of the microscopic polarization, because it assumes that the dipole moments $\vec{m}_i$ can be determined from confined and separable centers. While this may be the case for ideal ionic crystals, real atomic bonding is typically involving a mixture of ionic and covalent character. An increased delocalization of the electronic charge, which arises from covalent bonds and induced charges, makes a definition of confined polarization centers highly arbitrary. Furthermore, the estimated polarizations using the CLAUSIUS-MOSOTTI model are approximately one order of magnitude smaller than actually measured values [274].

A more sophisticated approach attempts to describe P from (periodic) charge distributions or charge density $\rho(\vec{r})$. The polarization is then given by:

$$\vec{P} = \frac{1}{V_{\mathrm{Samp}}} \int_{\mathrm{Samp}} \vec{r} \cdot \rho(\vec{r}) \, \mathrm{d}\vec{r}. \tag{2.9}$$

Here, the integration of $\rho(\vec{r})$ over the whole sample divided by the sample volume is inadequate, as the resulting polarization is composed of contributions from the bulk and the surface. A change of the surface charge density scales cubically with the sample geometry and, thus, alters the polarization depending on the size of the considered sample. Therefore, it is not a useful description for a bulk polarization. Also the use of the unit cell volume V_{cell}, which is experimentally accessible by X-ray diffraction, instead of V_{Samp} depends on location and shape of the cell. Furthermore, P can vanish by translation and averaging over many unit cells, which could only be overcome by assuming the CLAUSIUS-MOSOTTI model again. Thus, also the knowledge of the periodic charge distribution cannot be used for an adequate definition of the polarization.

While both approaches described above are attempts to assess the absolute polarization, considerations of polarization changes ΔP due to certain perturbations (e.g. changes of electric field, mechanical stress or temperature) are more promising. In principle, such a change can be seen as a charge flow inside of the (insulating) sample, which cannot be conducted through the surface. Then, the polarization can be described by

$$\Delta \vec{P} = \int \mathrm{d}t \, \frac{1}{V_{\mathrm{Cell}}} \int_{\mathrm{Cell}} j(\vec{r}, t) \, \mathrm{d}\vec{r}, \tag{2.10}$$

which is the basic equation of the "modern theory of polarization" (compare Ref. [275]). Here, $j(\vec{r}, t)$ is the current density in space and time of the adiabatic current flow. Thus, in contrast to the initially presented approaches no static charge distribution is involved but rather a dynamic flow of charges, which represents the bulk behavior and is in principle insensitive to the surface.

Actually, the formulation of such a transient current is very similar to experimental measurements, such as a ferroelectric hysteresis loop, changing pressure (piezoelectricity) or temperature (pyroelectricity) measurements (see Sec. 3). Here, the polarization is also expressed as the polarization difference between the initial ($t = 0$) and the final state (after Δt), as given in Eq. (2.11). In order to ensure adiabatic conditions Δt has to be very small.

$$\Delta \vec{P} = \vec{P}(\Delta t) - \vec{P}(t = 0) = \int_0^{\Delta t} j(t) \, \mathrm{d}t. \tag{2.11}$$

With that premise a coherent theory to predict the polarization of a material from first principles was pioneered by KING-SMITH, VANDERBILT and RESTA in the 1990s [141, 274]. Their quantum theoretical description is built around the so-called BERRY phase, which is suitable to describe an adiabatic process cycle yielding a different state than the initial. This can be seen as a quantum-mechanical analogon to the switching of $\vec{P}$ in a hysteresis loop, which describes different polarization states depending on the history of the applied electric field. The acquired phase difference of the respective BLOCH wavefunctions, traveling through the BRILLOUIN zone, is called the "BERRY phase". The reformulation into so-called center of crystalline WANNIER functions, which can be constructed from the BLOCH wavefunctions, provide an equivalent description. More detailed information on the complex quantum-mechanical description can be found in Ref. [141, 274, 275].

In summary, the interpretation of the polarization as a surface charge density is an intuitive picture to depict the phenomenological behavior of a material but not useful for an appropriate microscopic description and, thus, theoretical predictions. In contrast to assessing the absolute polarization, which is hindered by the lack of true confinable polarization centers and surface effects, considering the change of polarization is more appropriate. So far, this dynamic charge flow approach enabled the computational calculation of several physical quantities related to the polarization of a dielectric, especially BORN effective charges $Z^*_{j,\alpha\beta}$ (change of the polarization divided by the amount of a displaced ion), piezoelectric coefficients $\overset{3\rightarrow}{d}_{ij}$ and the spontaneous polarization $\vec{P}_\mathrm{S}$. The latter is the premise for the pyro- and ferroelectricity of certain dielectrics, which is explained in more detail below.

2.3. Pyroelectricity

The pyroelectric effect is generally described as the change of the dielectric displacement $\vec{D}$ due to a change of temperature T. In contrast to the thermoelectric effect, i.e. the appearance of an electric potential due to a spatial temperature gradient at the junction of of two material wires with different SEEBECK coefficients, the pyroelectric effect appears only due to temporal changes of the temperature. The proportionality factor between the change of $\vec{D}$ and T is the pyroelectric coefficient $\vec{p}$, which is given by:

$$\vec{p} = \frac{\mathrm{d}\vec{D}}{\mathrm{d}T}. \tag{2.12}$$

To illustrate the effect, the change of $\vec{P}$ is again described as a change of the surface charge density perpendicular to the polar axis of the material (explanation see below), causing an electric field outside the sample. Free charge carriers from the surroundings medium compensate this arising electric field and, thus, reestablish charge neutrality of the whole system (middle of Fig. 2.4). Changing the materials temperature, either by heating (top) or cooling (bottom), alters the surface charge density which in turn requires more or less compensational charges. This change can be described with:

$$\mathrm{d}Q = p \cdot A \cdot \mathrm{d}T, \tag{2.13}$$

in which A is the area of the metallized electrodes, which form a parallel plate capacitor with the dielectric, and T the temperature. It is also important to bear in mind, that the pyroelectric coefficient is usually a negative quantity, as the polarization generally decreases with rising temperature. In most materials the structure can be set up in such a way that
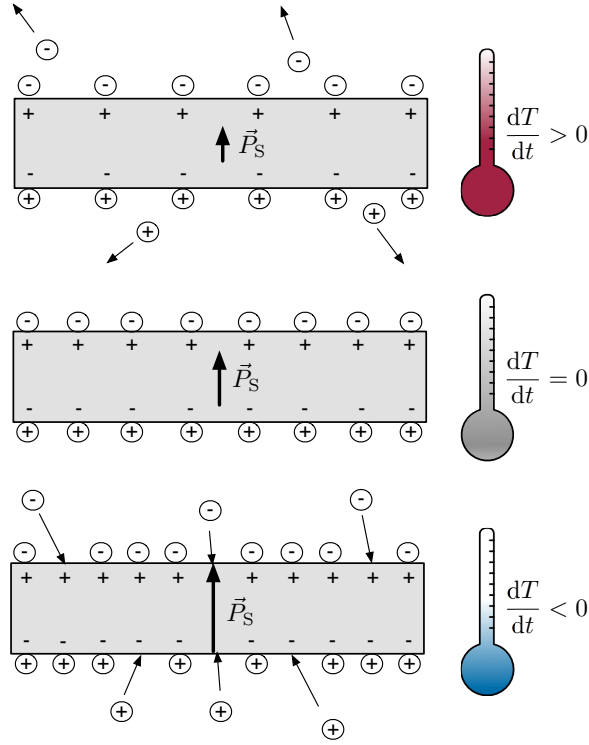
Fig. 2.4.: Phenomenology of pyroelectricity: A change of the spontaneous polarization $\vec{P}_\mathrm{S}$ due to heating (top) or cooling (bottom) and the accompanied flow of compensational charges. The center sketch represents thermal equilibrium.

the polar axis falls onto a unit cell axis resulting in a $\vec{p}$ with just one non-zero component, thus, only p_z (see below), is necessary. Therefore and for reasons of simplicity the absolute value of $\vec{p}$ is often used. Its time derivative gives the current flow I with

$$I = \frac{\mathrm{d}Q}{\mathrm{d}t} = p \cdot A \cdot \frac{\mathrm{d}T}{\mathrm{d}t}, \tag{2.14}$$

in which $\mathrm{d}T/\mathrm{d}t$ represents the rate of temperature change. Many principles to determine p rely on the measurement on the pyroelectric current I, as outlined in Sec. 3.

For the determination of p, careful considerations of the present conditions are the requisite as indicated by the red arrows in Fig. 2.1. When all involved state variables are unfixed, the total value of p is composed of four significant parts [191]:

$$p_n = \underbrace{\frac{\partial D_n}{\partial T}}_{p_\mathrm{prim}} + \underbrace{\sum_{i,j} \frac{\partial d_{nij}\sigma_{ij}}{\partial T}}_{p_\mathrm{sec}} + \underbrace{\sum_{i,j,k} \frac{\partial \mu_{nijk}\frac{\partial e_{ij}}{\partial r_k}}{\partial T}}_{p_\mathrm{tert}} + \underbrace{\sum_{i} \varepsilon_0 E_i \frac{\partial \varepsilon_{ni}}{\partial T}}_{p_\mathrm{fi}} + \dots, \tag{2.15}$$

in which $\overset{3\rightarrow}{d}$ is the piezoelectric tensor, $\overset{2\rightarrow}{\sigma}$ the mechanical stress, $\overset{4\rightarrow}{\mu}$ the flexoelectric tensor, $\overset{2\rightarrow}{e}$ the strain tensor, $\vec{r}$ the position vector. The indices n, i, j, k run over x, y, z and mark the tensor components[3]. The constituting parts of p are obtained by fixing different state variables, as denoted by the subscripts, which are:

---

[3]In rhombohedral, mono- and triclinic crystal systems a transformation from the crystal to the Cartesian coordinate system has to be performed [124].

- *primary* pyroelectric effect $p_{\text{prim}} = \left(\partial \vec{D}/\partial T\right)_{\overset{2\to}{e},\vec{E}}$ caused by the actual change of spontaneous polarization during temperature change [55, 161],

- *secondary* pyroelectric effect $p_{\text{sec}} = \left(\partial \vec{D}/\partial T\right)_{\overset{2\to}{\sigma},\vec{E}} - \left(\partial D/\partial T\right)_{\overset{2\to}{e},\vec{E}}$ arises from mechanical strain e and the piezoelectric effect due to the thermal expansion [55, 161],

- *tertiary* pyroelectric effect $p_{\text{tert}} = \left(\partial \vec{D}/\partial T\right)_{\overset{2\to}{\sigma},\vec{E}}$ produces a polarization change due to spatial strain gradients $\partial e/\partial r$, which can also be induced by non-uniform deformation during heating or cooling [52, 55, 161, 189], and

- *field-induced* pyroelectric effect $p_{\text{fi}} = \left(\partial \vec{P}_{\text{ind}}/\partial T\right)_{\overset{2\to}{e}}$ determined by the temperature dependence of the dielectric permittivity of materials in an external electric field ($\vec{E} \neq 0$).

Here, p_{prim} and p_{sec} are typically the most prominent, where p_{sec} is given from the difference between the pyroelectric coefficients at constant strain $p^{\overset{2\to}{e},\vec{E}} = \vec{p}_{\text{prim}}$ ($\overset{2\to}{e} = $ const.) and constant stress $\vec{p}^{\overset{2\to}{\sigma},\vec{E}}$ ($\overset{2\to}{\sigma} = $ const.) originating from piezoelectricity combined with thermal expansion [55, 161, 208, 233]. The connection can be deduced by transforming between the two GIBBS free energy densities $G(T, \overset{2\to}{\sigma}, \vec{E})$ and $G'(T, \overset{2\to}{e}, \vec{E})$, corresponding to these pyroelectric coefficients:

$$\vec{p}^{\overset{2\to}{e},\vec{E}} = -\left(\frac{\partial^2 G'(T, \overset{2\to}{e}, \vec{E})}{\partial \vec{E} \partial T}\right)_{\overset{2\to}{e},\vec{E}} = \left(\frac{\partial \vec{D}}{\partial T}\right)_{\overset{2\to}{e},\vec{E}} = p_{\text{prim}}, \tag{2.16}$$

$$\vec{p}^{\overset{2\to}{\sigma},\vec{E}} = -\left(\frac{\partial^2 G(T, \overset{2\to}{\sigma}, \vec{E})}{\partial \vec{E} \partial T}\right)_{\overset{2\to}{\sigma},\vec{E}} = \left(\frac{\partial \vec{D}}{\partial T}\right)_{\overset{2\to}{\sigma},\vec{E}} = p_{\text{prim}} + p_{\text{sec}}. \tag{2.17}$$

With Eq. (2.16) and (2.17) and by neglecting changes of the electric field ($\mathrm{d}E = 0$) the differential of the dielectric displacement $\vec{D}$ can be written as:

$$\mathrm{d}\vec{D} = \vec{p}^{\overset{2\to}{e}} \, \mathrm{d}T + \left(\frac{\partial \vec{D}}{\partial \overset{2\to}{e}}\right)_T \mathrm{d}\overset{2\to}{e}, \tag{2.18}$$

$$\mathrm{d}\vec{D} = \vec{p}^{\overset{2\to}{\sigma}} \, \mathrm{d}T + \left(\frac{\partial \vec{D}}{\partial \overset{2\to}{\sigma}}\right)_T \mathrm{d}\overset{2\to}{\sigma}. \tag{2.19}$$

The differential $\mathrm{d}\overset{2\to}{e}$ in (2.18) is now expressed as $\mathrm{d}\overset{2\to}{e}(T, \overset{2\to}{\sigma}, \vec{E})$ resulting in:

$$\mathrm{d}\vec{D} = \vec{p}^{\overset{2\to}{e}} \, \mathrm{d}T + \left(\frac{\partial \vec{D}}{\partial \overset{2\to}{e}}\right)_T \left[\left(\frac{\partial \overset{2\to}{e}}{\partial T}\right)_{\overset{2\to}{\sigma}} \mathrm{d}T + \left(\frac{\partial \overset{2\to}{e}}{\partial \overset{2\to}{\sigma}}\right)_T \mathrm{d}\overset{2\to}{\sigma}\right]. \tag{2.20}$$

A coefficient comparison for $\mathrm{d}T$ between (2.19) and (2.20) yields the following relation:

$$\vec{p}^{\overset{2\to}{\sigma}} = \vec{p}^{\overset{2\to}{e}} + \left(\frac{\partial \overset{2\to}{e}}{\partial T}\right)_{\overset{2\to}{\sigma}} \left(\frac{\partial \vec{D}}{\partial \overset{2\to}{e}}\right)_T = \vec{p}^{\overset{2\to}{e}} + \left(\frac{\partial \overset{2\to}{e}}{\partial T}\right)_{\overset{2\to}{\sigma}} \left(\frac{\partial \overset{2\to}{\sigma}}{\partial \overset{2\to}{e}}\right)_T \left(\frac{\partial \vec{D}}{\partial \overset{2\to}{\sigma}}\right)_T. \tag{2.21}$$

Thus, the secondary pyroelectric coefficient (at constant electric field $\vec{E}$) is given by

$$\vec{p}_{\text{sec}} = p^{\overset{2\to}{\sigma},\vec{E}} - p^{\overset{2\to}{e},\vec{E}} = \overset{2\to}{\alpha}^{\overset{2\to}{\sigma},\vec{E}} \overset{4\to}{c}^{T,\vec{E}} \overset{3\to}{d}^{T,\vec{E}}. \tag{2.22}$$

The parameter $\overset{2\to}{\alpha}\,^{\overset{2\to}{\sigma},\vec{E}} = \left(\partial^2 \vec{e}/\partial T\right)_{\overset{2\to}{\sigma},\vec{E}}$ is the thermal expansion tensor, $\overset{4\to}{c}\,^{T,\vec{E}} = \left(\partial^2 \overset{\to}{\sigma}/\partial^2 \vec{e}\right)_{T,\vec{E}}$ is the elastic stiffness tensor and $\overset{3\to}{d}\,^{T,\vec{E}} = \left(\partial \vec{D}/\partial^2 \overset{\to}{\sigma}\right)_{T,\vec{E}}$ is the piezoelectric stress coefficient. While the measurement at constant strain (totally clamped condition) is defined as the primary pyroelectric coefficient ($\overset{2\to}{p}\,^{\vec{e},\vec{E}} = p_{\mathrm{prim}}$), the measurement at constant stress (free expansion) yields the sum of primary and secondary pyroelectric coefficient ($\overset{2\to}{p}\,^{\overset{\to}{\sigma},\vec{E}} = p_{\mathrm{prim}} + p_{\mathrm{sec}}$).

At this point it is important to note that the behavior of an electret can be confused with a pyroelectric, especially when polymers are the object of interest [191]. Their non-vanishing polarization in the absence of an electric field does not necessarily originate from the crystal structure. It can be produced by a spatial separation of *frozen-in* positive and negative charge carriers stemming from a previous treatment. This is also referred to as *quasi-permanent electrical charges*, because the time constant of the charge decay can be up to several years [308]. Therefore also electrets show a hysteresis, which usually identifies a ferrorelectric. Only hysteresis measurements (see Sec. 3.2) at different frequencies reveal the underlying source of polarization, because unlike in electrets the hysteresis of a proper ferroelectric changes only little with frequency [259].

Apart from inorganic and organic materials also composites of both are often investigated, to combine for example beneficial mechanical and electrical properties of two material [101, 234, 262, 286, 377]. A general formula to assess the effective pyroelectric coefficient p of a composite with two constituents, e.g. a matrix and an inclusion material, was given by PLOSS *et al.* [261] with

$$p = \frac{\varepsilon - \varepsilon_{\mathrm{m}}}{\varepsilon_{\mathrm{i}} - \varepsilon_{\mathrm{m}}}p_{\mathrm{i}} + \frac{\varepsilon_{\mathrm{i}} - \varepsilon}{\varepsilon_{\mathrm{i}} - \varepsilon_{\mathrm{m}}}p_{\mathrm{m}}, \qquad (2.23)$$

in which ε is the effective permittivity of the composite and the indices m and i label the pyroelectric coefficient and permittivity of the matrix and the inclusion material, respectively.

Although pyroelectricity can be understood as a coupling between dielectric properties and fluctuations in the phonon density distribution caused by temperature changes, a theoretical prediction of $p(T)$ is very complex [45]. After the first quantitative measurements of the pyroelectric coefficient by ACKERMANN [4] in 1915 a model to describe the temperature behavior of p, especially at low temperatures, was given by BORN in 1945 [26]. Using quantum theory, the dynamical, electromagnetic, and optical properties of lattices were provided, including a description of primary and secondary pyroelectricity. BORN predicted a linear dependency of the pyroelectric coefficient on temperature ($p \propto T$) [26], aided by the experimental data of ACKERMANN. Although his initial statements were correct, giving the later accepted $p \propto T^3$ dependency, he adjusted the anharmonic terms in order to match the experimental data [80, 336].

After a dispute between SZIGETI and GROUT [99, 335, 336] in 1975/1976, the correlation $p \propto T^3$ and thus $p \propto C_{\mathrm{V}}$ stemming from the acoustic phonon contributions, is finally the generally accepted model of p at low temperatures. The approach by SZIGETI [336] defines the dipole density as the macroscopic dipole moment divided by the number of moles, which can be expressed as a power series with respect to little disturbances from the equilibrium state. Such disturbances stem from lattice vibrations, which can be described with lattice dynamical theory and especially with phonon modes responsible for the specific heat C_{V} [336]. Even the split-up of this expression into transversal and longitudinal modes shows T^3 dependency of each contribution. Thus, the whole expression is proportional to T^3, which

justifies the use of the DEBYE model, which describes the specific heat C_V, to predict the pyroelectric coefficient p at low temperatures. The $p \propto T^3$ behavior was later also confirmed by RADEBAUGH in 1978 using the third law of thermodynamics [273]. It has to be noted that the T^3 dependency applies for both, the primary and secondary pyroelectric coefficient, p_{prim} and p_{sec} respectively, as at least the thermal expansion $\overset{2\rightarrow}{\alpha}$ is also proportional to T^3 [82, 336].

While for $T \rightarrow 0$ the pyroelectric coefficient and specific heat are dominated by acoustic phonons, optical contributions increase at higher temperatures (above approximately $100\,\mathrm{K}$ [107, 174, 273]). Thus, a combination of the DEBYE model (for dominating acoustic phonons at low temperatures) and the EINSTEIN model (for dominating optical phonons at higher temperatures) has to be used in order to describe the temperature dependency of the pyro-electric coefficient [82, 310, 370]. Interestingly, the contribution of optical branches is more pronounced in ferroelectrics than in pure pyroelectrics [82] and dominates at high temperatures (above $20\,\mathrm{K}$ [174]). The resulting DEBYE-EINSTEIN model was given by GAVRILOVA *et al.* [82] with

$$p(T) = A \cdot \mathrm{D}(T/T_{\mathrm{D}}) + \sum_n B_n \cdot \mathrm{E}(T_{\mathrm{E}n}/T)$$

$$= A \cdot \left[\left(\frac{T}{T_{\mathrm{D}}}\right)^3 \int_0^{T_{\mathrm{D}}/T} \frac{\exp(x) \cdot x^4}{(\exp(x)-1)}\,\mathrm{d}x \right] + \sum_n B_n \cdot \left[\frac{\exp(T_{\mathrm{E}n}/T)}{(\exp(T_{\mathrm{E}n}/T)-1)^2} \right], \quad (2.24)$$

in which D and E are the DEBYE and EINSTEIN functions, respectively, and T_{D} and $T_{\mathrm{E}n}$ the corresponding DEBYE and EINSTEIN temperatures. A and B are scaling factors for each contribution having dimensions of a pyroelectric coefficient ($\mathrm{C\,K^{-1}\,m^{-2}}$). At this point it has to be noted that the mentioned temperatures may vary from those obtained by heat capacity measurements, because the underlying models are different, i.e. defining a power series with displacements of atoms for $C_V(T)$ and of a dipole density for $p(T)$. The latter includes also anharmonic contributions, while for the former only harmonic oscillators are involved [82].

It was assumed for a long time that the DEBYE integral has no analytical solution, which hinders its fitting to experimental data. A numerical solution is also hard to compute due to T_{D} in the upper limit of the DEBYE integral. Fortunately, DUBINOV *et al.* derived an exact integral-free expression of the DEBYE integral [63], which can be used for data fitting:

$$\mathrm{D}(x) = \frac{4}{5}\frac{\pi^4}{x^3} + \frac{3x\exp(-x)}{[\exp(-x)-1]} + 12\ln[1-\exp(-x)]$$

$$- \frac{36}{x}\mathrm{Li}_2[\exp(-x)] - \frac{72}{x^2}\mathrm{Li}_3[\exp(-x)] - \frac{72}{x^3}\mathrm{Li}_4[\exp(-x)]. \quad (2.25)$$

Here, the polylogarithm functions $\mathrm{Li}_s(x) = \sum_{k=1}^{\infty} x^k/k^s$ are used[4] and x has to be replaced by T_{D}/T. A PYTHON script providing a fitting algorithm of measured $p(T)$ data to Eq. (2.24) with the help of Eq. (2.25), was developed during this work and is available at `https://github.com/SvenJachalke/DEF`.

Deviations from the model given above stem from the pronounced anharmonic processes at higher temperatures as well as from a large amount of defects [82]. Nevertheless, good agreement between theoretical and experimental data using the DEBYE-EINSTEIN model were already obtained for a variety of materials, e.g. LiNbO$_3$ [310], AlN [312], ZnO [82],

---

[4]The first two members are $\mathrm{Li}_0(x) = \frac{x}{1-x}$ and $\mathrm{Li}_1(x) = -\ln(1-x)$.

ZnS [82] or triglycine sulphate (TGS) [82], to name only a few. In addition to the DEBYE-
EINSTEIN model also density functional perturbation theory (DFPT) approaches emerged
only in the last years, e.g. Ref. [179–181], to predict $p(T)$ from first principles and is still
under investigation and improvement.

2.4. Ferroelectricty

The spontaneous polarization $\vec{P}_S$ of ferroelectric materials, as the smallest subgroup in
Fig. 2.2, may switch between two stable orientations by applying a sufficient electric field
$\vec{E}$ higher than the coercive field strength E_C. Thus, polar crystals, whose polarization is not
switchable by an external electric field, e.g. the materials GaN or AlN in this work, are only
pyro- but not ferroelectric.

Unfortunately, there are no further crystallographic restrictions to distinguish a ferroelectric
from a pyroelectric solely from symmetry considerations. Here, the principle that a polar
ferroelectric structure is typically a "small" symmetry-breaking distortion from a non-polar
higher-symmetry structure is useful [271]. ABRAHAMS developed an empirical structural
criterion to predict ferroelectricity from crystallographic information. It states that the max-
imum displacement Δz along the polar axis with respect to the non-polar reference structure
has to be larger than 0.1 Å and must not exceed 1 Å [1]. The criterion was initially proposed
for $6mm$ point group symmetry [1] and, thus, also holds for the investigated III-nitride ma-
terial system presented in Sec. 5.1.1. It was also extended to other point and space groups
later [2]. Furthermore, it is very useful for systematic structure and polarization predictions
using first-principle calculations, by using unstable phonon modes as guides to find the lowest
energy in distorted structures [271, 272].

A material with a polar structure that is just slightly distorted from its high-symmetry non-
polar reference phase is $BaTiO_3$ with its polar low temperature phases, i.e. rhombohedral
(space group $R3m$), orthorhombic ($Amm2$) and tetragonal ($P4mm$) phase and its high tem-
perature non-polar cubic phase ($Pm\bar{3}m$) [5]. The difference between tetragonal $P4mm$ and
cubic $Pm\bar{3}m$ is exemplified in Fig. 2.5. All mentioned structures are quite similar, but the
displacement of the B-site cation titanium (Ti) within the oxygen (O) octahedron is the
pronounced structural distortion, which leads to the dipole moment and spontaneous polar-
ization $\vec{P}_S$ within the unit cell and, thus, is responsible for the polar properties.
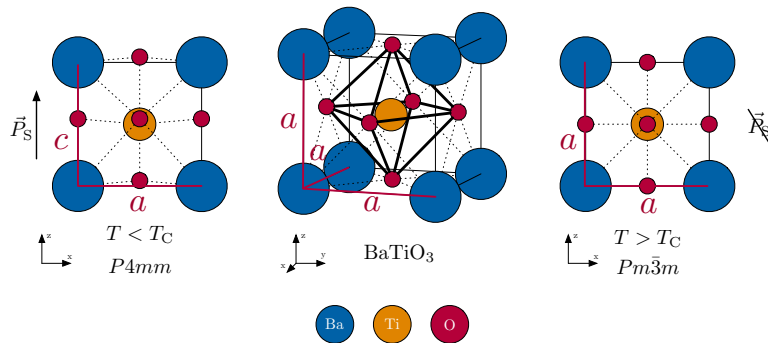
Fig. 2.5.: General perovskite structure of cubic $BaTiO_3$ (center). The tetragonal low temperature (left)
and cubic high temperature (right) modification show the appearance and disappearance of the spontaneous
polarization $\vec{P}_S$.

Furthermore, $BaTiO_3$ is a good example for a displacive ferroelectric, which is marked by a microscopic spontaneous polarization, e.g. by the off-center position of titanium in oxygen octahedron, being absent in its corresponding high temperature phase. The other type is an order/disorder ferroelectric with a microscopic polarization even in the high-temperature phase. In this case, the loss of macroscopic polarization is due to a random orientation of the microscopic dipole moments, which is, for instance, the case in the non-polar α-phase of the organic polymer polyvinylidene fluoride (PVDF).

The phenomenological characteristic of a ferroelectric is the appearance of a hysteresis loop, i.e. the strong non-linearity when measuring the polarization $\vec{P}$ with respect to an applied electric field $\vec{E}$, as shown in Fig. 2.6[5]. The ferroelectric hysteresis itself provides insight to several important parameters:

- coercive field strength E_C, at which $\vec{P} = 0$, i.e. opposing dipole orientations cancel out the macroscopic polarization. It can be obtained from the intercept of the hysteresis loop with the abscissa,

- saturation polarization P_{sat}, marking the entire parallel alignment of the dipoles at high electric fields (but below the breakdown field E_B); Above P_{sat} a linear change of $\vec{P}$ with rising $\vec{E}$ is restored [5],

- remanent polarization P_R, marking the remaining polarization at $E = 0$, which can be obtained from the intercept of the hysteresis loop with the ordinate axis, and

- spontaneous polarization P_S, which can be estimated from extrapolating the linear polarization course near P_{sat} back to $\vec{E} = 0$ [5].

At this point it has to be noted, that these different polarizations are often falsely used in the literature, i.e. P_S used for P_{sat} or P_S instead of P_R. Also it is important to bear in mind that a low sample resistivity (leaky dielectric) produces higher values for P_R and deformed hysteresis shapes, which has already led to misinterpretation of ferroelectricity in various materials [304]. For the sake of completeness, the switching of P_S results also in a mechanical strain e. The resulting e-E loop has a butterfly shape, which is also shown in Fig. 2.6 and constitutes another important characteristic of a ferroelectric.

In contrast to a ferroelectric, a pure dielectric material is marked by a linear dependency of P on E (see Fig. 2.7(b)). A paraelectric material is characterized by microscopic dipole moments, which get saturated at high electric fields (see Fig. 2.7(c)). While the blue lines in Fig. 2.7 show the ideal behavior for samples with an infinite resistivity (no losses due to ohmic conductivity), the red lines give an impression of how these shapes are deformed by a finite sample resistivity. Experimental considerations and interpretations of P-E measurements are outlined in Sec. 3.2.2.

To understand the switching of $\vec{P}_S$ in a ferroelectric material the knowledge of its domain structure is essential. A ferroelectric domain is a small 3-dimensional volume of constant value and parallel orientation of the dipole moments. Due to minimization of elastic and electrostatic energies, a ferroelectric solid is built of numerous domains separated by domain walls [5, 359]. Besides this, also non-uniform strain, microscopic defects and the thermal

---

[5]The vector arrows are omitted as the practical application and measurement of the electric field and polarization, respectively, involves only one component.
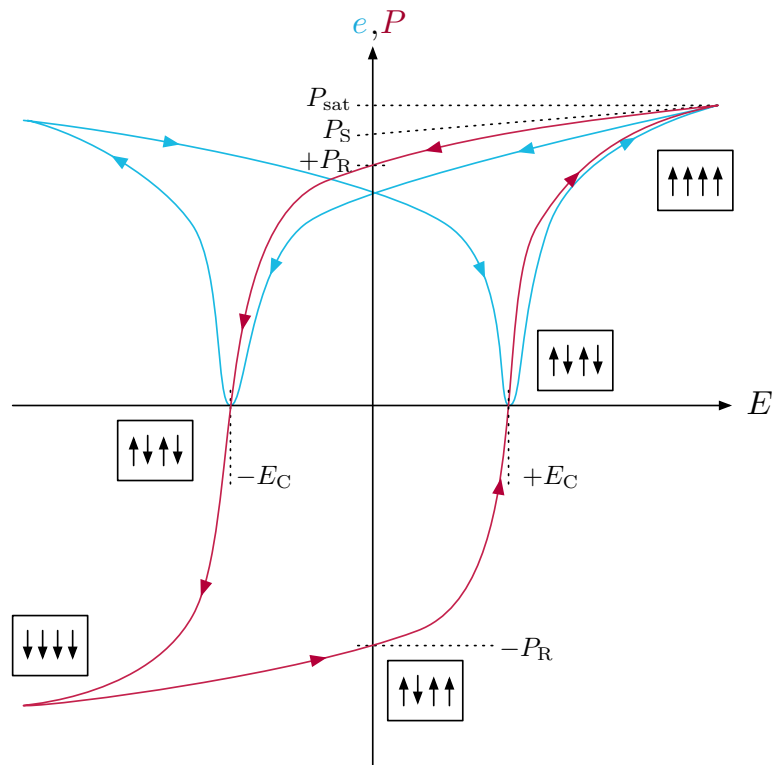
Fig. 2.6.: General shape of the ferroelectric hysteresis loop in a polarization P versus electric field E measurement (red). The butterfly loop is the varying mechanical strain e under applied electric field (cyan). P_{sat}, P_{S} and P_{R} are the saturation, spontaneous and remanent polarization, respectively. E_{C} marks the coercive field strength. The boxed arrows visualize the orientations of domains inside the material at different stages of the hysteresis.

(a) Ferroelectrics   **(b)** Dielectrics   **(c)** Paraelectrics
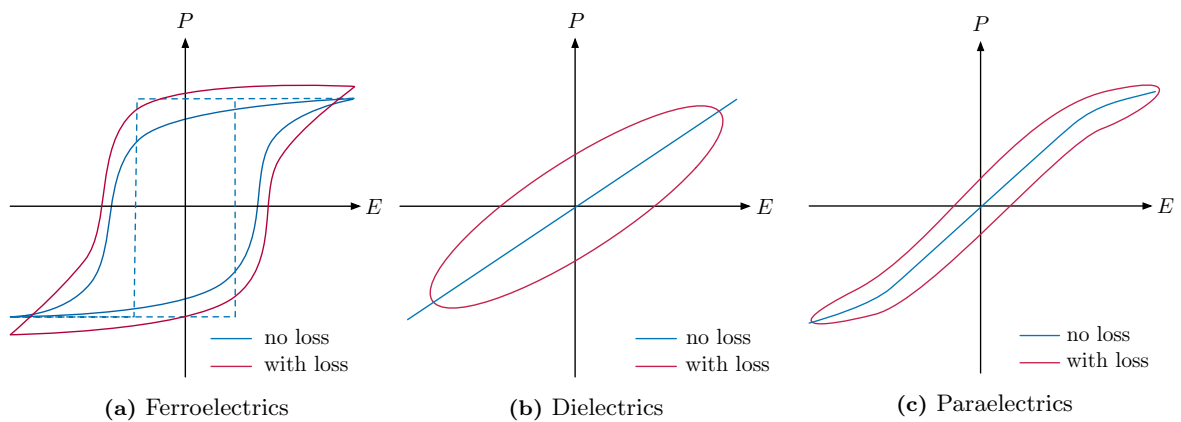
Fig. 2.7.: Polarization P versus electric field E below (a) and above (b,c) the CURIE temperature T_{C} in the ideal (infinite sample resistance) and real (finite sample resistance) case. The dashed blue line indicates the fictional single-domain switching.

(a) 180° (left) and 90° (right) domain configuration.

(b) Ising-type domain wall: Sole change of the magnitude of $|\vec{m}|$.

(c) Bloch-type domain wall: Out-of-plane rotation (while keeping its magnitude) of $\vec{m}$.

(d) Nèel-type domain wall: In-plane rotation (while keeping its magnitude) of $\vec{m}$.
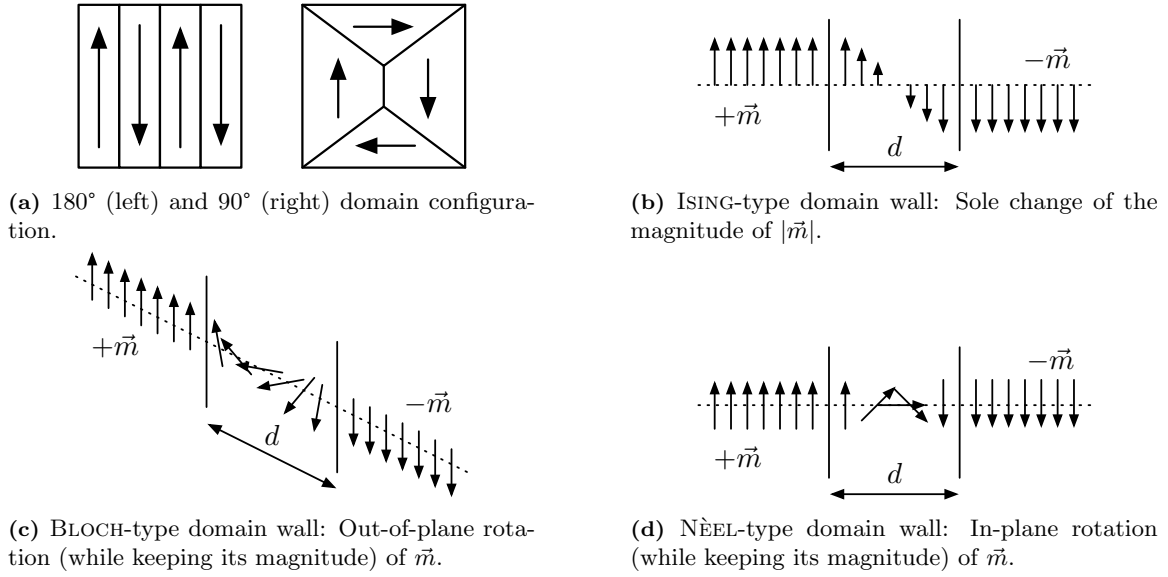
Fig. 2.8.: Possible ferroelectric domain configurations of a tetragonal structure (a) and the conception of the continuous flipping of the dipole moment $\vec{m}$ in a domain wall of width d (b). Redrawn from Ref. [359] and Ref. [104].

and electrical history can lead to a formation of domains [36]. Depending on the actual crystallographic structure, different orientations of neighboring domains are possible, e.g. 60°, 90°, 120° and 180° for an orthorhombic system [5]. Fig. 2.8(a) depicts 180° and 90° domains, which are typical for a tetragonal system, such as room-temperature $BaTiO_3$. Here, only a switching of 180° domains contributes to a reduction of electrostatic energy, while the 90° configurations are responsible for the minimization of elastic energy, also known as ferroelastic switching [5].

The switching mechanism of $\vec{P}_S$ due to the application of an external electric field can be quite complex and is typically understood as a motion of domain walls, i.e. assembling and dismantling of parallel polarization, which occurs on length scales of a few unit cells [5, 104, 271]. As shown in Fig. 2.8, inside the wall of width d between two domains the polarization steadily flips over to its reverse state, when applying an external electric field parallel to the polar axis. Originating from a ferromagnetic different types of domain wall exist, which are Ising type (change of magnitude but no rotation of $\vec{P}_S$), Bloch type (no change of magnitude but out-of-plane rotation of $\vec{P}_S$) and Nèel type (no change of magnitude but in-plane rotation of $\vec{P}_S$) as summarized in Fig. 2.8(b), Fig. 2.8(c), and Fig. 2.8(d), respectively [104]. Also a mixed domain wall type (Ising-Bloch or Ising-Nèel) is possible, especially in thin films [104]. Thus, the successive switching of dipole moments moves the domain wall depending on the field direction. Furthermore, the switching is considered as a nucleation-based process, i.e. an initially switched seed domain forces surrounding domains to switch to the same polarity until P_{sat} is reached [280, 352]. Structural imperfections of the material ("defects") can hinder the motion of domains. Such pinned domains cannot contribute to a switching of $\vec{P}_S$. As a final note, the switching of domains due to an external force is connected with an unwanted loss of energy to the material, typically released in form of heat [5]. A good review on the different loss mechanisms is given by Ref. [178].

2.5. Phase Transitions

Coupling phenomena such as pyro- and ferroelectricity do not persist over the entire range of the thermodynamic state variables but are rather linked to certain phases, which mark ranges of the state variables with the same features. Thus, properties may be lost or gained in transitions into other phases.

Regarding the state variable temperature, the most important is the CURIE temperature T_C, which is adopted from the CURIE-WEISS law of the magnetic susceptibility. Above T_C the material transforms into a non-polar phase, which represents the disappearance of the desired properties and, thus, is of profound practical importance. In the non-polar phase the hysteresis and, thus, also P_S and p vanish. Beside T_C there can be more phase transition temperatures connecting different polar phase, e.g. for $BaTiO_3$ (see Sec. 2.4). For crystalline materials such a phase transition is typically accompanied by a symmetry ascent of the underlying crystal structure, which often ends in a cubic phase as the highest possible symmetry. Due to the switching behavior of a ferroelectric, it can be repolarized after this phase transition by applying an external electric field during the cooling back to its polar phase. Depending on the polarization character, i.e. displacive or order/disorder type [175], either a dielectric or paraelectric phase exists at high temperatures (see Fig. 2.2 and Fig. 2.7), respectively. ABRAHAMS also provided an empirical relation[6] between the displacement relative to the non-polar reference phase and the value of T_C [1, 3, 271]. Although T_C is a parameter of a ferroelectric, pure pyro- and/or piezoelectrics can have a critical temperature, which is not necessarily named as such. Beside other material properties, e.g. heat capacity or dielectric permittivity, the pyroelectric coefficient is a very sensitive indicator for phase transitions, especially for the transition from a polar to another polar phase [150].

For a theoretical description of polar/non-polar phase transitions the LANDAU theory, i.e. a symmetry-based approach to describe the discontinuous transition between two distinct phases, was adopted by DEVONSHIRE for ferroelectrics [36, 60]. Basically, the transition is described with a certain order parameter, which is zero in the high-symmetry phase and changes continuously with descending symmetry. Obviously, in the case of a ferroelectric this order parameter is the polarization, which changes by surpassing T_C. While there is excellent literature covering this topic in much more detail (see Ref. [36, 96, 176]), the following should serve as a short summary, following the didactics of Ref. [36].

At first, the LANDAU-DEVONSHIRE theory assumes a spatially uniform polarization [36]. Then, the GIBBS free energy density G[7] is expressed as a power series of the order parameter polarization P, which is limited to symmetry allowed terms only and ignoring other state variables like mechanical strain. The free-energy is then given by:

$$F(P) = \frac{1}{2}aP^2 + \frac{1}{4}bP^4 + \frac{1}{6}cP^6 - EP. \qquad (2.26)$$

Here, a, b and c are coefficients, which characterize the transition type. Eq. (2.26) is typically truncated after the sixth term, but in some cases more terms can be necessary for an appropriate description, e.g. for PZT [36]. The parameter a is equivalent to the inverse of

---

[6]$T_C = (F/2k_B)(\Delta z)$, in which F is a force constant, k_B the BOLTZMANN constant and Δz the atomic displacement in z-direction with respect to non-polar high-temperature phase. The factor $F/2k_B$ is empirical and approx. $2 \times 10^4 \, K \, Å^{-2}$ [1].

[7]$G = F - EP$ [75].

the dielectric susceptibility χ above the transition[8], which has to follow the CURIE-WEISS law. Thus, a is given by

$$a = \frac{1}{\chi} = a_0(T - T_0), \tag{2.27}$$

in which T_0 corresponds to the CURIE temperature and a_0 is proportional to the inverse CURIE constant. The free energy below and above T_0 is exemplified in Fig. 2.9 showing that the ferroelectric phase is characterized by two local minima of P, which allows switching. In Eq. (2.26) only a is considered to be temperature-dependent, while b and c are not. Furthermore, a_0 and c are positive for all known ferroelectrics [36], thus, only b remains to become positive or negative and define the type of phase transition.

For $b < 0$ the transition is of second-order type, i.e. showing a continuous transition to $P = 0$ with rising temperature, which is typical for triglycine sulfate (TGS) [75]. The spontaneous polarization and dielectric susceptibility below the transition can be described by

$$P_S(T) = \sqrt{\frac{a_0}{b}(T_0 - T)} \text{ and} \tag{2.28}$$

$$\chi(T) = \frac{1}{2a_0(T_0 - T)}, \tag{2.29}$$

respectively and are depicted in Fig. 2.9(a). From Eq. (2.29) it is obvious that χ diverges at T_0, which corresponds to very large values for real materials. It has to be noted that such anomalies during a phase transition are also present for other material properties, e.g. specific heat.

Consequently, $b > 0$ defines a first-order phase transition, which can be found for example in BaTiO$_3$ [75]. Here, a negative b (with positive a and c) yields additional local minima for $F(P)$ in the non-polar state ($T > T_C$, see Fig. 2.9(b)). When a is reduced, which means that T is lowered, only two minima remain below T_C and $F(P)$ has the typical ferroelectric shape. However, T_C lies above T_0 and in between the non-polar phase exists as an additional local minimum in $F(P)$. At T_C, the order parameter changes discontinuously and drops abruptly to $P = 0$, while χ does not diverge as for a second-order phase transition (compare Fig. 2.9). The spontaneous polarization below T_C is given by [75]:

$$P_S(T) = \sqrt{-\frac{b}{2c}\left(1 + \sqrt{1 - \frac{4a_0 c(T - T_0)}{b^2}}\right)} \tag{2.30}$$

Here, also a transition enthalpy is necessary to achieve the first-order transition, which is typical for e.g. the change from the solid to liquid state [36, 75]. Since $F(P)$ has three degenerated minima at T_C (see Fig. 2.9(b)) the material exhibits a thermal hysteresis, i.e. the transition occurs below or above T_C, when the material is cooled or heated.

As mentioned by CHANDRA et al. clamping effects, especially in thin films, can significantly shift the transition temperature as well as the overall type of transition [36]. Furthermore, the general assumption of a uniform polarization of a bulk material is obsolete when considering thin film ferroelectrics, in which the domain structure is highly affected by the sample geometry. This non-uniformity with small spatial fluctuations in $\vec{P}$ is expressed by spatial gradients and is known as the LANDAU-GINZBURG theory. Although HfO$_2$ thin films are topic of this work but exhibit no phase transitions in the investigated temperature range

---

[8]An expression for $E(P)$ can be obtained by minimizing $F(P)$ and solving for $P = 0$.
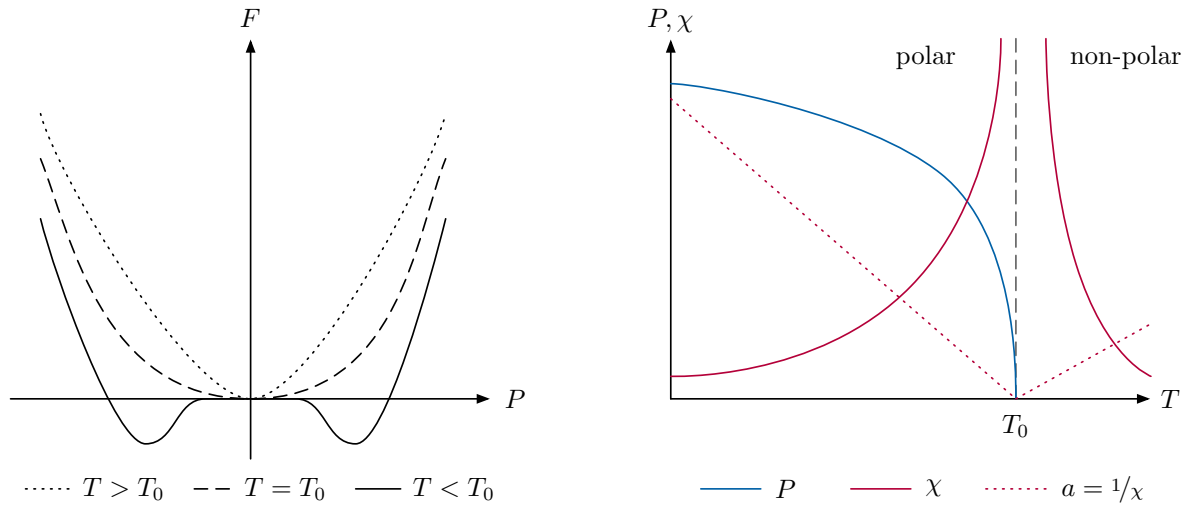
(a) 2nd order phase transition.
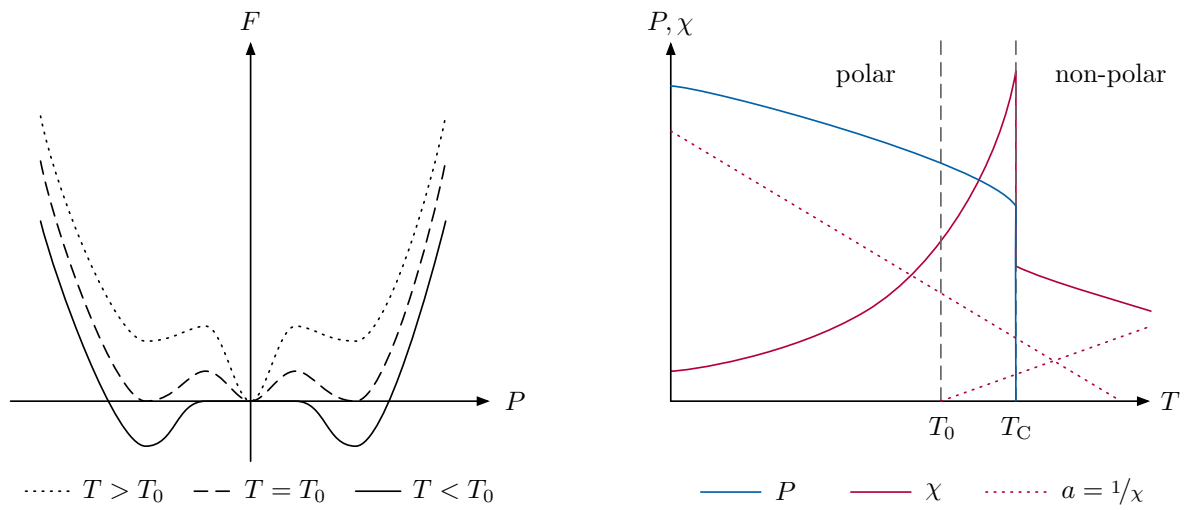
(b) 1st order phase transition.

Fig. 2.9.: Development of the free energy F with respect to polarization P (left) and polarization P as well as dielectric susceptibility χ with respect to T (right) for different types of phase transitions. Redrawn from Ref. [36].

(see Sec. 6.2) the interested reader is referred to the references mentioned above for more details.

In summary, the presented phenomenological theory of phase transitions is a powerful tool to investigate and optimize different materials but it is only as good as its input parameters. Appropriate coefficients for the power series can either be obtained by fitting experimental data or using first-principle calculations [36]. Thus, the phenomenological LANDAU-DEVONSHIRE-GINZBURG theory serves as a bridge between theory and experiment.

2.6. Applications and Figures of Merit

Besides being of fundamental interest, pyro- and ferroelectric materials offer a wide field of applications. While some of them have already made the step into mass production, a lot of them are still under development. As pyroelectrics are the main topic of this work, the following will focus on their applications.

The utilization of pyroelectric materials in commercial applications started in the 1960's with the usage in radiation detectors [160]. Since then, new application fields such as waste heat harvesters [152, 166, 205, 230, 235, 240], X-ray generators [31], pyroelectrocatalytic disinfection [103], radical [18] and hydrogen production [9, 135], as well as electrocaloric cooling [158] were investigated, but have not developed beyond laboratory scale yet.

By far the most utilized application is the uncooled detection of infrared (IR) radiation, i.e. converting wave lengths between $0.7\,\mu m$ to $1\,mm$ into an electrical signal, for in example in contactless thermometers (pyrometer) or motion detectors [160, 161, 163, 362]. Besides this BATRA and AGGARWAL listed about 49 specific applications, ranging from research, medical, industrial and government/military applications, such as gas analyzers, flame detection and broadband THz detectors [12]. The main advantages of a pyroelectric detector compared to a photon detector are the fast response time, very large spectral bandwidth, sensitivity in a wide temperature range, no need for additional detector cooling, low power requirements and low costs of production [12, 160]. The standard design of such a sensor is shown in Fig. 2.10. A $2\,mm \times 2\,mm$ LiTaO$_3$ single crystal of approximately $100\,\mu m$ thickness is commonly used as the active conversion material up to now. Thin metal layers as well as an additional absorption layer are necessary for the electrical connection and heat absorption, respectively. The latter is often realized as a black metal oxide or in form of a thin metal coating [12]. An attached transistor (e.g. JFET, MOSFET) or an operational amplifier is responsible for the detection of small charge changes. In order to correct a drift of the ambient temperature or piezoelectric microphonic noise from vibrations of the surrounding, the sensor is typically designed as a double element detector, in which two identical pyroelectrics are connected in parallel with opposite polarity. Here, only one active element is exposed to the IR radiation, while the other one is "blind". With this, the incident radiation can be distinguished from influences of the surrounding, because the latter affect both elements and, thus, cancel out perturbations [12].

As a lot of different detector designs emerged in the last decades, three specific figures of merit (FOM) were introduced to quantify the performance of the active pyroelectric material: The current responsivity

$$F_{\mathrm{I}} = \frac{p}{\rho c_p} \tag{2.31}$$

characterizes the maximum current, which can be generated. The voltage responsivity

$$F_{\mathrm{V}} = \frac{p}{\rho c_p \varepsilon_0 \varepsilon_{\mathrm{r}}} \tag{2.32}$$

characterizes the maximum voltage output. The detectivity

$$F_{\mathrm{D}} = \frac{p}{\rho c_p \sqrt{\varepsilon_0 \varepsilon_{\mathrm{r}} \tan \delta}}. \tag{2.33}$$

provides the voltage responsivity with the optimal signal-to-noise ratio. Here, p is the pyroelectric coefficient, ε_0 the permittivity of free space, ε_{r} the relative permittivity, $\tan \delta$ the dielectric loss tangent, ρ the mass density and c_p the specific heat capacity of the material at constant pressure [30, 362]. It has to be noted that the relevant FOM depends on the frequency range in which the detector operates (for more details see Ref. [258]). Furthermore, specific detectivities can be defined to analyze noise sources at different operation frequencies of the detector. While the JOHNSON noise of the preamplifiers resistance dominates at low frequencies, dielectric loss and preamplifier input voltage noise prevail at mid and high frequencies, respectively [373].

FOMs were also introduced for pyroelectric energy harvesting applications quantifying the materials capability to convert thermal into electrical energy. How much electrical energy can be harvested is given by [306]

$$F_{\mathrm{E}} = \frac{p^2}{\varepsilon_0 \varepsilon_{\mathrm{r}}}, \tag{2.34}$$

which was slightly modified by BOWEN *et al.* [29] to include the heat capacity c_p with

$$F_{\mathrm{E}}' = \frac{p^2}{\varepsilon_0 \varepsilon_{\mathrm{r}} \cdot (\rho c_p)^2}. \tag{2.35}$$

to show that beside a large p and low ε_{r} also a small c_p (step temperature rise) is necessary to maximize harvestable energy. The electro-thermal coupling factor k^2, a dimensionless number, characterizes the conversion efficiency of a pyroelectric material by [230]

$$k^2 = \frac{p^2 T_{\mathrm{h}}}{\rho c_p \varepsilon_0 \varepsilon_{\mathrm{r}}}. \tag{2.36}$$

Here, T_{h} is the upper temperature during the heat regeneration process.

Clearly, p, $\varepsilon = \varepsilon_0 \varepsilon_{\mathrm{r}}$, c_p and ρ determine the FOMs and, thus, are the subject of optimization. Therefore, its precise determination is essential to assess and maximize the performance of a pyroelectric material in an application or device.

Considering alternative pyroelectrics for a sensor application, LIU *et al.* reported that $p/\sqrt{\varepsilon}$ for displacive and order/disorder ferroelectrics (and, thus, all pyroelectrics) is nearly constant, although both parameters have a strong temperature dependency [182]. Furthermore, with LANDAU-DEVONSHIRE theory, the exact and material-independent value of this relation is derivable as

$$\frac{p}{\sqrt{\varepsilon}} = \frac{P_{\mathrm{S},0}}{\sqrt{2 C_{\mathrm{C}} T_{\mathrm{C}}}} \approx 3 \times 10^{-13}\,\mu\mathrm{C\,K^{-1}\,m^{-2}}, \tag{2.37}$$

in which $P_{\mathrm{S},0}$ is the spontaneous polarization at $T = 0\,\mathrm{K}$, C_{C} the CURIE-WEISS constant. The relation is valid for a series expansion of the free energy up to the sixth power of the polarization. For tri- and monoclinic crystal systems, the expansion has to be performed to
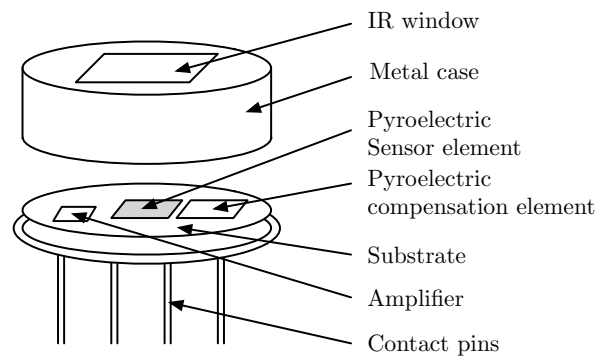
Fig. 2.10.: Schematic of a double-element pyroelectric infrared radiation detector. Adapted from Ref. [12].

powers of eight and twelve [350], respectively, which may slightly alter Eq. (2.37), although it holds for the monoclinic TGS.

For the sake of brevity, applications of ferroelectrics, such as utilizing their "high-k" (ε_r) in different capacitor applications (multilayer capacitors made of $BaTiO_3$, ferroelectric random-access memories, or as dielectric in dynamic random-access memories), electron emitters and liquid crystal light modulators [303], are not presented here.

3. Measurement Methods for the Pyroelectric Coefficient

The precise quantification of the pyroelectric coefficient p is indispensable for the characterization of pyroelectric materials and the development of pyroelectric-based devices. A summary of the variety of techniques to measure p is given in this chapter. It provides a classification after the thermal excitation as well as an outline of capabilities and drawbacks of the individual techniques. Most parts of this chapter were published in the article "How to measure the pyroelectric coefficient?" in the journal *Applied Physics Reviews*, Vol. 4(2), 021303, 2017 [129].

3.1. General Considerations

In principle the determination of p is the detection of the change in polarization during a defined thermal stimulation. To guarantee a precise measurement, several considerations regarding the experimental procedure have to be made and are presented below. These comprise different heating concepts for the thermal stimulation, the establishment of thermal equilibrium, electric contacts, and the separation of different parts of p as well as thermally stimulated currents. Tab. 3.1 provides a summary of all these considerations for each measurement technique, which will be described in Sec. 3.2 and 3.3 in detail.

3.1.1. Heating Concepts

For the determination of the pyroelectric coefficient, the polarization state is generally measured in various ways as a transient between two or more temperatures. Thus, regarding Eq. (2.12), the essential stimulus for every type of technique is a change of temperature. Its time dependence classifies the techniques into two groups: static methods, using different constant temperatures, and dynamic methods, using specific temperature-time functions.

Dynamic methods can be further divided into ramping methods, using a linear change of temperature with time, and waveform temperature changes. The change of spontaneous polarization $\vec{P}_S$ is often measured indirectly using certain physical quantities, e.g. electrical current or voltage. In combination with the stimulating temperature function every technique can be unambiguously distinguished.

All methods described in this work are systematized according to these concepts and summarized in Tab. 3.1.

Tab. 3.1.: Classification and evaluation overview: The symbol for each method is composed of the temperature excitation (blue) and the detected signal (red). A check mark depicts the unrestricted capability of the method, whereas a check mark in parentheses visualizes that the method is in principle capable, but this was not considered in the original work or might be complicated to realize. A cross indicates the impossibility of an evaluation criterion.

	Symbol	Name	Excitation	Measured signals	Evaluation parameters	Separation of				Mapping	Metallic electrode	Ref.
						p_{sec}	p_{tert}	p_{fi}	TSC			
static	Q	Charge compensation	const. temp.	Q (with V_{ref}), T	A, C_{ref}	(✓)	(✓)	✓	✗	(✓ $\geqq A_{\mathrm{crit}}$)	✓	[4]
		Sawyer-Tower Hysteresis	const. temp. $V_{\mathrm{in}}(t)$	P_{S} (with $V_{\mathrm{in}}(t)$, $V_{\mathrm{out}}(t)$), T	A, d, C_{ref}	(✓)	(✓)	✗	✗	(✓ $\approx 0.1\,\mu\mathrm{m}$)	✓	[288]
	ECE	Electrocaloric measurement	const. temp. $\mathrm{d}E$	$\mathrm{d}T, T$	$\rho, c_p(T)$	✗	(✓)	✗	(✓)	(✓ $\approx 10\,\mu\mathrm{m}$)	✓	[363,158]
	V_{fb}	Flatband voltage shift	const. temp. V	C, T	$A, C_{\mathrm{ox}}, \Phi_b(T)$	(✓)	(✓)	✗	✗	(✓)	✓	[201]
	XPS	Photoelectron spectroscopy	const. temp. $h\nu$	V_{sf}, T	$d, \varepsilon_{\mathrm{r}}$	✗	(✓)	✓	✗	(✓)	✗	[66]
	XRD	X-ray diffraction/ density funct. theory	const. temp. $h\nu$	$T, I_{\mathrm{X\text{-}ray}}$	$V_{\mathrm{UC}}, Z_{j,\alpha\beta}, u_{j,\beta}$	✗	(✓)	✓	✗	✗	✗	[357]
dynamic — *ramping*	V	Lang-Steckel method	temp. ramp (K/min)	$T(t), V(t)$	A, R_{L}	(✓)	(✓)	✓	✗	✓	✓	[164]
	Q	Glass method	temp. ramp (K/min)	$T(t), V(t)$	A, C_{F}	(✓)	(✓)	✓	✗	(✓ $\geqq A_{\mathrm{crit}}$)	✓	[88]
	I	Byer-Roundy method	temp. ramp (K/min)	$T(t), I(t)$	A	(✓)	(✓)	✓	(✓)	(✓ $\geqq A_{\mathrm{crit}}$)	✓	[32]
		Birefringence change	temp. ramp (K/s)	$T(t), n(t)$	$n_{\mathrm{to}}(T), n_{\mathrm{p}}(T), \varepsilon_{\mathrm{r}}$ $n_{\mathrm{e}}(T), n_{\mathrm{o}}(T), r$	(✓)	(✓)	✓	(✓)	✗	✗	[251]
	n	Refractive index change	temp. ramp (K/s)	$T(t), n(t)$	$n_{\mathrm{A}}(T), n_{\mathrm{S}}(T),$ $L_{\mathrm{S}}, L_{\mathrm{A}}, r, \varepsilon_{\mathrm{r}}, \lambda$	(✓)	(✓)	✓	(✓)	✗	✗	[267]
dynamic — *step-wise*	I	Thermal pulse	step-wise temperature	$F_0(t), I(f)$	$A, T(t)$	(✓)	(✓)	✓	(✓)	(✓ $\geqq A_{\mathrm{crit}}$)	✓	[42]
	V	Schein method	step-wise temperature	$F_0(t), V(t)$	$T(t)$	✓	✓	✓	✗	✓ $\approx 0.1\,\mathrm{mm}$	✗	[291,292]
	V	PyroSPM	step-wise temperature	$F_0(t), V_{\mathrm{tip}}(t)$	$d, \varepsilon_{\mathrm{r}}, T(t)$	✗	(✓)	✓	✗	✓ $\approx 0.1\,\mu\mathrm{m}$	✗	[98]
	LIMM	LIMM	step-wise/sinus. temperature	$F_0(f), I(f), f$	$A, T(t)$	✗	✗	✓	✓	✓ $\approx 1\,\mu\mathrm{m}$	✓	[13]
dynamic — *waveform*	V	Daglish method	triangular temperature	$T(t), I(t)$	A	(✓)	(✓)	✓	✗	(✓ $\geqq A_{\mathrm{crit}}$)	✓	[54]
	Q	Sussner method	sinusoidal temperature	Q (with $V(t)$), $T(t)$	A, C_{ref}	(✓)	(✓)	✓	(✓)	(✓ $\geqq A_{\mathrm{crit}}$)	✓	[334]
	V	Hartley method	sinusoidal temperature	$T(t), V(t)$	A, R_{L}, f	(✓)	(✓)	✓	(✓)	✓	✓	[111]
	I	Sharp-Garn method	sinusoidal temperature	$T(t), I(t)$	A, f, ϕ	(✓)	(✓)	✓	✓	(✓ $\geqq A_{\mathrm{crit}}$)	✓	[78,376]

A	area	ε_{r}	relative permittivity	q	elementary charge	n	refractive index	V_{UC}	unit cell volume
A_{crit}	critical area	F_0	heat flux	r	electro-optic tensor	n_{to}	... thermo-optic contribution	$Z_{j,\alpha\beta}$	Born effective charge
C	capacity	f	frequency	R_{L}	resistance of external load	n_{p}	... pyroelectric contribution	Φ_b	semiconductor bulk potential
C_{F}	feedback capacity	I	current	P_{S}	spontaneous polarization	n_{e}	... of extraordinary beam	ρ	mass density
C_{ox}	oxide capacity	$I_{\mathrm{X\text{-}ray}}$	X-ray Intensity	T	temperature	n_{o}	... of ordinary beam	ϕ	phase shift T-I
C_{ref}	reference capacity	L_{S}	sample length	t	time	n_{A}	... of surrounding air	λ	wavelength
c_p	specific heat capacity	L_{A}	surrounding air length	$u_{j,\beta}$	displacement vector	n_{S}	... of sample		
d	sample thickness	Q	charge	V	voltage				

The heating or cooling itself, i.e. the controlled change of temperature can be realized in different ways. The most common heaters are resistive heaters and PELTIER elements using JOULE heating and the thermoelectric effect, respectively. With an appropriate insulating material, e.g. boron nitride covering the metal wire of a resistive heater, very high operating temperatures ($>1000\,\mathrm{K}$) can be achieved, which is especially useful for ramping methods. A large variety of resistive heating elements exists, ranging from plate, coil to large oven heaters. The latter often produce a lot of electrical noise [191], which can interfere with the measurement of small pyroelectric signals. Thus, a good electric shielding against surrounding disturbances is required. Without a secondary active cooling, i.e. providing a low ambient temperature, cooling rates are very limited due to a slow heat transfer. GLASS *et al.* employed a gas flow dewar, flooded with liquid helium. A heating coil allowed a rapid temperature change of the helium from $10\,\mathrm{K}$ to $500\,\mathrm{K}$ making the setup well suited for low temperature measurements [88].

A typical PELTIER element has a relatively small temperature range of about $70\,\mathrm{K}$ with respect to the ambient temperature and a maximum operating temperature of approx. $200\,°\mathrm{C}$. In contrast to a resistive heater, it provides active cooling, which is beneficial for waveform temperature changes, but commercially available devices posses a plate-like shape of only limited size.

It is important to note that a certain heating concept typically involves the measurement of the sample temperature with a thermocouple or a resistive thermometer. This allows closed loop temperature control, e.g. with a PID controller, but this is not a general requirement.

In contrast, the absorption of radiation, e.g. from a focused light beam or an infrared laser [42, 191], provides an alternative heating concept, but typically without a direct measurement of the sample temperature. Higher excitation frequencies and steeper temperature changes are benefits of these concepts. Because only the light flux F_0 is tracked, a modeling of the temperature is required for a quantitative evaluation of p. This involves the determination of thermal parameters, e.g. heat capacity, which can be difficult to obtain, especially for thin films or complex layered samples. This type of heating is used for periodic pulse and LIMM techniques (see Sec. 3.3.3 and 3.3.4). To enhance absorption of the radiation, an appropriate material is deposited as an additional layer on the illuminated sample surface. With this concept cooling has to be realized separately due to the limited heat transfer.

SUSSNER *et al.* [334] used dielectric absorption for heating, by applying an alternating electric field $E = E_0 \cdot \sin(\omega t)$ of amplitude E_0 and angular frequency ω to the same measurement electrodes on the pyroelectric. The average power dissipation $\Psi = \varepsilon_0 \varepsilon_r \cdot \tan\delta \cdot E_{\mathrm{rms}}^2$ is given by the root mean square of the electric field E_{rms}, the permittivity $\varepsilon_0 \varepsilon_{\mathrm{r}}$ and loss tangent $\tan\delta$ of the pyroelectric. The method assumes a negligible thermal loss to the surrounding, which has to be ensured by the measurement setup. From mass density ρ and specific heat capacity c_p, the rate of temperature change is

$$\frac{\mathrm{d}T}{\mathrm{d}t} = \frac{\Psi}{\rho \cdot c_p}. \tag{3.1}$$

The loss tangent, i.e. the transformation of electric energy into thermal energy, needs to be characterized as a function of frequency to obtain the optimal absorption frequency and, thus, a sufficient heating rate.

3.1.2. Thermal Equilibrium

For every heating concept, a homogeneous heating of the sample is a basic requirement for a precise measurement of p. The time to establish thermal equilibrium between sample and heater determines the excitation frequency, heating rate, or duration between the temperature steps [161]. For waveform dynamic methods, a maximum thermal excitation frequency $f_{\max}$ can be theoretically estimated [62] by

$$f_{\max} \ll \frac{a}{\pi d^2} = \frac{\lambda}{\pi \rho c_p d^2}, \tag{3.2}$$

in which $a = \lambda/\rho c_p$ is the thermal diffusivity (composed of thermal conductivity λ, density ρ and specific heat capacity c_p) and sample thickness d. The derivation assumes a two-sided heating of the sample, which is often not the case. A more elaborate derivation for a single-sided and two-sided heating is given in Appendix A yielding a four times smaller $f_{\max}$, as well as a two orders of magnitude smaller $f_{\max}$ as derived by DIAS *et al.* for both heating scenarios. Thin film samples, with a surface diameter large compared to their thickness, allow frequencies up to several kHz [191], whereas for thick bulk materials a frequency in the mHz range is necessary (see Fig. 3.1).

Larger frequencies, producing no thermal equilibrium, are used in laser intensity modulation methods (LIMM, see Sec. 3.3.4). A modulated laser heats the sample from one side, generating a thermal wave within the sample [162, 260]. Thermal diffusivity a, material thickness d and frequency f of the laser modulation define the thermal penetration depth d_{p} by

$$d_{\mathrm{p}} = \sqrt{\frac{a}{\pi f d^2}}, \tag{3.3}$$

which thus allows a heating of different sample depths.

Slow heating with a PELTIER or resistive heater is typically used for bulk materials, justifying the low excitation frequencies, whereas fast optical heating is typically used for thin films. A low-frequency optical excitation is also possible [76], serving as a bridge between arbitrary waveform and LIMM methods (see Sec. 3.3). BHATIA *et al.* investigated sinusoidal stimulation with simultaneous current measurement in the frequency range of $0.02\,\mathrm{Hz}$ to $1.3\,\mathrm{MHz}$. Thermal excitation with a heating plate, so-called 2-Omega, and the LIMM method produce consistent results of p for different frequency ranges and heater systems [22].

Furthermore, a laterally homogeneous heating minimizes strain gradients produced by temperature gradients and avoids tertiary pyroelectricity, see Eq. (2.15). This is especially important for polymer and thin film samples as their low thermal conductivity, small YOUNG's modulus, large thermal expansion coefficient and possible growth induced strain gradients [191] can produce significant tertiary signals [189].

3.1.3. Electric Contact

Most techniques involve the measurement of electrical quantities, such as charge, capacitance, current, or voltage changes. Metallic contact pads on the sample surface of area A are often necessary to minimize contact resistance and signal disturbances. The contact quality, e.g. sufficient adhesion of the metal with the pyroelectric to guarantee a good connection with the external circuit, determines the choice of electrode material and deposition technique.
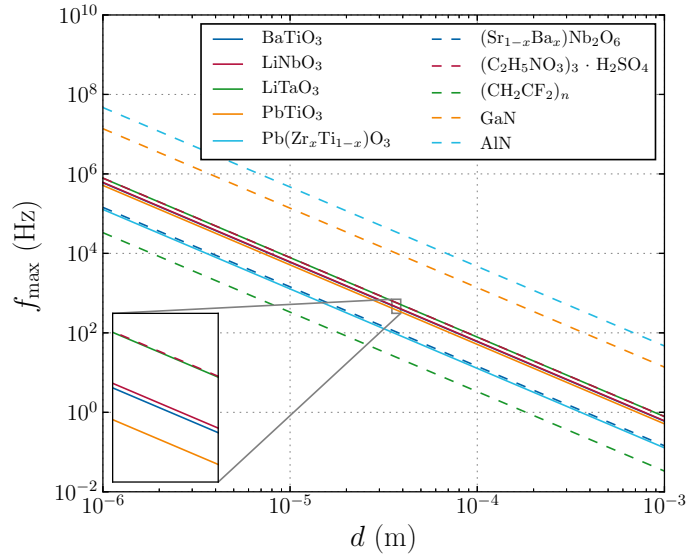
Fig. 3.1.: Maximum thermal excitation frequencies f_{max} with respect to the sample thickness d of common ferro- and pyroelectric materials. Parameters for the estimation using Eq. (3.2) are given in Appendix A.

Typically, square or circular contact pads are used to avoid electric field distortions as it can be the case for complex contact structure [191]. Contacts perpendicular to the polar axis avoid the measurement of a projection of p, although this can be corrected afterwards using crystallographic information [124]. The influences of ohmic versus non-ohmic contacts are outlined by LUBOMIRSKY *et al.* [191], whereby ohmic contacts should be generally preferred.

Metallic contacts can become a problem during poling, i.e. the application of a high electric field to parallelize the microscopic dipoles (ferroelectric domains) over the whole sample. The diffusion of metal atoms into the pyroelectric has to be prevented in order to avoid electrical shortening of the sample, especially at elevated temperatures. The poling process is particularly critical for thin film samples because lateral thickness inhomogeneities or large roughnesses can lead to the formation of pin-holes, which will also shorten the sample. Thus, polymers are often poled by corona poling, i.e. only one side of the sample is metallized and the other is bombarded with charged ions [21, 72, 86, 138]. Furthermore, an electrode deposition is problematic for samples, which prohibits metallic electrodes, i.e. in the XPS method (see Sec. 3.2.5) where the deposition would influence the sample surface or prevent further analysis [66].

For the measurement of electric signals, e.g. current, the electric resistance of the sample has to be large compared to the input impedance of the detection instrument. Otherwise the pyroelectric charge will vanish trough the sample. Evaluating the pyroelectric current response of samples with non-infinite resistance, the leakage through the sample has to be considered. An equation correcting this intrinsic conduction by previously measuring the sample resistance R_S and capacity C_S was given by WHATMORE *et al.* [360, 362]:

$$p = p_{\text{meas}} \sqrt{\left(1 + \frac{R_E}{R_S}\right)^2 + (\omega R_E C_S)^2}, \tag{3.4}$$

in which p_{meas} is the measured pyroelectric coefficient, ω the excitation frequency, C_S the sample capacity and R_S and R_E the sample resistance and input impedance of the used

electrometer, respectively. More details and the derivation of Eq. (3.4) are provided in Appendix C. Furthermore, it is recommended to use screened power and sensing wires as close as possible to the sample. Wire and electrode material with similar SEEBECK coefficients avoid thermoelectric signals [191].

In contrast to a potential-detecting method, a charge-based technique, i.e. a charge or current measurement, needs a critical area A_{crit} of the metallic contact to obtain measurable signals. With Eq. (2.13) and (2.14), a sensitivity X can be defined in order to estimate the minimal area A_{crit} for a respective measurement. It is defined by

$$A_{\mathrm{crit}} = \frac{X}{p}, \tag{3.5}$$

where the sensitivity is

$$X = \frac{\mathrm{d}Q}{\mathrm{d}T} \qquad \text{for a charge measurement and} \tag{3.6}$$

$$X = \frac{\mathrm{d}Q}{\mathrm{d}t}\frac{1}{\mathrm{d}T/\mathrm{d}t} = \frac{I}{\mathrm{d}T/\mathrm{d}t} \qquad \text{for a current measurement.} \tag{3.7}$$

Thus, the sensitivity is determined by the minimal detectable charge or current during a temperature change.

Assuming for example LiNbO$_3$ ($p = 83\,\mathrm{\mu C\,K^{-1}\,m^{-2}}$), an amperemeter with a lower detection limit of $10^{-13}\,\mathrm{A}$ and a moderate temperature change of $1\,\mathrm{K\,min^{-1}}$, A_{crit} is $7.23 \times 10^{-8}\,\mathrm{m^2}$ (square area with a lateral length of approximately $275\,\mathrm{\mu m}$). This area defines the spatial resolution of a current-based technique, of course depending on the p value of the material.

In order to map p over the sample surface with a charge-based method, it is recommended to start with large area contacts to get an estimate of the mean p and iteratively decrease A as far as good signals can still be detected. The mapping capability of each technique is also summarized in Tab. 3.1.

3.1.4. Separation of Contributions

Most measurement techniques determine the total pyroelectric coefficient, see Eq. (2.15). The separation into its constituting parts requires special measurement conditions. The capabilities of each measurement technique are summarized in Tab. 3.1.

The direct or indirect detection of P_{S} in static and dynamic methods yields always a combination of p_{prim} and p_{sec}, as outlined in Sec. 2.3. The secondary contribution can in principle be avoided by realizing totally clamped conditions, i.e. by providing constant strain $\overset{2\rightarrow}{e}$ in all dimensions. Unfortunately, this is a challenging task for practical measurements, because pressures to create constant strain typically break the material. However, from elastic stiffness, thermal expansion and piezoelectric coefficient the secondary contribution can be calculated to obtain the primary contribution p_{prim}. The field-induced contribution p_{fi} is only important when the application of external electric fields is necessary [108]. Otherwise, this contribution is absent. The tertiary contribution p_{tert} can be eliminated by ensuring thermal equilibrium, see Sec. 3.1.2, and a lateral homogeneous heating, which avoids temperature gradient-induced strain gradients.

3.1.5. Thermally Stimulated Currents

The release of trapped charges during the thermal excitation, also known as thermally stimulated currents (TSC), leads to an additional non-pyroelectric current contribution and a false interpretation of the signal in the quantitative determination of p. For example the poling process can inject charge carriers into the material, especially for doped single and polycrystals, ceramic or polymeric samples. In particular polymers and thin films are affected because they can usually trap large amounts of charges over a long time [191]. Trapping sites can be structural defects, impurities, inhomogeneities near amorphous-crystalline interfaces and grain boundaries, as well as polymer side branches, chain ends, entanglements and functional groups [308]. Beside current, also capacitance measurements are usually a disadvantageous choice, because the capacitance is composed of displacement, ohmic and charge-injection currents, without any chance of separation [191].

For clarification: Sometimes the term TSC also includes pyroelectricity, which then differentiates into pyroelectric (I_p) and non-pyroelectric (I_np) currents [132]. In this work, TSC is used only for non-pyroelectric current contributions.

Beside the misinterpretation as false pyroelectric current signals, TSC can lead to false phase transition temperatures, as outlined in Sec. 3.3.5. The preferred discharge of electrons at a specific temperature, utilized by thermally stimulated current analysis (TCA) [48, 120, 213, 214], does not necessarily coincide with the maximum of the pyroelectric coefficient, which is associated to the phase transition temperature. An appropriate preconditioning of the sample, e.g. shortening at an elevated temperature [191, 362] for several hours or performing several heating and cooling cycles, can minimize the effect.

TSCs are proportional to the temperature excitation and not to its time derivative [362]. A possibility to quantify and eliminate the TSC contribution from ramping methods below the phase transition temperature was given by WHATMORE *et al.* [362] (see Sec. 3.3.1). A measurement of the current I during heating (h) and cooling (c), described by

$$I_\mathrm{h}(T) = p(T) \cdot A \cdot \left(\frac{\mathrm{d}T}{\mathrm{d}t}\right)_\mathrm{h} + I_\mathrm{TSC}(T), \tag{3.8}$$

$$I_\mathrm{c}(T) = p(T) \cdot A \cdot \left(\frac{\mathrm{d}T}{\mathrm{d}t}\right)_\mathrm{c} + I_\mathrm{TSC}(T), \tag{3.9}$$

is necessary, in which $I_\mathrm{TSC}(T)$ is the magnitude of the thermally stimulated current. $I_\mathrm{TSC}(T)$ is then obtained from

$$I_\mathrm{TSC}(T) = \frac{\left(\frac{\mathrm{d}T}{\mathrm{d}t}\right)_\mathrm{c} I_\mathrm{h}(T) + \left(\frac{\mathrm{d}T}{\mathrm{d}t}\right)_\mathrm{h} I_\mathrm{c}(T)}{\left(\frac{\mathrm{d}T}{\mathrm{d}t}\right)_\mathrm{c} - \left(\frac{\mathrm{d}T}{\mathrm{d}t}\right)_\mathrm{h}}. \tag{3.10}$$

Using Eq. (3.10) together with (3.8) or (3.9) yields a TSC-free total and, thus, pure pyroelectric current. Due to the continuous temperature oscillation, waveform dynamic methods are especially capable to separate TSC contributions. The SHARP-GARN method [78, 79] provides a formalism to explicitly eliminate TSC (see Sec. 3.3.5). Tab. 3.1 also summarizes the possibility to exclude TSC for each method.

3.2. Static Methods

Static methods measure the change of polarization by a change of physical quantities between different constant temperatures. The resulting pyroelectric coefficient is a combination of p_{prim} and p_{sec}, when total clamping is not possible. Field induced, strain gradient and charge injection effects can in principle not be excluded.

3.2.1. Charge Compensation Method

The first reported method of a quantitative determination of pyroelectricity was performed by ACKERMANN in 1915 and was based on charge compensation [4]. Due to a temperature change and the pyroelectric effect, charges will flow on a compensation capacitor C_{ref}. A HANKEL electrometer, i.e. a capacitor with a conductive filament, is biased by a voltage V_{ref} to nullify the pyroelectric potential developed during a temperature step $\Delta T = T_2 - T_1$. The pyroelectric coefficient p is then given by

$$p = \frac{V_{\mathrm{ref}} \cdot C_{\mathrm{ref}}}{A \cdot \Delta T}, \tag{3.11}$$

in which A is the area of the deposited metal contact. The sample itself is placed inside a homogeneously heated medium, e.g. paraffin oil or different gases [4].

An improved accuracy was achieved later by GAVRILOVA, SIL'VESTROVA and SIL'VESTROV who used more sensitive electronic electrometers, providing an automatic charge compensation [81, 161]. An equivalent electric circuit is shown in Fig. 3.2. The step-wise heating causes an exponential voltage shape (similar to the dynamic method of CHYNOWETH, see Sec. 3.3.3). The pyroelectric coefficient is given by

$$p = \frac{1}{1 - \exp\left(-\frac{t+t_1}{\tau_{\mathrm{th}}}\right)} \cdot \left[\frac{V_{\mathrm{comp}} \cdot C_{\mathrm{comp}}}{A \cdot \Delta T} + \frac{V_0 \cdot t}{R \cdot A \cdot \Delta T}\right], \tag{3.12}$$

in which t_1 is the time lag and V_0 the sensitivity of the electrometer, t the time, τ_{th} the thermal time constant, R_{S}, R and C_{S}, C the resistance and capacity of the sample and voltage source, respectively. The measurement is prone to samples with a raised electrical conductivity, because it assumes a large sample resistance R_{S} and large compensator resistance R_{comp} compared to R.
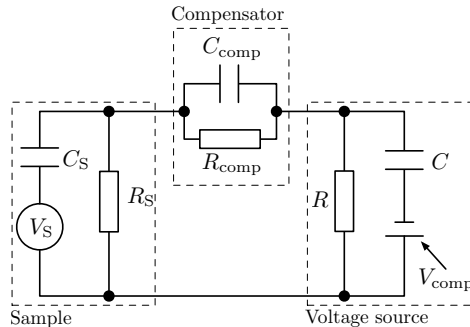

Fig. 3.2.: Equivalent circuit of the charge compensation method after GAVRILOVA, redrawn from Ref. [81]: V, R and C denote voltage, resistance and capacity, respectively.

The dynamic ramping method by GLASS [88] (see Sec. 3.3.1) is in fact a further improvement by measuring the voltage over a reference capacitor, while the temperature increases linearly.

The charge compensation provides a precise determination of p at a constant temperature, assuming a small ΔT during which p changes little [161]. The spatial resolution of p is determined by A_{crit} (see Sec. 3.1.3), like for all charge-based methods. As mentioned in Sec. 3.1.5, charge based methods do not allow a separation of TSC.

3.2.2. Hysteresis Measurement Method

As outlined in Sec. 2.4, the ferroelectric hysteresis describes the non-linear dependency of the polarization $\vec{P}$ with respect to the applied electric field $\vec{E}$. Before describing the extraction of p from such measurements, the general concept of hysteresis measurements is reviewed.

Practical polarization P versus E loops are measured using the simple SAWYER-TOWER bridge circuit [28, 288], shown in Fig. 3.3, as first approach. Here, the capacitor C_{S} represents the ferroelectric sample, while C_{ref} is of well-defined capacitance. A matching shunt resistor R_{ref} is often used to compensate ohmic conductivity (R_{S}) of the ferroelectric material (see below). Assuming ideal capacitors, the charge Q on both has to be equal. An oscilloscope detects the voltage drop $V_{\mathrm{ref}}(t)$ across the reference capacitor C_{ref} ($C_{\mathrm{ref}} \gg C_{\mathrm{S}}$), which represents the polarization of the sample by

$$P(t) = \frac{V_{\mathrm{ref}}(t) \cdot C_{\mathrm{ref}}}{A}, \tag{3.13}$$

in which A is the electrode area. From the input voltage $V_{\mathrm{in}}(t)$, typically a triangular or sinusoidal function, the electric field at the sample is given by

$$E(t) = \frac{V_{\mathrm{in}}(t) - V_{\mathrm{ref}}(t)}{d}, \tag{3.14}$$

in which d represents the sample thickness. The frequency f of the $V_{\mathrm{in}}(t)$ waveform can range between mHz and kHz, depending on material parameters like thickness and electrode area.
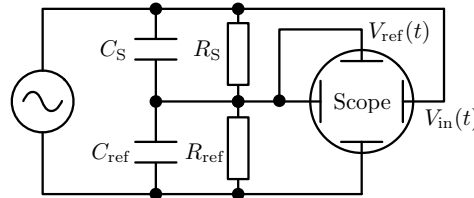
Fig. 3.3.: SAWYER-TOWER circuit redrawn after Ref. [191, 288]. C_{S}, R_{S} and C_{ref}, R_{ref} are the capacity and resistance of the ferroelectric sample and the reference capacitor, respectively.

Instead of a reference capacitor, also the measurement of the voltage drop over a reference resistance R_{ref} is possible, allowing a direct measurement of the transient current (which is generally composed of ohmic and displacive current). The so-called shunt method uses a single and well-known reference resistance R_{ref} connected in series with the ferroelectric capacitor. The corresponding circuit diagram is shown in Fig. 3.4(a). While the applied electric field is again calculated with Eq. (3.14), the polarization is reconstructed by integrating the current
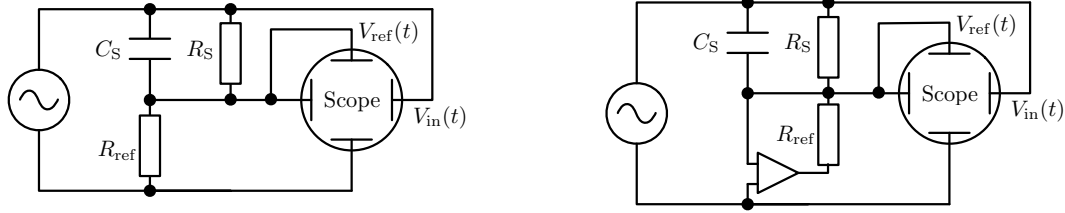
(a) Shunt method circuit adopted from Ref. [299]. C_S, R_S and R_{ref} are identical to Fig. 3.3.

(b) Virtual ground method circuit adopted from Ref. [299]. Here, the voltage drop at R_{ref} is inverted by an operational amplifier.

Fig. 3.4.: Shunt and virtual ground circuit diagrams as alternatives to the SAWYER-TOWER circuit.

$I(t)$, obtained from voltage V_{ref} and resistance R_{ref}, since it equals the corresponding charge divided by the contact area A:

$$P = \frac{Q}{A} = \frac{1}{A} \int I(t) \, \mathrm{d}t = \frac{1}{A \cdot R_{ref}} \int V_{ref}(t) \, \mathrm{d}t. \tag{3.15}$$

Compared to the shunt method, the virtual ground method additionally includes an inverting operational amplifier (see Fig. 3.4(b)), allowing the full excitation voltage to drop over the ferroelectric capacitor C_S, which eliminates parasitic cable capacities [299, 344]. Interestingly, both methods are similar to shunt and feedback amperemeter, respectively, used to measure low electrical currents. In contrast to the SAWYER-TOWER circuit no additional matching shunt resistor can be included to compensate increased ohmic conductivity of the ferroelectric material. An elimination of the conductivity contribution is possible with previous capacity C_S and dielectric loss $\tan \delta$ measurements of the sample (see Appendix B).

Most real samples are no ideal capacitors, i.e. an electrical leakage current can occur due to various conduction mechanisms such as SCHOTTKY injection, FOWLER-NORDHEIM tunneling, grain boundaries and defects [271]. In case of pronounced ohmic conductivity, also known as a leaky dielectric, blown-up hysteresis loops occur as shown in Fig. 2.7) and the obtained remanent polarization P_R is not of ferroelectric origin [175, 271, 304]. It gets even more complicated, when the electrical conductivity is non-linear with the electric field. Here, an apparent saturation of the polarization is simply due to the reduction of the dielectric constant a high electric fields [271]. Furthermore, non-linear leakage currents, i.e. more insulating at lower than at higher fields, could lead to a rounding of the hysteresis loops and to an overestimation of P_R [271, 299]. At this point it has to be noted that a leaky dielectric is just one possibility of hysteresis deformation. Beside ohmic conduction, SCHENK *et al.* summarized the most prominent alterations of hysteresis loops and a blurred P_R determination (for further details see Ref. [299]). The most important are:

- The imprint effect, leading to a shift of the hysteresis along the E axis. It is equivalent to an internal bias field due to the domain structure of the material or space charge layers.

- The grain size variation gives rise to a general rounding of the hysteresis, which corresponds to a distribution of the coercive field E_C [89, 115].

- The wake-up and fatigue behavior correspond to a progressing expansion and compression, respectively, of the hysteresis during continuously cycling the material. The latter could be seen as an aging effect and defects, which pin domain walls, are considered to be responsible.
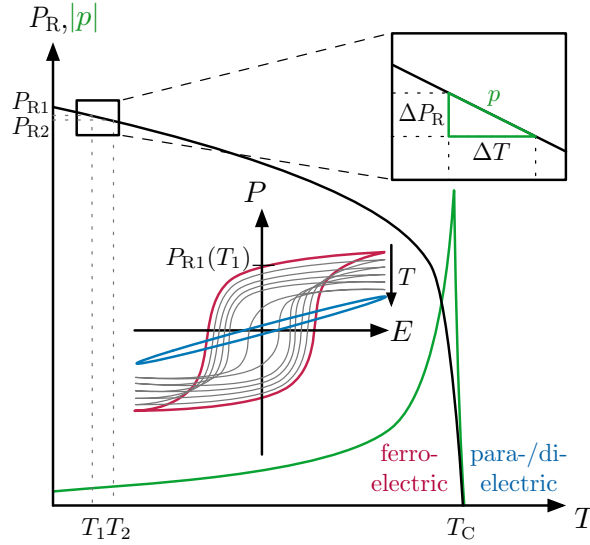
Fig. 3.5.: Schematic of the $P_R(T)$ relation for a ferroelectric material undergoing a first order phase transition, determined from hysteresis measurements at several temperatures (see inset). The slope of $P_R(T)$ defines the pyroelectric coefficient p.

- Anti-ferroelectricity, marked by a double hysteresis, but nearly no remanent polarization due to two equal sublattices of opposite spontaneous polarization.

Also the SAWYER-TOWER test circuit itself may lead to a deformation of the hysteresis loop, originating from unavoidable circuit elements, especially the input impedance and capacity of the oscilloscope, R_{osci} and C_{osci}, respectively, adding to the finite resistance of the dielectric material [212]. In past decades, several circuit improvements, e.g. compensation of circuit effects [61, 282, 317], have been presented. Also a numerical method to restore the true hysteresis shape and additionally extract resistivity R_S and dielectric permittivity ε_r was proposed by BOUREGBA *et al.* [28]. A correction of Eq. (3.13) and (3.14) for the finite sample resistance R_S and oscilloscope resistance R_{osci} is therefore possible, enabling the measurement at higher driving frequencies. As all of these influences affect the shape of measured hysteresis loops and, thus, the obtained remanent polarizations P_R, careful experimentation is absolutely necessary. A first step is to measure at several different frequencies because the $P(E)$ characteristic is independent of driving frequencies over a wide range, however artifacts are typically not [191, 271]. The PUND method (positive up negative down) is a more advanced technique to rule out such artifacts [196, 271]. Here, a specific sequence of positive and negative voltage pulses is applied in order to differentiate between true switching and leakage currents (see Ref. [271]).

The careful measurement of the remanent polarization P_R (the difference to the often mistakenly used P_S is given in Sec. 2.4) at two or more fixed temperatures gives the temperature dependency of the remanent polarization $P_R(T)$, see Fig. 3.5. Its derivative with respect to the temperature is the pyroelectric coefficient p (see Eq. (2.12)). The phase transition temperature T_C is marked by the vanishing of $P_R(T)$. To determine the pyroelectric coefficient with the hysteresis measurement method requires a ferroelectric and is, thus, unsuitable for pure pyroelectrics. Furthermore, it is impractical for materials with a coercive field strength higher than the breakdown field strength ($E_C > E_{br}$), e.g. LiNbO$_3$ [206, 229], which prevents a polarization reversal. Also, if the compensation of the ohmic conductivity, e.g. by the shunt resistor, is not possible, the method becomes inappropriate.

Conventionally, macroscopic metallic electrodes are deposited for the field application, which prohibits a spatial mapping of p. However, scanning probe microscopy (SPM) allows mapping and manipulation of domain structures of ferroelectrics [69, 100, 290] with resolution down to several nanometers [100] and could be utilized for $P_\mathrm{S}(T)$ retrieval without deposited electrodes. This approach is especially favorable for thin film samples, due to the low voltages which have to be applied, in contrast to bulk material.

A separation of effects due to released charges is not possible, because the application of the electric field may refill and deplete electronic trap states, which can influence the measured polarization of the material. The spontaneous polarization at different temperatures for constant stress is given by (compare Sec. 2.3):

$$P_\mathrm{S}^{\overset{2}{\vec{\sigma}},\vec{E}} = \int p^{\overset{2}{\vec{\sigma}},\vec{E}}\,\mathrm{d}T = \int \left(\vec{p}_\mathrm{prim} + \vec{p}_\mathrm{sec}\right)\mathrm{d}T = \int \left(\overset{2}{\vec{p}}^{\,\vec{e},\vec{E}} + \overset{2}{\vec{\alpha}}^{\vec{E}}\,\overset{4}{\vec{c}}^{\vec{E},T}\,\overset{3}{\vec{d}}^{T}\right)\mathrm{d}T. \quad (3.16)$$

Thus, P_S at constant stress is always composed of primary and secondary pyroelectricity. Under constant strain, the spontaneous polarization only includes the primary contribution.

3.2.3. Direct Electrocaloric Measurement

The electrocaloric effect (ECE), the inverse process to pyroelectricity, describes a change of entropy S, due to a change of electric field $\vec{E}$ (see Fig. 2.1). Using the MAXWELL relations, the pyroelectric coefficient p at constant electric field E is generally represented by

$$p = \left(\frac{\partial S}{\partial E}\right)_T = \left(\frac{\partial P}{\partial T}\right)_E. \quad (3.17)$$

The temperature change $\mathrm{d}T$ due to the electric field change $\mathrm{d}E$ (from E_1 to E_2) can be calculated from [158]

$$\mathrm{d}T = -\frac{T}{\rho c_p}\int_{E_1}^{E_2}\left(\frac{\partial P}{\partial T}\right)_E \mathrm{d}E. \quad (3.18)$$

With the knowledge of the mass density ρ and specific heat capacity c_p at temperature T, the pyroelectric coefficient is determined when measuring $\mathrm{d}T$ during the electric field change $\mathrm{d}E$. Such an ECE measurement can be performed directly or indirectly. A detailed review on the theory of ECE measurements is given by KUTNJAK *et al.* [157, 158]

The indirect approach involves the measurement of ferroelectric hysteresis loops at different temperatures (see Sec. 3.2.2 and Ref. [158]). The direct technique is the precise detection of $\mathrm{d}T$ with the help of a calorimeter, typically a modified differential scanning calorimeter (DSC) [158]. The heat flow is measured during the application of an electric field at constant ambient temperature T. By rearranging Eq. (3.18), p is given by

$$p = -\frac{\rho c_p}{T}\cdot\frac{\mathrm{d}T}{\mathrm{d}E}, \quad (3.19)$$

which is composed of all contributions to p and assumes no field and temperature dependence of ρ and c_p.

First quantitative measurements were performed by WISEMAN and KUEBLER on Rochelle salt [363, 364], using a constant temperature chamber, which ensured homogeneous heating

and, thus, eliminate the tertiary contribution. The precise measurement of the temperature change plays the key role in such experiments. ECE temperature changes of common ferroelectric materials are typically small and in the range of 10^{-4} K to 10^{-3} K, involving several measurement efforts: The measurement instruments, e.g. thermocouple and voltage amplifier, have to provide very low noise levels and the heat capacities of the components, e.g. wires, have to be small compared to that of the sample [363].

A spatial detection of temperature changes is difficult in a calorimeter, preventing a mapping of p, especially with metal electrodes on opposite sample surfaces for the application of the electric field. Scanning thermal microscopy (SThM) uses a platinum thermometer tip to detect the spatial distribution of temperature changes below 0.1 K [137, 157]. This could allow a spatial detection of p with a resolution of several tens of µm, which was not yet reported.

The application of an electric field causes TSCs and intrinsic electric conduction, which seems to have no influence on the result as no currents are measured. However, the absorption of these charges can produce JOULE heat, which influences the very sensitive temperature measurement. This is typically negligible for dielectrics with low electrical conductivity [158].

3.2.4. Flatband Voltage Shift

To measure the pyroelectric coefficient of semiconductors, e.g. wurtzite type III-V compound semiconductors, MATOCHA *et al.* described the flatband voltage shift method [201].

Capacitance-voltage (C-V) curves of a metal-oxide-semiconductor (MOS) stack, in which the semiconductor is the pyroelectric, are recorded at different temperatures. The flatband voltage V_{fb}, i.e. the voltage applied to the metal contact to compensate band bending in the semiconductor, shifts due to a pyroelectrically induced change of the semiconductor bulk potential Φ_{b}. With the temperature dependency of the semiconductor bulk potential $\Phi_{\mathrm{b}}(T)$, the oxide capacitance C_{ox}, and the metal electrode area A, the pyroelectric coefficient is given by:

$$p = -\frac{C_{\mathrm{ox}}}{A} \cdot \frac{\mathrm{d}(V_{\mathrm{fb}}(T) - \Phi_{\mathrm{b}}(T))}{\mathrm{d}T}. \tag{3.20}$$

During the temperature increase, the bias voltage for the C-V measurement has to be zero in order to minimize influences of mobile charges.

The temperature steps between two C-V characteristics should be small enough in order to get $p(T)$, marked by different slopes of $(V_{\mathrm{fb}} - \Phi_{\mathrm{b}})$ over T, but large enough to detect a measurable difference of V_{fb}. The technique is, thus, preferable for materials or temperature ranges where p changes little with T. Near a phase transition, smaller temperature steps can be used due to a rise of p.

Although the method involves the processing of the MOS stack, it is beneficial for pyroelectric semiconductors, especially in the form of thin films, due to the high capacity stemming from their low thickness. They typically exhibit a higher conductivity compared to common insulators, hindering a measurement of surface compensational charges. The obtained pyroelectric coefficient is considered free of tertiary and field-induced contributions. Spatial resolution is limited by the $\varepsilon_{\mathrm{r}} A/d$ ratio, which defines the minimal measurable capacitance.

3.2.5. X-ray Photoelectron Spectroscopy Method

Photoelectron spectroscopy can be utilized to determine the pyroelectric coefficient without the need to measure conventional electric signals, as described by EHRE *et al.* [66].

The sample is irradiated with low power (approx. $1.5\,\mathrm{W}$) monochromatic X-rays, leading to the emission of photoelectrons. The kinetic energy E_{kin} of the released electrons is given by

$$E_{\mathrm{kin}} = h\nu - E_{\mathrm{B}} - \phi - q \cdot V_{\mathrm{sf}}, \tag{3.21}$$

in which $h\nu$ is the incident X-ray photon energy, E_{B} the binding energy, ϕ the spectrometer work function, q the elementary charge and V_{sf} the surface potential. Under ultra high vacuum conditions (UHV, pressure approximately $10^{-10}\,\mathrm{mbar}$) no compensation of the surface potential from surrounding charges occurs and V_{sf} is directly sensitive to the surface charges Q_{sf} and, thus, to P_{S}.

To calculate the pyroelectric coefficient, a parallel plate capacitor of thickness d is assumed, yielding the surface charge Q_{sf} by

$$Q_{\mathrm{sf}} = \varepsilon_0 \varepsilon_{\mathrm{r}} \cdot V_{\mathrm{sf}} \cdot \frac{A}{d}, \tag{3.22}$$

in which A is the sample surface area and ε_0 and ε_{r} the relative and vacuum dielectric permittivity, respectively. When changing the temperature of the sample, $\partial Q_{\mathrm{sf}}/\partial T$ is generated due to the pyroelectric effect. Combining Eq. (2.12) (here represented by $\mathrm{d}Q_{\mathrm{sf}}/\mathrm{d}T = A \cdot p$) with Eq. (3.22) yields the pyroelectric coefficient:

$$p = \frac{\varepsilon_0 \cdot \varepsilon_{\mathrm{r}}}{d} \cdot \frac{\mathrm{d}V_{\mathrm{sf}}}{\mathrm{d}T}. \tag{3.23}$$

For small $\mathrm{d}T$, p is calculated from the temperature-dependent shift of the surface potential.

The method offers a precise detection of the surface potential V_{sf} with no need for metallized electrodes. The thickness d and the relative permittivity ε_{r} have to be known, which can be measured easily compared to other properties. The strong temperature dependency of ε_{r} near a phase transition has to be considered. Parasitic effects like thermoelectricity and photoelectricity can be eliminated with a time delay to reach thermal equilibrium and the usage of a very low X-ray photon flux, respectively. Released bulk charges due to thermal excitation can alter the surface potential. As outlined in Sec. 3.1.5, annealing at elevated temperature could minimize them. Assuming a constant E_{B}, constant ϕ and small temperature steps, the technique provides $p(T)$ and T_{C}. The spatial resolution of p is determined by the beam spot size of the incident radiation, which is typically in the range of $5\,\mathrm{\mu m}$ or above, giving a poor resolution compared to SPM based techniques. Focusing the X-ray spot increases the incident particles per area and leads to additional non-pyroelectric, photoelectric charges, which may be the main problem of the method. The use of an electron flood gun, in order to compensate carriers due to the photoeffect, would also eliminate the pyroelectric charges. Effects due to adsorption and desorption of remaining charged molecules (especially negative ones) can alter the XPS results for p. The measurement at the negative side of the sample is recommended because positive ions are less common in a vacuum system [66]. Secondary and tertiary pyroelectricity can contribute to the resulting pyroelectric coefficient of this method, due to additionally produced surface charges. The latter contribution can be neglected when ensuring homogeneous heating. EHRE *et al.* also mentioned that this method can give further information about ferroelectricity and piezoelectricity and may lead a way to explore the mechanism of spontaneous polarization and the role of surface contamination [66].

3.2.6. X-ray Diffraction and Density Functional Theory

A rather sophisticated static approach for determining the pyroelectric coefficient is the combination of single crystal X-ray diffraction (XRD) with density functional theory (DFT), which was first reported by WEIGEL *et al.* [357] for $LiNbO_3$ and $LiTaO_3$. Accordingly, the crystal structure, i.e. the lattice parameters and atomic positions, is determined by using a four-circle single-crystal X-ray diffractometer and a cryostream to enable different temperatures. The temperature-dependent data is then combined with DFT-calculated BORN effective charges (BEC) in order to compute the atomic displacement and, thus, the spontaneous polarization P_S at a constant temperature T. The total polarization results from the summation of the polarization of the individual atomic species [321]. With the concept of BORN effective charges $Z_{j,\alpha\beta}$, the change of the spontaneous polarization $\vec{P}_{S,\alpha}$ in direction α is given by

$$\vec{P}_{S,\alpha} = \frac{q}{V_{UC}} \sum_{j=1}^{N} Z_{j,\alpha\beta} \cdot \vec{u}_{j,\beta}, \tag{3.24}$$

in which q is the elementary charge, V_{UC} the volume of the unit cell, $\vec{u}_{j,\beta}$ the displacement vector of an atom j relative to its position in the non-polar phase, N the number of atoms in the unit cell, and α and β two different spatial directions [253, 357]. To approximate the temperature dependency of the polarization (either experimentally determined by XRD or simulated by molecular dynamics) lattice parameters and atomic positions have to be used as boundary conditions for the DFT calculations. The polarization at different temperatures gives the pyroelectric coefficient p via Eq. (2.12). The obtained results are reported to be comparable with other methods for the investigated materials $LiNbO_3$ and $LiTaO_3$ [357, 358].

Other approaches based on XRD comprise the CLAUSIUS-MOSSOTTI ansatz [43, 218] and the integration of the reconstructed electron density distribution over the crystallographic unit cell in order to calculate P_S and eventually p. As outlined in Sec. 2.2, calculating P_S as the sum of dipole moments has proven inadequate [271]. Both approaches use the experimental electron density, which is difficult to obtain correctly, in particular when covalent and ionic bond contributions coexist. With the combined XRD/DFT approach real-structure influences (such as defects or foreign phases) on the pyroelectric coefficient can be discriminated from ideal-structure influences (i.e. the perfect arrangement of atoms), which is beneficial for improvements of the microstructure of pyroelectrics.

Field-induced pyroelectricity is absent due to non-biasing conditions. Ensuring homogeneous heating minimizes the tertiary contribution. In contrast to the SAWYER-TOWER method (see Sec. 3.2.2), the method is also suitable for non-ferroelectric pyroelectrics. Identical to the XPS technique, no metallic contacts are necessary. A spatial resolution of p is not possible using a laboratory diffractometer, because the sample is typically smaller than the beam size. In contracts, a microfocus X-ray tube (beam size of approx. $50\,\mu m$) or a *nano-beam* synchrotron X-ray source may remedy this limitation. The thermally induced release of charges influences the electron density and, thus, may alter its calculation and also the obtained P_S.

3.3. Dynamic Methods

In contrast to static methods, dynamic methods utilize a continuous change of temperature, which is typically given by a linear or periodic function. Due to the prevailing measurement of electrical quantities and non-biasing conditions, the field-induced contribution of the pyroelectric coefficient is absent. Analogously to the static methods, a combination of primary and secondary contribution is mostly measured However, some methods explicitly allow a separation of TSC.

3.3.1. Temperature Ramping Methods

A temperature ramping technique was first described by LANG and STECKEL [164], using a voltage measurement while constantly heating the material. The pyroelectric is described as a charge generator with capacity C_S and resistance R_S. It is connected to an amplifier, represented by a shunt resistor R_{sh} and a high impedance voltmeter. The equivalent circuit and further information are given in Fig. 3.6(a). For dominating sample resistance ($R_{sh} \ll R_S$) and large thermal time constants compared to the electrical time constant ($\tau_{th} \gg \tau_{el}$), the voltage response V yields the pyroelectric coefficient by

$$p = \frac{V}{A \cdot R_S \cdot \mathrm{d}T/\mathrm{d}t}. \tag{3.25}$$

A similar technique was introduced by GLASS [88], using a coulombmeter to measure the charge flow on a feedback capacitor C_F (see Fig. 3.6(b)). The coulombmeter, as the only available low impedance device at this time [191], measures the charge flow on the feedback capacitor C_F. The capacity C_F should be large ($1\,\mu\mathrm{F}$ to $10\,\mu\mathrm{F}$ [88, 362]) in order to achieve long integration times. The continuous charging of the capacitor is amplified with an operational amplifier (OPV). The voltage represents the amount of spontaneous polarization change of the crystal:

$$V = \frac{A}{C_F} \int_{P_1}^{P_2} \mathrm{d}P_S = \frac{A}{C_F} \int_{T_1}^{T_2} p \cdot \mathrm{d}T, \tag{3.26}$$

where $\mathrm{d}P_S = p \cdot \mathrm{d}T$, see Eq. (2.12). The continuous increase of the temperature, which is described by a linear function, leads to a pyroelectric coefficient of

$$p = \frac{V \cdot C_F}{A \cdot (T_2 - T_1)}. \tag{3.27}$$

Of course, the difference between T_1 and T_2 should be small to avoid the measurement of an averaged p.

With the appearance of precise low-impedance amperemeters, BYER and ROUNDY modified the GLASS approach to a current-based method [32]. Using Eq. (2.12), the electric current $I = \mathrm{d}Q/\mathrm{d}t = p \cdot A \cdot \mathrm{d}T/\mathrm{d}t$ gives the pyroelectric coefficient as

$$p = \frac{I}{A \cdot \mathrm{d}T/\mathrm{d}t}, \tag{3.28}$$

assuming that the produced current I only stems from pyroelectric contributions. Using Eq. (3.28) each measured current value and its corresponding temperature value will give
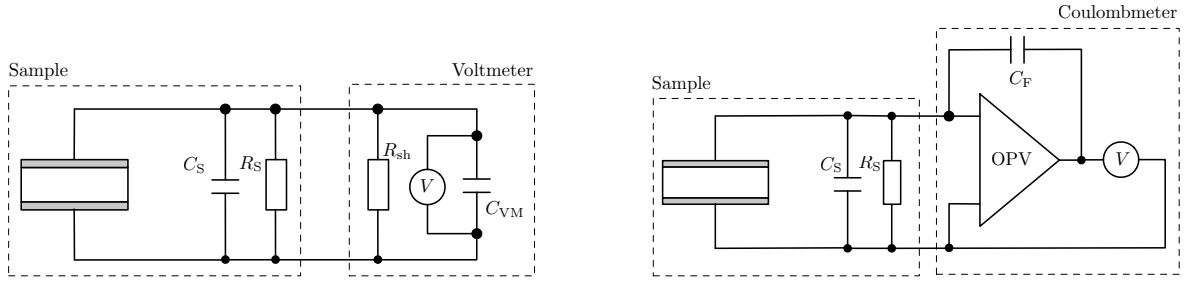
(a) Lang-Steckel circuit: The pyroelectric sample is connected to an amplifier, represented by a shunt resistor R_{sh} and a high impedance voltmeter with its capacity C_{VM}. Redrawn from Ref. [164].

(b) Glass circuit: The pyroelectric sample is connected to feedback capacitor C_{F} and the voltage is measured with an operational amplifier (OPV). Redrawn from Ref. [88].

Fig. 3.6.: Circuit diagrams for thermal ramping methods. The pyroelectric sample is represented by a charge generator and a capacity and resistance, C_{S} and R_{S}, respectively.

$p(T)$. The disappearance of the current (and thus a maximum and subsequent vanishing of p) marks the phase transition temperature T_{C}.

Metallic electrodes are typically added to both sides of the material. A single-side Byer-Roundy modification uses a hovering electrode, represented by a plasma generated by a radioactive ^{241}Am source [113]. Ionization of the air gap between sample surface and electrode ensures a high enough electrical conductivity for a current measurement.

The main advantage of these ramping methods is their simple setup. Apart from a metalized sample, just a temperature-controlled oven, an amperemeter, and a data acquisition system are needed. This is the reason for their widespread application, especially for ceramics [17, 37, 58, 356, 372], but also single crystals [200, 289] and thin films [38, 123]. Their simplicity is also their weakness, because they are unable to separate TSC from pyroelectric current. This often leads to a misinterpretation of the electric signal, especially in defect-rich samples, e.g. semi-crystalline polymers, ceramics, and thin films.

Jiménez et al. considered that an actual heating element cannot produce a perfect linear slope. It is always disturbed by small temperature fluctuations, which are more pronounced in the first time derivative than in the temperature evolution itself [132]. Thus, quick temperature changes amplify the pyroelectric current, which can be fitted to Eq. (3.28) in small temperature intervals, which gives more or less TSC-free p. Jimenez et al. call this technique a "simplified" dynamic method [132].

3.3.2. Optical Methods

Parravicini et al. demonstrated for single crystalline LiNbO$_3$ that a temperature-induced birefringence variation dn can be associated with pyroelectricity [251].

The optical setup described by Parravicini [251] is presented in Fig. 3.7(a). Under open-circuit conditions $D = 0$ and the developing electric field of the material is given by:

$$\mathrm{d}E_{\text{p}} = -\frac{1}{\varepsilon_0 \varepsilon_{\text{r}}} \mathrm{d}P_{\text{S}} = -\frac{p}{\varepsilon_0 \varepsilon_{\text{r}}} \mathrm{d}T. \tag{3.29}$$
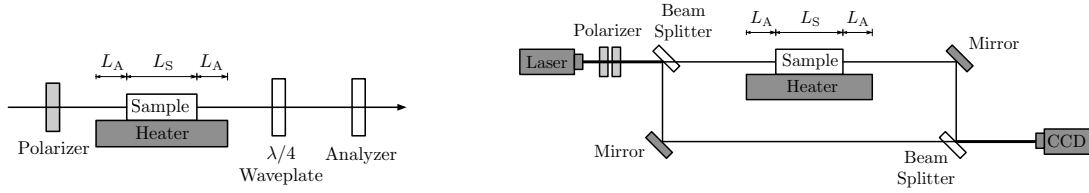
(a) Setup of PARRAVICINI's all-optical technique. Here, λ stands for the wavelength and not for the thermal conductivity. Redrawn from Ref. [251].

(b) Principle of the interferometric setup. Adapted from Ref. [267].

Fig. 3.7.: Different setups for the optical characterization of the pyroelectric coefficient p.

The total change of birefringence in the case of pyroelectrics is given by

$$\mathrm{d}n = \mathrm{d}n_{\mathrm{to}} + \mathrm{d}n_{\mathrm{p}}, \tag{3.30}$$

summing up the changes resulting from thermo-optic (n_{to}) and pyroelectric (n_{p}) effect.

The measurement is performed in two steps: First, the measurement of $\mathrm{d}n$ (involving both contributions) and second, the measurement under short-circuit conditions, in which $\mathrm{d}n = \mathrm{d}n_{\mathrm{to}}$ (no E_{p}). Unfortunately, the second step requires metallic electrodes, which have to be shortened to achieve $E_{\mathrm{p}} = 0$. Alternatively, the second step can be solved analytically by using SELLMEIER's equation [251, 267]. Also here, pure thermo-optic coefficients are only determined at $E_{\mathrm{p}} = 0$. For an in-line monitoring during production, a set of thermo-optic coefficients has to be determined on reference samples to avoid the deposition and removal of metallic electrodes. The actual technique to measure the birefringence change is the so-called SÉNARMONT method, a phase detection technique measuring the phase shift between ordinary and extraordinary beam polarization, which is proportional to the birefringence. For a material with one polar axis (which is parallel to the optical axis), the temperature dependency of the pyroelectric field is given by

$$\mathrm{d}E_{\mathrm{p}}(T) = -2\frac{\mathrm{d}n_{\mathrm{p}}(T)}{n_{\mathrm{e}}^3(T)r_{33}(T) - n_{\mathrm{o}}(T)r_{13}(T)}, \tag{3.31}$$

where n_{o}, n_{e} and r_{ij} represent the refractive index of ordinary and extraordinary beam and the electro-optic coefficients, respectively. In combination with Eq. (3.29) this gives P_{S} and consequently the pyroelectric coefficient:

$$p(T) = \frac{2}{(n_{\mathrm{e}}^3(T)r_{33}(T) - n_{\mathrm{o}}(T)r_{13}(T)) \cdot \varepsilon_0\varepsilon_{\mathrm{r}}} \cdot \frac{\mathrm{d}n_{\mathrm{p}}(T)}{\mathrm{d}T}. \tag{3.32}$$

It is assumed that ε_{r} is temperature-independent, which is not true for larger temperature ranges and especially when phase transitions occur. Then, the $\varepsilon_{\mathrm{r}}(T)$ has to determined.

Measuring the change of the refractive index $\mathrm{d}n$ of non-birefringent materials for the determination of p was first described by POPESCU *et al.* [267], as shown in Fig. 3.7(b). A laser beam passes two polarizers in order to control power and polarization of the incident light. Sample and reference ray interfere on a CCD camera. The optical phase shift between two consecutive interference fringes is correlated to a refractive index change given by

$$\mathrm{d}\Phi = \frac{2\pi}{\lambda}\left(\mathrm{d}n_{\mathrm{S}} \cdot L_{\mathrm{S}} + \mathrm{d}n_{\mathrm{A}} \cdot 2 \cdot L_{\mathrm{A}}\right), \tag{3.33}$$

in which Φ is the total phase shift, L_{A} and L_{S} the surrounding air and sample length, n_{A} and n_{S} the refractive index of air and sample, respectively, and λ the wavelength of the incident

light. The total phase shift $\Phi = \Phi_S + \Phi_A$ is the sum of the phase shift due to thermally induced refractive index changes of sample (S) and surrounding air (A), respectively. Air is also heated because the sample does often not cover the total area of the heating element. This corresponding area is also penetrated by the light beam, which introduces a non-negligible contribution to the total phase shift. The phase shift attributed to the sample is furthermore divided in two parts according to Eq. (3.30). The pyroelectric contribution to the refractive index is given by

$$\mathrm{d}n_p = -\frac{1}{2} n^3 r_{\text{eff}} \mathrm{d}E_p, \tag{3.34}$$

in which n is the refractive index of the bulk, r_{eff} the electro-optic coefficient corresponding to the incident light polarization (in Ref. [267] $r_{\text{eff}} = r_{33}$) and E_p the electric field generated by the sample. The thermo-optic contribution is generally given from the temperature-dependent SELLMEIER equation by

$$\mathrm{d}n_{\text{to}} = \left(\frac{\partial n_S}{\partial T} \right)_{E=0} \mathrm{d}T. \tag{3.35}$$

The term $(\partial n_S / \partial T)_{E=0}$ is the thermo-optic coefficient of the sample, which is usually only given for a material with a specific polarization direction. As well as for the birefringence method, these coefficients have to be determined at $E_p = 0$, which requires shortened electrodes on the material surfaces. The contribution of heated air in Eq. (3.33) is given by

$$\mathrm{d}n_A = \left(\frac{\partial n_A}{\partial T} \right)_{E=0} \mathrm{d}T, \tag{3.36}$$

where $(\partial n_A / \partial T)_{E=0}$ is the thermo-optic coefficient of the surrounding air. In practice, it can be determined by heating and measuring the interference shift without the sample. The surrounding temperature has also an influence on the refractive index change so that a constant outer temperature is required. The combination of Eq. (3.33), (3.30), (3.34) and (3.35) results in

$$\mathrm{d}E_p = \frac{1}{n^3 r_{\text{eff}}} \cdot \left[2 \left(\frac{\partial n_S}{\partial T} \right)_{E=0} \mathrm{d}T + 4 \frac{L_A}{L_S} \left(\frac{\partial n_A}{\partial T} \right)_{E=0} \mathrm{d}T - \frac{\lambda}{\pi L_S} \frac{\mathrm{d}\Phi}{} \right]. \tag{3.37}$$

Using Eq. (3.29), the pyroelectric coefficient is given by:

$$p = -\frac{\varepsilon_0 \varepsilon_r}{n^3 r_{\text{eff}}} \cdot \left[2 \left(\frac{\partial n_S}{\partial T} \right)_{E=0} + 4 \frac{L_A}{L_S} \cdot \left(\frac{\partial n_A}{\partial T} \right)_{E=0} - \frac{\lambda}{\pi L_S} \cdot \frac{\mathrm{d}\Phi}{\mathrm{d}T} \right]. \tag{3.38}$$

Consequently, Eq. (3.38) provides the temperature dependency of the pyroelectric coefficient $p(T)$.

Both optical methods use a simple setup, i.e. a conventional interferometer equipped with a heating stage and thermometer. Also the measurement time is short in comparison to other methods. In contrast, many optical parameters, such as n (bulk), r_{eff}, $\partial n / \partial T$, and geometric parameters, such as L_S, L_A, are necessary. Electro-optic coefficients for air and sample are difficult to obtain and they are specific for the polarization direction of the incident light. Furthermore, their temperature dependency is usually only given by an empirical relation, thus, it is necessary to measure at constant surrounding temperature. POPESCU et al. mentioned that the use of a low power laser source, e.g. 100 nW, minimizes parasitic photorefractive-photovoltaic effects [267]. Also the contribution of heated air to the total refractive index (L_A distance in Fig. 3.7(b)) alters the result. Measuring under vacuum conditions could eliminate that problem. A separation between primary and secondary effect seems possible, since clamping could minimize the secondary contribution. After the determination of appropriate thermo-optic coefficients, an in-line monitoring during the production of pyroelectrics seems conceivable, because an optical and non-destructive measurement is given. The main drawback is its limited application field, because only pyroelectrics which are transparent for the incident wavelength and electro-optically active can be characterized.

3.3.3. Periodic Pulse Technique

Following the temperature ramping methods mentioned before, the first periodic technique was described by CHYNOWETH and demonstrated on the model ferroelectric BaTiO$_3$ [42]. The advantage of periodic methods is the phase-sensitive signal detection, providing higher signal-to-noise ratio and accuracy [22].

The periodic pulse technique requires a modulated light source to produce a square-wave heating of the sample, typically realized with a modulated IR laser or another appropriate light source of known heat flux F_0. To ensure thermal equilibrium, the on/off-frequency is determined from material parameters (see Sec. 3.1 and Eq. (3.3)). A frequency range of $10^{-2}\,\mathrm{Hz}$ to $10^3\,\mathrm{Hz}$ [42, 67, 127] is common, especially for thin film samples. The heating is performed via heat radiation, whereas the cooling also includes heat convection and conduction[191]. Metallic electrodes are necessary to measure the current response. Typically, a current-to-voltage converter is used to record the fast electric response.

The basic measurement setup and a theoretical temperature evolution and current response are shown in Fig. 3.8. Characteristic for optical heating is that the actual temperature is not measured, thus, requiring a modeling of $T(t)$. After the heat input, the temperature with respect to time $T(t)$ for establishing thermal equilibrium is expressed by an exponential function [191]

$$T(t) = T_{\mathrm{Amp}} \left[1 - \exp\left(-\frac{t}{\tau_{\mathrm{th}}} \right) \right],\qquad(3.39)$$

in which the thermal relaxation time τ_{th} is given by

$$\tau_{\mathrm{th}} = \frac{C}{\lambda} = \frac{m \cdot c_{\mathrm{p}}}{\gamma \cdot A},\qquad(3.40)$$

and the temperature amplitude T_{Amp} by:

$$T_{\mathrm{Amp}} = \frac{F_0}{\lambda}.\qquad(3.41)$$

C is the heat capacity, c_{p} the specific heat capacity, m the mass, λ the thermal conductance, γ the heat transfer coefficient, A the illuminated area of the sample and F_0 the heat flux. Current response $I(t)$ of the sample and F_0 are the measured quantities during the experiment.

To interpret the current response and extract the pyroelectric coefficient p, a mathematic model of the mentioned thermodynamic parameters, i.e. heat capacity, density, thermal conductance and heat transfer coefficient, is necessary. For thin films and multilayers this is more complex as a precise determination of all necessary parameters can be difficult. The modeling for several thin film types was outlined by LUBOMIRSKY et al. [191]. With the first time derivative of the temperature function and the general current response of a pyroelectric, $I = p \cdot A \cdot \mathrm{d}T/\mathrm{d}t$, the time dependence of the current after the heat input is given by:

$$I(t) = p \cdot A \cdot \frac{F_0}{C} \cdot \exp\left(-\frac{t}{C/\lambda} \right).\qquad(3.42)$$

The pyroelectric coefficient is given from Eq. (3.42) by setting $t = 0$:

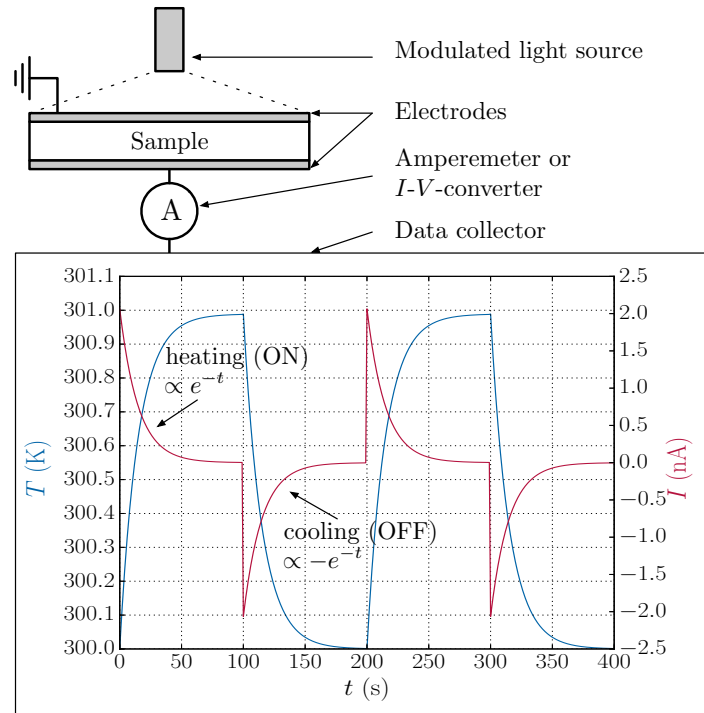$$p = \frac{I_{\mathrm{Amp}} \cdot C}{A \cdot F_0}.\qquad(3.43)$$

Fig. 3.8.: Schematic laser pulse setup with simulated current and temperature signal for a LiTaO$_3$ single crystal with 1 mm thickness and a diameter of 15 mm. Parameters: $c_M = 0.33\,\mathrm{W\,K^{-1}}$, $\lambda = 0.022\,\mathrm{W\,K^{-1}}$, $p = 176\,\mu\mathrm{C\,K^{-1}\,m^{-2}}$ and a comparably low excitation frequency $f = 10\,\mathrm{mHz}$.

The main advantage of this technique is the high frequency and, thus, short measurement time, which can be realized especially for small sample thicknesses. Furthermore, it produces large temperature changes $\mathrm{d}T/\mathrm{d}t$ compared to other dynamic methods, pronouncing the pyroelectric current signal [132]. As for all dynamic techniques, it is suitable for every pyroelectric, including non-ferroelectrics. Discharge of thermal traps is indicated by an asymmetric current waveform due to a discharge on heating, but not during cooling. The high frequency and cycle number minimize the influence of the TSC due to a quasi-continuous discharging of traps. Care has to be taken in choosing the wavelength of the incident light, because photocurrents (which can be several orders of magnitude higher than the pyroelectric current) have to be avoided [191].

The biggest problem of this method is the determination of the actual temperature [81], as outlined above. Diffuse and specular scattering of the laser light complicate the determination of the absorbed energy (only a part of the heat flux F_0 will be absorbed). Depositing a black absorption layer, usually carbon, on top of the upper electrode reduces the diffuse scattering problem.

A separation of primary and secondary pyroelectric coefficient is not possible. The illumination of one sample electrode impedes the realization of a clamped measurement condition. Although, the use of a transparent clamping material, covering the illuminated electrode, seems possible. A pronounced tertiary effect is to be expected, when using a focused light source. A mapping by scanning the sample or the light source is again limited by the minimal area A_{crit}.

A lot of modifications and extensions of this method have been published. SIMHONY and SHAULOV described an improved evaluation algorithm, which enables the simultaneous deter-

mination of the pyroelectric coefficient p, dielectric permittivity ε_r and specific heat capacity c_p by taking initial slope, rise and fall time of the voltage response into account [315]. ZAJOSZ added the theoretical model to calculate the spontaneous polarization P_S and the thermal diffusivity a [374].

EHRE $et\ al.$ demonstrated this technique for pyroelectric thin films on insulating substrates. Their modification works also with a pyroelectric substrate [68].

SCHEIN $et\ al.$ utilized an optical heating from the backside of a LiNbO$_3$ disk and a non-contact electrostatic measurement (no metallized electrodes) on the front side [293]. The potential is nullified to the surface potential, which is similar to the technique developed by GROTEN $et\ al.$ (see below). The method maps the surface potential distribution in two dimensions with a spatial resolution of 0.1 mm [292]. The laser spot only heats a small portion of the whole sample, which creates a lateral partial clamping, enabling the separation of primary, secondary and tertiary pyroelectric coefficient [291, 292].

GROTEN $et\ al.$ extended a scanning probe microscope to determine the pyroelectric coefficient on the nanometer scale and called it pyroelectric scanning probe microscopy (PyroSPM) [98, 323]. The method is based on the detection of the polarization change via KELVIN probe force microscopy (KPFM). A voltage to nullify the force between tip and sample is applied and combined with a macroscopic, periodic, and step-wise heating via a laser diode from the backside of the sample. The total pyroelectric coefficient is then given by

$$p = \frac{\varepsilon_0 \varepsilon_\mathrm{r}}{d} \cdot \frac{\mathrm{d}V_\mathrm{tip}}{\mathrm{d}T}, \tag{3.44}$$

in which $\mathrm{d}V_\mathrm{tip}$ is the change of the surface potential and d the layer or sample thickness. To minimize diffuse scattering and increase absorption of the incident light, a layer of black carbon may be deposited on the backside of the substrate or sample. As with the conventional thermal pulse technique, the temperature function has to be calculated for the respective sample. Beside the backside contact, no metallic coating is necessary. The resolution of this technique is about 50 nm to 200 nm, depending on tip sharpness, field spreading, sample morphology, and field contribution of the tip cone and the cantilever. The resolution is about one order of magnitude better compared to the LIMM methods described in the next section.

Recently, GHANE-MOTLAGH demonstrated a non-radiative step-wise heating and cooling approach by oscillating the pyroelectric material between a hot and cold reservoir with the help of an electromagnetic actuator (for more details see their Ref. [84]). Interestingly, it is quite similar to waste-heat energy harvesting setups, e.g. in Ref. [166, 205, 235].

3.3.4. Laser Intensity Modulation Methods

The laser intensity modulation method (LIMM), developed by LANG and DAS-GUPTA [162], uses a laser source to periodically irradiate the pyroelectric sample. The arising pyroelectric current is measured in amplitude and phase (in- and out-of-phase component) via a deposited metal electrode (sometimes opaque electrodes [260]), which additionally serves as heat absorbing layer, and thus, determines the spatial distribution of the polarization in two or three dimensions. Changing the frequency f of the incident thermal wave allows the characterization of the polarization P_S with respect to different penetration depths d_p (see Sec. 3.1.2) [15,

162, 260, 331]. Simultanously, the generated pyroelectric currents are measured, thus, the critical area A_{crit} has to be taken into account but typically the whole surface is coated with opaque electrodes [162]. A detection of spatial polarization distributions with a resolution of $0.5\,\mu\text{m}$ in d_{p} is of interest [260] especially for thin films.

The data analysis for this method is quite complex, because it needs a numerical deconvolution of the frequency dependence of the pyroelectric current (usually referred to as pyroelectric current spectra) to reconstruct the spatial distribution of P_{S} [162]. It involves assumptions on heat loss to the surrounding air and encircling sample, as well as the solution of the heat conduction equation. By simultaneously measuring the sample temperature (e.g. by monitoring the resistance of the metal electrode [13, 14]), it is possible to extract the pyroelectric coefficient without the need of modeling $T(t)$.

By scanning the laser [331] or the sample [23, 106, 209, 255, 270, 330] it is possible to get 2D and 3D information of the polarization distribution [106, 197, 209, 331], visualizing domain structures [106] and polar inclusions [270]. The spatial resolution (x and y) of the 2D image is in the range of several μm [106, 197] and in principle limited by the beam size, wavelength, scanning step size and the thermal diffusion length. A focused laser (focusing LIMM – FLIMM) improves the resolution down to $660\,\text{nm}$ [197, 320], which could be further improved by advanced image processing [269]. Recent literature refers to this technique as pyroelectric scanning microscopy (PSM) [65, 243, 255, 320] or scanning pyroelectric microscopy (SPEM) [144, 269, 270]. In contrast to the classic sinusoidal laser modulation of LIMM, a step-wise or chopped light intensity is often used in PSM/SPEM. It is then described as an intermediate between the periodic pulse technique and classic LIMM.

A separation of the primary pyroelectric coefficient from the secondary is only in principle possible, as totally clamped conditions are impractical. Field-induced contributions can be avoided due to the absence of an electric field. The method can give rise to tertiary pyroelectricity, because the focused laser source leads to strong lateral temperature gradients. A minimization of TSC-related currents is only possible by a high cycle number or previous shortening at elevated temperature.

3.3.5. Harmonic Waveform Techniques

An alternative to the aforementioned ramping and periodic pulse techniques is a harmonic thermal excitation. DAGLISH *et al.* reported a periodic triangular temperature excitation while simultaneously detecting the square-wave pyroelectric current [54, 57, 133, 134]. Its amplitude I_{Amp} can be extracted by FOURIER transformation or fitting (see Fig. 3.9(a)) yielding the pyroelectric coefficient by

$$p = \frac{I_{\text{Amp}}}{A \cdot \mathrm{d}T/\mathrm{d}t}, \tag{3.45}$$

in which the surface area A and heating rate (slope of each half wave) $\mathrm{d}T/\mathrm{d}t = 4 \cdot T_{\text{Amp}} \cdot f$, have to be inserted. Due to the need for metallized electrodes the spatial resolution is limited to A_{crit}.

For a sinusoidal temperature change the time-dependent temperature function $T(t)$ is generally represented by

$$T(t) = T_{\text{Amp}} \cdot \sin(\omega t + \phi_T) + b \cdot t + T_0, \tag{3.46}$$

in which T_{Amp} is the temperature amplitude, $\omega = 2\pi f$ the angular frequency (derived from frequency f), ϕ_T the phase shift (typically set to zero), T_0 the offset temperature, and b the heating/cooling rate superimposed on the oscillation.

Sussner et al. measured the change of charge using the voltage response $V(t)$ across a known external capacitor C_{ref}, which yields the pyroelectric coefficient by

$$p = \frac{C_{\mathrm{ref}}}{A} \cdot \frac{\mathrm{d}V}{\mathrm{d}t} \cdot \frac{1}{\mathrm{d}T/\mathrm{d}t}. \tag{3.47}$$

Sussner et al. also applied dielectric heating [334], as mentioned in Sec. 3.1.1, where $\mathrm{d}T/\mathrm{d}t$ is given by Eq. (3.1). In order to determine $p(T)$, the temperature dependency of all involved parameters is necessary. Metallic contacts are needed for the charge measurement limiting the lateral resolution to A_{crit}.

The simultaneous recording of the voltage response and a fit to the sinusoidal wave model similar to Eq. (3.46) was firstly reported by Hartley et al. (see Fig. 3.9(b)) [111]. The pyroelectric coefficient p is then given by

$$p = \frac{V_{\mathrm{Amp}}}{A \cdot T_{\mathrm{Amp}} \cdot \omega \cdot R_{\mathrm{L}}}. \tag{3.48}$$

Here, V_{Amp} is the voltage amplitude, T_{Amp} the temperature amplitude, ω the angular frequency of the temperature stimulation and R_{L} the resistance of the external load. The method assumes a phase difference between voltage and temperature oscillation of exactly 90°. Parasitic effects, e.g. TSC, could result in a phase shift of $\neq 90°$. A separation, as done by Sharp and Garn for current-based measurements (see below), is possible by adding $\sin(\phi)$ to Eq. (3.48), in which ϕ is the phase difference between temperature and voltage. The determination of T_{C} is possible, when measuring p at different offset temperatures T_0 ($b = 0$ in Eq. (3.46)) or combining the temperature oscillation with a linear function ($b \neq 0$ in Eq. (3.46)). Modern measurement instruments (with resolutions of µV and mK) are able to measure very small signals and reduce the relative error compared to the original work [164].

Similar to the Hartley approach, a sinusoidal temperature waveform was used by Sharp and Garn, but now measuring the pyroelectric current I directly. The phase information of the oscillations enables a separation between pyro- and non-pyroelectric currents [78, 79].

The technique associates a non-pyroelectric, thermally stimulated current (TSC) I_{np} to any kind of charges in the material, which are released during the thermal excitation. This current is approximated by

$$I_{\mathrm{np}}(T) = I_{\mathrm{np},0} + B_{\mathrm{T}} \cdot T, \tag{3.49}$$

in which $I_{\mathrm{np},0}$ is a temperature-independent current and B_{T} a temperature coefficient (dimension of $\mathrm{A\,K^{-1}}$), describing the nature of the thermal traps [78]. The pyroelectric current on the other hand is given by

$$I_{\mathrm{p}} = p \cdot A \cdot \frac{\mathrm{d}T}{\mathrm{d}t}, \tag{3.50}$$

involving pyroelectric coefficient p, surface area of the sample A and first time derivative of the temperature function. Combining Eq. (3.49), (3.50) and the first time derivative of Eq. (3.46), yields a total (I_{T}), an alternating (I_{AC}) and a constant (I_{DC}) current as follows:

$$I_{\mathrm{T}}(t) = I_{\mathrm{DC}} + I_{\mathrm{AC}}, \tag{3.51}$$

$$I_{\mathrm{DC}}(t) = I_{\mathrm{np},0} + B_{\mathrm{T}} \cdot (T_0 + bt) + p \cdot A \cdot b, \tag{3.52}$$

$$I_{\mathrm{AC}}(t) = B_{\mathrm{T}} \cdot T_{\mathrm{Amp}} \cdot \sin(\omega t) + p \cdot A \cdot \omega \cdot T_{\mathrm{Amp}} \cdot \cos(\omega t). \tag{3.53}$$

(a) Schematic of a triangular temperature and generated square-wave current waveform. Redrawn from Ref. [133].

(b) Schematic signal of a sinusoidal temperature excitation and generated voltage waveform as realized by HARTLEY *et al.* [111].

(c) Schematic signal of the SHARP-GARN technique. Cyan and magenta are the pyroelectric (I_p) and non-pyroelectric (I_np) contributions, respectively.
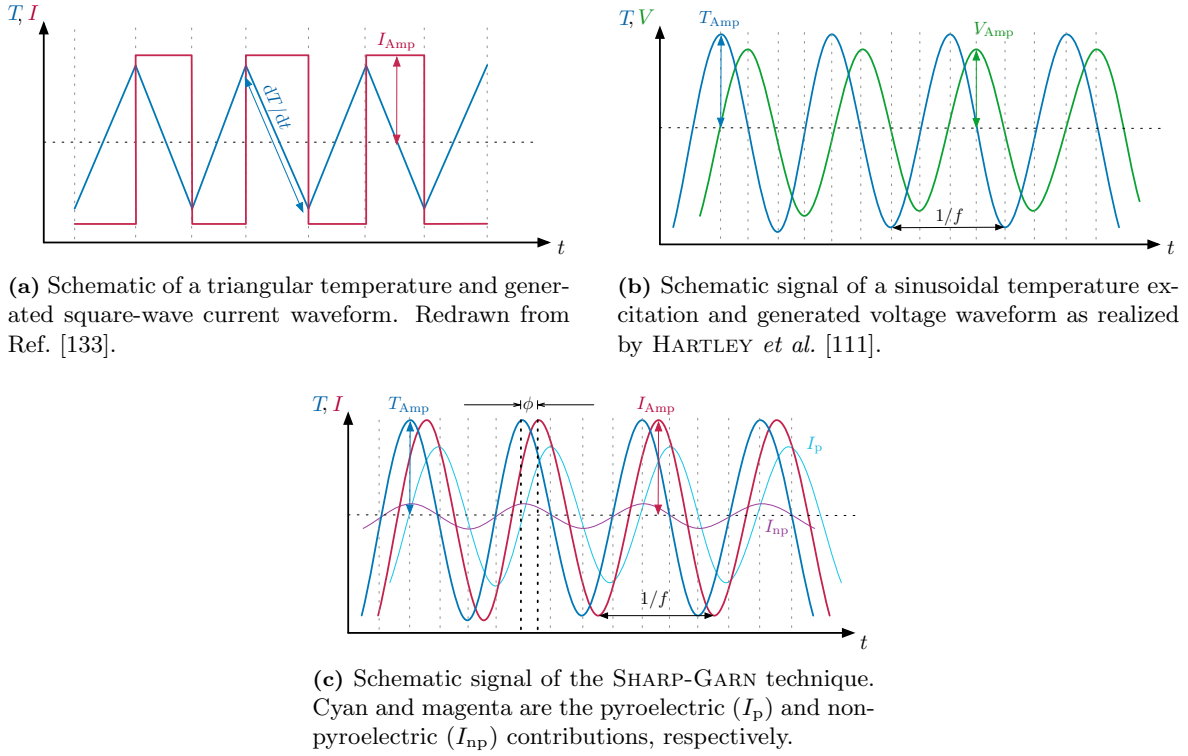
Fig. 3.9.: Schematics of arbitrary waveform techniques visualizing the stimulating temperature and measured signal functions.

The AC part of the current is, thus, described by two oscillating parts. In Eq. (3.53) the non-pyroelectric part is in phase with the sinusoidal temperature function, while the pyroelectric part is 90° out of phase, which stems from the applied first time derivative to obtain the pyroelectric current. From the the phase difference

$$\phi = \phi_\mathrm{I} - \phi_\mathrm{T} \tag{3.54}$$

between current and temperature, the pyroelectric coefficient is given by:

$$p = \frac{I_\mathrm{Amp} \cdot \sin(\phi)}{A \cdot \omega \cdot T_\mathrm{Amp}}. \tag{3.55}$$

Hence, a phase shift of $\phi = 90°$ represents a pure pyroelectric signal [62, 78, 79, 261]. A combination of non-pyroelectric and pyroelectric signals exists for $\phi \neq 90°$, as sketched in Fig. 3.9(c). In order to extract the parameters for this equation, fitting or FOURIER decomposition of the recorded data is necessary. Alternatively, measuring the current amplitude with a lock-in amplifier at the excitation frequency also provides these parameters, with an improved signal-to-noise ratio. Real and imaginary part of the current again distinguish between pyroelectric and non-pyroelectric current, as it is performed by PLOSS *et al.* [261, 262].

All waveform methods enable a quasi-continuous evaluation of $p(T)$ by slightly shifting the offset temperature with the term $b \cdot t$ in Eq. (3.46). A part-wise evaluation of every period gives p at the averaged temperature of the respective oscillation. The parameter b has to be chosen to ensure a quasi-constant offset temperature, i.e. $2\pi/\omega \cdot b \ll 1$, which also determines the temperature resolution of $p(T)$. These dynamic methods appear as very versatile, especially the SHARP-GARN and HARTHLEY method, as most of the general considerations are realizable (compare check marks in Fig. 3.1). Beside the separation of TSCs, also the

modeling of the temperature course with the help of thermal parameters is unnecessary, as the actual temperature is typically directly measured. This, together with the relatively low experimental effort, make these techniques very attractive and, thus, the Sharp-Garn technique was realized in the setup described in the following chapter.

4. Pyroelectric and Ferroelectric Characterization Setup

The purpose of this chapter is to describe the established measurement environments used for the characterization of the investigated pyro- and ferroelectrics in this work. They enable the determination of the pyroelectric coefficient and polarization depending on temperature.

The first part of this chapter briefly recapitulates the measurement of the pyroelectric coefficient as a function of temperature with the setup developed by MEHNER [207], because several contributions were made during this work. It utilizes the SHARP-GARN approach [78, 79] (see Sec. 3.3.5) for its advantages compared to other techniques outlined in Chapter 3. The present work adds several specific setup improvements, e.g. advanced electric circuitry and the ability to measure the pyroelectric coefficient of nanometer-sized thin films. Furthermore, the evaluation algorithm, which calculates the pyroelectric coefficient, its temperature dependency and related data from the measured raw signals, was developed. This fully automated evaluation is bundled in the PYTHON program PYROFIT, which was constantly developed and improved during this work.

The second part is dedicated to the setup extension, which allows polarization P versus electric field E hysteresis loop measurements of a ferroelectric sample. It includes the description of the instrumentation, controlling and evaluation of the applied Shunt method (see Sec. 3.2.2) bundled in the PYTHON software HESMCTRL. With this, the type of polarization, i.e. di-, para-, ferro- or even antiferroelectricity, as well as important material parameters, such as remanent polarization P_R and coercive field strength E_C of thin films as well as bulk materials, can be analyzed.

4.1. Pyroelectric Measurement Setup

4.1.1. Setup and Instrumentation

The central measurement setup to determine the pyroelectric coefficient is built around a sample stage contained in a stainless steel vacuum chamber. It allows a defined temperature change of the mounted sample while continuously recording certain electrical data. Photographs and a schematic of the setup are shown in Fig. 4.1 and Fig. 4.2, respectively. The main components of the setup are listed below, while their interplay is described in more detail in the following:

- a stainless steel vacuum chamber, comprised of a feedthrough for all electrical lines (1), vacuum sensor (2), and sample stage (3, described in more detail below),

- a power supply (HP 3632A) for heating and cooling via a 15 W Peltier element (Quick-cool) on top of the sample stage,

- a multimeter (Keithley 2700) for the acquisition of the sample temperature via 4-wire resistance measurements of one or two Pt100 resistive thermometers,

- a hot plate adjusting the temperature of the whole measurement chamber, allowing higher maximum temperatures (see below),

- a feedback amperemeter/electrometer (Keithley 6514 or Keithley 6517B) to acquire electrical signals, mostly small electrical currents in the pA and nA range,

- a high-voltage supply, e.g. Keithley 6517B (1 kV), Stanford Research System PS350 (5 kV) or another, for sample poling, i.e. the parallel alignment of ferroelectric domains via constant current poling (tested up to 5 kV), and

- a "Switchable Amperemeter Protection Circuit" (SAP), containing a computer-controlled protection circuit (see Fig. 4.4), which can be switched into the measurement circuit to protect damages from unpredictable high-voltage breakdowns of the sample during a poling procedure.

The sample stage (see Fig. 4.3) consists of the Peltier element, which is glued with the help of heat-conducting paste to an aluminum block as heat sink, which in turn is attached to the bottom of the stainless steel vacuum chamber. A bottom copper contact is fixed to the Peltier element with the help of thermal conducting glue. Furthermore, the copper serves also as an additional heat spreader, balancing potential temperature fluctuations and should prevent lateral temperature inhomogeneities, which could give rise to the tertiary contributions of the total pyroelectric coefficient (see Sec. 3.1.4). A Pt100 thermometer is directly glued on top of the copper plate and additionally electrically isolated with epoxy resin. The top contact is achieved by either another copper plate, which is directly pressed onto the metalized sample (Fig. 4.3(a)), or by using a fine metal needle, which can be positioned on the sample surface (Fig. 4.3(b)). The first option allows top contact geometries fitting the exact sample size and shape and additionally permits the integration of a second Pt100 thermometer. Typically, rectangular and circle-shaped circuit board parts of different sizes were used. While the first option is more suitable for large contact pads on large samples, such as single crystals, ceramics or thick polymer films, the latter is favorable for small contact pads on thin films. Furthermore, the fixation of the sample can reduce, albeit not eliminate, the secondary contribution to the total pyroelectric coefficient (see Sec. 3.1.4).

The controlling software "Pyroelectric Measurement Control" (PMC), written by E. Mehner in Visual Basic, operates all connected measurement devices via a GBIP-Bus and RS232/485 connections. The HP 3632A power supply and temperature-acquiring Keithley 2700 multimeter form a closed-loop PID controller, enabling a temperature precision of a few mK [207]. While the actual maximum excitation frequency depends on material parameters such as thermal diffusivity α and thickness d (see Sec. 3.1.2 and Appendix A), a maximum excitation frequency of approximately 200 mHz represents the upper limit of the measurement setup [207]. Especially for samples with a thickness of over 1 mm, the maximum excitation frequency has to be restricted to lower frequencies as exemplified in Fig. 3.1 for traditional pyro- and ferroelectrics. With the present setup, an up to two orders of magnitude smaller frequency than the predicted one (see Fig. 3.1) has proven to be satisfying, because of the

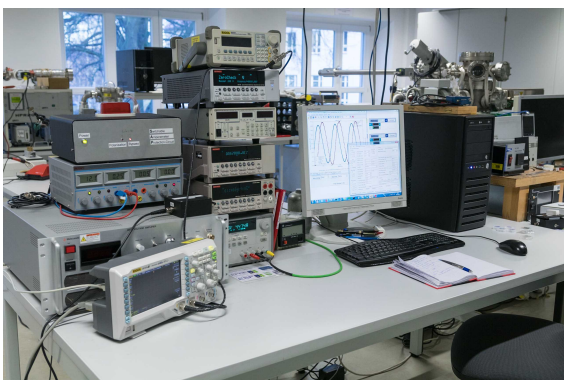**(a)** Overview of the pyroelectric measurement setup environment.
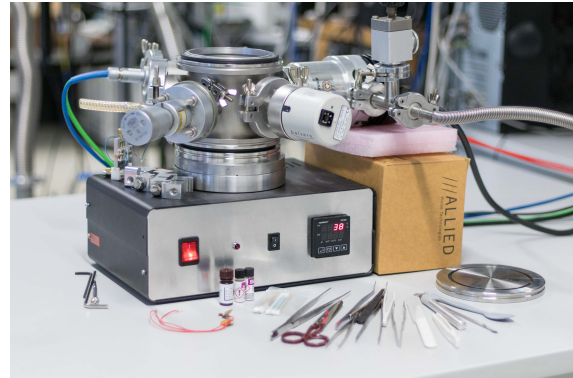
(b) Vacuum measurement chamber standing on the hot plate.
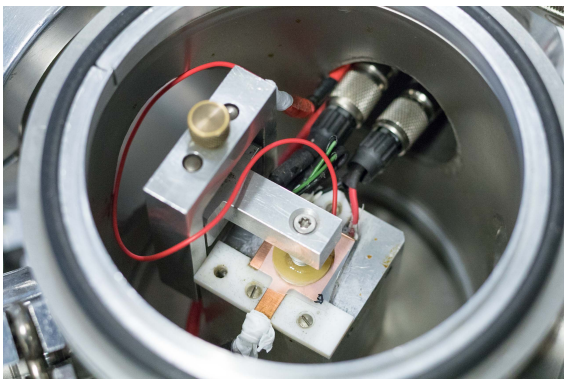
(c) Sample stage with fixture for large contact pads. See also Fig. 4.3(a).

(d) Sample stage with adjustable needle contact for small contact pads. See also Fig. 4.3(b).

(e) Measurement hardware, comprised of controlling computer and characterization instruments.

(f) Switchable Amperemeter Protection Circuit (SAP) box.

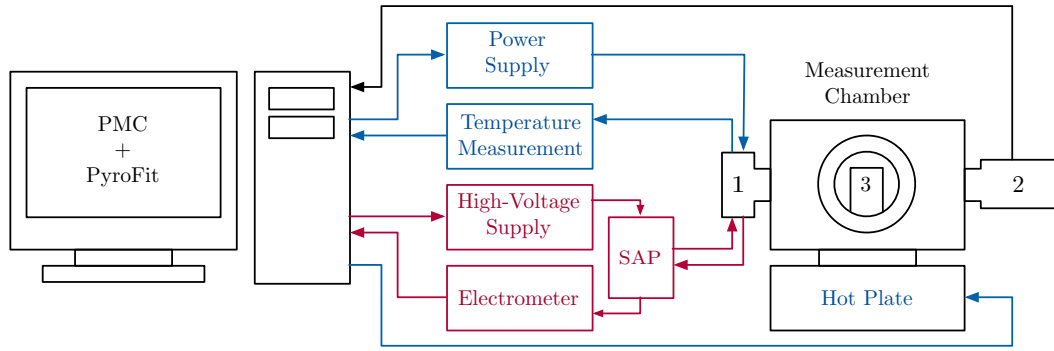**Fig. 4.1.:** Photographs of the pyroelectric measurement setup.

Fig. 4.2.: Schematic of the pyroelectric measurement setup. The controlling computer, running the PMC software, controls all devices (visualized by the arrows), which are connected to the measurement chamber via a vacuum-sealed feedthroughs (1). The Switchable Amperemeter Protection Circuit (SAP) includes the protection circuit, necessary during a polarization measurement (see below). The vacuum sensor (2) is optional. The sample stage (3) inside the chamber holds heater and sample (more details in Fig. 4.3). It has to be noted that the components marked in red can be replaced by other instruments for the detection of other electrical quantities. Components marked in blue are necessary for the temperature control.
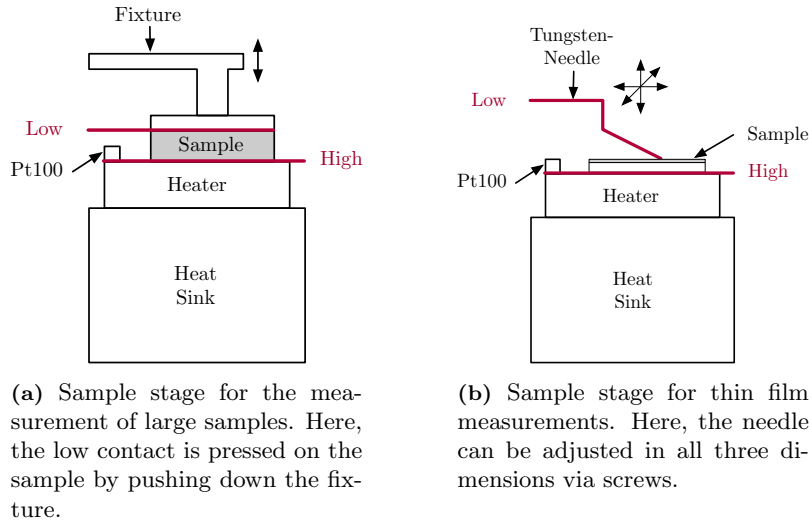

(a) Sample stage for the measurement of large samples. Here, the low contact is pressed on the sample by pushing down the fixture.

(b) Sample stage for thin film measurements. Here, the needle can be adjusted in all three dimensions via screws.

Fig. 4.3.: Possible sample stage configurations used for the characterization of differently shaped pyroelectrics. The heat sink is made of aluminum, while the heater is a PELTIER element. The bottom contact is sheet of copper.

non-ideal heat transfer from heater to sample. Practically, a frequency of $10\,\mathrm{mHz}$ to $50\,\mathrm{mHz}$ serves as a good starting point for most samples up to $0.5\,\mathrm{mm}$ thickness.

In order to achieve higher absolute temperatures and to access a larger measurement range or study temperature-induced phase transitions of a material a hot plate below the vacuum chamber is necessary to heat the entire sample stage. A single PELTIER element can only produce a temperature difference of approximately $70\,\mathrm{K}$ relative to the present ambient temperature, thus, the surrounding temperature has to be lifted. The maximum temperature is limited by the maximum operation temperature of approximately $170\,^{\circ}\mathrm{C}$ of the PELTIER element. The hot plate is controlled via an additional Omega CN7800 PID controller, which is also remote-controlled via the computer.

The electrical connection to the high and low contact on the sample stage is achieved by PTFE-isolated coaxial and triaxial cables, which are high-voltage resistant up to $10\,\mathrm{kV}$. Sealed FISCHER connectors and sockets were used for wiring to the inside of the vacuum
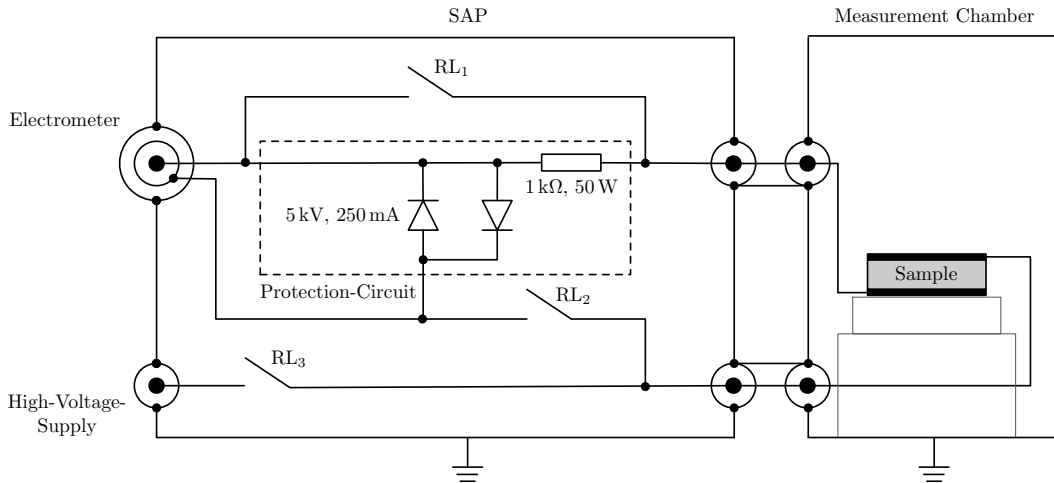
Fig. 4.4.: Electrical circuitry of the pyroelectric measurement setup. During a pyroelectric current measurement reed relay RL_1 and RL_2 are closed, while RL_3 remains open. When applying high voltages the reversed positions activate the protection circuit, consisting of a resistor and two opposing diodes. The circuit was adopted from Ref. [341].

chamber. The latter serves, besides the good thermal isolation, as an electrical noise shield and provides a high-voltage resistant environment for poling with high electric fields. Current noise levels of approximately 200 fA (direct connection to sample stage without SAP) to 2 pA (connection via SAP) can be achieved.

The poling of the material before a measurement of the pyroelectric coefficient can be achieved in different ways, e.g. by applying a sufficient constant voltage or by cycling the voltage during a hysteresis measurement (see Sec. 4.2). To prevent an immediate breakdown of the sample, the voltage is increased step-wise in a way that the leakage current trough the sample is kept constant at a certain level. This procedure is usually termed constant current poling and can be applied in corona (CCCP) and contact poling [21, 72, 85, 86]. The latter is used in the pyroelectric measurement setup, where the high-voltage can be supplied by several high-voltage sources with different output ranges, e.g. Keithley 6517B (up to 1 kV) and Stanford Research Systems PS350 (up to 5 kV). As mentioned before, the vacuum chamber provides a high-voltage resistant surrounding for the sample, which unfortunately cannot completely prevent a discharge through the sample for very high electric fields. Such a breakdown can damage the attached electrometer, thus, a good protection is necessary. For this purpose, the "Switchable Amperemeter Protection Circuit" (see Fig. 4.1(f)) was developed. Its circuitry, used components, and connection with the coaxial/triaxial instrument inputs are shown in Fig. 4.4 including the attached sample stage . At high voltage the two parallel back to back diodes become conductive, thus charge is flowing to the ground and the high-voltage breaks down. The resistor limits the current flow to prevent damage to the diodes [341]. For low current measurements below 10 pA signals, the protection circuit has be excluded from the circuitry as outlined in Ref. [341]. The three high-voltage resistant reed relays RL_1, RL_2 and RL_3 are necessary to enable or disable the protection circuit, depending whether a low noise pyroelectric current measurement or poling procedure is intended. All relays are remote-controlled with the computer via a relay card. It has to be noted that the usage of the SAP increases the overall background noise from approximately 200 fA to 2 pA for the measurement of the pyroelectric current.

Different temperature profiles combined with the acquisition of various electrical quantities enable a broad spectrum of possible measurement techniques for p, especially dynamic method

as outlined in Chap. 3. Due to the possibility of precise temperature and low-noise current acquisition, the SHARP-GARN method (see Sec. 3.3.5) is the preferentially used, allowing single-temperature – $p(T_0)$ – as well as temperature-dependent – $p(T)$ – measurements from approximately 0 °C to 170 °C. With the setup minimal pyroelectric coefficients of approximately $10^{-4}\,\mu\mathrm{C\,K^{-1}\,m^{-2}}$ can be detected with an error between 1 % to 5 %, depending on the presence of TSCs, contact area size and electric current magnitude [207]. Further details on calibration, precision, and data acquisition are given by MEHNER in Ref. [207].

4.1.2. Automated Sharp-Garn Evaluation of Pyroelectric Coefficients

As the PMC software is responsible for instrument control and data acquisition, the next step for a complete automated pyroelectric characterization system is the processing and evaluation of the raw signals. For this, the program PYROFIT[9] was developed during this work in the programming language PYTHON. It uses several extension packages, primarily NUMPY, LMFIT and MATPLOTLIB for data handling, fitting and visualization, respectively. The current script version 0.9.9 includes over 2400 code lines and is still in development in order to improve functionality, compatibility and performance. A flowchart describing the components of the program is given in Fig. 4.5 and will be briefly described in the following.

After reading all data files created by PMC a filter removes overflow values created by the measurement instrument as well as values above and below a user specific threshold value as this dramatically increases the robustness of the subsequent signal fitting. The next step is the identification of the present measurement type, i.e. whether a SHARP-GARN or another approach was utilized. The decision is made using the previously selected settings in PMC, which leads to different evaluation scenarios. The extraction of the thermal excitation parameters serves as initial values for the temperature and electrical signal fit. Besides the SHARP-GARN method, the script has much more capabilities including the evaluation and visualization of constant current poling profiles, temperature oscillations under constant electric field (e.g. see Ref. [108]) or electrical conductivity σ_{el} measurements. The latter is performed by measuring the sample resistance R_{S} at different temperatures and using sample area A and thickness d to calculate σ_{el}. Also the relative dielectric permittivity ε_{r} and loss tangent $\tan\delta$ and their temperature dependency is provided by capacity measurements with an LCR bridge assuming a parallel plate capacitor model. The following will focus on the SHARP-GARN technique, i.e. the evaluation of p at a single offset temperature T_0 or its temperature dependency $p(T)$.

The measured raw signals were typically recorded at different sampling frequencies for current and temperature, which makes an interpolation step necessary to bring both data sets to a common time grid. As the current PMC version samples both quantities with approx. 2 Hz, the interpolation is not necessary any more, but still used to align the slightly different timestamps. A subsequent visualization (see Fig. 4.6) of the temperature (blue dots) and current signal (red dots) gives the user a first impression, whether the measurement was successful or not. Then a prompt asks for the electrode area in m^2 before starting the fitting procedure. Here, the smallest common area in case of asymmetric electrodes has to be entered, as its corresponding volume (with sample thickness d) generates the pyroelectric

---

[9]The full source code, example data sets and future updates are available on `https://github.com/SvenJachalke/PyroFit`.
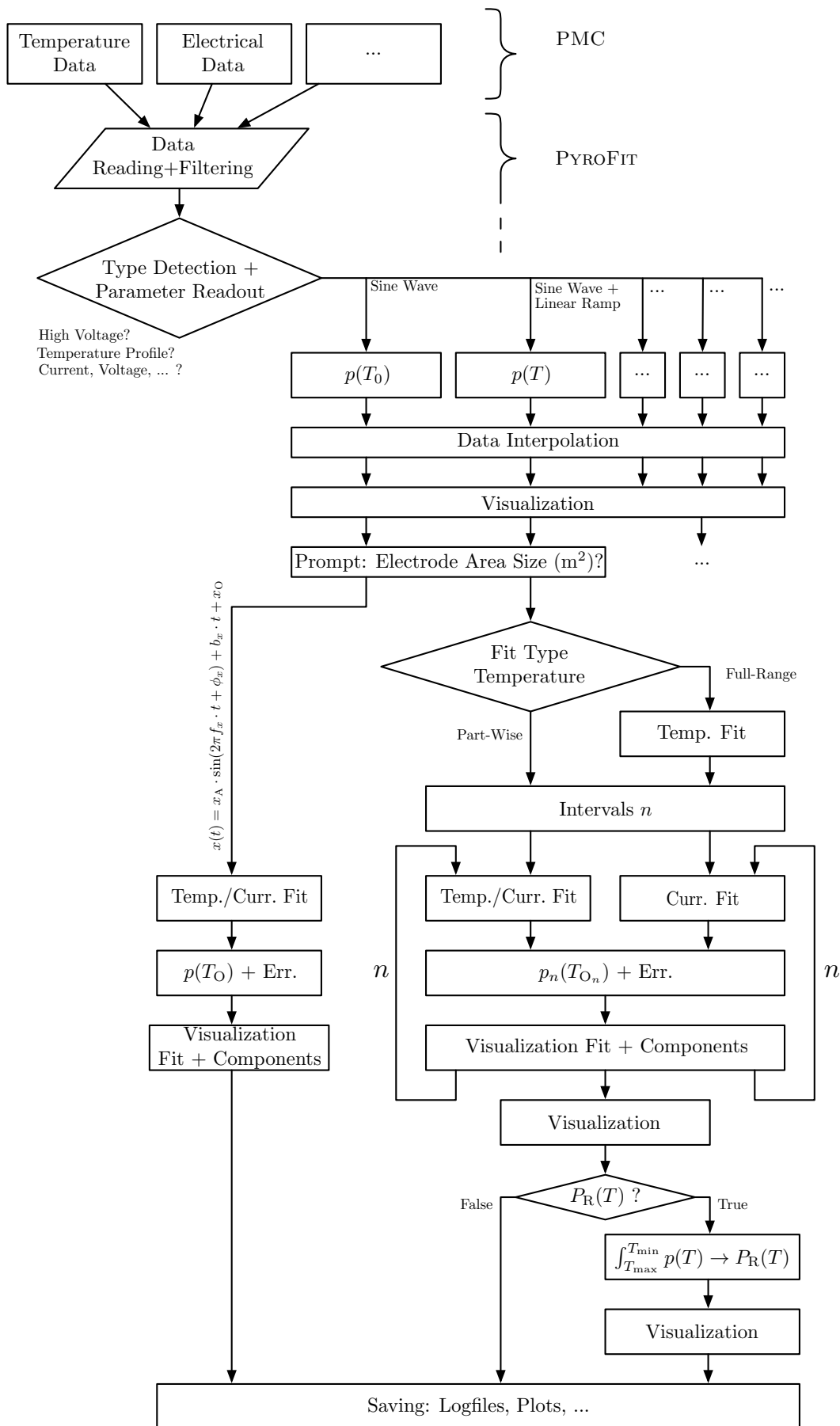
Fig. 4.5.: Program flowchart visualizing the working principles of PYROFIT.

current flow. It has to be noted that the script allows quick access to often used electrode areas and their corresponding statistical errors for standard electrode configurations.

For a single-temperature measurement the interpolated data sets are fitted to a combination of sinusoidal wave and linear function (compare to Eq. (3.46))

$$x(t) = x_{\mathrm{Amp}} \cdot \sin(2\pi f_x + \phi_x) + b_x \cdot t + x_{\mathrm{O}} \qquad (4.1)$$

by the least-square algorithm of the LMFIT package, which supports constraints of the fitting parameters. Here, x represents the signal type, i.e. temperature T or current I, x_{Amp} the amplitude, f_x the frequency, ϕ_x the phase shift, b_x the slope of the linear background and x_{O} the offset of the respective signal. The starting point of the fit can be specified by the user in order to ignore unwanted, initial signal oscillations caused by the PID controller. The whole temperature data is fitted at first and the extracted frequency is passed to and fixed in the subsequent current fit. It has proven to perform the fits without additional amplitude and phase constraints although only a positive amplitude and a range of $\pm\pi$, respectively, are reasonable. Thus, absolute values of x_{Amp} with a corresponding shift of ϕ_x by $\pm\pi$ are formed in order to omit algebraic sign confusions in subsequent calculations. Also, fitted phase values above 2π or below 0 will be transformed into the reasonable range ensuring human legibility. In order to inspect the results graphically, the fitted signals are displayed in combination with the measured data. The total phase shift ϕ is then calculated by:

$$\phi = \phi_T - \phi_I \qquad (4.2)$$

and passed, together with T_{Amp}, I_{Amp} and area A to the SHARP-GARN formula (see Eq. (3.55)) to obtain p at the offset temperature T_{O}. The relative error $\Delta p/p$ is calculated using the law of propagation of uncertainty:

$$\frac{\Delta p}{p} = \left| \frac{\Delta I_{\mathrm{A}}}{I_{\mathrm{A}}} \right| + \left| \frac{\Delta \phi}{\tan \phi} \right| + \left| \frac{\Delta A}{A} \right| + \left| \frac{\Delta T_{\mathrm{A}}}{T_{\mathrm{A}}} \right| + \left| \frac{\Delta f}{f} \right|, \qquad (4.3)$$

in which Δ marks the absolute error of the respective quantities. Typically, the total error is given on a 3σ level (with σ being the standard deviation estimated from the covariance matrix of the least-square algorithm), which can be adjusted by the user. Here, ΔA has to be estimated from the standard deviation of the area determination. Systematic instrument errors in I and T are small, i.e. below 1 % and, thus, are neglected. From the phase shift ϕ the non-pyroelectric in-phase and pyroelectric out-of-phase current contributions are calculated and visualized together with the measured data.

The end of this first branch is the saving of the results and visualization plots into separate text files. An example plot is shown in Fig. 4.6 for a $5.0\,\mathrm{mm} \times 5.0\,\mathrm{mm} \times 0.1\,\mathrm{mm}$ LiNbO$_3$ single crystal.

The $p(T)$ determination is carried out by a sinusoidal wave temperature oscillation superimposed with a linear or triangular function. In contrast to a single-temperature measurement, a single evaluation cycle is not appropriate, because of the presence of non-constant background currents (b_I, I_{O}) over a large temperature range. Here, the algorithm presented for the single-temperature measurement can in principle be executed for a certain number of slices of the whole data set, i.e. partially fitting the current in individual data subsets. The size of such a slice can be specified by the user, but is typically set to two temperature oscillations by default. The obtained value of p_n in slice n is associated to the mean temperature T_0 of the respective interval. Thus, looping the procedure described for a single-temperature measurement over all intervals gives the temperature dependency of p as indicated in Fig. 4.5.
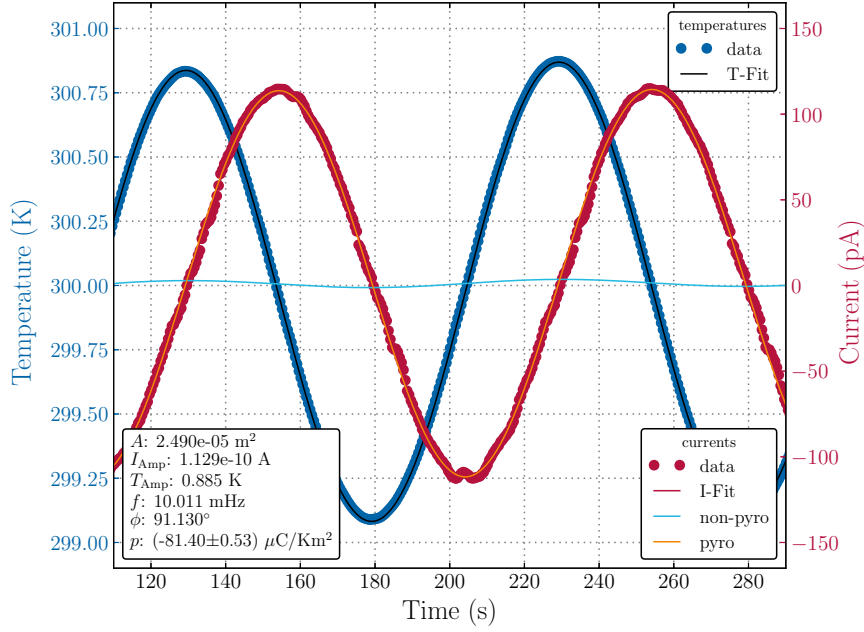
Fig. 4.6.: PYROFIT output plot of a single-temperature measurement combining raw data and fit visualization.

The interval size and heating rate b_T define the temperature resolution of p, which becomes large when both parameters become small. For low measurement frequencies, e.g. below 5 mHz the interval size is comparably large, thus, the heating rate has also to be small. As an example, the evaluation of two temperature oscillations at a heating rate of $10 \, \mathrm{K \, h^{-1}}$ and a frequency of 10 mHz gives a temperature resolution of approx. 0.5 K.

A secondary plot (see Fig. 4.7(b)) allows a detailed inspection of the fitted and calculated values with respect to the temperature. It contains:

- Top left: $p(T)$ as primary output (and, when selected, $P_R(T)$ – see below),

- Top right: the ratio between pyroelectric and non-pyroelectric current contribution/amplitudes $I_p/I_{np}(T)$,

- Bottom left: $I_{Amp}(T)$, $I_O(T)$ and $\phi(T)$ to judge the current fit,

- Bottom right: the reduced current amplitude x^2/I_{Amp}^2 as a "goodness of fit", which yield approximately 1 for a good fit.

In case of a phase transition, visible by a maximum and/or a subsequent vanishing of p, the remanent polarization $P_R(T)$ can be recovered by numerically integrating the $p(T)$ data, based on:

$$P_R(T) = \int_{T_C}^{T_{min}} p(T') \, \mathrm{d}T'. \tag{4.4}$$

The transition temperature T_C can be selected graphically from the $p(T)$ plot, setting $P_R(T_C) = 0$ as followed from the theory. At this point it has to be noted that in case of very sharp phase transitions, the course of $P_R(T)$ is underestimated. This is because the large current spikes, resulting from the short passing of T_C within one temperature oscillation, prohibit a good sine wave fit and, thus, yield inaccurate values. In this case, the
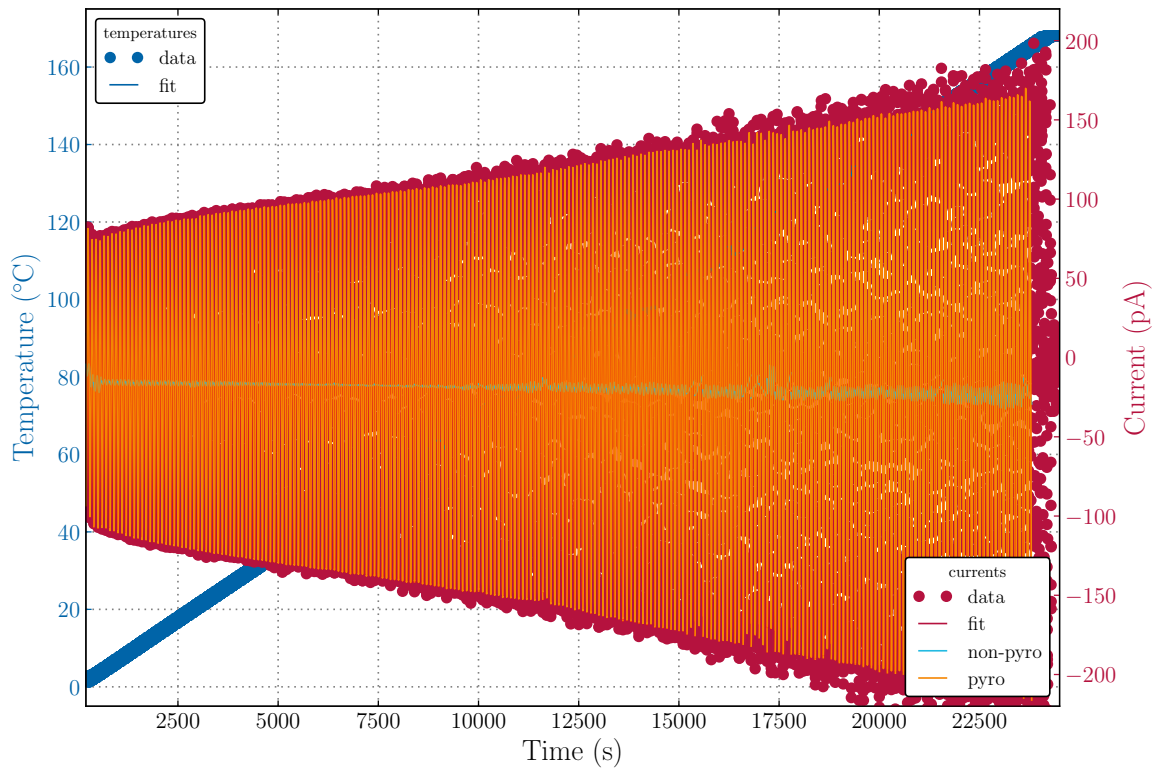
(a) Raw signal plot of temperature (left axis, blue) and current (right axis, red) together with the fitted curves and pyroelectric (orange) and non-pyroelectric (cyan) current contributions. Due to the length of the measurement single oscillations are not visible.
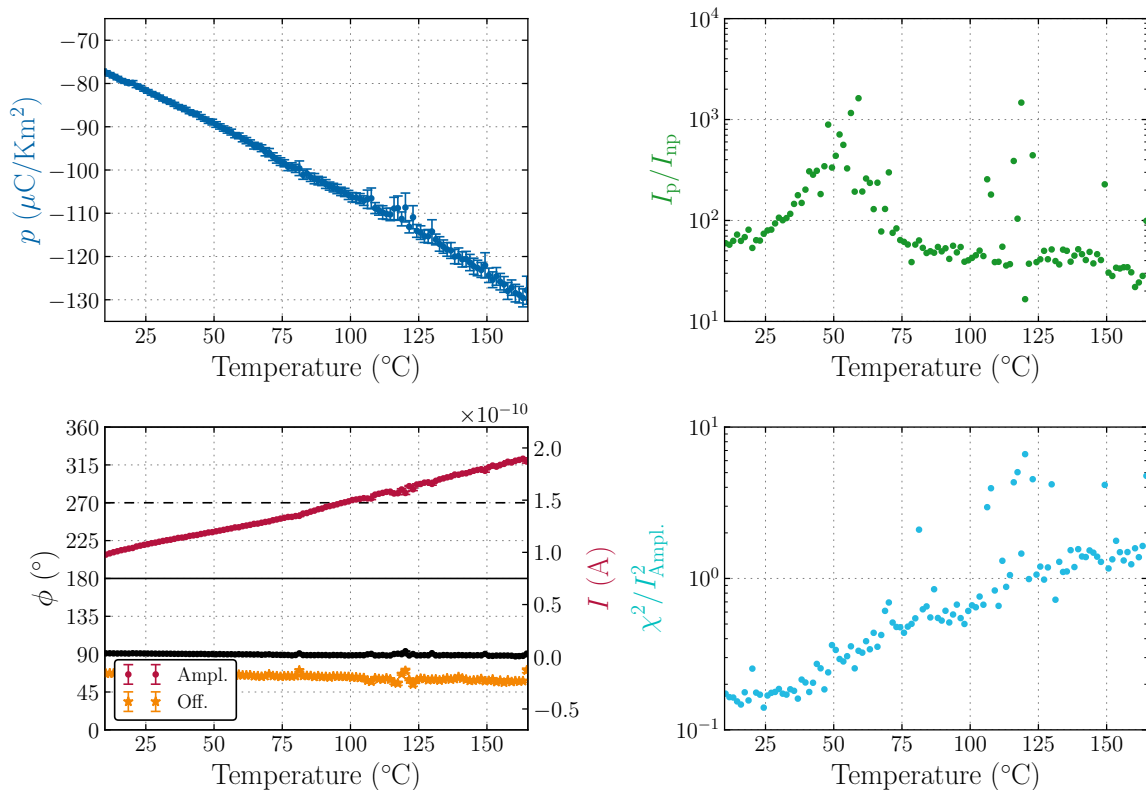
(b) Detail plot of fitted and calculated parameters with respect to the temperature as described in the text.

Fig. 4.7.: PYROFIT output plots for a temperature-dependent measurement of the pyroelectric coefficient.

(a) Low temperature.   **(b)** Medium temperature.   **(c)** High temperature.
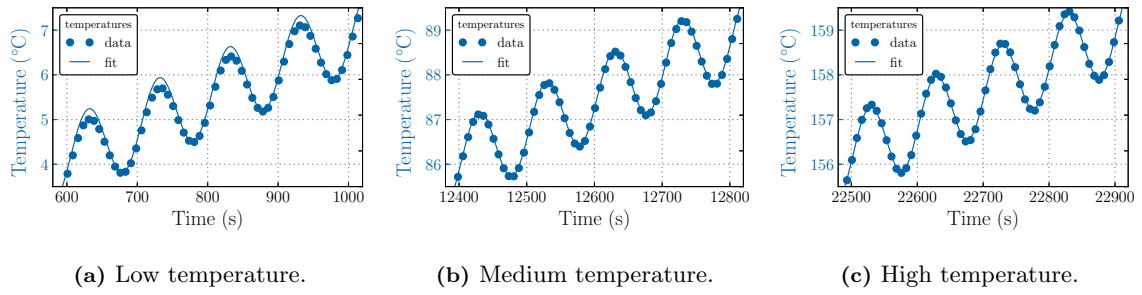
Fig. 4.8.: Full-range temperature curve fit at different temperatures.

BYER-ROUNDY technique (Sec. 3.3.1) or the SAWYER-TOWER method (Sec. 3.2.2) can provide more accurate results. Nevertheless, the phase transition temperatures of ferro-/ferro- and ferro-/para-/dielectric transitions can be precisely determined.

As indicated in Fig. 4.5, the fitting for the $p(T)$ evaluation can be done in different ways. Initially, the whole unsliced temperature signal was fitted to Eq. (4.1) and a slicing was only performed on the current signal, based on the assumption of an accurate temperature profile throughout the measurement. Unfortunately, the latter is not always assured for measurements with a large temperature span, e.g. from $0\,°C$ to $170\,°C$. While the PID parameters of the controller are tuned at ambient temperature, they are not optimal at low and high temperatures. A slightly detuned controller causes deviations in the temperature signal, leading to a fit overestimation at low and underestimation at high temperatures (compare fits in Fig. 4.8). Fortunately, the sinusoidal shape is maintained throughout the whole temperature range. As a consequence, the same part-wise fitting procedure as for the current has to be applied to the temperature signal.

A comparison between the full-range and part-wise fit of the temperature is shown in Fig. 4.9. Here, the differences of ϕ, T_O and T_{amp} are most pronounced visible. The latter has a double-plateau shape for the part-wise approach with a kink point at approx. $75\,°C$, which is probably associated with the increasing influence of the hot plate raising the temperature of the whole measurement chamber. The associated errors of the part-wise approach are comparable to the full-range one, albeit approx. two orders of magnitude worse for f_T and b_T. Nevertheless, this has no significant influence on the error of p, because the dominating errors are those of I_{Amp} ($\approx 65\,\%$) and T_A ($\approx 24\,\%$ of the total error of p).

The dramatic impact of different temperature fit results on $p(T)$ can be seen in Fig. 4.9(c). Here, the part-wise fitting approach provides higher absolute values of p, especially at lower temperatures, due to a more precise determination of T_{Amp} and ϕ_T. These results now match those of a single-temperature measurement (compare to room temperature measurement in Fig. 4.6). The described problem is less pronounced for smaller temperature ranges and initial offset temperatures near the tuning point of the PID controller.

4.1.3. Further Examples

This last subsection on the pyroelectric measurements is meant to serve as a brief outline of investigations, which are beyond the scope of this work, but were also conducted during the time of this thesis with the help of the described setup.
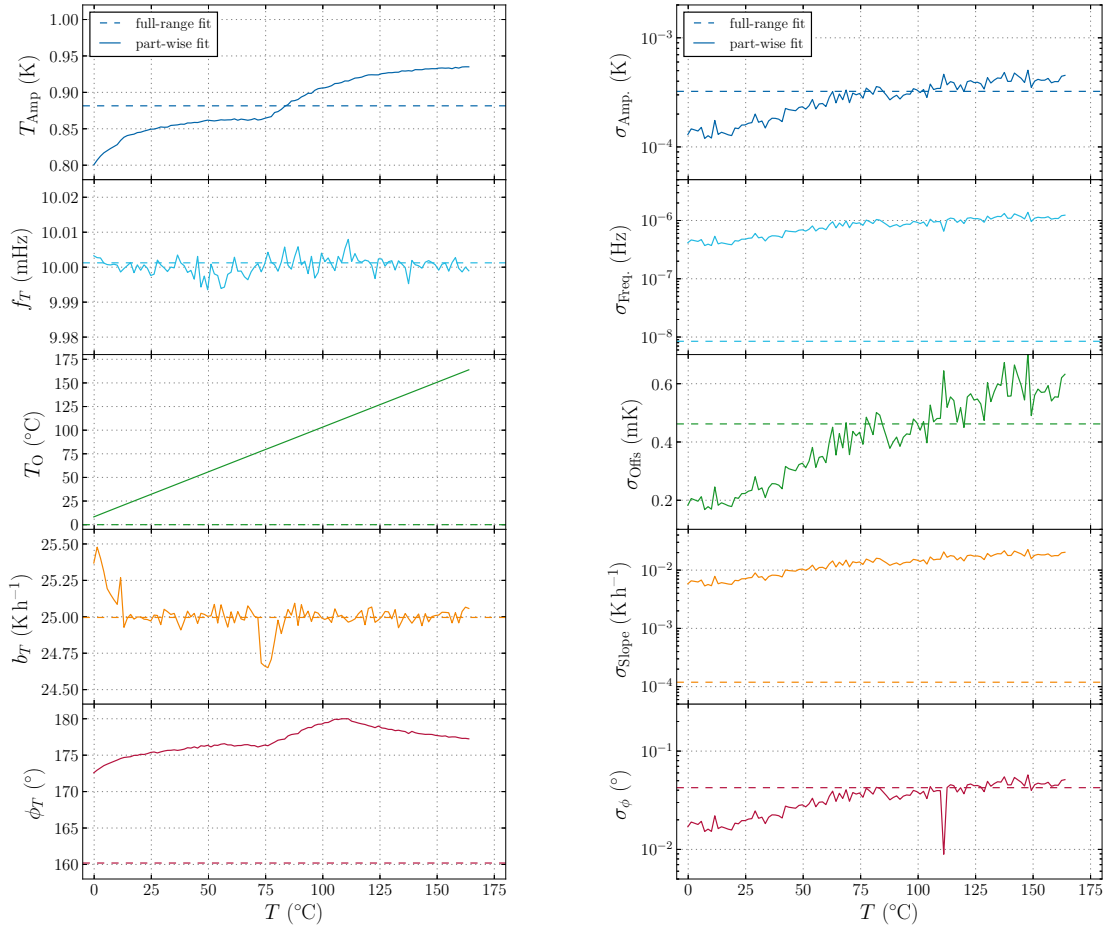
(a) Fitting values with respect to temperature.

(b) Corresponding statistical error values.
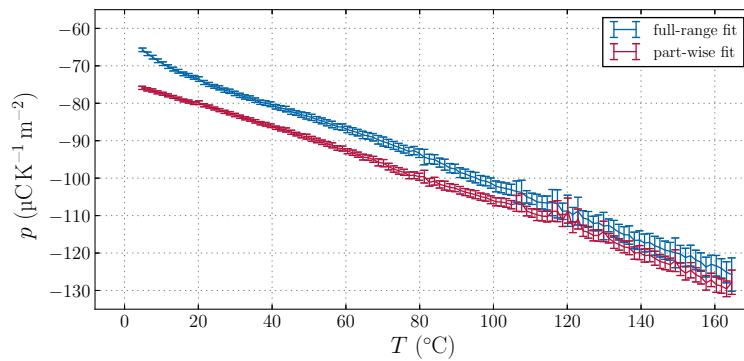
(c) Calculated $p(T)$ dependency.

Fig. 4.9.: Comparison of fitting parameters (T_{Amp}, f_T, T_{O}, b_T, ϕ_T) between full-range and part-wise temperature fit and its influence on the determination of p with respect to the temperature T. The fitting is performed on the dataset shown in Fig. 4.7. The dashed line (full range) represents the fit of Eq. (4.1) over the entire temperature signal, while the solid line shows the fit in individual intervals.

Pyroelectricity in Strontium Titanate: The model perovskite strontium titanate ($SrTiO_3$) has the cubic point group $Pm\bar{3}m$ under ambient conditions, which due to its centrosymmetry is non-polar and, thus, does not exhibit pyroelectricity. Applying an external electric field to opposite sample surfaces of a $SrTiO_3$ single crystal (known as electroformation) leads to the migration of oxygen vacancies and the formation of the so-called "migration-induced field-stabilized polar" (MFP) phase, which was first reported by HANZIG *et al.* [109]. Due to the applied electric field, oxygen vacancies drift from the anode to the cathode, and leave behind a distorted crystal structure with a polar character at the anode. For further details on the mechanism see Ref. [108–110, 140]. The verification of the pyroelectric properties could serve as a proof of the polar character of the MFP phase beside its theoretical prediction. Thus, pyroelectric measurements have to be carried out under applied electric field, i.e. applying the SHARP-GARN method in combination with a typical electroformation experiment with the help of an appropriate voltage source (e.g. Keithley 6517B). The resulting current response due to the applied electric field and the continuous temperature oscillation are shown in Fig. 4.10(a). Here, a superposition of a typical electroformation background (I_F) and a sinusoidal signal due to the temperature change (I_{th}) is present. Furthermore, the changing phase relationship between current and temperature oscillations from near in-phase to nearly out-of-phase with respect to the temperature is depicted in the insets (I)-(IV) of Fig. 4.10(a). While the current signal is dominated by non-pyroelectric TSC currents, analyzing the phase shift ϕ at the beginning and the end of the electroformation reveal a emerging pyroelectric contribution (see Fig. 4.10(b)). Here, a phase difference before and after the change of oscillation type (Inset (c) in Fig. 4.10(a)) represents the pyroelectric contribution of the MFP phase, yielding a pyroelectric coefficient of approx. $30\,\mu C\,K^{-1}\,m^{-2}$. Using this proof of pyroelectricity, symmetry considerations suggest the space group $P4mm$ for the MFP phase, which was later confirmed by RICHTER *et al.* using resonant X-ray diffraction [277]. Further details on the pyroelectricity in the MFP phase of $SrTiO_3$ can be found in Ref. [108]. KHANBABAEE *et al.* subsequently verified the implied piezoelectric properties of the MFP phase [140].

Phase Transition in P(VDF$_{70}$-TrFE$_{30}$): Polyvinylidene fluoride (PVDF) and its copolymer polyvenylidene trifluoroethylene (P(VDF-TrFE)) are organic polymers, which show ferroelectric behavior when crystallized in the polar β phase. Then, a so-called *all-trans* configuration of the CH_2, CF_2 and CHF groups leads to a dipole moment perpendicular to the carbon backbone chain. Hence, ferro-, pyro- and piezoelectric properties are present, which were investigated and applied since the 1970's. While the β phase of pure PVDF can only be obtained by stretching the material, its copolymer directly crystallizes into the polar phase. In contrast to the homopolymer, the copolymer has a CURIE transition below its melting point from a polar, low-temperature (LT) into an assumed non-polar, paraelectric high-temperature (HT) phase. The CURIE temperature T_C decreases from $120\,°C$ to $60\,°C$ with rising amounts of TrFE. Investigating $p(T)$ of P(VDF$_{70}$-TrFE$_{30}$) of different suppliers showed that a non-vanishing p can be measured above T_C when the material is poled in its LT as well as in its HT phase, as shown in Fig. 4.11. Instead of vanishing, $p(T)$ changes its sign and smoothly fades to zero after a second extremum, close to the dissolution temperature of the HT phase. This behavior is likely more due to the tertiary (flexoelectric) than secondary (piezoelectric) contribution, since $p(T)$ is much more sensitive to heating rate changes than variations of the mechanical load (see Ref. [208]). Furthermore, the behavior is reversible, i.e. the algebraic sign of $p(T)$ can be flipped by applying an electric poling field of opposite polarity, which hints to ferroelectricity also in the HT phase. Unfortunately, a complementary experimental proof via P-E hysteresis loop measurements is hindered by the increased electrical conductivity of the HT phase. Further experimental details and structural investigations on the proposed space group $Fmm2$ for the HT phase can be found in Ref. [208].
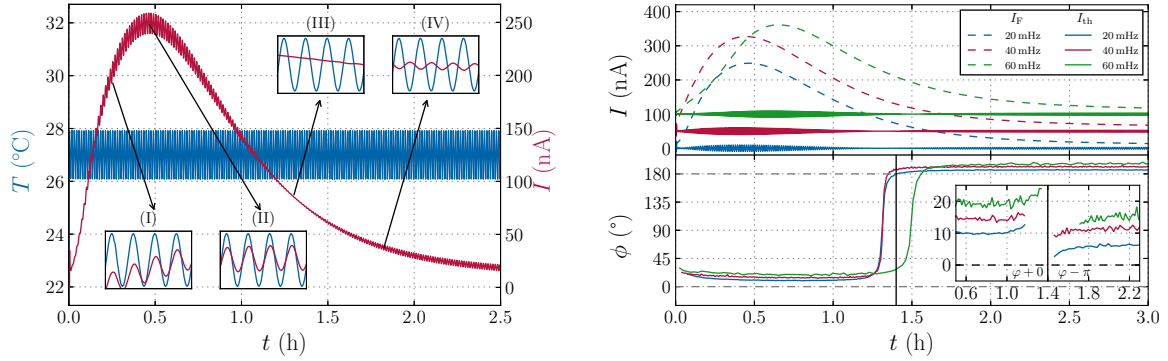
(a) Current response of a SrTiO$_3$ single crystal during electroformation using an external electric field of $1\,\mathrm{MV\,m^{-1}}$ superimposed by a sinusoidal temperature excitation: (a)–(b) in-phase current-temperature behavior during oxygen vacancy migration, (c) disappearance of temperature-induced modulation of current response, and (d) reversed sign in-phase current-temperature behavior, when defect separation is finished and the MFP phase is established. Same current scale for all insets highlights amplitude changes in I_{th}.

(b) Top: Electroformation of a SrTiO$_3$ single crystal in the external electric field superimposed by a sinusoidal temperature excitation at different frequencies: decomposition of time-dependent current I into forming current I_{F} and thermal current I_{th}. Data sets are shifted by $50\,\mathrm{nA}$ to increase readability. Bottom: Time-dependent phase shift of pyroelectric current response. The inset shows phase shift behavior at the transition point, which was adjusted by π before the transition to emphasize the change in pyroelectricity.

Fig. 4.10.: Results on the pyroelectricity in SrTiO$_3$ during an electroformation. The figures were reproduced from the original raw data in accordance with Ref. [108].
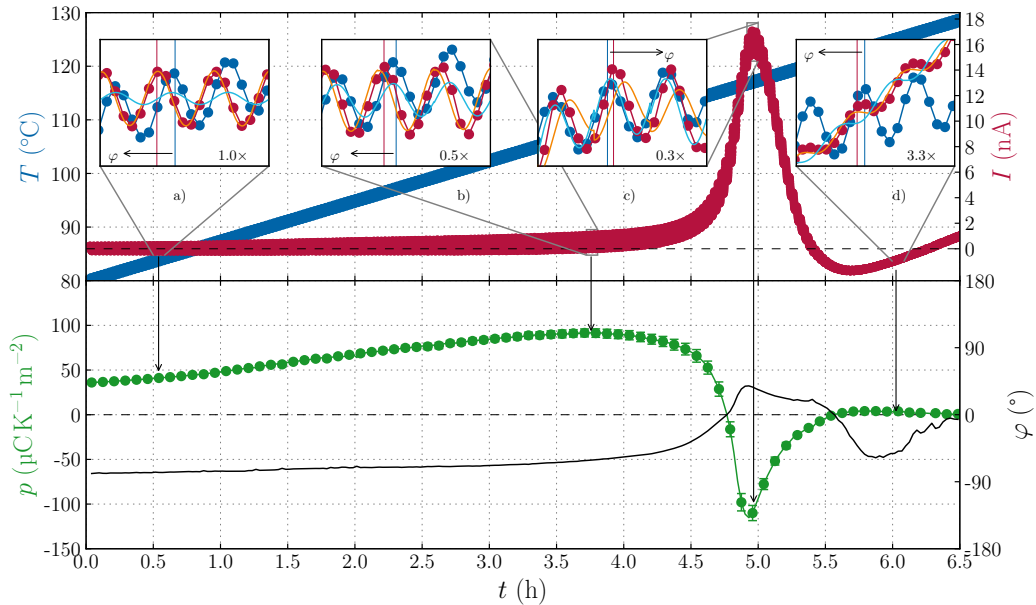
Fig. 4.11.: Raw data trace of a pyroelectric current measurement for a P(VDF$_{70}$-TrFE$_{30}$) sample, poled in the HT phase at $80\,^{\circ}\mathrm{C}$ with $20\,\mathrm{MV\,m^{-1}}$ for $4\,\mathrm{h}$. The sample was heated with $0.125\,\mathrm{K\,min^{-1}}$, while the temperature was continuously cycled with an amplitude of $0.5\,\mathrm{K}$ at $10\,\mathrm{mHz}$. Insets show details of current amplitude and phase shift ϕ at characteristic temperatures: a) measurement start, b) at T_{C}, c) current extrema and d) close to amorphisation. Inset plots only show every thirtieth data point and the current is scaled with respect to temperature for optical clarity (scaling factor indicated). Figures were reproduced from the original raw data in accordance with Ref. [208].

4.2. Hysteresis Loop Measurements

4.2.1. Instrumentation

The measurement of ferroelectric hysteresis loops is an extension of the pyroelectric measurement setup presented in Sec. 4.1. Here, the polarization P versus electric field E characteristic is determined using the shunt method, as outlined in Sec. 3.2.2. Beside the polarisation type, it provides coercive field strength E_C as well as remanent polarization P_R of a ferroelectric material (see Sec. 2.4) at a defined temperature. The vacuum chamber and heating stage of the pyroelectric measurement setup enable the application of high voltages (up to several kV for bulk materials) and temperatures in the range of $0\,°C$ to $170\,°C$. Thus, beside the SHARP-GARN and BYER-ROUNDY method also the SAWYER-TOWER method (see Sec. 3.2.2) can be used to determine the total pyroelectric coefficient p from the change of P_R with T in the same setup.

To realize the measurement the red components in Fig. 4.2 are replaced by other instruments, which are here an arbitrary waveform generator (HP 33120A), a high-voltage amplifier (Matsusada AMT-5B20) and an oscilloscope (Rigol DS1074Z). The replaced components and the principal circuitry are shown in Fig. 4.12 and Fig. 4.13, respectively.
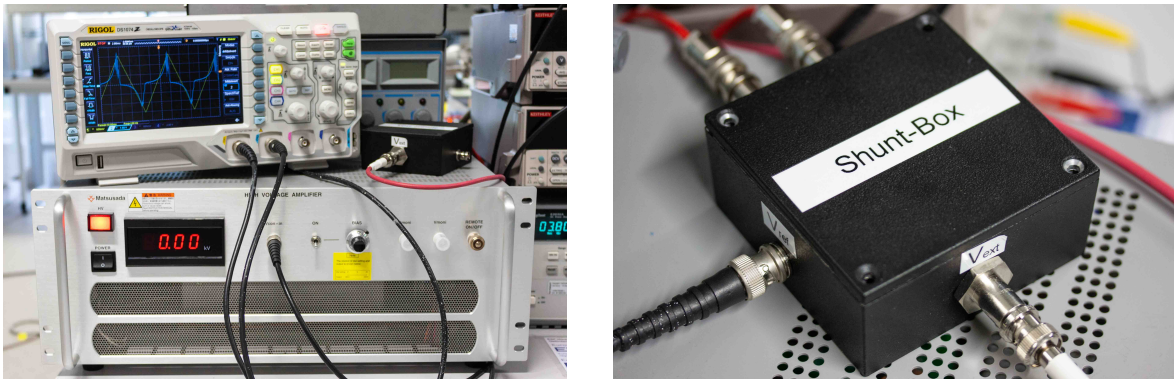
(a) High-voltage amplifier (Matsusada AMT-5B20), oscilloscope (Rigol DS1074Z), shunt box and arbitrary waveform generator (HP 33120A, not shown) are the essential components of the hysteresis measurement setup.

(b) Close up of the "Shunt Box", which forms the central hub of the hysteresis measurement setup and contains all necessary circuitry and connectors to attach the other components as well as the exchangeable reference resistor R_{ref}.

Fig. 4.12.: Measurement instruments to perform P-E hysteresis loops.

The arbitrary waveform generator provides a triangular voltage signal with an amplitude V_{Amp} between $\pm50\,\mu V$ and $\pm10\,V$ at frequencies f between $100\,\mu Hz$ and $100\,kHz$, which represents the maximum applied electric field $E = {}^{V_{Amp}}/d$ using the sample thickness d. When necessary, the signal is amplified by the voltage amplifier[10] in order to provide the necessary field strength to overcome E_C and detect the saturation range of the hysteresis loop. In case of the Matusada AMT-5B20 a maximum voltage of up to $5\,kV$ at a maximum frequency of $20\,kHz$ (maximum slew rate of $360\,V\,\mu s^{-1}$) can in principle be applied [204]. The stability and ripple of the amplifiers output voltage is rated below $0.02\,\%$, while an $0.5\,\%$ offset [204] of the output voltage has to be tolerated.

---

[10] The high-voltage amplifier is often not necessary for thin film samples (e.g. the HfO_2 samples in Sec. 6.2), as the voltage range of $\pm10\,V$ of the arbitrary waveform generator is already enough to achieve a polarization switching of the material.
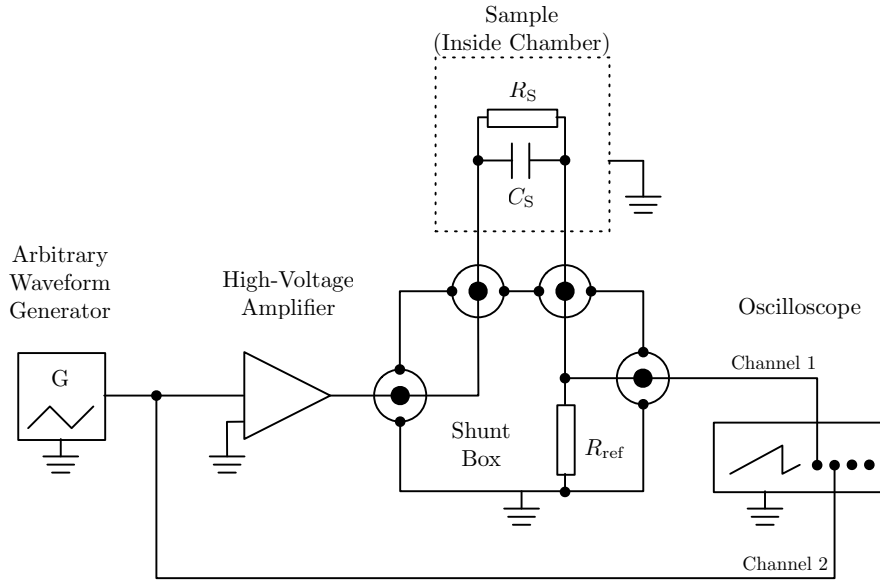
Fig. 4.13.: Electrical circuitry to measure P-E characteristics.

The "Shunt Box" (see Fig. 4.12(b)) contains all connectors for oscilloscope, voltage input and output to the sample, as well as the circuit board with the reference resistor R_{ref}. The precision of the latter is rated at 0.1 %, as it has to be as good as possible in order to minimize the error of the current to voltage conversion. As the resulting displacement current strongly depends on the electrode area of the sample and the applied frequency of the input signal the resistance of R_{ref} has to be adjusted in order to create an appropriate voltage drop which can be acquired within the ± 10 V range of the oscilloscope. The connection between vacuum chamber and sample is made via high-voltage resistant PTFE coaxial cables, BNC and vacuum-sealed Fischer connectors. The communication with the computer for controlling the waveform generator and reading the oscilloscope is established via a GPIB and TCP/IP LAN connection, respectively. The measurement procedure, hysteresis calculations and visualization are described in Sec. 4.2.2.

To record the applied electric field E, the voltage signal $V_{\mathrm{in}}(t)$ from the waveform generator is recorded on the first channel of the oscilloscope via a parallel connection. Thus, a full voltage drop over the ferroelectric (and large sample resistance R_{S}) is assumed and is, in contrast to Fig. 3.4(a), not directly measured accross the sample, but across sample and shunt box. Simultaneously, the voltage drop over the reference resistor $V_{\mathrm{ref}}(t) = V_{\mathrm{out}}(t)$ is recorded on the second channel of the oscilloscope, enabling a current to voltage conversion of the displacement current I. The voltage and time accuracy of the oscilloscope is given with 4.0 % to 4.5 % and 0.0025 %, respectively[11] and is thus the dominating error source of the setup. It has to be noted that the error can be higher [281], if the measured signals are not adjusted appropriately for the data acquisition. The displayed signal has to fit the full scale of the respective range of the oscilloscope for an optimal usage of the dynamic range of the analog-to-digital converter (ADC) at 8 bit. In the future, a 12 Bit ADC could improve the measurement of large switching peaks through more precise digitization. A clipping of the signal must be avoided, as it shrinks the calculated polarization (see Sec. 4.2.2). Summarizing all accuracies gives a total instrumentation error of 4 % to 5 % for P and E.

---

[11]According to the manual [281] the error is the sum of 3 % gain accuracy, 1 % offset accuracy and $\approx$0.4 % digitizing error at 8 bit. The latter can be scaled down to $\approx$0.02 % by using an oscilloscope with 12 bit resolution for example.

4.2.2. Measurement and Evaluation

The controlling program for the automated measurement and evaluation of the P-E characteristic is called HESMCTRL[12] ("Hysteresis Evaluation with Shunt Method Control"), which is written in PYTHON and will be briefly described in the following.

The program has dedicated submodules as indicated by the bold ".py" boxes in the program flowchart given in Fig. 4.14, in order to perform measurements and later evaluation/visualization independently. This is of particular importance for later data inspection as well as for the developement of a graphical user interface (GUI), which is intended in the future. Irrespective of a new measurement or an evaluation of existing raw data, the reading of the "measurement settings file" is the initial step. It contains all necessary sample information (e.g. sample name, contact area, thickness), instrument parameters (e.g. voltage amplitude, amplification factor, reference resistance) as well as additional information (e.g. temperature). This file has to be created before a measurement following a given template. After a measurement this file is stored together with the raw data and results for reasons of traceability. The communication with the HP 33120A arbitrary waveform generator and Rigol DS1074Z oscilloscope is built upon the qtlab/HP_33120A[13] and the ds1074z[14] packages, respectively.

The general measurement procedure is given in the left branch of Fig. 4.14. Before the data acquisition, the instruments are configured according to the settings file (e.g. amplitude and frequency of the waveform generator), while the signal outputs remain disabled. Unfortunately, the auto ranging of the oscilloscope cannot be triggered remotely (up to now) and is relatively slow. Based on the set instrument parameters, i.e. amplitude and frequency of the waveform generator, the timebase and the scale divider of the oscilloscope on the input channel (Ch1) are set automatically, in a way that two periods can be recorded. The scale divider of the second Channel (Ch2) has to be set manually. The acquisition starts by triggering the triangular voltage shape from the waveform generator, which is followed by subsequent read-out of the oscilloscope. At this point is has to be noted that an averaging of the data dramatically increases the data quality. For this, either an interval averaging (set by the oscilloscope itself) or an external averaging can be used. While the internal option is only available for frequencies above $\approx 1\,\mathrm{Hz}$, the external provides also an averaging for slow excitation frequencies, e.g. $100\,\mathrm{mHz}$ for bulk samples. Here, the "force trigger" command is used to record equal successive datasets, which are stored and averaged by HESMCTRL. Furthermore, the usage of the waveform generators "burst mode" is highly recommended. In this mode a sequence of a certain number of triangular periods followed by a short pause is generated. This ensures that the measurement stops at exactly $0\,\mathrm{V}$ and not at an undefined potential, which could cause a partial polarization reversal. This is especially important for subsequent characterizations, e.g. the measurement of p.

The evaluation procedure is outlined in the right branch of Fig. 4.14. The calculation of E and P is performed using Eq. (3.14) and (3.15), respectively, with the sample thickness d and contact area A from the measurement settings file. If desired, an eventual off-centering from $0\,\mathrm{V\,m^{-1}}$ on the E axis can be corrected from the residual between minimum and maximum electric field. This difference $E_{\mathrm{bias}} = |E_{\mathrm{min}} - E_{\mathrm{max}}|$ can be used to characterize the internal

---

[12]The full source code, example data sets and future updates are available on `https://github.com/SvenJachalke/HESMCtrl`.
[13]`https://github.com/heeres/qtlab`
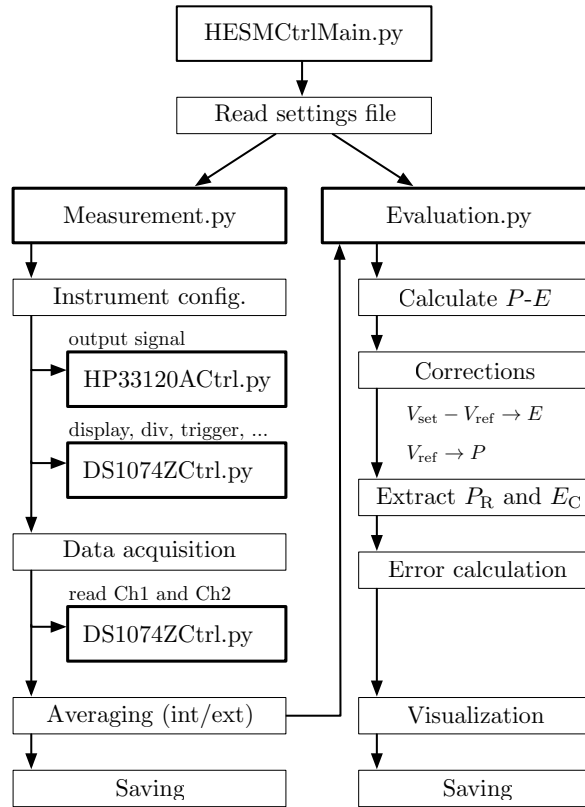[14]`https://github.com/pklaus/ds1054z`

Fig. 4.14.: Program flowchart, visualizing the working principles of of HESMCTRL.

bias of a ferroelectric, caused for example by imprint effects [6, 167, 239, 355]. Before the numerical integration of the corresponding displacement current I measured at R_{ref} the offset current I_{offs}, i.e. the slight shift or asymmetry around the oscilloscope's zero line, has to be removed, as it can cause an unclosed hysteresis loop. I_{offs} is calculated from the mean of two subsequent periods or can be entered manually in the measurement settings file. Additionally, with the knowledge of the sample capacity C_{S} and loss tangent $\tan\delta$ the loss current I_{loss}, i.e. the ohmic contribution to the charge Q, can be subtracted from I with:

$$I_{\mathrm{loss}}(t) = V_{\mathrm{in}}(t) \cdot 2\pi f \cdot C_{\mathrm{S}} \cdot \tan\delta. \tag{4.5}$$

A detailed derivation of Eq. (4.5) is given in Appendix B. The total instrumentation error of the calculated P is given by:

$$\frac{\Delta P}{P} = \left|\frac{\Delta R_{\mathrm{ref}}}{R_{\mathrm{ref}}}\right| + \left|\frac{\Delta A}{A}\right| + \left|\frac{\Delta V_{\mathrm{in}}}{V_{\mathrm{in}}}\right| + \left|\frac{\Delta V_{\mathrm{out}}}{V_{\mathrm{out}}}\right|, \tag{4.6}$$

which amounts to a total of approx. 9 % to 10 %. An improved error and thus accuracy could be achieved with a more precise oscilloscope or digitizer with improved dynamic range.

The remanent polarization P_{R} and coercive field E_{C} are extracted from the P-E loop by averaging approx. 10 absolute values close to the zero crossing of the abscissa and ordinate axis, respectively. Additionally, the statistic error of P_{R} and E_{C} from these calculations is estimated from the standard deviation, which in principle has to be added to the error originating from the measurement instruments, yielding a total absolute accuracy of approximately 12 % for P_{R}, The visualization of the raw signal and the corresponding P-E diagram marks the end of the evaluation branch.

4.2.3. Examples

This section provides some examples of hysteresis measurements and should demonstrate the ferroelectric characterization possibilities..

Fig. 4.15 exemplifies a plot obtained with HESMCTRL for a samarium-doped lead magnesium niobate – lead titanate ceramic (Sm:PMN-0.29PT)[15]. A rectangular-shaped hysteresis was obtained with $P_R = 21.26(48)\,\mu\text{C cm}^{-2}$ and $E_C = 0.26\,\text{MV m}^{-1}$. Furthermore, it is a good example for a truly saturated hysteresis, i.e. no change of P_R and E_C with increasing voltage amplitude (see Fig. 4.16(a) and its inset). This is not always the case, as shown later in Sec. 6.2 for HfO_2, where P_R still increases without saturating before the electrical breakdown. Using the heating stage of the setup also temperature-dependent hysteresis measurements can be obtained, which are also exemplified for Sm:PMN-0.29PT in Fig. 4.16(b). A pyroelectric coefficient of $-1244(149)\,\mu\text{C K}^{-1}\,\text{m}^{-2}$ between $27\,°\text{C}$ and $35\,°\text{C}$ can be obtained, which is close to the results of the SHARP-GARN approach ($1124.1(26)\,\mu\text{C K}^{-1}\,\text{m}^{-2}$ at $27\,°\text{C}$). As it can be seen from Fig. 4.16(b), relatively large temperature steps causing a comparable large polarization change, are necessary to distinguish different remanent polarizations and extract a pyroelectric coefficient. Here, the SHARP-GARN setup (see Sec. 4.1) offers more precision and resolution of $p(T)$.
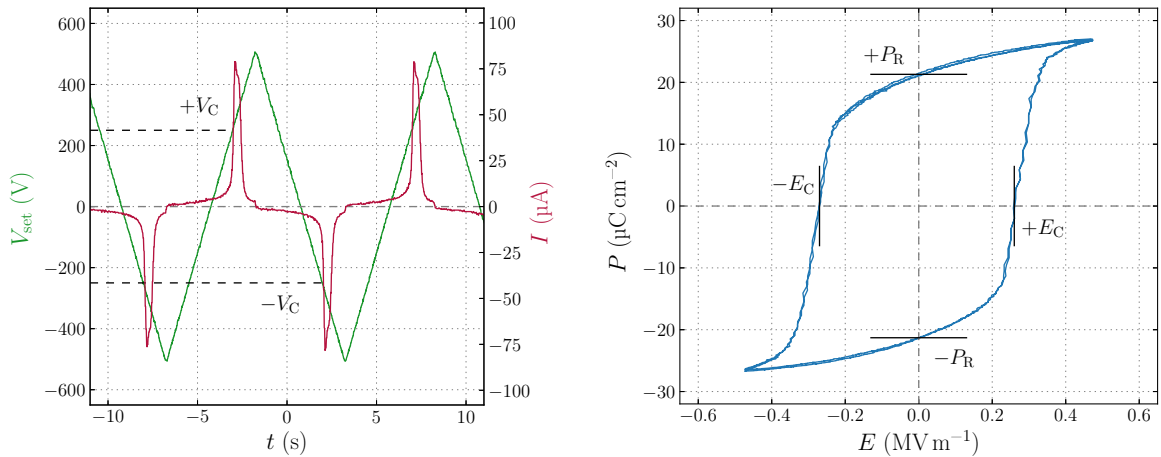
(a) Applied voltage V_{set} (green) and corresponding transient current response I (red). $\pm V_C$ marks the voltage corresponding to $\pm E_C$.

(b) Calculated P-E relation after transient current integration.

Fig. 4.15.: Visualization of the hysteresis measurement of the Sm:PMN-0.29PT ceramic sample of thickness $d = 1\,\text{mm}$ and area $A = 9.41 \times 10^{-5}\,\text{m}^2$. A voltage amplitude of $500\,\text{V}$ was applied. Solid lines mark coercive field strength E_C (with corresponding voltage V_C) and remanent polarization P_R.

Fig. 4.17 shows the frequency dependence of the remanent polarization P_R of a lead zirconate titanate (PZT) ceramic[16] in the range of $50\,\text{mHz}$ to $100\,\text{Hz}$. The shape of the hysteresis and P_R remain relatively stable up to $\approx 0.5\,\text{Hz}$. The decrease of P_R with rising frequency is explained by the fact that the switching in a ferroelectric ceramic is a nucleation-based process [280, 352] mediated by the movement of domain walls, defects, grain boundaries and stress [11], i.e. higher frequencies suppress the full switching of polarization, especially for thick samples (see

---

[15]Thanks to FEI LI from Pennsylvania State University for providing a sample with the highest pyroelectric coefficient measured with our setup so far. For further information about the samples and also the very high piezoelectric properties see Ref. [172].

[16]The samples, type PIC151, were supplied by PI Ceramics Germany.

Sec. 2.4). Here, $50\,\mathrm{mHz}$ marks the lower limit of the waveform generator, while above $100\,\mathrm{Hz}$ strong signal distortions hinder the correct determination of the hysteresis. At approximately $145\,\mathrm{Hz}$ the distortions dominate the entire signal and break the sample, possibly because of the strong piezoelectric deformation within the clamped sample.
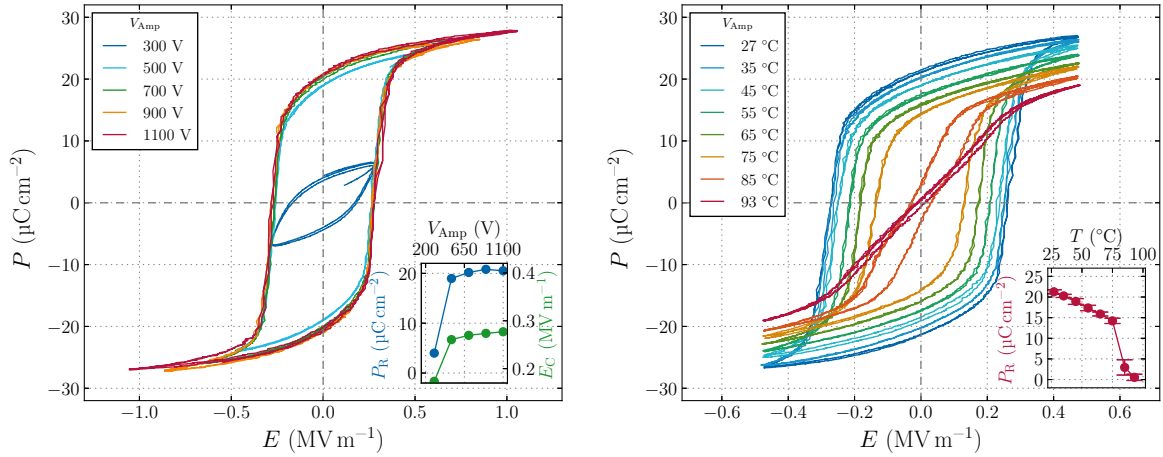
(a) Voltage amplitude dependency: A fully polarized sample is obtained, as can be seen by the saturated P_R and E_C in the inset.

(b) Temperature dependency: Decreasing hysteresis and P_R (see inset) with increasing temperature up to the CURIE temperature T_C, where the hysteresis vanishes.

Fig. 4.16.: Evolution of the hysteresis shape of Sm:PMN-0.29PT.
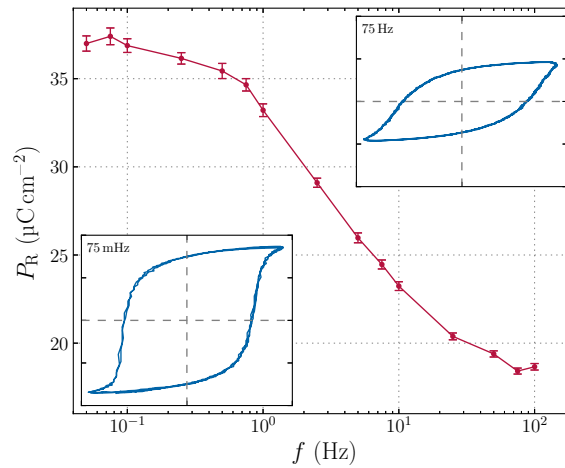

Fig. 4.17.: Remanent polarization P_R of PZT depending on the frequency f of the cycled electric field E. The insets (same scaling) show the hysteresis loops measured at an electric field amplitude of $2\,\mathrm{MV\,m^{-1}}$ at the indicated frequencies. The thickness of the sample was $0.5\,\mathrm{mm}$ and the electrode area $7.52 \times 10^{-5}\,\mathrm{m^2}$.

5. Investigated Material Systems

This chapter is devoted to the general and polar properties of III-V compound semiconductors and doped hafnium oxide material systems as their ferro- and pyroelectricity were investigated throughout this work.

5.1. III-Nitride Bulk Semiconductors GaN and AlN

As compound semiconductors play an increasingly important role for recent technologies, investigating their proper manufacturing and physical characteristics is of particular importance. Artificially created materials composed of the main group III and V elements, especially nitride compounds such as aluminum nitride (AlN), gallium nitride (GaN) and indium nitride (InN), were intensively investigated throughout the last decades. Their structure, polar properties, growth, as well as current and potential applications are shortly outlined in this section, with particular attention to GaN and AlN.

5.1.1. General Structure and Spontaneous Polarization

The III-V compound semiconductors AlN, GaN and InN have two possible crystallographic polymorphs: the cubic non-polar zincblende and the hexagonal polar wurtzite structure [97, 232].

The first one is a metastable, face-centered cubic (fcc) configuration, related to a cubic close-packing (ABCABC...) but resembling the diamond structure with a diatomic basis of atoms at $(0, 0, 0)$ and $(^1/_4, {}^1/_4, {}^1/_4)$. The point and space group are $\bar{4}3m$ and $F\bar{4}3m$ (No. 216), respectively. The inversion symmetry resulting from the cubic structure give this modification a non-polar character [97]. For GaN also a cubic rocksalt structure exist but only for very high pressures of approximately 65 GPa [93, 117, 232].

The dominating configuration is the wurtzite structure, which is related to a hexagonal close-packing (hcp, ABAB...) and shown in Fig. 5.1. This structure has two independent lattice parameters a and c, while the angle between the identical a directions is 120° and between a and c is 90°. The lattice parameters change with varying III element is shown in Fig. 5.2 for AlN, GaN and InN. The structure consists of two hexagonal sublattices, one for the metal cation and one for the anion nitrogen (N). The stacking sequence of AaBbAa results from the anion shift u (reduced coordinate representing a fraction of c) along the c axis with respect to the cation. The point and space group are $6mm$ and $P6_3mc$ (No. 186), respectively. Lattice planes and directions in a hexagonal system are generally expressed using BRAVAIS-MILLER indices, i.e. $hkil$ numbering, which gives e.g. $[0\,0\,0\,1]$ for the c axis. The latter is also the polar axis of the unit cell because of the different bond lengths and electron negativities within the
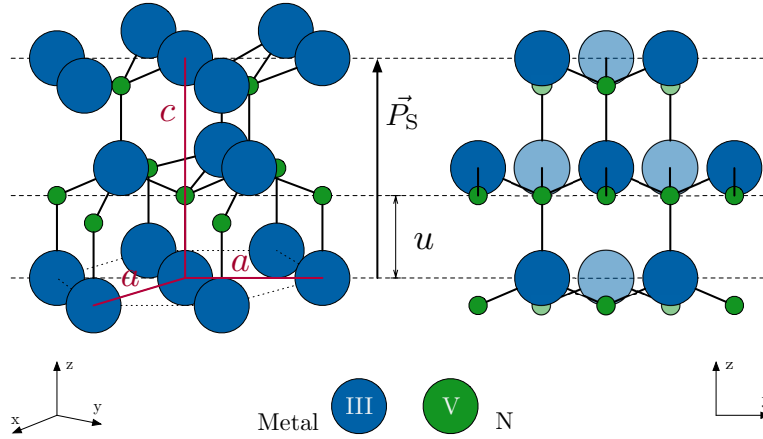
Fig. 5.1.: Schematic model of the wurtzite structure.

tetrahedral coordination of anions and cations [97, 117, 192, 383]. In other words, the built-in spontaneous polarization P_S of the wurtzite structure results from the non-equivalent centers of positive (cations) and negative (anions) charges, giving the unit cell its permanent dipole moment [87]. This seems quite similar to common ferroelectric perovskites, except the fact, that the resulting dipole moment of III-V compound semiconductors cannot be switched between two stable states by an external electric field. As the bonding type is approximately half ionic and half covalent [47], this rigid configuration is responsible for maintaining the wurtzite structure up to its decomposition temperature of approximately 1000 °C [149]. This and the metastable character of the non-polar zincblende structure interfere with the fact that ferroelectricity arises from a small structural distortion of a non-ferroelectric reference phase (see Sec. 2.4). Furthermore, using the prediction criterion presented by ABRAHAMS (see also Sec. 2.4), the deviation from the non-polar phase is given by $c \cdot u$ yielding 1.98 Å, which exceeds the maximal allowable deviation of approximately 1 Å. Thus, wurtzite-type III-V compound semiconductors are not ferro- but purely pyroelectric.

The polarization $\vec{P}_S$ is defined in terms of the cation–anion bond, i.e. the vector from the positive III element to the negative V element $[0\,0\,0\,1]$ is defined as positive or metal polar, while the opposite direction $[0\,0\,0\,\bar{1}]$ is negative or anion polar [383]. Due to the different termination of opposite surfaces, i.e. Ga or N face, also physical properties vary including chemical reactivity, electronic structure, optical reflectivity, impurity incorporation, and more [383].

As it can be seen in Fig. 5.2, the spontaneous polarization $\vec{P}_S$ seems to be correlated with the displacement parameter u, i.e. high u (and high c/a) gives a high $\vec{P}_S$. Here, AlN is characterized by the highest $\vec{P}_S$ (and u) with $-8.1\,\mu\mathrm{C\,cm^{-2}}$ to $-10.30\,\mu\mathrm{C\,cm^{-2}}$, followed by InN ($-3.2\,\mu\mathrm{C\,cm^{-2}}$ to $-4.43\,\mu\mathrm{C\,cm^{-2}}$) and GaN ($-2.2\,\mu\mathrm{C\,cm^{-2}}$ to $-8.0\,\mu\mathrm{C\,cm^{-2}}$)[17]. Although the parameters scatter among different references, the general trend between the III-V semiconductors remains. Assessing the magnitude of the spontaneous polarization is quite complex, as an experimental determination in the form of a hysteresis measurement is not possible due to the non-switchable polarization of the material. Thus, only polarization differences are accessible theoretically as well as experimentally [383]. Theoretical calculations are mainly based on *ab-initio* density functional theory (DFT) methods. Here, $\vec{P}_S$ is calculated from u and BORN effective charges $Z_{j,\alpha\beta}j$ with respect to the non-polar zincblende structure. Unfortunately, slight differences in u yield large variations in $\vec{P}_S$ leading to a wide

---

[17]A range of P_S is given due to the different values given in the literature [16, 19, 20, 87, 159, 369].
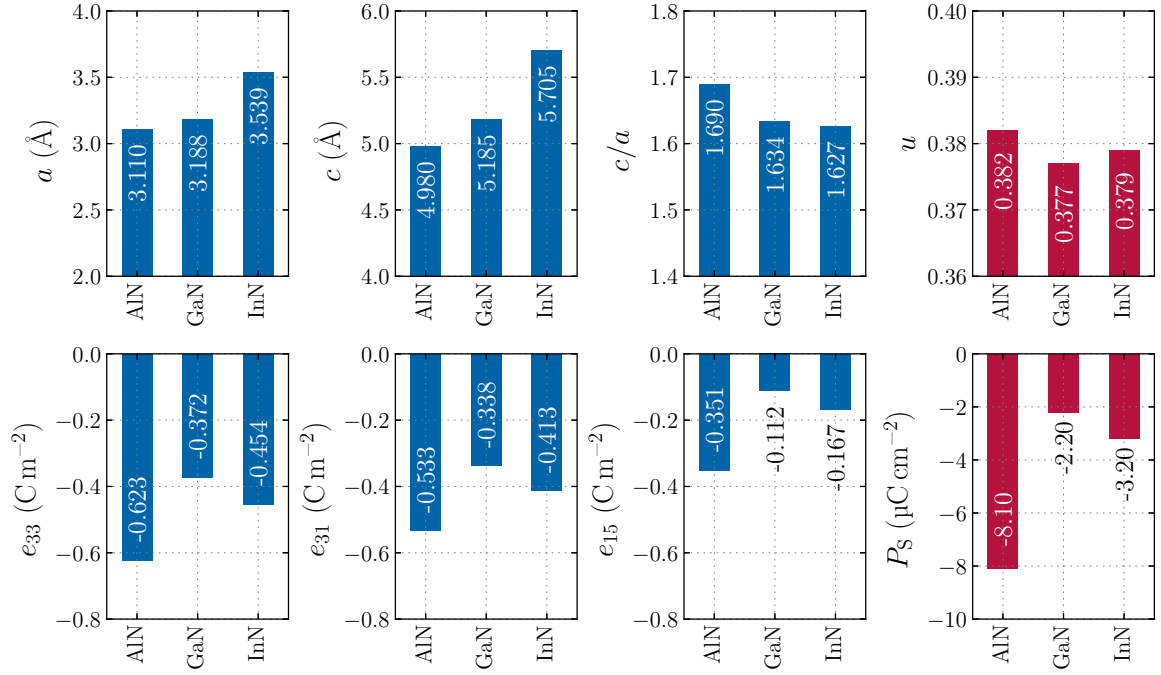
Fig. 5.2.: Graphical representation of the structural and theoretical electronic parameters. Values are taken from Ref. [16, 19, 20, 87, 159, 369].

range of published values [16, 19, 20, 87, 383]. Simultaneously, experimental data on $\vec{P}_\mathrm{S}$ are very rare and rely on the determination of non-linear susceptibilities and the application of LANDAU-GINZBURG theory [46, 369, 383] (see Sec. 2.5). Surprisingly, good accordance between the fitted data and theoretical calculations was achieved although no ferroelectricity is present. LÄHNEMANN *et al.* provided the first direct estimation of $\vec{P}_\mathrm{S}$ by investigating GaN microcrystals with micro photoluminescence and cathodoluminescence spectroscopy. Here, stacking faults represent the zincblende structure, for which $\vec{P}_\mathrm{S}$ is zero and serve as reference state for the calculations [159, 383].

Beside the challenging task to provide precise values for P_S, the polar character and the band gap of the material system are of particular importance for current and future applications and, thus, will be outlined in the next section.

5.1.2. Applications

Using III-nitride semiconductors for light emitting diodes (LEDs) and laser diodes (LDs) is the first major application field. The direct band gap materials AlN (6.2 eV [171]), GaN (3.45 eV [171]), InN (0.7 eV [171, 203, 215]) form a continuous alloy system (Al,Ga,In)N, which allows tuning of the band gap energy E_g. The direct band gap with respect to the lattice parameter a for AlN, GaN and InN compared with other semiconductors is given in Fig 5.3. Alloying enables the coverage of a wide spectral range from the infrared (IR) to the deep ultraviolet region (UV) for the emission and absorption of radiation. Here, the InN-GaN system is used to cover the visible spectrum (VIS), while the AlN-GaN system is mainly used to develop deep-UV devices. Achieving *p*-type doping in usually *n*-type GaN and the report of the first *p*-*n* junction based solely on GaN, driven by the work of AMANO *et al.* [8] and NAKAMURA *et al.* [226–228] paved the way for GaN as the material mainly used
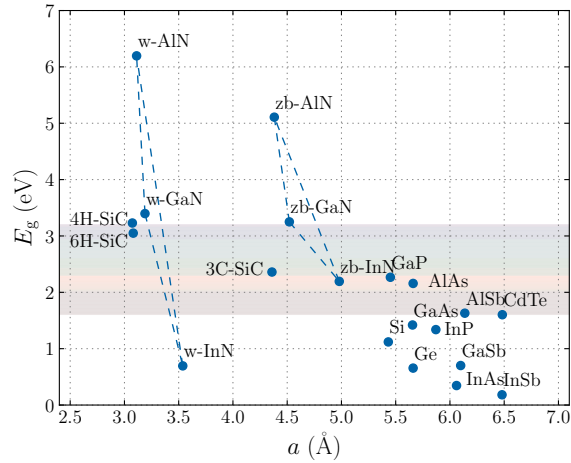
Fig. 5.3.: Direct band gap E_g with respect to the lattice parameter a of different semiconductors. "w" and "zb" correspond to the wurtzite and zinkblende structure type, respectively. The color bar represents the energy range of visible light. The figure is adapted from Ref. [121, 232].

in blue and green LEDs today. Luminescence conversion, i.e. the partial conversion of blue light with the help of yellow phosphor, dominates the market of white LEDs today due to the comparably simple manufacturing [378]. Beside their high conversion efficiencies, the compact size, high brightness and long lifetime are additional reasons for their wide distribution. General improvements comprise the optimized light extraction by minimizing total reflection and maximizing the quantum efficiency, i.e. the ratio between generated photons and electron-hole recombinations. While the first is mainly achieved by surface engineering, the latter can be improved dramatically by confining charge carriers in multiple quantum wells (MQWs), decreasing non-radiative defects and using electron blocking layers made of AlGaN [378].

Also, the adjustable band gap can be used for photovoltaic light conversion, especially of the InGaN system. Here, power conversion efficiencies of up to 50 % [378] were achieved, outperforming the best silicon-based solar cells. Due to the good resistance against high energy radiation, it is further interesting for space applications. The commercial breakthrough is currently hindered by the fabrication of thin material with appropriate crystal quality and electrical parameters [378]. While $\vec{P}_S$ is advantageous for future high-power electronics (see below), it is quite unfavorable for solid-state lighting applications due to the so-called quantum-confined STARK effect[18], which results from the polarization mismatch between different III-V nitrides in epitaxial heterostructures [217]. Here, the decreased photon emission efficiency and emission energy of the utilized quantum well heterostructures lowers the overall performance of the device [169, 211, 338, 339].

The second major application is the use in high-power and high-frequency applications, due to superior properties such as high band gap, high breakdown voltage and large electron mobility of GaN compared to silicon. The strong polarization difference between GaN and (Al,Ga)N layers leads to a spatial confinement of electrons and the formation of a two-dimensional electron gas (2DEG). The resulting high electron density and mobility are utilized in high electron mobility transistors (HEMT) and enable high operation voltages and frequencies

---

[18]In a quantum well layer the electrons and holes are pulled towards the opposite sides of the well due to the built-in electric field, which results from the spontaneous polarization perpendicular to the well. As a consequence, the emission energy of the electron-hole recombination is shifted towards lower energies and the overall efficiency is decreased [211].

also at high temperatures. Current investigations comprise optimizing the device design and reducing production cost [378].

A minor application of the III-nitrides is spintronics due to the induced magnetic properties by doping e.g. GaN with rare-earth metals or manganese (Mn) [177, 378]. Applications with lower importance are energy harvesting using the thermoelectric effect due to the comparably high SEEBECK coefficient [190] and photoelectrochemial water splitting [136].

The polar character is furthermore responsible for the piezoelectric and of course for the pyroelectric properties of the material system. Both could enable high-temperature sensor applications, due to the good thermal stability and thermal conductivity. Piezoelectricity plays also a crucial role for the mentioned quantum-confined STARK effect, as it acts as an additional polarization field on top of the spontaneous one in strained (Al,Ga,In)N layer systems [338]. Thin films of AlN can also be used as piezoelectric element for micro-electromechanical systems (MEMS) for e.g. energy harvesting applications [122, 139, 257, 325, 345], actuator [318], transducer, and microwave filter applications [64]. Reported theoretical piezoelectric coefficients e_{ij} are also given in Fig. 5.2. Applications for the pyroelectric effect are relatively rare, but it was recently demonstrated to use thin films of AlN as wavelength-selective infrared detectors [368]. Also an uncooled IR detector based on GaN was recently demonstrated [90, 91], but instead of utilizing the pyroelectric effect the shift of the resonance frequency of the micromechanical system due to near IR radiation was monitored. Furthermore, the pyroelectric properties seem to be of particular interest for optoelectronic applications, because the variation of $\vec{P}_\mathrm{S}$ with temperature T represents a change of the internal electric field and, thus, affects the charge carrier concentration at the crystal surfaces.

5.1.3. Crystal Growth and Doping

Before manufacturing devices, the growth of high-quality substrate material is essential, since the crystal quality highly affects the overall performance. Dislocations in the active layers of optoelectronic devices, for instance, reduce the internal quantum efficiency [112]. Thus, especially for short wavelength devices such as UV diodes, the dislocation density has to be reduced by optimized growth processes [146].

The traditional growth of crystalline material is often based on the CZOCHRALSKI or the vertical gradient freeze (VGF) technique, both relying on the liquid phase of the material. Unfortunately, nitride semiconductors dissociate and sublimate into liquid metal (e.g. Ga) and gaseous nitrogen (N$_2$) at elevated temperatures. Fig. 5.4(a) shows the equilibrium $p_\mathrm{N2} - T$ (nitrogen pressure and temperature) curve of the considered III-V semiconductors. At a pressure of 100 kPa the decomposition temperature of AlN (2300 °C), GaN (800 °C) [171, 268] and InN (400 °C) are comparably high [171, 268] and rise with increasing nitrogen pressure. As proposed by UTSUMI (see Fig. 5.4(b)), a liquid phase and thus congruent melting is possible for GaN, but only at high temperatures and pressures above 2200 °C and 6 GPa, respectively [348]. Thus, other growth techniques than cooling from a melt have to be employed, which are mainly heteroepitaxy methods, i.e. the material is grown via a chemical or physical vapor deposition technique on a foreign substrate like sapphire or silicon [383]. As excellent reviews on the available growth techniques are available (see e.g. Ref. [87, 112, 117, 232, 383]), only hydride vapor phase epitaxy (HVPE) and physical vapor transport (PVT) are briefly outlined here, as they were used to grow GaN and AlN single crystal samples, respectively, for the pyroelectric measurements.
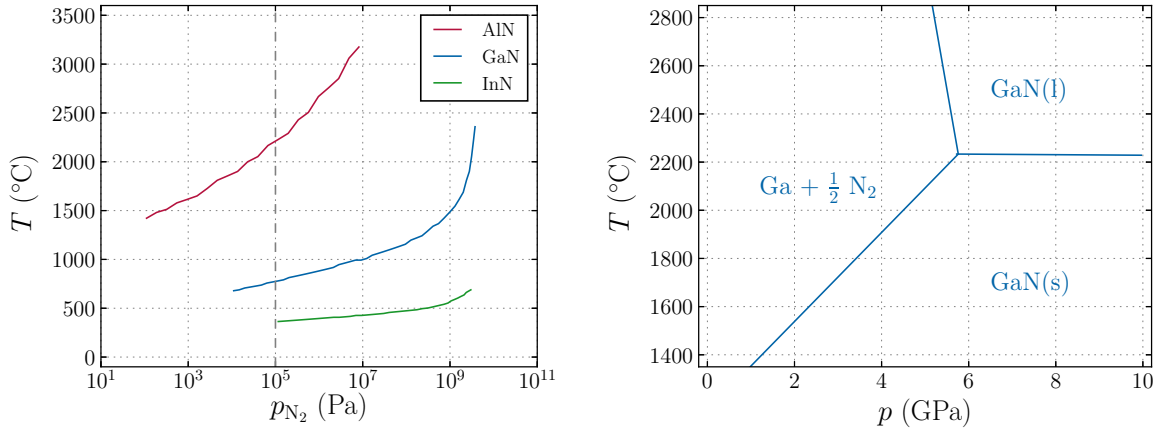
(a) Equilibrium nitrogen pressure-temperature curves for AlN, GaN and InN. Towards higher temperatures dissociative sublimation takes place. The figure was redrawn from Ref. [268].

(b) Simplified phase diagram of GaN, revealing a liquid phase only above approx. 2200 °C and 6 GPa. The figure was redrawn from Ref. [348].

Fig. 5.4.: Phase diagrams of AlN, GaN and InN showing the stability of the solid phase with respect to pressure p and temperature T.

Vapor phase epitaxy (VPE), i.e. growth of a crystalline material from a gaseous phase, uses either metal-organic compounds or hydrochloric acid as precursors to form a gaseous metal compound, which subsequently reacts with ammonia (NH_3). Compared to metal-organic vapor phase epitaxy (MOVPE) and molecular beam epitaxy (MBE), hydride vapor phase epitaxy (HVPE) exhibits high growth rates, high purity and crystal quality, which makes it especially attractive for mass production of GaN [117]. The chlorination, i.e. transferring liquid gallium to gallium monochloride (GaCl), is mainly performed under usual growth conditions with hydrochloric acid (HCl):

$$ Ga(l) + HCl(g) \rightleftharpoons GaCl(g) + \frac{1}{2} H_2(g). \tag{5.1} $$
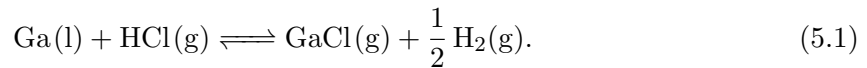
The unstable gallium monochloride reacts with gaseous ammonia to gallium nitride at the hot substrate surface:

$$ GaCl(g) + NH_3(g) \longrightarrow GaN(s) + H_2(g) + HCl(g). \tag{5.2} $$
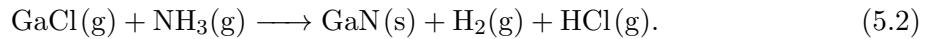
Both reactions take place at separate locations, which lead to the devolopement of different reactor designs, as summarized by HOFMANN [117]. Although the prevalent growth direction is along the polar c axis when using expensive substrate materials, good surface morphology and stability can be obtained. If the polar properties are an issue for certain applications, also the growth along non-polar directions is possible [383].

Also physical vapor transport (PVT) [112, 316, 381] can be applied to grow bulk III-V semiconductors in a homo- or heteroepitaxial way. A comprehensive review on the PVT growth process, strategies and impact on the crystal quality was given by HARTMANN et al. [112]. The growth material (AlN) is sublimated from a crucible at very high temperatures in a nitrogen atmosphere (compare Fig. 5.4(a)), which can be described by:

$$ AlN(s) \rightleftharpoons Al(g) + \frac{1}{2} N_2(g), \tag{5.3} $$
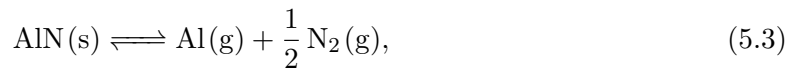
by neglecting conceivable further vapor species, such as Al_xN. A temperature gradient of approx. $10\,\mathrm{K\,cm^{-1}}$ along a typical vertical reactor setup is responsible for the transport of vapor species (e.g. Al, N_2, Al_xN) from the sublimation to the recrystallization zone. While the

latter is typically placed at the top of the reactor, the former is at the lower end of the reactor. With nitrogen pressures of several hundred millibar the transport is mainly dominated by diffusion. The condensation and subsequent recrystallization requires a seed crystal, which can be either AlN itself (homoepitaxy) or another material, such as SiC (hetereoepitaxy). Due to the lower temperature, the left side of Eq. (5.3) is favored, thus solid AlN is formed. Interestingly, the pressure and temperature window for optimal crystal quality and growth rate is determined by the seed material and can for instance differ over several hundreds of Kelvin. Also the crucible material limits the structural perfection of the resulting crystal, because it has to be chemically stable up to very high temperatures, which is the reason for the use of pure tungsten or tantalum carbide (TaC). The general growth rate of more than $100\,\mu m\,h^{-1}$ is comparable with those obtained for HVPE growth of GaN [112]. Although this method is very promising for high-quality crystals, the higher necessary temperatures compared to HVPE and the expensive TaC crucible material seems to hinder a mass production of AlN using PVT.

The growth of GaN and AlN, irrespective of the applied method, is typically accompanied by so-called unintentional doping (UID), i.e. the unpreventable incorporation of impurities. Due to the harsh conditions during growth, e.g. high temperatures and reactive gaseous substances, different parts of the reactor setup are the main source of contamination. For HVPE GaN the predominant impurity elements are silicon (Si) and oxygen (O) due to the degradation of quartz parts, as well as iron (Fe) and boron (B) stemming from steel and ceramic parts [117, 347]. Here, Si is the main reason for the "built-in" n-type conduction of GaN due to incorporation of Si on a Ga lattice site [228]. This formed $Si_{Ga}^{\bullet}$ defect[19] has a binding energy of approximately $30\,meV$ below the conduction band [24, 216, 279, 314, 353]. Thus, at room temperature most electrons are injected into the conduction band, which in combination with the high electron mobility is the reason for the increased electrical conductivity [117]. Beside Si, also oxygen (O) [94, 302] and germanium (Ge) [118] yield shallow donor levels in GaN. A good overview on the different donor levels generated by different dopants on different lattice sites is given in Ref. [117]. For AlN grown by PVT O, C and Si, as well as elements stemming from the utilized crucible material are the typically contaminants [112]. In contrast to GaN no n-type conduction is created by these contaminations in AlN [112]. One of the most interesting impurities in AlN is scandium (Sc), as the mixed allow system $Al_{1-x}Sc_xN$ ($x < 0.55$) is known for a dramatic increase of the piezoelectric constant by a factor of 2 to 3 [59, 156, 217], which also affects the pyroelectric behavior (see Sec. 5.1.4).

As the impurity concentration highly depends on the used growth conditions and affects the physical properties of the III-V compound semiconductors, keeping the impurity concentrations low is one of the current challenges for crystal growth. Another way to suppress high electrical conduction in GaN is the intentional doping with elements forming deep trap states within the band gap, which compensate the free charge carriers. This material is typically referred to as "semi-insulating" GaN and typical doping elements are iron (Fe) [193], manganese (Mn) [365], and C [305]. Unfortunately, conventional doping approaches (e.g. diffusion or ion implantation) are not viable for GaN and AlN due to small diffusion coefficients [147, 225] and the degradation at very high temperatures [149]. Therefore, only doping during the growth process by adding chemical compounds to the growth atmosphere containing the dopant atoms is possible. Electrical insulation of GaN is crucial for the determination of its pyroelectric coefficient, thus resistivity measurements are the first necessary step.

---

[19]Here, the KRÖGER-VINK notation was used, which describes a Si atom on a Ga lattice site with one positive charge with respect to the lattice.

5.1.4. Pyroelectricity

As data on pyroelectric coefficients of III-V compound semiconductors are comparably rare and diverse, this section will provide an overview on the present literature serving as comparison for the measurement results on p presented in Sec. 6.1.2. Accordingly, Fig. 5.5 summarizes all present pyroelectric coefficient data for III-nitride semiconductors.

An initial room temperature value for p of $4.8\,\mu\text{C}\,\text{K}^{-1}\,\text{m}^{-2}$ in sputtered AlN layers was provided by Dubois and Muralt [64], who used the dynamic method by Daglish (see Sec. 3.3.5). The subsequent study by Fuflyigin $et\ al.$ [77] is the most cited study for the pyroelectric coefficient of AlN, stating a similar absolute value between $6\,\mu\text{C}\,\text{K}^{-1}\,\text{m}^{-2}$ and $8\,\mu\text{C}\,\text{K}^{-1}\,\text{m}^{-2}$ for $(0\,0\,0\,1)$ thin films grown on $(1\,1\,1)$ n-type Si substrate. Here, a simplified Sharp-Garn method was used (see Sec. 3.3.5). Unfortunately, no fabrication method was mentioned and also no proof of the proposed small temperature dependency of p was given. While the values for MBE films are comparably lower ($0.3\,\mu\text{C}\,\text{K}^{-1}\,\text{m}^{-2}$ to $0.4\,\mu\text{C}\,\text{K}^{-1}\,\text{m}^{-2}$) [307], sputtered layers are reported to have larger pyroelectric coefficients ranging from $10.7\,\mu\text{C}\,\text{K}^{-1}\,\text{m}^{-2}$ to $51.02\,\mu\text{C}\,\text{K}^{-1}\,\text{m}^{-2}$ [49–51, 324], which were all measured with the Chynoweth method (see Sec. 3.3.3). AlN layers fabricated by chloride-hydride epitaxy (CHE, similar to HVPE) are reported to offer a p value of approximately $2000\,\mu\text{C}\,\text{K}^{-1}\,\text{m}^{-2}$ [154], which is very doubtful. In contrast to thin films, a p value for free-standing bulk single crystals was given by Shaldin $et\ al.$ [312]. Here, $p(T)$ was measured in the temperature range of $4.2\,\text{K}$ to $300\,\text{K}$ (see Fig. 5.5) for a PVT crystal with the Byer-Round method (see Sec. 3.3.1). The room temperature value is approximately $5\,\mu\text{C}\,\text{K}^{-1}\,\text{m}^{-2}$, which fits quite well to the studies of Fuflyigin $et\ al.$ [77] and Dubois $et\ al.$ [64]. Although the overall temperature dependency is relatively small, it seems to increase near room temperature. Recently, Kurz $et\ al.$ investigated the influence of Sc incorporation of sputtered $\text{Al}_{1-x}\text{Sc}_x\text{N}$ thin films on the pyroelectric coefficient. As expected from the increase of the piezoelectric constant also p increases with rising Sc content. Here, a maximum value of $p = 9.98(20)\,\mu\text{C}\,\text{K}^{-1}\,\text{m}^{-2}$ was obtained for $x = 0.3$ [156]. Furthermore, $p(T)$ was investigated in the range of $20\,^\circ\text{C}$ to $80\,^\circ\text{C}$ using the Sharp-Garn method. Yan $et\ al.$ conducted theoretical calculations using the Debye model (compare Sec. 2.3) to estimate the course of $p_{\text{prim}}(T)$ from $0\,\text{K}$ to $1000\,\text{K}$. Here, the room temperature value of $p_{\text{prim}} = 0.9\,\mu\text{C}\,\text{K}^{-1}\,\text{m}^{-2}$ from Ref. [64] was used, giving relatively small absolute p values and suggesting that p_{sec} plays a dominating role.

Regarding GaN, the number of publications providing a value of p is much smaller. An initial pyroelectric coefficient of $0.85\,\mu\text{C}\,\text{K}^{-1}\,\text{m}^{-2}$ was given by Bykhovsky $et\ al.$ for layers of $3\,\mu\text{m}$ to $5\,\mu\text{m}$ thickness grown by MOVPE [33]. In contrast, Matocha $et\ al.$ reported a value of $5.93\,\mu\text{C}\,\text{K}^{-1}\,\text{m}^{-2}$ [201], using the flatband-voltage shift method (see Sec. 3.2.4). A value of $4.81\,\mu\text{C}\,\text{K}^{-1}\,\text{m}^{-2}$ was subsequently given for HVPE GaN layers [202], which was used by Yan $et\ al.$ to predict the temperature dependency of the primary pyroelectric coefficient using the Debye-Einstein model (see Eq. (2.24) in Sec. 2.3). Liu $et\ al.$ used first-principle calculations to estimate $p(T)$ from Born effective charges and the temperature-dependent change of the displacement parameter u (more details are given in Ref. [179, 180]), providing a room temperature value of approximately $3\,\mu\text{C}\,\text{K}^{-1}\,\text{m}^{-2}$ [180]. In contrast to AlN, the range of published p values is very narrow and, thus, more reliable albeit no error bars are typically given. Furthermore, no values from free-standing bulk crystals are provided.

While a pyroelectric coefficient for InN is practically absent in the literature, a recent study reports a value of $8.425\,\mu\text{C}\,\text{K}^{-1}\,\text{m}^{-2}$ for an InN/GaN heterostructure [107].
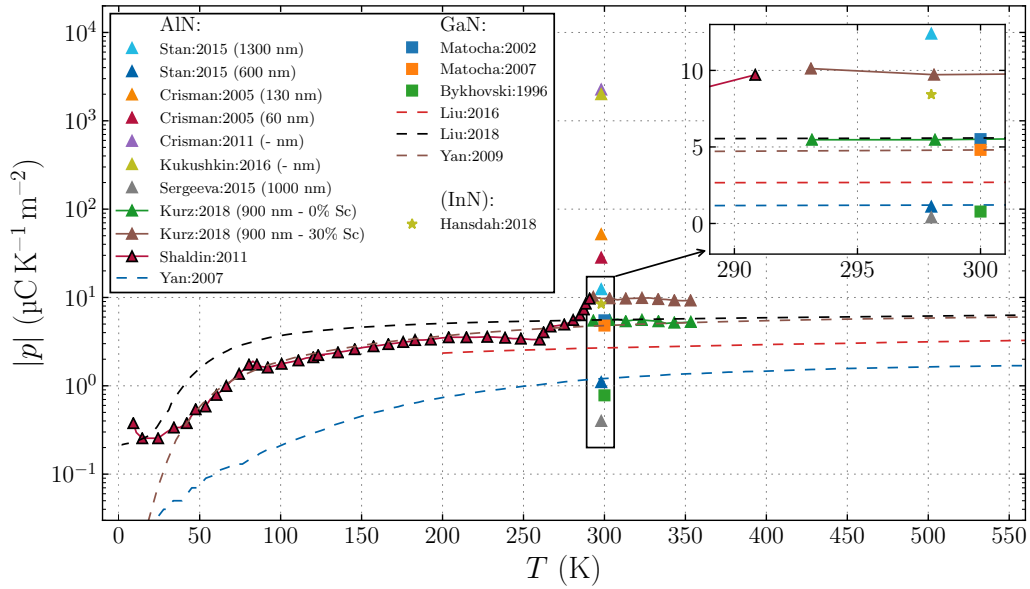
Fig. 5.5.: Summary of published pyroelectric coefficient values with respect to the temperature for different III-N compound semiconductors. Here, a single marker represents a value measured at a single temperature (typically room temperature), while temperature-dependent experimental and theoretical values are depicted as marker with a solid line and a dashed line, respectively. The values for AlN and GaN were taken from Ref. [49, 51, 154, 156, 307, 312, 324, 371] and [33, 180, 181, 201, 202, 370], respectively. The InN value by HANSDAH [107] must be treated with caution as a GaN/InN heterostructure was used for its determination.

5.2. Hafnium Oxide Thin Films

The dielectric hafnium oxide has gained an increasing attention in the semiconductor industry during the last decades due to its suitability for memory applications. Its general structure and application fields are shortly reviewed here, while special focus lies on the ferroelectric properties, which can be found in thin films and also determine its pyroelectric properties.

5.2.1. General Structure and Applications

Hafnium(IV) oxide (HfO_2), typically referred to as hafnia, is the most common and most stable oxide of the transition metal hafnium. It is a colorless crystalline solid with a large density of $9.68\,\mathrm{g\,cm^{-3}}$ and a comparably high hardness. The large refractive index of 1.8 to 2.4, the wide band gap of $5.68\,\mathrm{eV}$, low absorption, and good robustness are the reason for its utilization for optical and protective coatings [105].

The crystalline structure of HfO_2 is similar to that of ZrO_2 and exhibits a monoclinic baddeleyite phase, i.e. point group $2/m$ and space group $P2_1/c$ (No. 14) under ambient conditions, due to the sevenfold coordination of hafnium-oxygen bonds [40]. With rising temperature the material adopts a tetragonal phase at $1720\,°C$ ($4/m\ 2/m\ 2/m$, $P4_2/nmc$, No. 137) and a cubic phase ($4/m\ \bar{3}\ 2/m$, $Fm\bar{3}m$, No. 225) at $2600\,°C$, before melting at approximately $2800\,°C$ [53, 222, 285, 287, 354]. While the transition from the monoclinic to the tetragonal phase is accompanied with a change in volume and shearing of the unit cell by approximately $4\,\%$ and $9°$, respectively, no volume change occurs from the tetragonal to the cubic structure [354]. Two orthorhombic phases ($Pbca$ and $Pmnb$) were observed for high pressures above $4\,\mathrm{GPa}$ and $14\,\mathrm{GPa}$, respectively [238]. This transition is also accompanied by an increase of the cell volume by about $8\,\%$. The corresponding phase diagram is shown in Fig. 5.6. Also the crystal structures of the ambient pressure phases are shown in Fig. 5.7. Due to their centrosymmetry, all these bulk phases are non-polar, i.e. exhibit no ferro- or pyroelectric properties.
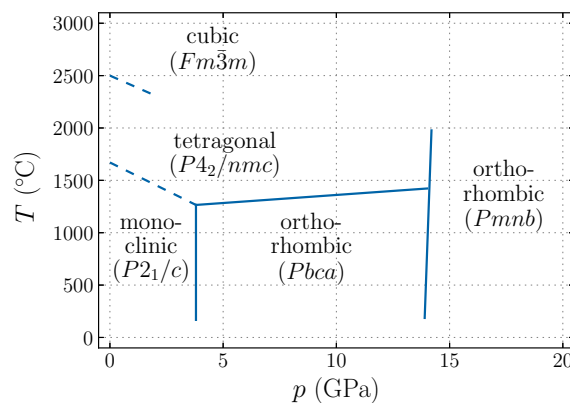
Fig. 5.6.: Bulk phases of HfO_2 with respect to temperature T and pressure p. Adapted from Ref. [238].

Due to its good temperature stability, HfO_2 is used as a high-temperature insulation material, e.g. for thermocouples [242]. Its high ionic conductivity for oxygen and dielectric constant attract attention in the fields of resistive switching [165, 250] and high-k memory applications, respectively. Even in its amorphous state, HfO_2 exhibits an ε_r of approximately 21. Thus, it is already utilized by INTEL since 2007 as gate material for complementary metal-oxide-semiconductor (CMOS) devices in order to replace SiO_2 and enable a further downsizing of

Fig. 5.7.: Three non-polar crystal structures of HfO$_2$ typically found in bulk material and the crystal structure of the polar orthorhombic phase responsible for the ferroelectric properties in thin films. Adapted from Ref. [198].

memory cells [25, 34, 125, 294]. Furthermore, its high thermal stability and high breakdown field between $3.9\,\mathrm{MV\,cm^{-1}}$ and $6.7\,\mathrm{MV\,cm^{-1}}$ are of great advantage for such applications [40]. The fabrication of thin films is possible by a variety of techni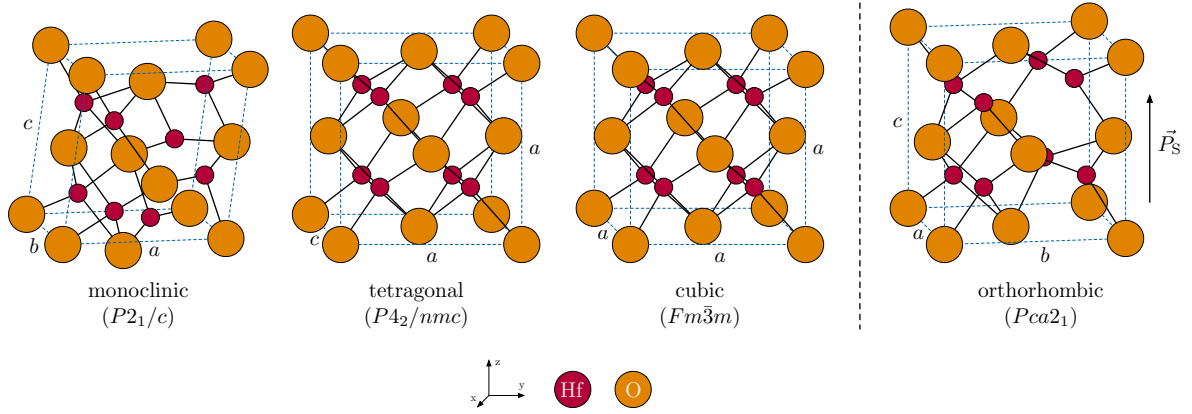ques, including physical vapor deposition (PVD, e.g. sputtering and pulsed laser deposition), and chemical deposition, e.g. metal organic chemical vapor deposition (MOCVD), atomic layer deposition (ALD), and chemical solution deposition (CSD) as summarized by CHOI *et al.* [40]. Here, an ALD process is considered as the most reliable process concerning surface morphology, thickness control and impurity concentration. When crystallized into the mononclinic phase, ε_r drops to 16 to 18, while it increases for the tetragonal (26 to 70) and cubic phase (29 to 39) [34, 296]. Thus, a delayed crystallization as well as the stabilization of higher symmetry phases with higher ε_r at room temperature was the goal of ongoing studies [294]. Here, the influence like different dopants, thermal treatment, deposition technique, growth temperature, surface energy effects, strain resulting from grain size and layer thickness, and mechanical encapsulation form an extensive pool of adjustable parameters [264].

5.2.2. Polar Properties in Thin Films

The discovery of ferroelectricity in silicon-doped HfO$_2$ thin films fabricated via ALD was published by BÖSCKE *et al.* in 2011 [27]. It was found, that the crystallization with a TiN capping layer by post metal annealing (PMA) was necessary to obtain polar properties of the dielectric. This mechanically confined crystallization was the prerequisite for the ferro-electricity in HfO$_2$:Si, but not for other dopants, as reported for yttrium doping (HfO$_2$:Y), although it improves the remanent polarization of the material [224]. The polar properties were attributed to the formation of a novel non-centrosymmetric orthorhombic phase [27], which was first found in ZrO$_2$ by KISI *et al.* [142].

Since then, the origin of the ferroelectric properties of HfO$_2$ thin films has always been attributed to the formation of an orthorhombic phase $Pca2_1/Pbc2_1$[20] (No. 29). Although four orthorhombic phases ($Pmn2_1$, $Pca2_1$, $Pbca$, $Pbcm$) were proposed [287], only two of them ($Pca2_1$ and $Pmn2_1$) are non-centrosymmetric and, thus, fulfill the requirement for a spontaneous polarization (see also Fig. 5.7).

---

[20]$Pca2_1$ is the more common description of the non-centrosymmetric orthorhombic phase of HfO$_2$, while $Pbc2_1$ is just another setting of the same space group [294].

Phase analyses via gracing-incidence X-ray diffraction [27, 219, 220, 222, 224, 246, 249, 287, 294, 327] indicate that $Pca2_1$ may be responsible for the polar properties. On the other hand, there is a remaining doubt in the scientific community because of the complex pattern analysis due to low layer thickness and the coexistence of monoclinic, orthorombic, tetragonal and cubic phases in the film. Especially the overlapping intensities of the strongest reflections for the cubic, tetragonal and orthorhombic phase, which occur at similar positions, make a quantitative analysis quite challenging [244]. SANG et al. used aberration corrected high-angle annular dark-field scanning transmission electron microscopy (HAADF-STEM) and position averaged convergent beam electron diffraction (PACBED) to investigate the structure of gadolinium-doped hafnium oxide (HfO$_2$:Gd), showing $Pca2_1$ as the most prominent phase [287]. The same phase was reported for similar ZrO$_2$ thin films, which also gives rise to ferroelectricity in such thin films [168, 173, 294, 328].

The report of ferroelectricity in hafnia-based thin films further pushed the interest of the semiconductor industry in the material system due to the possibility of ferroelectric field effect transistors (FeFET) and ferroelectric random access memories (FRAM), which are considered to fill the so-called "memory gap"[21] [74, 223, 248, 300, 343, 349]. The full compatibility with state-of-the-art CMOS technology is an enormous advantage compared to traditional perovskite-based materials, since HfO$_2$ is comparably easy to fabricate with CVD and PVD techniques [241, 249, 297, 313] even in 3D structures [265]. Also chemical solution deposition (CSD), as a cheaper approach, has proven to be capable of producing ferroelectric films with thicknesses beyond 100 nm [328]. The major integration challenge is the improvement of the field-cycling stability, i.e. the reduction of the so-called "wake-up" and "fatigue" effects, because the write and read-out process of a memory has to be stable for as many cycles as possible [254]. While the first effect describes an increase of P_R after several initial field cycles, the latter corresponds to a drop of P_R with increasing cycle number. The physical reason for the observed wake-up is attributed to a de-pinning of domains, a cubic to orthorhombic phase transformation or a redistribution of oxygen vacancies [95, 254, 326, 379], while the fatigue is due to the generation of new defects leading again to a pinning of domains [254].

5.2.3. Doping Effects

The doping of HfO$_2$ was initially applied to increase the crystallization temperature of the thin films [294]. Since the discovery of ferroelectricity in HfO$_2$, the corresponding number of publications steadily increases, showing that a polar phase can be produced due to doping with various elements (see Tab. 5.1) and dimensional confinement with the help of metallic capping layers of platinum (Pt) [224, 327], iridium (Ir) [186], and titanium nitride (TiN) [153, 220]. Beside a raise of the crystallization temperature, also a drop in the total formation energy of the orthorhombic phase compared to the competing non-polar phases is anticipated by the doping. Increasing the doping concentration of smaller (Si^{4+}, Al^{3+}, Zr^{4+}) as well as larger (Gd^{3+}, La^{3+}, Sr^{2+}) dopants than Hf^{4+} yields a general compositional transition from a dominating monoclinic, orthorhombic to tetragonal or cubic phase mixture [294]. Each dopant has its respective concentration window and optimum concentration, at which P_R and the orthorhombic phase fraction are maximal. This is exemplified in Fig. 5.8(a) for selected dopants. Furthermore, the reported maximum P_R values are summarized in Tab. 5.1. Doping concentrations far off the optimum can either lead to a non-polar behavior again or

---

[21]Denoted as the gap between the access time of volatile, but fast memory near the processing unit (e.g. DRAM) and the non-volatile, but slow storage medium (e.g. HDD, FLASH).
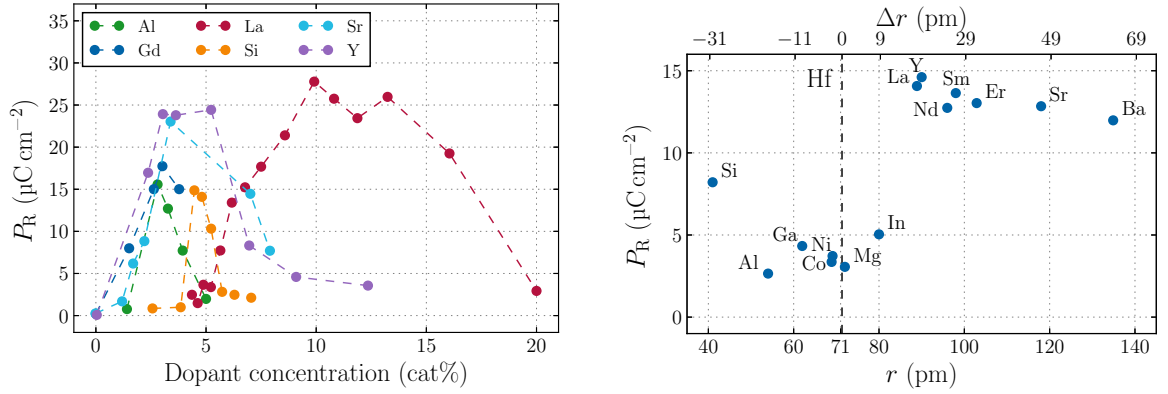
(a) Remanent Polarization P_R with respect to doping concentration depicting the different concentration windows for the respective dopants. The figure shows data combined from Ref. [294], [301] and [326].

(b) Remanent polarization P_R with respect to ionic radius r of different dopants introduced into HfO$_2$. Here, Δr represents the difference from the ionic radius of Hf. Redrawn and modified from Ref. [326].

Fig. 5.8.: Dopant influences on the remanent polarization of ferroelectric HfO$_2$.

even antiferroelectricity, as shown for Si [27], Al [221] and Zr doping [222]. As reported by STARSCHICH (see Fig. 5.8(b)), an ionic radius of the dopant above 85 pm and, thus, slightly larger than Hf, is best to significantly increase the remanent polarization [326]. Here, smaller dopants seem to have no enhancing influence on the ferroelectric properties, which is in contrast to the reports on Al, Zr and Si doping of HfO$_2$.

Several theoretical works indicate that defects, introduced by the different dopants, are favorable to achieve the ferroelectric phase. MATERLICK *et al.* reported a stabilization of the orthorhombic phase due to the doping with II-valent Sr [199] with the help of density functional theory (DFT). Here, the Sr$''_{Hf}$ defect without a compensating oxygen vacancy[22], created from the substitution of Hf with Sr in an oxygen-rich environment, increases the bond length to neighboring oxygen atoms, which leads to a lower formation energy of the orthorhombic phase. Also for III-valent and IV-valent dopants, such as Al, Y, La, and Si, C, Ge, Ti, Sn, Ce, Zr, respectively, first-principle studies reveal different defect types, e.g. substitution with and without compensating vacancies, as stabilizer for the ferroelectricity in HfO$_2$ [155, 199].

While doping is regarded as the main driver for the formation of the ferroelectric properties, recent reports show that even undoped material can become ferroelectric [198, 244, 264]. A maximum value of 10.6 μC cm^{-2} for P_r in undoped layers was achieved by POLAKOWSKI *et al.* [264], which was further enhanced to 13.6 μC cm^{-2} by PAL *et al.* [244]. Here, the capping electrode, thermal budget during crystallization, layer thickness, and grain size seem to play the key role [264]. A typical capping layer of TiN is deposited in a chemical vapor deposition (CVD) process near the crystallization temperature of HfO$_2$. This lead to a partial crystallization before the actual crystallization step via rapid thermal annealing (RTA) and the formation of the monoclinic phase is preferred, thus, hindering ferroelectricity. The deposition via room temperature physical vapor deposition (PVD) leaves the HfO$_2$ layer amorphous. It will undergo crystallization only in the subsequent RTA step and, thus, quenching (also known as encapsulated crystallization) leads to the assumed orthorhombic phase. That ferroelectric properties can be enhanced with TiN and TaN capping electrodes, may be attributed to the increased crystallization temperature of HfO$_2$ layers with dopants such as Si [27, 185].

---

[22]Here, the KRÖGER-VINK notation was used, which describes a Sr atom on a Hf lattice site with a twofold negative charge with respect to the lattice site.

Tab. 5.1.: Summary of values of maximum P_R for different dopants in HfO$_2$, their respective concentration (as provided in mole, atomic or cationic percent) and layer thicknesses d.

Dopant	P_R (μC cm^{-2})	Concentration	d (nm)	Ref.
undoped	$10-14$	–	6	[244, 264]
Al	3	5.2 mol%	43	[326]
	6	7 mol%	16	[220]
	15	–	12	[265]
Ba	12	7.5 mol%	43	[326]
Co	4	5.2 mol%	43	[326]
Er	13	5.2 mol%	43	[326]
Ga	4	5.2 mol%	43	[326]
Gd	12	2 mol%	10	[219]
	17	3.5 cat%	27	[287]
In	5	5.2 mol%	43	[326]
La	$10-13$	1.0 mol%	10	[153]
	14	5.2 mol%	43	[326]
	17	2.1 at%	10	[39]
	27	$10-13$ cat%	12	[301]
Lu	8	5 at%	30	[346]
Mg	3	7.5 mol%	43	[326]
Ni	4	5.2 mol%	43	[326]
Nd	12	5.2 mol%	43	[326]
Si	$6-10$	$3.8-4.3$ cat%	$10-40$	[245]
	8	$2.0-3.7$ cat%	12	[130]
	$8-13$	3.8 mol%	$10-50$	[194]
	10	4.0 mol%	10	[27]
	12	3.7 cat%	36	[276]
	$5-21$	$2-6$ mol%	10	[184–187]
Sm	14	5.2 mol%	43	[326]
Sr	13	7.5 mol%	43	[326]
	23	3.4 mol%	10	[296]
Y	13	5.2 mol%	$18-70$	[327]
	15	2.0 mol%	12	[241]
	24	5.2 mol%	10	[224]
Zr	$5-15$	50 cat%	$10-25$	[246]
	8	5 cat%	$195-390$	[328]
	10	50 cat%	10	[375]
	17	50 cat%	9	[222]
	17	64 cat%	20	[319]

Thus, stabilizing the ferroelectric phase cannot be attributed solely to the dopant itself, but more to a well controlled fabrication process. Furthermore, a grain size reduction due to a lowering of the layer thickness increases the surface-to-volume energy ratio. Thus, the surface energy becomes dominant and the orthorhombic phase with lower surface energy is favored [198, 264]. Relating P_R and layer thickness d (see Tab. 5.1), a thickness reduction seems to have a positive influence on P_R.

5.2.4. Pyro- and Piezoelectricity

While investigating and improving the ferroelectric properties, exploiting the related piezo- and pyroelectric properties is an obvious implication as it could open a wide field of new applications beyond memory technology, such as radiation sensors or waste heat and vibrational energy harvesters.

Values for piezoelectric coefficients are rare and have to be extracted from displacement-voltage curves, e.g. measured with the help of double-beam laser interferometry (DBLI) experiments [27, 328]. In the initial publication by BÖSCKE *et al.* such experiments were already conducted, resulting in a piezoelectric coefficient of approximately $4\,\mathrm{pm\,V^{-1}}$. Since that, experiments and investigations on the piezoelectric behavior are only occasionally reported. Recently, piezoelectric constants of around $10\,\mathrm{pm\,V^{-1}}$ for pure and magnesium-doped $\mathrm{ZrO_2}$ [328, 329] and $6\,\mathrm{pm\,V^{-1}}$ for $\mathrm{HfO_2{:}Y}$ [327] were published.

Publications dealing with the pyroelectric properties of $\mathrm{HfO_2}$ are also rare. Some studies used temperature-dependent hysteresis loop measurements (see SAYWER-TOWER method in Sec. 3.2.2) to determine pyroelectric coefficients [115, 247] of up to $1300\,\mathrm{\mu C\,K^{-1}\,m^{-2}}$, which are comparably large. In contrast, the SHARP-GARN method (see Sec. 3.3.5) gains an increased attention, as the recent works by SMITH *et al.* [319] and MART *et al.* [194] demonstrate. Here, smaller but more reliable pyroelectric coefficients between $48\,\mathrm{\mu C\,K^{-1}\,m^{-2}}$ and $84\,\mathrm{\mu C\,K^{-1}\,m^{-2}}$ were reported.

As investigations on pyro- and piezoelectricity in $\mathrm{HfO_2}$ lack of comprehensive studies, especially with respect to the different doping and fabrication possibilities of the material, the investigation of the pyroelectric properties can pave the way for further discoveries and applications in this field and, thus, is part of this work. As a first step, the main focus lies here on the pyroelectric characterization of Si-doped material. Also, first investigations on the different dopants are outlined in Sec. 6.2.

6. Results

The results which were obtained with the SHARP-GARN method and setup described in Sec. 3.3.5 and 4.1, respectively, are summarized in this chapter. The first part comprises the characterization of the pyroelectric coefficient p as well as its temperature dependency of the bulk III-V semiconductors GaN and AlN using the SHARP-GARN technique for the first time. Here, the influence of the intentional doping of the material is discussed. Part of these results were published together with PATRICK HOFMANN in the article "The pyroelectric coefficient of free standing GaN grown by HVPE" in the journal *Applied Physics Letters*, Vol. 109(14), 142906, 2016 [128]. The second part comprises the pyroelectric properties of doped HfO_2, proving that the SHARP-GARN method can also be applied to thin films with a thickness of several tens of nanometer. Here, the doping with silicon and its influence on the polar properties have been investigated. The results were published in the article "The pyroelectricity of silicon-doped hafnium oxide thin films" in the journal *Applied Physics Letters*, Vol. 112(14), 142901, 2018 [130]. Also, the impact of other dopants on the pyroelectric properties is given as an outlook for further investigations.

6.1. The Pyroelectric Coefficient of Free-standing GaN and AlN

6.1.1. Sample Preparation

The investigated free-standing GaN single crystals were provided by NaMLab Dresden and Freiberg Compound Materials (FCM)[23]. They were grown by HVPE in a commercially available vertical reactor and in step flow growth mode at elevated temperature [351] (see Sec. 5.1.3). Since unintentional doping (UID) and, thus, n-type conductivity (see Sec. 5.1.3) are present, a measurement of the pyroelectric coefficient was not possible. In order to reduce the electrical conductivity, intentional doping with Fe, Mn and C was applied. As the incorporation is only possible during growth, these elements were added with the help of appropriate precursor substances[24] mixed to the reaction atmosphere.

Fe and Mn occupy the Ga lattice site and trap excess electrons present due to the UID by changing their oxidation state, i.e. from Fe^{3+} to Fe^{2+} (Fe'_{Ga}) and from Mn^{3+} to Mn^{2+} (Mn'_{Ga}), respectively [117, 193, 365]. Also the amphoteric dopant C acts as an electron acceptor, when incorporated on sites of the N sublattice, which is preferentially the case for the used growth conditions [305]. Also optical properties are affected by doping as Fe and Mn doping are the source of additional luminescence [117, 382] and show different coloring of the respective samples (see Fig. 6.1(a) and 6.1(b)).

---

[23]Many thanks to PATRICK HOFMANN and his colleagues for their superior scientific expertise and the fruitful discussions.

[24]Typically via chlorination of elemental dopants similar to the method described in Ref. [119]. For Fe also the incorporation via biscyclopentadienyl iron (Cp_2Fe) [117] is possible.

The doping concentration[25] of GaN:Fe and GaN:Mn was determined by wavelength dispersive X-ray fluorescence spectroscopy (WDXRF), using a BRUKER S8 Tiger with rhodium radiation, yielding approximately $2 \times 10^{18} \, \mathrm{cm}^{-3}$ for both dopants. As C can not be detected via XRF in GaN:C, secondary ion mass spectroscopy (SIMS) was applied. An average bulk concentration of approximately $2 \times 10^{16} \, \mathrm{cm}^{-3}$ was determined, which drastically rises close to the sample surface (see Fig. 6.2). Due to doping, the samples show an electrical conductivity σ_{el} in the range of $10^{-5} \, \mathrm{S} \, \mathrm{m}^{-1}$ to $10^{-9} \, \mathrm{S} \, \mathrm{m}^{-1}$. It has to be noted, that σ_{el} has to be smaller than approximately $10^{-5} \, \mathrm{S} \, \mathrm{m}^{-1}$ for a reliable determination of p. In case of GaN:Fe the obtained doping concentration is close to the upper limit of appropriate electrical conductivity, which was obtained during an Fe and C co-doping concentration series.

For reasons of comparability all samples were cut into squares with an edge length of $10 \, \mathrm{mm}$, ground and polished to a total thickness between 500 and $600 \, \mathrm{\mu m}$ (see Fig. 6.1). In order to level conchoidal fracture inhomogeneities on the N-face, stemming from the substrate removal, a polishing was executed, whereas the Ga-face was left as-grown. After polishing, the N-face typically exhibits a so-called sub-surface damage (SSD) [367]. Therefore, the region below the surface, which differs in microstructure and composition from the bulk, has been removed via an etching in an alkalihydroxide. This is possible as the N-face is chemically less stable than the Ga-face [102]. Furthermore, a removed SSD should avoid surface influences on the measurement of p. Titanium electrodes with a thickness of approximately $100 \, \mathrm{nm}$ were deposited on the $(0\,0\,0\,1)$ and $(0\,0\,0\,\bar{1})$ surfaces by DC magnetron sputtering at room temperature, using a specially designed shadow mask (see Fig. 6.1(b)). To account for the rounded edges the exact electrode area A was measured from photographs using the software IMAGEJ.

Free-standing AlN samples were prepared by PVT at the "Institut für Kristallzucht" (IKZ), Berlin[26]. As the UID samples have no significant electrical conductivity and, thus, was not an issue for the pyroelectric characterization, doping was primarily applied to investigate its influence on p, as the results of GaN suggested (see below). Therefore, in comparison to an UID sample (O, C and Si as main contaminants), AlN:Si and AlN:Sc were investigated. Here, the latter is of particular interest as the mixed alloy system AlN-ScN improves the piezoelectric properties (see Sec. 5.1.3). In contrast to the gaseous precursors in the HVPE process, solid substances with a sufficient vapor pressure, i.e. $TaSi_2$ and ScN, served as dopant sources during PVT growth. The concentration of Si and Sc in AlN was also determined by XRF, yielding $7 \times 10^{19} \, \mathrm{cm}^{-3}$ and $2 \times 10^{20} \, \mathrm{cm}^{-3}$, respectively. The mechanical preparation, i.e. c-plane cut into flat plates, lapping and chemical-mechanical polishing, was performed at IKZ leading to a sample thicknesses between 250 and $440 \, \mathrm{\mu m}$. Both doped samples show differently colored areas (see Fig. 6.3), which represent different growth facets. Here, the light yellow colored area represents the desired $(0\,0\,0\,1)$ direction, while the uncolored area at the sample edge is typically a $(1\,0\,\bar{1}\,0)$ direction. Thus, only the colored areas were used for deposition of electrodes as only these contribute to the pyroelectric current I and, thus, p. Sputtered Ti on both sides also served as metallic electrodes for the electrical characterization. The exact area was again determined from photographs.

The lattice parameter c was measured on a Bruker D8 Discover high resolution X-ray diffractometer in parallel beam geometry using Cu-Kα_1 radiation by determining the exact peak

---

[25]Since a quantitative analysis yields mass percent c_m, the concentration c in cm^{-3} was calculated by $c = c_m \cdot \rho \cdot N_{\mathrm{A}}/m_i$, in which ρ is the mass density of the respective matrix (e.g. $6.15 \, \mathrm{g} \, \mathrm{cm}^{-3}$ for GaN [126]), N_{A} the AVOGADRO constant and m_i the molar mass of the respective dopant i.

[26]Many thanks to CARSTEN HARTMANN and his colleagues for supporting the investigations.

(a) 3" GaN:Mn single crystal directly after growth by HVPE.

(b) Employed shadow mask used for the sputtering of Ti electrodes.

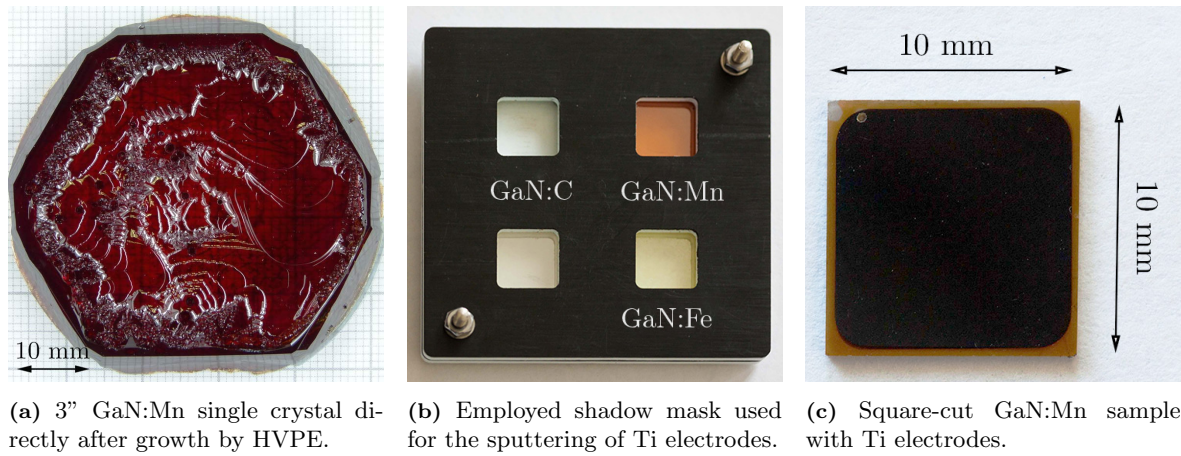**(c)** Square-cut GaN:Mn sample with Ti electrodes.

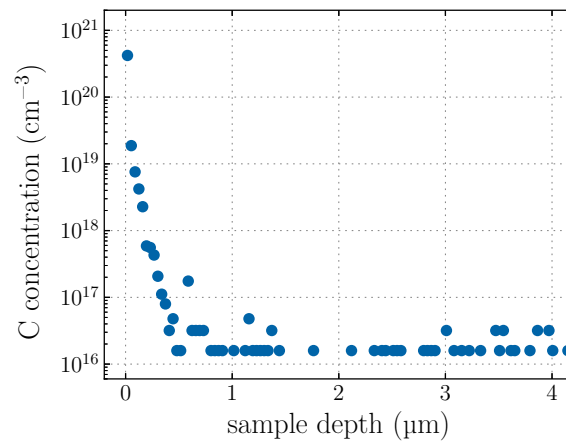**Fig. 6.1.:** Preparation steps for the pyroelectric characterization of semi-insulating GaN.

Fig. 6.2.: SIMS profile measured at RTG Mikroanalyse Berlin of GaN:C revealing non-homogeneous doping towards the surface.
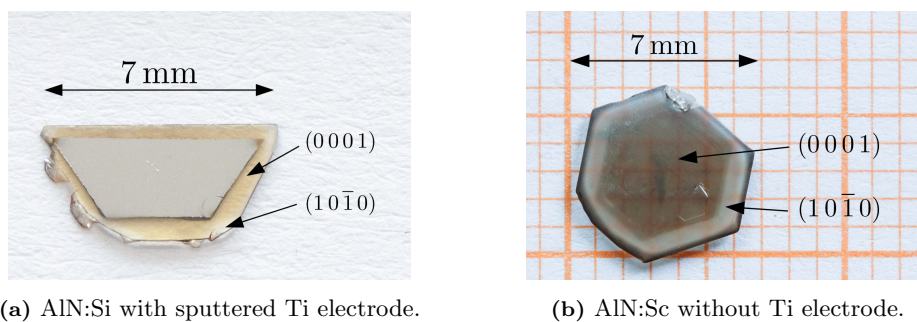

(a) AlN:Si with sputtered Ti electrode.

(b) AlN:Sc without Ti electrode.

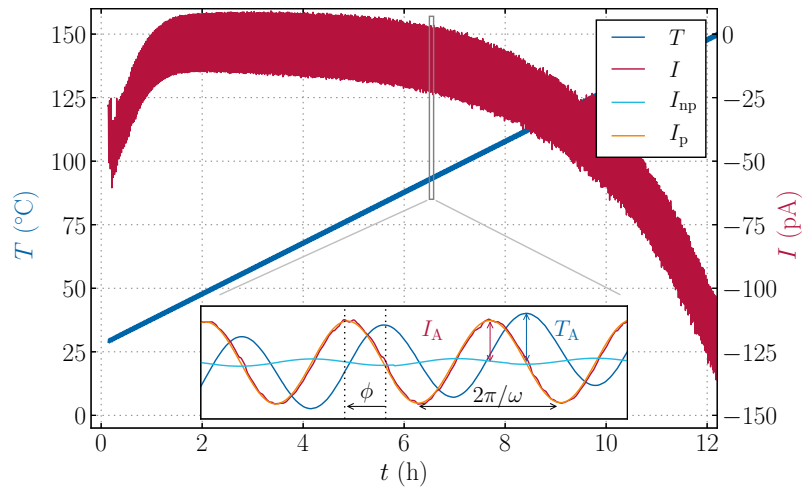**Fig. 6.3.:** AlN samples grown via PVT at IKZ Berlin.

Fig. 6.4.: Raw data forming the basis of the $p(T)$ calculation, depicting the applied temperature stimulation $T(t)$ (blue) and measured electric current $I(t)$ (red) for the GaN:C sample. The inset shows a typical evaluation range in one to three periods. Also the pyroelectric current contribution I_p (orange) is displayed together with the non-pyroelectric contribution I_np (cyan).

position of the 0006 reflection at room temperature. It has to be noted, that the lattice parameters of GaN and AlN were measured at FCM and Institute of Experimental Physics (IEP), respectively, but with similar setups. Therefore, the error bars displayed in Fig. 6.6(a) for GaN show the standard deviation of the mean lattice parameter determined at multiple positions on the respective samples, because the lateral homogeneity was primarily important. Since the AlN samples were too small for lattice constant mapping, the measurements of AlN were conducted at a single position. Thus, the errors in Fig. 6.6(b) for AlN were obtained from the diffractometer equalization function fit[27] of the $(0\,0\,0\,2)$, $(0\,0\,0\,4)$ and $(0\,0\,0\,6)$ reflections. The electrical characterization, i.e. the measurement of the pyroelectric coefficient p, its temperature dependency and electrical conductivity σ_el, was performed with the setup described in Sec. 4.1.

6.1.2. Pyroelectric Measurements

As the pyroelectric coefficient is expected to be comparably small (see Fig. 5.5 and Tab. D.1), low current signals during the thermal stimulation will be present. As the amplitude signal of $I(t)$ is in the lower pA range, the SAP was excluded from the measurement circuit (see Fig. 4.4) in order to reduce the current noise level below $200\,\mathrm{fA}$. Here, also the comparably large sample size of approximately $1\,\mathrm{cm}^2$ is beneficial to increase the current response.

As an example for a pyroelectric measurements, the excitation temperature $T(t)$ and current response $I(t)$ is shown in Fig. 6.4 for the GaN:C sample. From the overall phase shift ϕ of 89° to 93° between $T(t)$ and $I(t)$, a sole pyroelectric current signal contribution can be deduced within the measurement accuracy of the setup. Also, the ratio between pyroelectric and non-pyroelectric current amplitude of $I_\mathrm{p}/I_\mathrm{np} \approx 10$ (compare current contributions in Fig. 6.4), justifies the deduction of a dominating pyroelectric current contribution. The remaining deviation in ϕ of −1° to 3° lies within an acceptable range and is attributed to the sample-specific thermal contact resistance at the bottom contact of the sample.

---

[27] "D3" type, see Ref. [322]
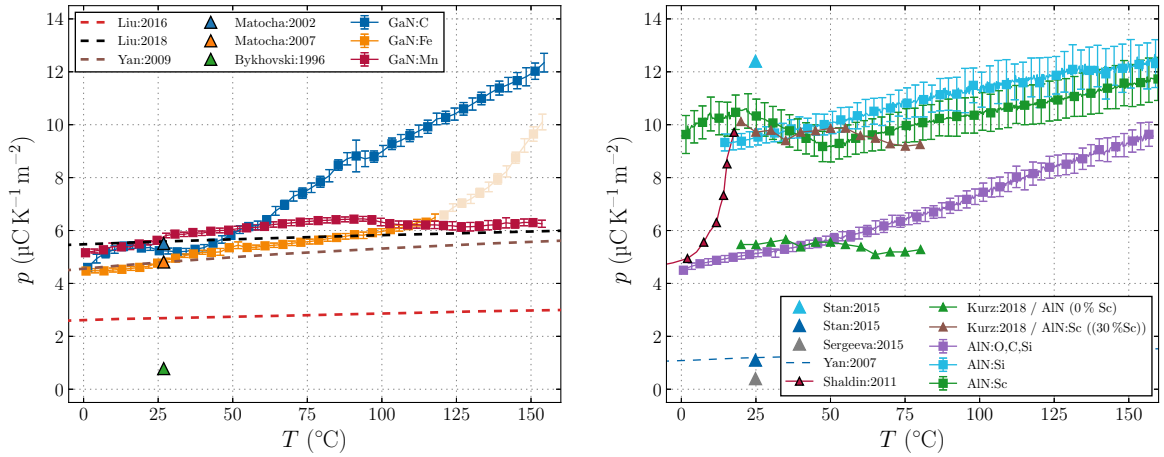
(a) The pyroelectric coefficient $p(T)$ of GaN in comparison to YAN *et al.* [370], LIU *et al.* [180, 181], MATOCHA *et al.* [201, 202] and BYKHOVSKI *et al.* [33].

(b) The pyroelectric coefficient $p(T)$ of AlN in comparison to STAN *et al.* [324], SERGEVA *et al.* [307], YAN *et al.* [371], SHALDIN *et al.* [312] and KURZ *et al.* [156].

Fig. 6.5.: Measured pyroelectric coefficients p (square marker and line with error bars) as a function of temperature T for the differently doped III-N semiconductor samples compared to previously published experimental (triangle markers) and theoretical (dashed lines) data. For optical clarity only every tenth data point is shown for the measured data.

A summary of $p(T)$ for all measured GaN and AlN samples in comparison with the literature values (compare also Fig. 5.5) is shown in Fig. 6.5(a) and Fig. 6.5(b), respectively, revealing the slight differences between the differently doped III-N semiconductors. In general, the pyroelectric coefficient as well as its temperature dependency is comparably small. The measured data of bulk material is in sufficient agreement with most of the literature data, mainly published for thin film material. In accordance with the literature also no phase transition, i.e. no extrema in $p(T)$, have been detected for any sample.

Focusing on gallium nitride, GaN:Mn and GaN:Fe do not exhibit a significant temperature dependency of p, whereas GaN:C changes its value from 4.6 to $12.4\,\mu\text{C}\,\text{K}^{-1}\,\text{m}^{-2}$. Thus, in comparison to GaN:Fe and GaN:Mn, the GaN:C sample shows the steepest increase of $p(T)$, which will be discussed in Sec. 6.1.4. The slopes for Fe- and Mn-doped sample are comparable, whereas the p values are separated by approx. $0.7\,\mu\text{C}\,\text{K}^{-1}\,\text{m}^{-2}$ in the lower temperature range. At elevated temperatures $p(T)$ of GaN:Fe seems to rise exponentially, which will also be discussed in Sec. 6.1.4. In comparison to communications of experimental values by BYKHOVSKI *et al.* [33], the obtained values at $27\,^{\circ}\text{C}$ in this study are larger by a factor of 2 to 10. In contrast, the determined values for p agree well with the experimental values by MATOCHA *et al.* [201, 202]. The very recent theoretical calculations by LIU *et al.* [179, 181] fit much better to the experimental values than initially proposed [180], showing the continuous improvement of the DFPT approach. Also a good agreement with the theoretical prediction by YAN *et al.* is observed. Nevertheless, this is no surprise, as their calculations are scaled to the experimental value by MATOCHA *et al.* [370].

Similarly to GaN, the measured values of bulk AlN are partially in good agreement with previously published thin film data. Regarding the low-temperature data of SHALDIN *et al.* [312], the measured data of bulk UID AlN (AlN:O,C,Si) sample fits nicely around $0\,^{\circ}\text{C}$. The steep increase of SHALDIN's data between $0\,^{\circ}\text{C}$ and $20\,^{\circ}\text{C}$ appears to be a measurement artifact, evidenced by the fact that these data points do not fit to the general trend of $p(T)$ in the original work (see also Fig. 5.5) and the absence of phase transitions in this temperature

range. Comparing to the recent work of KURZ *et al.* [156], the measured data of UID free-standing AlN fits very good to the sputtered AlN thin film layers with a thickness of only 900 nm. Also the measured AlN:Sc is in good accordance to the thin film results by KURZ *et al.*, albeit the Sc content being different. Compared to UID AlN the Sc incorporation nearly doubles the pyroelectric coefficient at room temperature, which is similar to the piezoelectric coefficient d_{33} [156]. This is also the case for AlN:Si, yielding the same overall increase of p from approximately $9\,\mu\mathrm{C\,K^{-1}\,m^{-2}}$ to $12\,\mu\mathrm{C\,K^{-1}\,m^{-2}}$ between $0\,°\mathrm{C}$ and $160\,°\mathrm{C}$ as for AlN:Sc. In contrast, the experimental thin film results obtained by STAN *et al.* [324] and SERGEVA *et al.* [307] as well as the theoretical predictions by YAN *et al.* [371] do not fit very well. The latter is explained by the used lower experimental value and, thus, wrong scaling factor used for the calculations.

Comparing the general trend of AlN with GaN, the slope of $p(T)$ of AlN is slightly higher, which is surprising as the phase transition, e.g. dissociative sublimation (see Fig. 5.1.3), is much higher for AlN. Typically a low transition temperature leads to a steeper increase of p at temperatures below the phase transition. Calculating the figures of merit for sensor and energy harvesting applications shows only small differences in F_I and F_V. The values used for the calculation and the respective FOMs in comparison with other materials are given in the appendix in Fig. D.1 and Tab. D.1. Here, k^2, F_E and F'_E are nearly identical and very low compared to traditional ferroelectrics. Thus, III-N semiconductors are less attractive for energy harvesting applications than conventional ferroelectrics. While the current responsivity F_I for sensor applications is also very low, the voltage responsivity F_V corresponds to $22\,\%$ of the standard material $LiNbO_3$.

6.1.3. Lattice Influence

The pyroelectric coefficient p is correlated with the spontaneous polarization $\vec{P}_\mathrm{S}$, which in turn is associated with the displacement parameter u. As experimental access is quite complex, it seems reasonable to discuss the connection between p and the magnitude of the polar lattice parameter c (parallel to u) as a first step. Because the measurement of p with the SHARP-GARN method is an averaging technique calculating a mean p for the entire sample, it is valid to use a mean lattice parameter c for this discussion. The $p(c)$ relation at $27\,°\mathrm{C}$ is visualized Fig. 6.6, indicating a linear behavior. Here, the smaller the lattice parameter c, the higher is the absolute value of the pyroelectric coefficient. The influence of doping on the lattice parameter is also known from other dopants [283]. With a change in P_S, the semiconductor becomes more sensitive to temperature stimulations and p varies as well.

At this point it is important to note that Fig. 6.6(a) cannot be associated directly to the temperature dependency of p in Fig. 6.5(a). The lattice parameter c generally increases with rising temperature [170], while P_S decreases. A direct calculation of $p(T)$ (Fig. 6.5(a)), which is the slope of $P_\mathrm{S}(T)$, from $p(c)$ at $27\,°\mathrm{C}$ (Fig. 6.6(a)) is not possible, because one has to evaluate $P_\mathrm{S}(T)$ from $c(T)$, which is not given with the present data. Nevertheless it can be said, that by choosing an appropriate lattice parameter c and, thus, determining P_S, the pyroelectric properties of the material can be tailored slightly.

Furthermore, this linear model provides an explanation for the variation of the previously published pyroelectric coefficients of GaN. The investigated thin films on sapphire substrate exhibit a small thickness compared to the free-standing GaN of the present investigation. The discrepancy to the p values of BYKHOVSKI *et al.* ($p = 0.78\,\mu\mathrm{C\,K^{-1}\,m^{-2}}$) may therefore arise from residual strain present in the lattice of the $2\,\mu\mathrm{m}$ to $5\,\mu\mathrm{m}$ MOVPE GaN thin films

Tab. 6.1.: Pyroelectric coefficients p and lattice parameter c at $27\,^{\circ}\mathrm{C}$ for the samples under investigation.

Sample	$p\ (\mu\mathrm{C\,K^{-1}\,m^{-2}})$	$c\ (\text{Å})$
GaN:Fe	4.918 ± 0.059	5.18576 ± 0.00005
GaN:C	5.342 ± 0.098	5.18569 ± 0.00002
GaN:Mn	5.599 ± 0.064	5.18564 ± 0.00009
AlN:O,C,Si	5.161 ± 0.013	4.98527 ± 0.00009
AlN:Si	9.606 ± 0.029	4.98483 ± 0.00006
AlN:Sc	1.023 ± 0.063	4.98659 ± 0.00012

due to the influence of the substrate. According to HIRAMATSU *et al.* a thin GaN film on a sapphire substrate exhibits a too large lattice parameter c, due to the different thermal expansion coefficients $\overset{2\rightarrow}{\alpha}_{\mathrm{GaN}} < \overset{2\rightarrow}{\alpha}_{\mathrm{sapphire}}$ and the consequentially large thermal stresses from cooling after the growth [114]. Following the proposed model this artificially decreases p and, thus, explains the observed difference of one order of magnitude compared to the presently measured values. Additional to the strain resulting from the lattice mismatch between substrate and epitaxial layer, the difference in thermal expansion coefficients leads to a significant amount of stress during cool down from growth to room temperature [70]. Then, the presence of flexoelectricity [191], especially in the case of thin films, cannot be excluded [35]. The lattice parameters of the measured free-standing bulk crystals are assumed as relaxed, thus the obtained values of the total pyroelectric coefficient p are not influenced by flexoelectricity, except GaN:C (see Sec. 6.1.4). The lattice parameters by MATOCHA *et al.* for HVPE GaN samples can be assumed as relaxed compared to that of BYKHOVSKI *et al.* (c approximately $5.190\,\text{Å}$ according to Ref. [114]) hence, showing a pyroelectric coefficient with only a small influence of strain. Although their investigated samples are considered thin compared to the thickness of the samples of the present study, they show a good agreement with the p values at $27\,^{\circ}\mathrm{C}$.

The applied growth method also influenced the lattice parameters of AlN [237] and, thus, could also here explain the different published values of p (see Fig. 5.5). Taking the results of this work into account, a value larger than $12\,\mu\mathrm{C\,K^{-1}\,m^{-2}}$ seems to be unreliable and cannot be explained with small changes of the lattice. Unfortunately, the linear $p(c)$ relation does not hold for doped AlN, as p falls with increasing lattice parameter c only in the case of the UID and Si-doped sample. An increased c lattice parameter is present for the Sc-doped

(a) GaN

(b) AlN
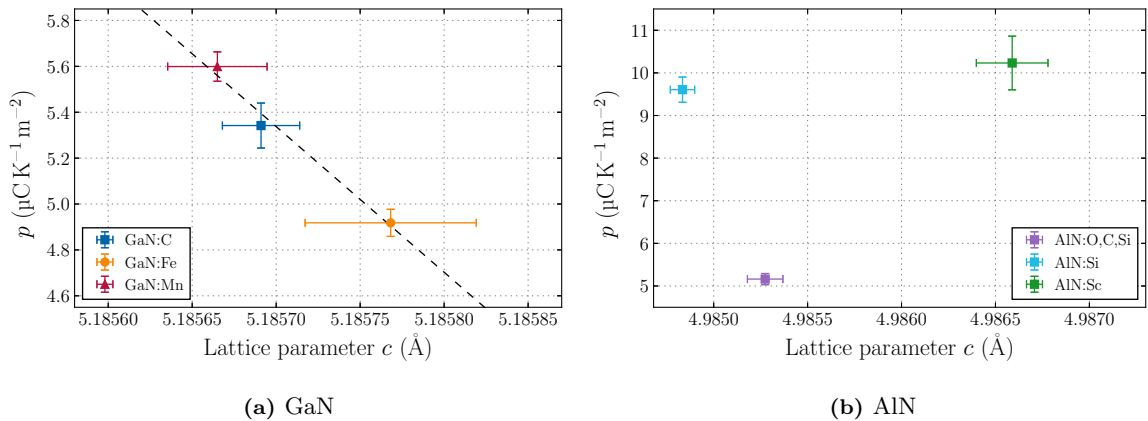
Fig. 6.6.: Pyroelectric coefficient at $27\,^{\circ}\mathrm{C}$ as a function of the lattice parameter c for the differently doped AlN and GaN samples. The broken black line indicates a linear dependency.

material, which has a similar or larger p than AlN:Si and UID AlN, respectively. As GaN and AlN have isomorphic structure, this implies either a doubtful different mechanism controlling the pyroelectricity or that c might be the wrong quantity to monitor. Maybe u could serve as a more appropriate quantity, but this would necessitate full structure solutions from single crystal X-ray diffractometry.

6.1.4. Slope Differences

Beside the room temperature values, also the $p(T)$ slopes of the differently doped GaN samples merit further discussion. The disproportionate increase of $p(T)$ of GaN:Fe above 120 °C is a misinterpretation of the SHARP-GARN method. In order to explain this, the raw data as well as the fitted phase difference ϕ of the GaN:C and GaN:Fe sample are shown in Fig. 6.7. The background signal of the current measurement of approximately 2 pA rises with increasing temperature, which can indicate a developing non-pyroelectric current contribution. This increased current background is especially large for GaN:Fe compared to the other samples. Comparing Fig. 6.7(a) and Fig. 6.7(b), a difference of about two orders of magnitude between the current scales is present. Furthermore, the phase shift ϕ between current and temperature oscillation gains an increased in-phase contribution, i.e. it deviates from 90° (pyroelectric) towards 0° (non-pyroelectric) at elevated temperatures clearly hinting to dominating non-pyroelectric TSC signals.

For small background currents and dominating out-of-phase contributions, as in Fig. 6.7(a), the evaluation of $p(T)$ with the SHARP-GARN approach is reliable. While this is the case for all other dopants, it is not for GaN:Fe. The pronounced TSC at elevated temperatures can be associated to the ionization of the $\mathrm{Fe}'_{\mathrm{Ga}}$ defect, which actually served as compensational dopant. The electrical conductivity σ_{el} with respect to the temperature T, measured within the same setup as the pyroelectric coefficient, is shown in Fig. 6.8. A thermal activation energy E_{A} of 596.8 meV is obtained[28], which is in good accordance to published values of the energy level of the $\mathrm{Fe}'_{\mathrm{Ga}}$ defect below the conduction band [266, 278]. The thermal ionization of a trap level is non-linear, but the SHARP-GARN approach takes only linear thermally stimulated currents into account. Thus, a disproportionate increase of the current amplitude I_{amp} combined with a remaining non-zero, but nearly zero phase shift ϕ (see lower right in Fig. 6.7(b)), still yield a non-zero p. As the exponential course of $I_{\mathrm{amp}}(T)$ dominates in Eq. (3.55) (page 47), also $p(T)$ follows this trend. Thus, p of GaN:Fe is not reliable (indicated as transparent markers in Fig. 6.5(a)) as its calculation is distorted by non-linear TSC.

Focusing on GaN:C, the increase of p with T is steeper than for all other investigated samples. As the current response I and phase shift ϕ remain relatively stable with T (see Fig. 6.7(a)), the evaluation of p is not disturbed by non-linear TSC. The reason might be the unintended inhomogeneous doping of the sample. As shown in Fig. 6.2, the concentration of C increases within a length of approximately 1 µm by about four orders of magnitude towards the sample surface. NI *et al.* recently reported that a high C doping concentration leads to a shift from tensile to compressive strain, due to the prevalent substitution of Ga or N with C [236]. Thus, a change of strain towards the surface forms a strain gradient along the polar c axis and gives rise to tertiary or flexoelectric pyroelectricity, assuming that this strain gradient is also temperature-dependent.

---

[28]A least square fit was performed using $\sigma_{\mathrm{el}} = A \cdot \exp(-E_{\mathrm{A}}/k_{\mathrm{B}}T)$, in which A is a constant, E_{A} the activation energy, k_{B} the BOLTZMANN constant and T the temperature.
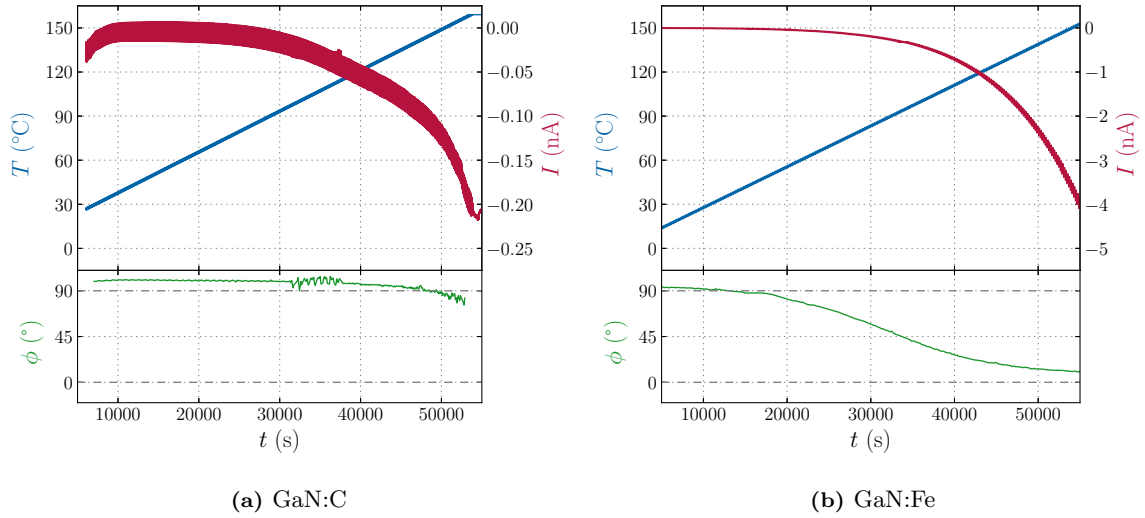
(a) GaN:C

(b) GaN:Fe

Fig. 6.7.: Raw data comparison between differently doped GaN samples. Upper plots show the raw data of applied temperature stimulation $T(t)$ and measured electric current $I(t)$, which form the basis for the $p(T)$ calculation. The lower plots provide the evaluation of the respective phase shift ϕ.
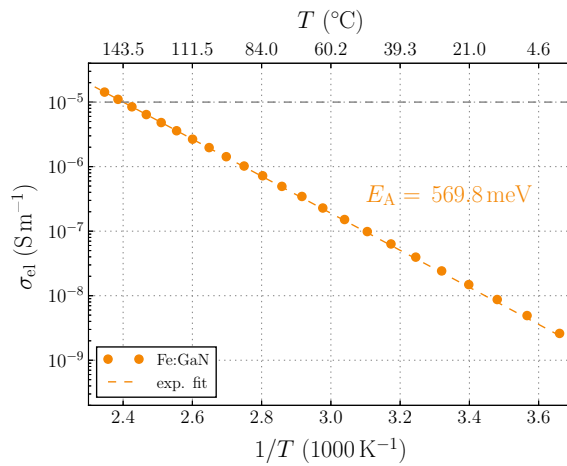

Fig. 6.8.: Electrical conductivity σ_{el} of GaN:Fe with respect to the reciprocal temperature $1/T$.

6.2. Pyroelectricity of Doped Hafnium Oxide

6.2.1. Sharp-Garn Measurement on Thin Films

Pyroelectric coefficients of HfO_2 have been typically determined by the SAWYER-TOWER method, i.e. calculated p from the change of P_R with T obtained from hysteresis measurements at different temperatures, except the work by SMITH *et al.* [319] and MART *et al.* [194]. Here, the SHARP-GARN method (see Sec. 3.3.5) was used, to evidence that not only the period pulse technique (see Sec. 3.3.3) can be applied for the characterization of p of thin films. A verification of the previous results is in the sense of good scientific practice and demonstrates the thin film capabilities of the measurement setup. Furthermore, the present work extends this approach by adding measurements of p at varying temperatures to reconstruct the course of the remanent polarization P_R.

For a typical sample the layer stack as well as the contact pad layout are shown in Fig. 6.9. To identify different top contact pads, rows are numbered with arabic numerals, while columns are labeled by roman letters with ascending size. Here, typically the D pads with a size of approx. $0.150(1)\,\mathrm{mm}^2$ were used for the determination of p and P_R as the measured current increases with electrode area (compare to Eq. (3.7)). As the pad size represents the area, which is used for the evaluation of p and P_R, the precise pad size and corresponding error were determined from microscopy images for each sample. While the upper contact pad was connected with the tungsten needle (see Fig. 4.3(b)), the bottom connection was established with the help of silver conductive paint at the wafer edge. The latter connection can furthermore enhance the heat transfer from heater to sample.

To show the suitability of the setup described in Sec. 4.1, the measurement results of a 20 nm thick $Hf_{1-x}Zr_xO_2$ sample for $x = 0.5$ are shown below, which serve as direct comparison to the result obtained by SMITH *et al.* [319]. An example of the pyroelectric measurement is shown in Fig. 6.10(a), revealing the dominating pyroelectric current contribution with an overall phase shift of approximately 95°. The small current amplitude, usually lower than $1\,\mathrm{pA}$, requires low noise levels, which is why the SAP had to be excluded from the electrical circuitry. Furthermore, the good signal quality of such low currents demonstrates the precision of the setup. A pyroelectric coefficient of $34.4(28)\,\mathrm{\mu C\,K^{-1}\,m^{-2}}$ was obtained, which is in very good accordance with SMITH *et al.* (approximately $30\,\mathrm{\mu C\,K^{-1}\,m^{-2}}$). Intermediate hysteresis loop
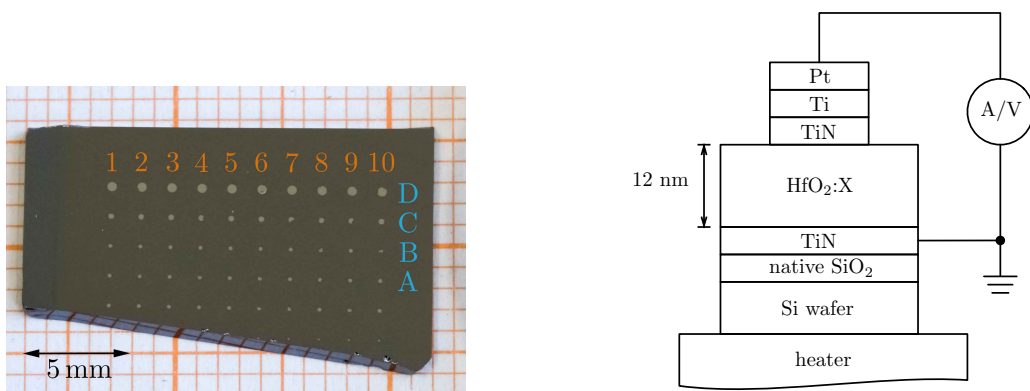
(a) Top contact pad layout of a typical HfO_2 thin film stack processed on a Si wafer.

(b) Capacitor stack layout (see Ref. [276]), where X symbolizes different dopants of HfO_2.

Fig. 6.9.: Sample preparation for the electrical characterization of HfO_2 thin films.
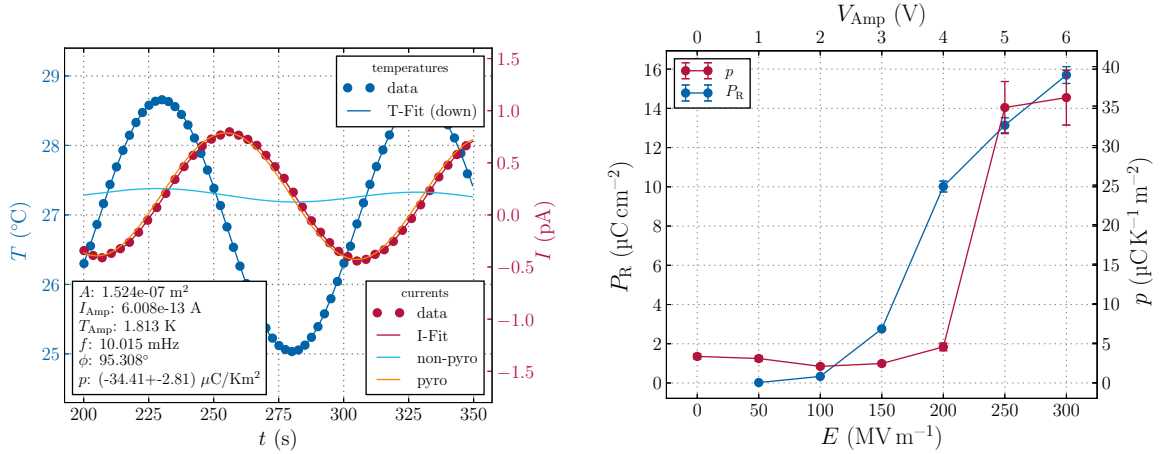
(a) Raw signal and Fit of a pyroelectric measurement for a 20 nm $Hf_{0.5}Zr_{0.5}O_2$ thin film.

(b) Remanent polarization P_R and pyroelectric coefficient p with respect to applied electric field E.

Fig. 6.10.: Ferro- and pyroelectric characterization of a $Hf_{0.5}Zr_{0.5}O_2$ thin film serving as reference system.

measurements give the corresponding remanent polarization P_R and additionally serve as poling step for the subsequent determination of p. The obtained values of P_R (measured at 1 kHz) and p with respect to the applied voltage amplitude, i.e. electric field strength, are shown in Fig. 6.10(b). A full hysteresis and, thus, maximized P_R and p are obtained for an electric field strength of above approximately $225\,\text{MV}\,\text{m}^{-1}$. The upper limit is given by the breakdown voltage of the samples, which typically lies between $300\,\text{MV}\,\text{m}^{-1}$ and $400\,\text{MV}\,\text{m}^{-1}$ for all samples measured in this work.

6.2.2. Effects of Silicon Doping

As outlined in Sec. 5.2.2, doping the material with a variety of elements stabilizes the ferroelectric phase of HfO_2. The variation of the ferroelectric properties due to the doping with silicon was first demonstrated by BÖSCKE et al. [27], followed by the works of LOMENZO et al. [184–187], HOFFMANN et al. [115] and RICHTER et al. [276]. An investigation on its related piezo- and pyroelectric properties is still pending, which might enable further applications beyond the memory technology. This is where the present work comes into play, while another very recent study investigated the impact of thickness and field-cycling stability for a fixed Si content [194]. While both are important parameters, the dependence on compositional changes is of particular importance for future applications and device manufacturing and, thus, was subject of this work[29].

Sample Preparation and Characterization Capacitors formed by approximately 12 nm thick HfO_2:Si sandwiched between 12 nm thick titanium nitride (TiN), titanium (Ti) and platinum (Pt) top and bottom electrodes were fabricated at NaMLab Dresden as described elsewhere [276]. The stack is shown in Fig. 6.9(b), in which the Si content of the HfO_2:Si layer was adjusted by varying the ratio of HfO_2 to SiO_2 cycles during ALD between 30:1 and 8:1. This resulted in a Si concentration between 1.6 at% and 3.8 at% (atomic percent, i.e. [Si]/[Hf+Si+O]) as determined by time-of-flight secondary ion mass spectrometry (TOF-SIMS) and outlined previously [276]. The corresponding cationic ratios Si/[Si+Hf], as com-

---

[29]Many thanks to TONY SCHENK, MIN HUYK PARK and UWE SCHROEDER from NaMLab Dresden for providing the samples and the comprehensive discussion about the whole HfO_2 topic.
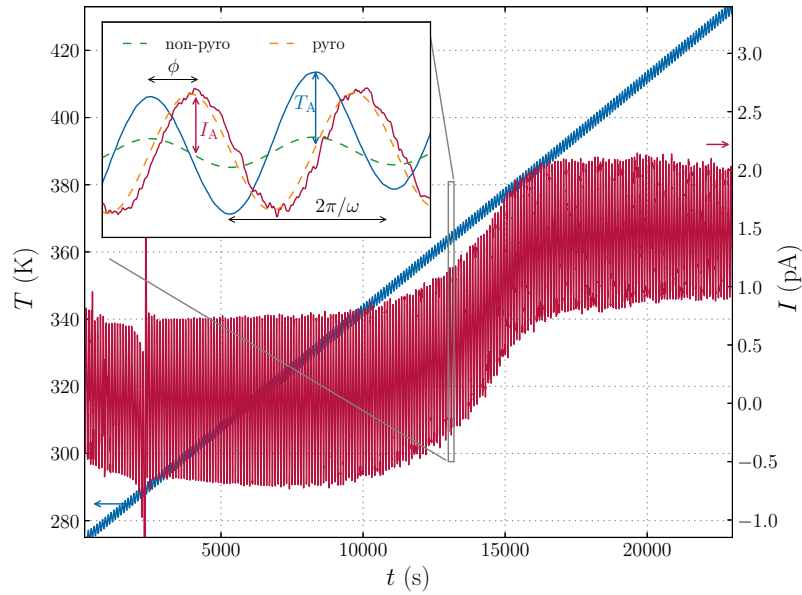
Fig. 6.11.: Raw data forming the basis for the $p(T)$ calculation, exemplifying applied temperature stimulation $T(t)$ (blue) and measured electric current response $I(t)$ (red) of HfO_2:Si with a Si concentration of $2.2\,\text{at}\%$. Inset: Typical evaluation range of p over two periods as well as the decomposition of pyro- and non-pyroelectric current contributions obtained from fitting the shown parameters.

monly used in publications other than Ref. [276], range between $3.2\,\text{cat}\%$ and $11.1\,\text{cat}\%$, respectively. All samples were annealed in nitrogen atmosphere for $20\,\text{s}$ at $800\,°\text{C}$ to crystallize the capacitor stacks.

Ferroelectric hysteresis measurements were performed with the shunt method as outlined in Sec. 4.2 to characterize the polarization of the samples. Here, a reference resistance of $R_{\text{ref}} = 1\,\text{k}\Omega$ and a voltage amplitude and measurement frequency of $3.5\,\text{V}$ and $1\,\text{kHz}$, respectively, were used. The value of P_{R} was measured after 10^3 to 10^4 cycles in order to minimize influences of the wake-up and fatigue effects [210, 295, 298, 379]. The actual temperature course and measured current signal for the pyroelectric coefficient evaluation are exemplified in Fig. 6.11 for HfO_2:Si with a Si concentration of $2.2\,\text{at}\%$. A temperature amplitude T_{A} of $2\,\text{K}$, a frequency of $10\,\text{mHz}$ and a heating rate of $25\,\text{K}\,\text{h}^{-1}$ were used for the thermal stimulation. An overall phase shift ϕ of approx. $100°$ between temperature and current was observed showing the dominating pyroelectric current contribution. The deviation from the ideal value of $90°$ stems from TSC originating from trapped charges due to the initial field cycling. This is in accordance with a recent report using up to 10^5 field cycles [194]. The signals are qualitatively similar for all samples and the uncertainty of p is estimated from the statistical errors of the fitted signals and the pad area on a 1σ level. Furthermore, an HP 4284A precision LCR meter was used to determine the dielectric constant ε_{r} of the samples, which, in addition to p, is necessary to calculate the figures of merit for energy harvesting and IR sensor applications.

Concentration Influence The evolution of the hysteresis with increasing Si concentration is summarized in Fig. 6.12. It shows typical non-polar (orange), ferro- (blue) and antiferroelectric (green background) shapes depending on the Si concentration, which is in good agreement with recent results [115, 276].

It has been argued before [276, 309] that field-induced ferroelectricity is a more general and more appropriate description for the double-hysteresis loops compared to the original

definition of antiferroelectricity by KITTEL [143]. In recent years, however, the term antiferroelectricity has commonly been used in a wider sense [116, 194, 248, 249, 276, 309] including the present case of a transition from a non-polar tetragonal to a polar orthorhombic phase. Therefore, and for the sake of convenience, the term antiferroelectricity is used in accordance to this wider sense in the following. Ferroelectricity is obtained for Si concentrations from approximately 1.9 at% to 2.5 at%, while antiferroelectric behavior exists for Si concentrations of around 2.5 % to 3.5 at%. Below 2.0 at% and above 3.5 at% a linear dielectric P-E shape reveals the non-polar character of the layer.

The resulting values of P_{R} from the axis intercepts are shown in Fig. 6.13 with respect to the Si concentration. Also the values of the pyroelectric coeffcient p at room temperature determined using the SHARP-GARN method are provided. The comparison between untreated sample, poled after a P-E measurement, and after heating during a $p(T)$ measurement shows the differences due to thermal treatment and poling. Fitted fractions of the monoclinic (space group $P2_1/c$), orthorhombic ($Pca2_1$) and tetragonal ($P4_2/nmc$) phases obtained from refinement according to PARK et al. [249] are also given in Fig. 6.13. P_{R} and p rise and fall simultaneously, depending on the Si concentration peaking at an Si concentration of 2.0 at% with maximum absolute values of $46.2(61)\,\mu\mathrm{C\,K^{-1}\,m^{-2}}$ and $8.21(22)\,\mu\mathrm{C\,cm^{-2}}$, respectively. These maxima correspond nicely to the changes in phase fractions shown in Fig. 6.13. Due to a purely monoclinic phase for low Si content the corresponding samples exhibit a non-polar character. The maximum of the polar orthorhombic phase fraction between 1.9 at% and 2.5 at% Si is the reason for the maximum of the polar properties. The strongly constricted hysteresis with a non-zero remanent polarization for Si concentrations of 2.5 at% and 3.5 at% stems from a mixture of the tetragonal and the monoclinic phase. It seems that the tetragonal phase gives rise to antiferroelectric behavior. Samples with a concentration above 3.5 at% remained amorphous, which explains the vanishing of the polar properties. While nearly all samples show a negligible pyroelectric coefficient in the unpoled state, i.e. before an initial P-E measurement, a pyroelectric coefficient of approximately $10\,\mu\mathrm{C\,K^{-1}\,m^{-2}}$ can be measured with the SHARP-GARN method for a Si concentration of 2.0 at%. This is an
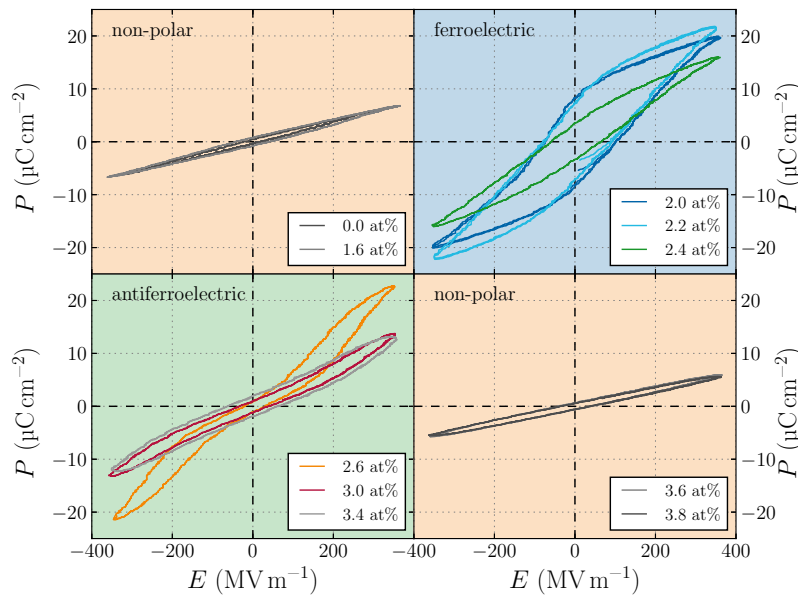

Fig. 6.12.: Hysteresis of non-polar (top left and bottom right), ferroelectric (top right) and antiferroelectric (bottom left) HfO$_2$:Si, depending on the Si concentration. The hysteresis loops were measured with the shunt method using a triangular voltage sweep of 3.5 V amplitude and 1 kHz frequency at room temperature.
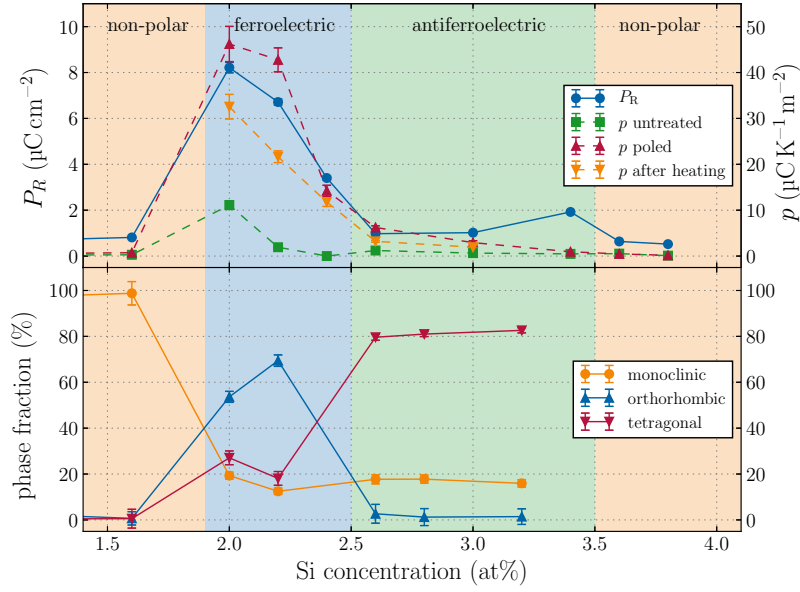
Fig. 6.13.: Top: Remanent polarization P_R and pyroelectric coefficient p depending on Si concentration in HfO$_2$:Si. Bottom: Fitted fractions of individual phases depending on Si incorporation obtained by RIETVELD refinement according to Ref. [249].

indication for aligned domains, already established by the fabrication process. The origin of this phenomenon is still unclear and, thus, needs further investigation, such as TEM studies of grain orientations or X-ray texture measurements.

Pyroelectric coefficients obtained from a continuous electric field-cycling method may be much higher than those obtained by a method with absent electric field, as recently shown in HfO$_2$:Si [115]. A possible explanation could be the different degree of polarization of the films at different temperatures. Typical hysteresis loops of HfO$_2$:Si show no complete polarization (see non-saturated P_R in Fig. 6.10, Fig. 6.12 and Ref. [115, 276]), i.e. the maximum electric field before breakdown is not sufficient to completely polarize the thin films. This can be seen from hysteresis measurements with increasing electric field amplitude, which give an increasing P_R with field [319]. The obtainable fraction of the full polarization may further depend on temperature, despite the use of equal field amplitudes. Calculating the pyroelectric coefficient from such data means to use only a temperature-dependent fraction of the full P_R, so that the maximum achievable p can actually be higher. In contrast to that, field-free methods start from an initial polarization value without changing this polarization state during the temperature variation.

The dependencies of ε_r on measurement frequency f, temperature T, and Si concentration are shown in Fig. 6.14 and are in good accordance with previous reports [276]. While ε_r depends only slightly on f and T, the largest influence is due to the doping with Si. The value of ε_r in the ferroelectric region peaks at the transition from the ferroelectric to the antiferroelectric phase region and is followed by a decrease towards higher Si concentrations. At the transition from the antiferroelectric to the non-polar state, an additional maximum of ε_r is present, which is more pronounced at higher temperature and lower measurement frequencies. Due to the low operation frequencies of the mentioned applications (typically below 100 Hz), the values measured at room temperature and at a frequency of 100 Hz form the basis of the figure of merit calculations.
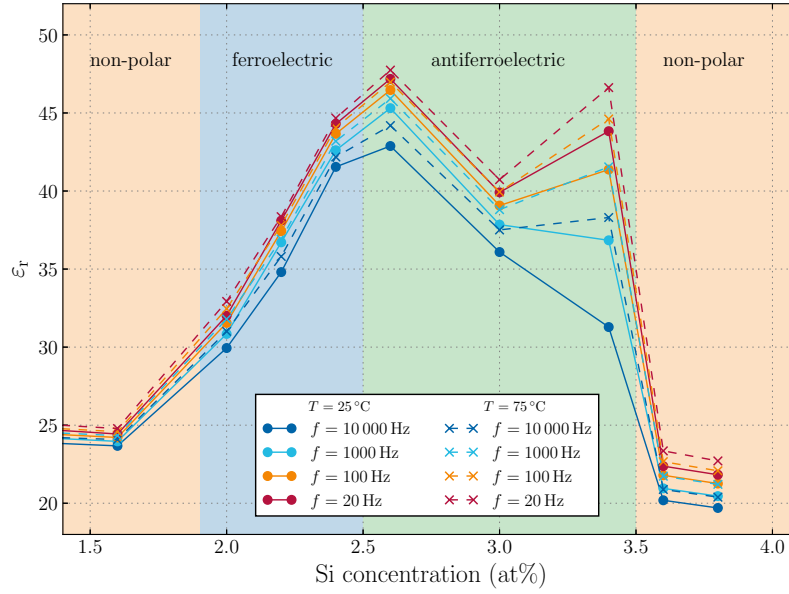
Fig. 6.14.: Dielectric permittivity ε_{r} of HfO$_2$:Si depending on measurement frequency f, temperature T, and Si concentration.

Temperature Dependency   The $p(T)$ curves determined using the SHARP-GARN method for ferro- and antiferroelectric HfO$_2$:Si are shown in Fig. 6.15, revealing varying temperature dependencies of P_{R} for different Si doping concentration. A Si concentration of $2.0\,\mathrm{at\%}$ has an almost constant $p(T)$ behavior in the investigated temperature range. For larger Si concentrations, the absolute pyroelectric coefficient drops to lower absolute values and slightly decreases with increasing temperature, which is in accordance with previous results [115]. Although p generally increases close to a phase transition, the decreasing behavior may stem from the grain size effect mentioned by HOFFMANN *et al.* [115]: Smaller grains have a lower transition temperature and, thus, get already depolarized at lower temperatures. The fact that p at room temperature after poling is always lower after a heating step (see Fig. 6.13) supports this. Another explanation could be the increased internal bias field caused by charge redistribution, which lowers P_{R} and thus p after heating the material [73, 95, 254]. The Si concentration of $2.4\,\mathrm{at\%}$, which is close to the transition from the ferro- to the antiferroelectric phase, is an exception to this general trend. Here, p rises with increasing temperature, which indicates a temperature-driven transition from the ferro- to the antiferroelectric phase, so that P_{R} varies more and, thus, p increases. For Si concentrations above $2.5\,\mathrm{at\%}$, marked by antiferroelectric behavior and low P_{R}, p remains nearly constant at relatively low absolute values for the complete investigated temperature range. A CURIE temperature, i.e. phase change temperature to a non-polar phase, was not detected from the $p(T)$ measurements and, thus, a temperature-induced phase transition is not present in the investigated temperature range. The initial value of p can be recovered by poling the sample again.

By integrating the obtained $p(T)$ data, and adding the value of P_{R} at room temperature (obtained from hysteresis measurements), the remanent polarization dependency can be reconstructed. The absolute change and absolute value of the remanent polarization, $\Delta P_{\mathrm{R}}^*(T)$ and P_{R}^*, respectively, without the use of an external electric field for their determination are summarized in Fig. 6.16. P_{R}^* is marked with an asterisk because the different degree of polarization at different temperatures obtained from a hysteresis measurement may differ from that of a temperature-dependent pyroelectric coefficient measurement. The slight change of P_{R}^* is nearly linear with T, corresponding to the almost temperature-invariant p for all Si
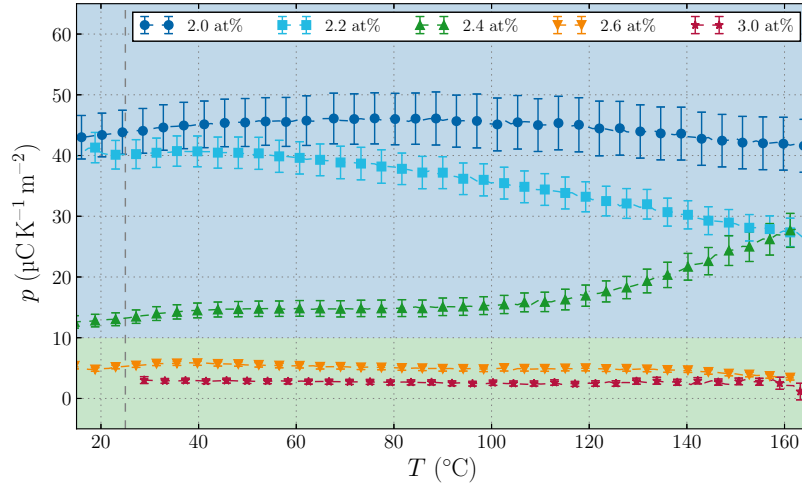
Fig. 6.15.: Pyroelectric coefficient as a function of temperature $p(T)$ for different Si concentrations in HfO$_2$.
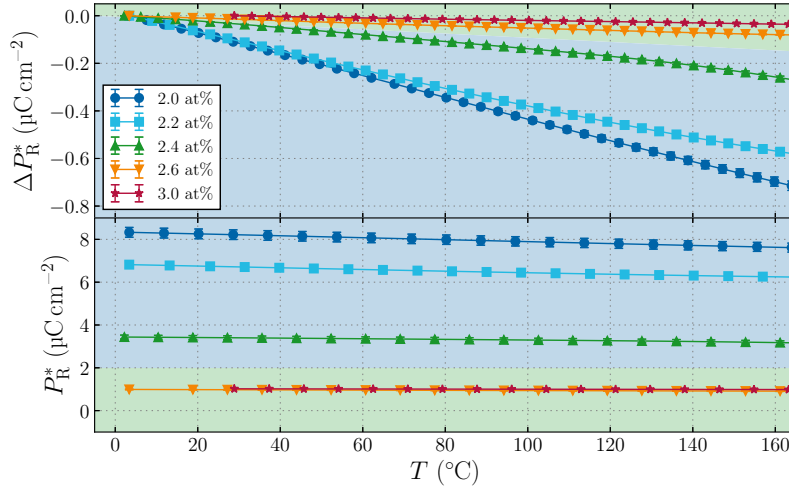

Fig. 6.16.: Top: Absolute change of the remanent polarization ΔP_R^* with respect to temperature T calculated by integrating the data of Fig. 6.15. Bottom: Absolute value of P_R^* using the room temperature values from Fig. 6.13 as offset.

concentrations. The largest variance of P_R^* is again present for the most polar 2.0 at% sample, caused by the largest pyroelectric coefficient. Here, P_R^* changes by approximately 13 % over the temperature range of 170 K. All other concentrations show a smaller absolute change of P_R^* with temperature, accompanied with smaller absolute values of P_R^* and p (see bottom of Fig. 6.16). Compared to the absolute value of P_R^*, the change ΔP_R^* is quite small, leaving P_R^* quasi constant with T. This is not necessarily expected from HfO$_2$:Si, as it is considered as a rather "fragile" system due to its smaller concentration window for ferroelectric properties compared to other dopants and its related increased sensitivity to the impact of grain size and oxygen vacancies [276]. However, its ferro- and pyroelectric properties remain relatively stable between ambient and elevated temperatures. This is especially promising for future applications and device manufacturing.

Figures of Merit and Material Comparison   Tab. 6.2 and Fig. 6.17 summarize the calculated FOMs for sensor and energy harvesting applications (see Sec. 2.6) depending on the Si concentration of HfO$_2$:Si. To estimate the error bars in Fig. 6.17, relative errors of approximately 6 % for p and ε_r, and 0.3 % for $\tan \delta$ were assumed.

Tab. 6.2.: Calculated figure of merit values of HfO$_2$:Si for various Si concentrations at room temperature ($T = 25\,°$C). A constant specific heat capacity $C_V = 2.63 \times 10^6$ J m^{-3} K^{-1} (from specific heat $C_p = 274.26$ J kg^{-1} K^{-1} [380] and mass density $\rho = 9.60$ g cm^{-3} [131]) and an upper temperature $T_\mathrm{h} = 300$ K were assumed. The values of $\tan\delta$ and ε_r at a measurement frequency of 100 Hz were used.

Si (at%)	p $\times 10^{-6}$ (C K^{-1} m^{-2})	ε_r	$\tan\delta$	k^2 $\times 10^{-4}$	F_E (J m^{-3} K^{-2})	F'_E $\times 10^{-13}$ (m^3 J^{-1})	F_I $\times 10^{-12}$ (m V^{-1})	F_V $\times 10^{-2}$ (m^2 C^{-1})	F_D $\times 10^{-6}$ (m$^{3/2}$ J$^{-1/2}$)
1.6	0.00	24.21	0.01	0.00	0.00	0.00	0.00	0.00	0.00
2.0	46.22	31.55	0.03	8.71	7.65	11.03	17.55	6.28	6.19
2.2	42.76	37.42	0.04	6.29	5.52	7.96	16.24	4.90	4.46
2.4	14.22	43.66	0.25	0.60	0.52	0.75	5.40	1.40	0.55
2.6	6.22	46.47	0.02	0.11	0.09	0.14	2.36	0.57	0.81
3.0	2.93	39.07	0.02	0.03	0.03	0.04	1.11	0.32	0.39
3.4	0.00	31.37	0.07	0.00	0.00	0.00	0.00	0.00	0.00
3.6	0.00	21.79	0.03	0.00	0.00	0.00	0.00	0.00	0.00
3.8	0.00	21.25	0.03	0.00	0.00	0.00	0.00	0.00	0.00

The highest p value for 2.0 at% Si in HfO_2 is quite similar to the recently published values of $48\,\mu C\,K^{-1}\,m^{-2}$ and $65\,\mu C\,K^{-1}\,m^{-2}$ by SMITH et al. [319] and MART et al. [194] for 20 nm $Hf_{1-x}Zr_xO_2$ ($x = 0.64$) and 10 nm HfO_2:Si, respectively. Accordingly, the maximum figures of merit are $k^2 = 8.71(156)$, $F_E = 7.64(137)\,J\,m^{-3}\,K^{-1}$, $F_E' = 11.03(198) \times 10^{-12}\,m^3\,J^{-1}$, $F_I = 17.55(105)\,m\,V^{-1}$, $F_V = 6.28(75) \times 10^{-2}\,m^2\,C^{-1}$ and $F_D = 6.19(76)\,m^{3/2}J^{-1/2}$. Compared to other well-known ferro- and pyroelectrics the values of p at room temperature are larger than for single crystal III-V compound semiconductors, such as GaN [128, 201] and AlN [77, 311] and similar to organic semi-crystalline polymers like PVDF [188] and its copolymer P(VDF-TrFE) [188, 208]. Inorganic perovskite-type single crystals, e.g. $LiNbO_3$ [160], $LiTaO_3$ [160] as well as lead-based materials, e.g. modified PZT ceramics and thin films [263, 361, 376] and PMN-PT [306, 340] provide much higher pyroelectric coefficients. Comparing the maximum F_I values (more relevant than F_V for small area elements with comparably low ε_r [361]), a similar tendency as for p is present. In contrast to industry leading $LiTaO_3$ single crystals, HfO_2:Si provides only a third of its F_I and half of its F_V. The exact values of all mentioned materials are given in Appendix D. While the thin film processing of ferroelectric materials can be quite complex, the fabrication of HfO_2 thin films is comparably easy and already well established for CMOS applications. Additionally, the read-out chip might be processed on the same silicon substrate. Different designs of thin film IR sensors are already proposed and summarized by BATRA et al. [12]. Nonetheless, it should be kept in mind that this is just a first assessment without years of intensive optimizations as for other materials. Necessary additional considerations include thermal time constants, low thermal conductance and matching capacity between detector element and attached amplifier chip, all of which are important factors to optimize IR sensors [361]. A first prototype of such a thin film sensor was recently demonstrated by MART et al. [195]. Here, a silicon substrate with deep-trench HfO_2:Si capacitors were fabricated, which drastically increases the active area and improves the FOMs.

6.2.3. Dopant Comparison

As different dopants can induce the ferroelectric properties in HfO_2, also an influence on the pyroelectric properties seems obvious. For this, differently doped samples (Al, Gd, La, Sr and Zr)[30] with doping concentrations yield a maximum remanent polarization were investigated. All thin films had a similar thickness of approximately 10 nm and where polarized with their respective maximum voltage amplitude during a previous hysteresis loop measurement before the pyroelectric characterization. It has to be noted that the dopant concentration is given in cat% here, due to missing at% results via TOF-SIMS. The 2.0 at% HfO_2:Si sample, yielding maximum p and P_R, has a corresponding cationic concentration of 3.7 cat%.

A first assessment of the dopant influence on p and $p(T)$ is shown in Fig. 6.18. Albeit the absolute value of p e.g. at room temperature (see dashed line) is different with respect to the dopant, $p(T)$ remains relatively stable with temperature for Si, Sr and Zr. In contrast to them, the remaining dopants Al, Gd and La show a comparably steeper increase of p.

The comparison of p with the respective P_R at room temperature is given in Fig. 6.19. It is basically expected that large p gives also large P_R. Al, Gd and Sr lead to nearly identical p and P_r, while Zr has a higher p and also a higher P_r. For La, and Si the situation is different. While P_R for La is comparably high, the respective p is quite small. Furthermore,

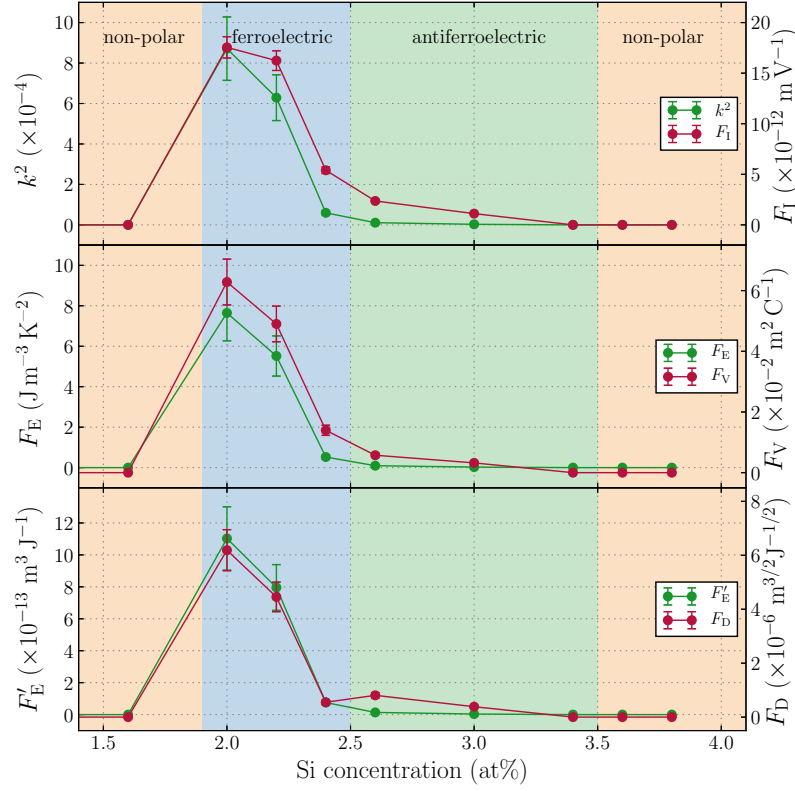---

[30]Thankfully provided by NaMLab Dresden.

Fig. 6.17.: Figures of merit of HfO$_2$:Si for energy harvesting (k^2, F_E, F_E') and IR sensors (F_I, F_V, F_D) depending on the Si concentration at room temperature ($T = 25\,^\circ$C).

the Si-doped sample has a reversed behavior, i.e. the lowest measured P_r gives a nearly equal p as for the highest measured P_r of the La sample.

For the sake of completeness, the temperature course of the remanent polarization is provided in Fig. 6.20 via numerical integration of $p(T)$, again providing the absolute change ΔP_R^* and the absolute value P_R^*. As expected from Fig. 6.18, the rather flat slopes of $P_\mathrm{R}^*(T)$ are dominated by the absolute value of p and not its temperature dependency. Here, 50 cat% HfO$_2$:Zr has the largest slope, but $P_\mathrm{R}^*(T)$ remains again relatively stable in the investigated temperature range for all dopants.

It has to be assumed that although the introduction of different dopants enhances the ferroelectric properties, i.e. the remanent and saturation polarization (see Sec. 5.2.3), this cannot be translated directly to its temperature dependency, i.e. the corresponding pyroelectric coefficient. Beside a dopant influence also microstructural influences, e.g. grain size distribution and its connected phase transition temperature range [115], have to be considered to explain the behavior. Unfortunately, such investigations, e.g. by scanning electron microscopy or gracing incidence X-ray diffraction with a synchrotron radiation source are beyond the scope of this thesis, but should be considered in the future. Especially the fact that two Hf$_{0.5}$Zr$_{0.5}$O$_2$ (50.0 cat% HfO$_2$:Zr) samples with similar P_R of approximately 17 to 18 μC cm^{-2} showed a huge pyroelectric coefficient difference (41 μC K^{-1} m^{-2} and 71 μC K^{-1} m^{-2}, not shown here), suggests a microstructural influence rather than a dopant influence. Simultaneously, extended pyroelectric measurement series are necessary to clearly verify the results and exclude sample to sample variations.
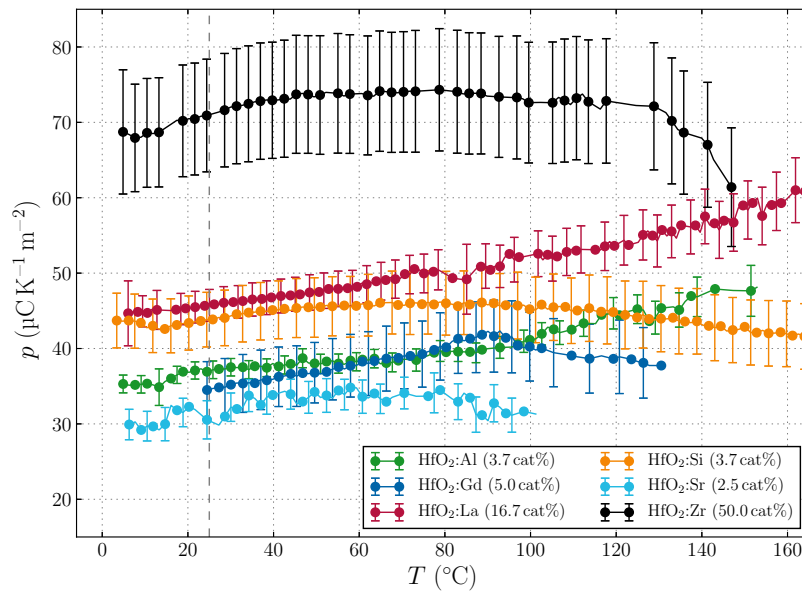
Fig. 6.18.: Comparison of $p(T)$ of differently doped HfO_2 thin films. The dashed line marks the room temperature values shown in Fig. 6.19.
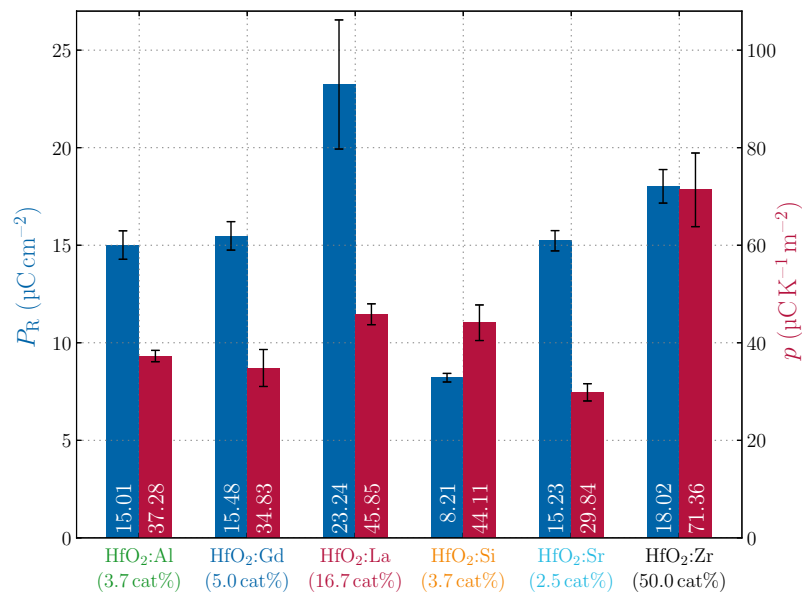

Fig. 6.19.: Correlation of remanent polarization P_R (blue) and pyroelectric coefficient p (red) for differently doped HfO_2.
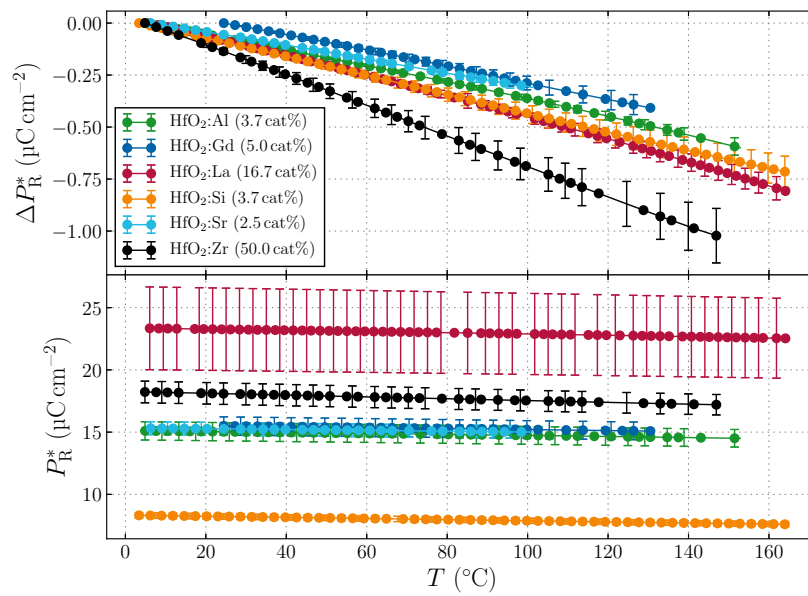
Fig. 6.20.: Top: Absolute change of the remanent polarization ΔP_R^* with respect to temperature T calculated by integrating the data of Fig. 6.18. Bottom: Absolute value of P_R^* using the room temperature values from Fig. 6.19 as offset.

7. Summary and Outlook

Pyroelectric materials as a subgroup of dielectric matter offer a wide field of applications, ranging from traditional and currently most used IR sensor technology to waste heat energy harvesting and chemical catalysis. The pyroelectric coefficient p, as a measure of the polarization change due to temperature changes of non-centrosymmetric and polar crystalline matter, is crucial to assess the performance of a material in a device and, thus, its precise characterization is an indispensable prerequisite.

The quantification of p generally comprises a defined thermal excitation while simultaneously tracking a certain physical quantity, leading to a variety of possible techniques. An overview of approximately 20 different techniques, as outlined in Chapter 3, was provided in order to evaluate and select a suitable measurement method. As it turned out, a systematization by the basic measurement setup and thermal excitation, i.e. constant (static) and varying (dynamic) temperature with time, can be found. Also the evaluation of p and its temperature dependency with regard to the separation of different contributions (primary, secondary and tertiary pyroelectricity), separation of TSC, spatial detection capability, necessity of metallized electrodes and additional necessary physical quantities was given (see Tab. 3.1). It has to be noted that the published review paper [129] during this work represents all quantitative methods published between the 1915 and 2017.

Fig. 7.1 provides a graphical systematization arranging all methods by their basic measurement setup and temperature excitation. Methods involving the detection of electrical quantities can be realized with the first setup type in Fig. 7.1. Also harmonic waveform methods are solely realized with the first type. Only a periodic pulse technique including a charge measurement was not yet reported. The remaining types are either static or ramping methods and use an additional voltage or light source. Techniques using a light source as well as the PyroSPM and SCHEIN method work without metal electrodes on the sample surface. Metal electrodes typically hinder a mapping of p on the nanoscale. The change of the spontaneous polarization P_S, which is measured by static methods, always yields a combination of p_prim and p_sec. Total clamping, i.e. providing constant strain $\overset{2\rightarrow}{e}$, could theoretically eliminate p_sec, but is impractical in reality.

The wide spread occurrence of ramping techniques, as a subset of dynamic methods, is explainable by their simple setup requirements. A uniform heating has to be ensured in order to eliminate p_tert, but also here a combination of p_prim and p_sec is measured. Ramping techniques are prone to a false interpretation of the measured signals, when TSC is present. This is the case for samples with high defect concentrations, e.g. ceramics, polymers, thin films or doped materials. Optical methods may serve as an in-line monitoring tool during the production of pyroelectrics, due to their contactless measurement principle and the avoidance of metallic contacts. The remaining dynamic methods are popular for their capability to separate non-pyroelectric effects. PSM and FLIMM techniques provide the best spatial resolution for a measurement of p down to the nanoscale. The highest spatial resolution was achieved with the periodic pulse method in a scanning probe microscope.
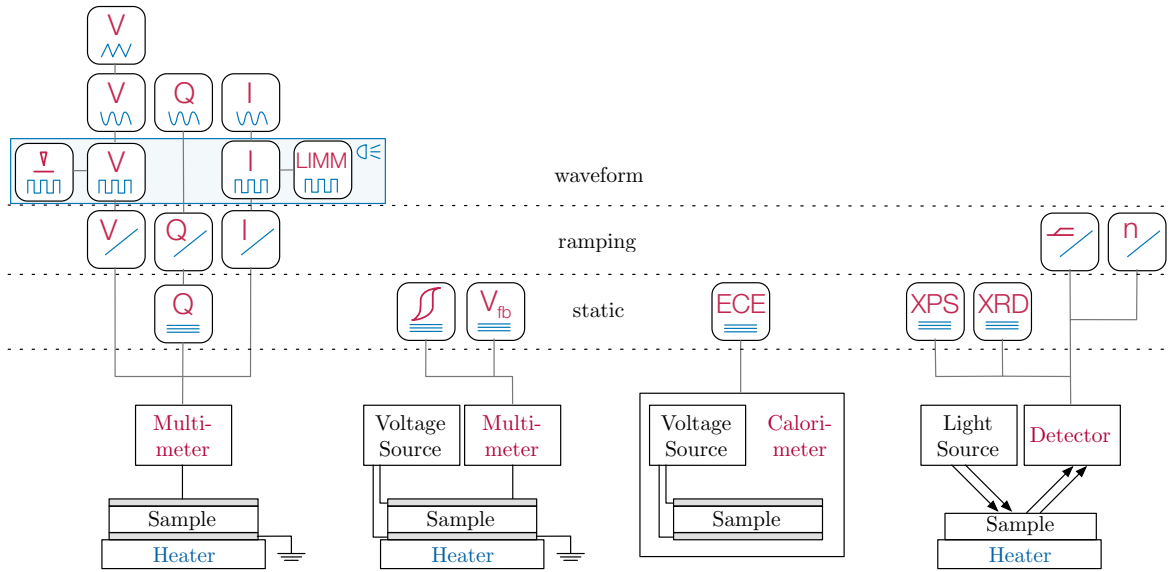
Fig. 7.1.: Systematization of pyroelectric measurement methods using pictographs from Tab. 3.1: All techniques are categorized into four main setups, which differ in the need for metallized electrodes, heater (optical heating is additionally marked by the blue lamp), additional excitation (voltage or light source) and detected signal. Furthermore, the pictographs are aligned according to their temperature profile. The multimeter represents a generalized instrument to measure electrical quantities.

In order to select a suitable measurement technique, material parameters, the occurring contributions to the pyroelectric coefficient and potential disturbing effects have to be considered. Here, Tab. 3.1 and Fig. 7.1 provide possible choices for an eligible choice. The SHARP-GARN and HARTLEY waveform techniques appear attractive, because they satisfy almost all relevant aspects. Furthermore, the low instrumentation and modeling effort and a small number of easily accessible parameters are advantageous, albeit without providing spatial resolution. The capability to separate TSC from the measured signal makes these techniques appropriate for every type of material, i.e. single crystals as well as defect-rich ceramics, polymers and thin films.

An exact measurement of electrical quantities while assuring an accurate thermal excitation was realized in the setup by ERIK MEHNER [207] (see also chapter 4). Here, the SHARP-GARN approach, i.e. measuring the short-circuit current during a sinusoidal temperature stimulation, was employed. Pyroelectric coefficients as low as $10^{-4}\,\mu\mathrm{C\,K^{-1}\,m^{-2}}$ with an error of approx. $5\,\%$ can be detected with this setup. Several instrumental improvements, such as an improved electrical contacting of the sample or a computer controlled high-voltage protection circuit, and foremost the post-processing of the acquired raw data to extract p and its temperature dependency $p(T)$ were the essential contributions, as outlined in Chapter 4. The PYROFIT program bundles these evaluations and also includes other types of measurement principles, e.g. the BYER-ROUNDY method, constant current poling or resistivity/conductivity measurements, which are accessible by the setup.

As it turned out, the imperfections of the heating system, e.g. the non-linearity of the offset temperature, has to be treated in data evaluation by part-wise fitting of the temperature curve. This is especially crucial when measuring over a wide temperature range. Improving the situation need a more sophisticated temperature regulation approach, e.g. the implementation of PID zones for different temperature ranges. In order to achieve a wider temperature range, i.e. enabling higher and lower temperatures, the heating system could to be reworked to include a separate cooling unit, e.g. flowing liquid nitrogen through the heat sink, com-

bined with a resistive heater instead of a PELTIER element. An increased excitation frequency could be possible, when designed as a thin film heater. Recent improvements comprise the measurement of the sample capacity C_S and its loss tangent $\tan\delta$ with an HP 4275A precision LCR meter, providing the relative dielectric permittivity ε_r with respect to temperature T and frequency f. Hence, also investigations of relaxor ferroelectrics, marked by a strong frequency dependency of ε_r, become possible.

As most pyroelectrics are also ferroelectric, the quantification of the remanent polarization P_R is of particular importance, since the temperature dependency of the related spontaneous polarization P_S represents p. This was achieved by extending the pyroelectric characterization setup with fully automated measurements of the ferroelectric hysteresis loop, i.e. the non-linear P-E characteristic. This allows the determination of the remanent polarization P_R and coercive field strength E_C with an accuracy of approximately 12%. Here, the error might be reduced by using a more advanced oscilloscope, a high-resolution lock-in amplifier or digitizer. Instrument communication, data recording and post processing are bundled within the HESMCTRL software. Future upgrades could be a graphical user interface or the merging with the PMC software used for the pyroelectric coefficient measurements. A loop-selective reading of the oscilloscope would allow the tracking of the P-E hysteresis with increasing cycle number, e.g. to investigate the fatigue or wake-up behavior of HfO_2 (see Sec. 5.2) in the future. In order to get the full input voltage drop over the sample, an inverting operational amplifier (see virtual ground method in Fig. 3.4(b)) could be integrated into the electrical circuitry. Altogether, the present setup is a cost-effective alternative to commercially available equipment, e.g. by AIXACCT[31], with comparable specifications. The biggest advantage of the present setup is the possibility of combining the determination of all relevant parameters of ferro- and pyroelectrics, such as $P(T)$ (or $P_R(T)$), $p(T)$, $R(T)$, $\varepsilon(T)$ and $\tan\delta(T)$, within the same device. Furthermore, temperature-dependent investigations of the P-E hysteresis are now possible and, thus, allow a direct comparison of different techniques to determine p.

This setup with its extensions and improvements can be seen as an all-in-one ferroelectric/pyroelectric characterization system. Furthermore, a double beam laser interferometer setup is currently in development, which will pave the way for the quantification of piezoelectric coefficients and, thus, the separation between primary and secondary pyroelectricity.

The described SHARP-GARN setup was utilized to investigate the pyroelectric properties of novel materials in this work. It enabled investigations of the organic polymer polyvinylidene fluoride (PVDF), its copolymer with trifluoroethylene (P(VDF-TrFE)) [208], ceramic solutions of lead magnesium niobate with lead titanate (PMN-PT), and modified single crystalline strontium titanate ($SrTiO_3$) [108]. The main focus of Chapter 5 and 6 lies on the characterization of the free-standing III-V bulk compound semiconductors gallium nitride (GaN) [128] and aluminium nitride (AlN) as well as thin films of the transition metal oxide hafnium oxide (HfO_2) [130].

Motivated by a lack of reliable pyroelectric coefficients for GaN and AlN, which were also preferentially published for thin films, the SHARP-GARN method was used for the first time to measure p of bulk material grown by HVPE and PVT. Here, doping with different elements was applied to compensate the unintentional n-type conductivity in GaN and study the dopant influence on p and $p(T)$ in AlN as well as GaN. At room temperature the obtained values are in good accordance with the few published values and are only slightly affected by the dopant. For GaN, a linear dependency between the measured pyroelectric coefficient

---

[31]https://www.aixacct.com/html/prod/memprods_tf2000E_fe.php (visited on 01st November, 2018)

and the c lattice parameter indicates a lower p with increasing c. Unfortunately, this model does not hold for doped AlN, since Si- and Sc-doped samples show an enlarged p (up to a factor of 2), which do not follow the respective c lattice parameter. Thus, tracking c alone cannot explain the origin of the enhancement of p. From $p(T)$ measurements for GaN and AlN a small temperature dependency of the pyroelectric coefficient is visible, which is in good accordance with theoretical predictions. Here, C- and Fe-doped GaN are an exception as their $p(T)$ dependencies differ, which is explainable by an inhomogeneous doping for GaN:C and non-linear thermally stimulated currents at higher temperatures for GaN:Fe, respectively.

Considering III-N semiconductors for IR sensor and energy harvesting applications, the pyroelectric coefficient and corresponding FOMs are small compared to traditional ferroelectrics and can only slightly be adjusted by structural modification (see Fig. D.1). While doping has only little influence on p, a mixed alloy system provides probably a notable improvement. This is known from the piezoelectric properties and is also valid for p, as shown in this work and recently by KURZ et al. [156] in the $Al_xSc_{1-x}N$ system. A recent ab initio study by THOLANDER et al. [342] suggests an increase of d_{33} up to a factor of nine by mixing AlN, GaN and InN with ScN and YN. From the obtained results, it seems obvious that this holds also for an improvement of p, although there is no experimental proof yet. Here, the change of ε_r is further important, as it also influences the FOMs. As the increase of p is accompanied by a rise of ε_r for ferroelectrics, it would be interesting, if this also holds for pure pyroelectrics (see Sec. 2.6). Another possibility to increase p would be the utilization of strain effects and, thus, pronouncing the secondary and tertiary pyroelectric contribution. Inhomogeneous doping profiles could be a first approach as the results of GaN:C suggest. Using this, differently doped layers, doping concentration gradients or stacks produced by different growth methods (e.g. HVPE and MOVPE) to produce strain inside the material might give an insight. Also, the promising DFPT approaches could serve as a first theoretical assessment of this theory. In contrast to the overall small p, the pyroelectric property is expected to persist up to very high temperatures, preferably the decomposition temperature, which could be investigated with an upcoming setup providing an even wider temperature range.

The second material system, which was investigated in this work, was doped thin films of hafnium oxide, because they gained an increased scientific interest due to the discovery of a ferroelectric modification. Here, doping the material with various elements is currently seen as the main driver for the formation of a polar orthorhombic phase. As a first step to investigate the related pyroelectric properties of the material, measurements of p and $p(T)$ were conducted for Si-doped HfO_2 demonstrating the capability of the SHARP-GARN technique and setup also for thin films. Dynamic P-E hysteresis measurements and the electric field-free determination of the pyroelectric coefficient p were used to correlate the polar properties to the phase fractions of the material. Pronounced ferro- and pyroelectric properties emerge for Si concentrations between 1.9 at% and 2.5 at%. Maximum values of $p = 46.2(61)\,\mu C\,K^{-1}\,m^{-2}$ and $P_R = 8.21(22)\,\mu C\,cm^{-2}$ were found for a Si concentration of 2.0 at%. Furthermore, a good correlation between the orthorhombic phase fraction and the pronounced polar properties was shown. Deviations from previously published values of p by measuring temperature-dependent hysteresis loops likely stem from an incomplete polarization. Although the corresponding FOMs (see Fig. D.1) are lower than perovskite-like ferroelectrics, they are better than those for III-N semiconductors and comparable to organic PVDF and its copolymer P(VDF-TrFE). Temperature-dependent measurements of p in the range of 0 to $170\,°C$ reveal a nearly constant behavior of the pyroelectric coefficient and remanent polarization. Compared to other dopants a stable ferroelectric phase is harder to establish in silicon-doped HfO_2, but its polarization changes only little in the typical operation temperature range of a potential device. This, together with the well-established fabrication

process, makes HfO_2 a promising candidate for integrated IR sensors as recently shown by MART *et al.*. Here, a silicon substrate with deep-trench structures drastically increases the active area and, thus, improves the FOMs [195].

Pyroelectric investigations of other dopants such as Al, Gd, La, Sr and Zr show that enhanced ferroelectric properties cannot be easily transferred to the corresponding pyroelectric coefficient. This is especially pronounced for HfO_2:La with a maximum P_R of $23.24\,\mu C\,cm^{-2}$, but a p of only $45.85\,\mu C\,K^{-1}\,m^{-2}$, which is similar to HfO_2:Si offering a P_R of only $8\,\mu C\,cm^{-2}$. Here, studying microstructural influences, e.g. the grain size distribution, may explain the different behavior. Unfortunately, such investigations were beyond the scope of this work as well as extended pyroelectric measurement series to exclude sample-to-sample variations. Understanding the dopant influence on p could further improve potential applications beyond the memory devices. Also measurements of the piezoelectric properties should be included in the future to estimate the contribution of secondary pyroelectricity to the total pyroelectric coefficient of the HfO_2 thin films. In accordance with the results of HfO_2:Si, the remanent polarization changes only little with temperature for all dopants. This is beneficial for potential applications, as the the polar properties remains relatively stable, even at elevated temperatures.

A. Pyroelectric Current and Phase under Periodic Thermal Excitation

A.1. Two-side Heating

Here, a detailed derivation of the frequency influence on the current amplitude A_I and phase shift ϕ of dynamic methods (Sec. 3.3), as introduced by DIAS *et al.* [62], is presented.

Starting point is a pyroelectric sheet, with thickness d and surface area A, sandwiched between two heating elements. If the sample thickness is small compared to its diameter, the spread of temperature T can be solved using the one dimensional heat conduction equation with x perpendicular to the surface of the sample:

$$\frac{\partial T}{\partial t} = a \frac{\partial^2 T}{\partial^2 x}. \tag{A.1}$$

The thermal diffusivity $a = \lambda/\rho \cdot c_p$ is defined by heat conductivity λ, mass density ρ and specific heat capacity c_p. The solution of this differential equation is the space- and time-dependent temperature distribution $T(x,t)$ relative to the surrounding temperature. For a setup with two heaters, the following boundary condition is valid:

$$T(0,t) = T(d,t) = T_0 \cdot e^{\mathrm{i}\omega_0 t}, \tag{A.2}$$

describing a periodic temperature stimulation with amplitude T_0 and angular frequency $\omega_0 = 2\pi f$, given by the frequency f. For simplification of the solution, the dimensionless space parameter

$$y = \frac{x}{d} \tag{A.3}$$

and the complex modified circular frequency

$$\omega = (1 + \mathrm{i})\sqrt{\frac{\omega_0}{2\alpha}} \quad \text{with} \quad \alpha = \frac{a}{d^2} \tag{A.4}$$

are introduced. The solution consists of a periodic and a transient term. The latter can be neglected because it vanishes quickly, so that only the periodic part has to be considered. The ansatz

$$\begin{aligned} T(y,t) &= T_\omega(y) \cdot e^{\mathrm{i}\omega_0 t} \\ &= [A\cosh(\omega y) + B\sinh(\omega y)] \cdot e^{\mathrm{i}\omega_0 t} \end{aligned} \tag{A.5}$$

separates the time-dependent oscillation $e^{\mathrm{i}\omega_0 t}$ from the space-dependent part $T_\omega(y)$ introducing parameters A and B. Inserting the boundary conditions (A.2) into Eq. (A.5) reveals the solution of the differential equation:

$$T(y,t) = T_0 \left[\cosh(\omega y) - \tanh\left(\frac{\omega}{2}\right)\sinh(\omega y) \right] \cdot e^{\mathrm{i}\omega_0 t}. \tag{A.6}$$

A graphical visualization is given in Fig. A.1(a).

The calculation of the pyroelectric current I is possible by determining the spatially averaged temperature $\bar{T}$ given by

$$\bar{T} = T_0 \int_0^1 \left[\cosh(\omega y) - \tanh\left(\frac{\omega}{2}\right) \sinh(\omega y) \right] \mathrm{d}y \cdot e^{\mathrm{i}\omega_0 t}, \tag{A.7}$$

$$\bar{T} = \frac{2T_0}{\omega} \tanh\left(\frac{\omega}{2}\right) \cdot e^{\mathrm{i}\omega_0 t}. \tag{A.8}$$

From $I = p \cdot A \cdot \mathrm{d}T/\mathrm{d}t$, the current is given by:

$$\begin{aligned} I &= pA \frac{\partial \bar{T}}{\partial t} \\ &= I_\omega \cdot e^{\mathrm{i}\omega_0 t} \\ &= 2pAT_0 \alpha\omega \tanh\left(\frac{\omega}{2}\right) \cdot e^{\mathrm{i}\omega_0 t}, \end{aligned} \tag{A.9}$$

in which $\alpha\omega = {}^{\mathrm{i}\omega_0}/_\omega$ was used. Thus, the current response consists of an oscillation ($e^{\mathrm{i}\omega_0 t}$) and an ω-dependent part (I_ω), which is analogous to Eq. (A.6). For further simplification

$$z = \sqrt{\frac{\omega_0}{2\alpha}} = \sqrt{\frac{\omega_0 d^2}{2a}} = \sqrt{\frac{\pi f d^2}{a}} \tag{A.10}$$

is introduced, leading to the following absolute values:

$$|\omega| = \sqrt{2} \cdot z, \tag{A.11}$$

$$\left| \tanh\left(\frac{\omega}{2}\right) \right| = \frac{\sqrt{\sinh^2(z) + \sin^2(z)}}{\cosh(z) + \cos(z)}, \tag{A.12}$$

$$|I_\omega| = 2\sqrt{2} \cdot pAT_0 \alpha z \cdot \frac{\sqrt{\sinh^2(z) + \sin^2(z)}}{\cosh(z) + \cos(z)}. \tag{A.13}$$

If z is known, see Eq.(A.10), the pyroelectric coefficient p can be calculated from the measured current amplitude $|I_\omega|$ (see Fig. A.1(c)). The arguments of the complex numbers are:

$$\arg(\omega) = \arctan\left(\frac{z}{z}\right) = \frac{\pi}{4} = 45°, \tag{A.14}$$

$$\arg\left(\tanh\left(\frac{\omega}{2}\right)\right) = \arctan\left(\frac{\sin(z)}{\sinh(z)}\right), \tag{A.15}$$

$$\arg(I_\omega) = 45° + \arctan\left(\frac{\sin(z)}{\sinh(z)}\right). \tag{A.16}$$

A graphical illustration is shown in Fig. A.1(d)

Because $\arg(I_\omega)$ is available from the measurement and not dependent on p, one can gain additional information about the thermal diffusivity a (through z) by the same experiment used to determine $|I_\omega|$. If it is possible to determine $\arg(I_\omega)$ and $|I_\omega|$ with good precision, p and a follow directly. For this, z has to be determined from $\arg(I_\omega) = \phi$ using Eq. (A.16) by

$$\tan(\phi - 45°) = \frac{\sin(z)}{\sinh(z)}, \tag{A.17}$$

which is usually only solvable by graphical or numerical methods. The temperature conductivity

$$a = \frac{\pi f d^2}{z^2} \tag{A.18}$$

can then be determined from z. The pyroelectric coefficient follows from the current amplitude $|I_\omega|$ using Eq. (A.13):

$$
\begin{aligned}
p &= \frac{|I_\omega|}{2\sqrt{2} \cdot A T_0 \alpha \omega \cdot \frac{\sqrt{\sinh^2(z) + \sin(z)}}{\cosh(z) + \cos(z)}} \\
&= \frac{|I_\omega|}{\sqrt{2} \cdot A T_0 \frac{\omega_0}{z} \cdot \frac{\sqrt{\sinh^2(z) + \sin(z)}}{\cosh(z) + \cos(z)}}.
\end{aligned} \tag{A.19}
$$

A.2. One-side Heating

The heating from one side is typically more practical than a two-side heating, changing the boundary conditions in Eq. (A.2). For the simplest case of a sample isolated from the surrounding at the top, the boundary conditions are

$$T(0, t) = T_0 \cdot e^{i\omega_0 t} \quad \text{and} \quad \frac{\partial T}{\partial x}(d, t) = 0. \tag{A.20}$$

If the heat transfer on the non-heated side is dominated by convection, radiation or heat conduction (e.g. via an electrode), the second boundary condition at $x = d$ has to be adjusted appropriately. Inserting the new boundary conditions (A.20) into the general solution (A.5) gives

$$
\begin{aligned}
T(y, t) &= T_\omega(y) \cdot e^{i\omega_0 t} \\
&= T_0[\cosh(\omega y) - \tanh(\omega)\sinh(\omega y)] \cdot e^{i\omega_0 t}.
\end{aligned} \tag{A.21}
$$

A graphical visualization is shown in Fig. A.1(b).
The determination of the pyroelectric current is analogous to the two-sided case and given by

$$
\begin{aligned}
I &= pA\frac{\partial \bar{T}}{\partial t} \\
&= I_\omega \cdot e^{i\omega_0 t} \\
&= pAT_0 \alpha \omega \tanh(\omega) \cdot e^{i\omega_0 t}.
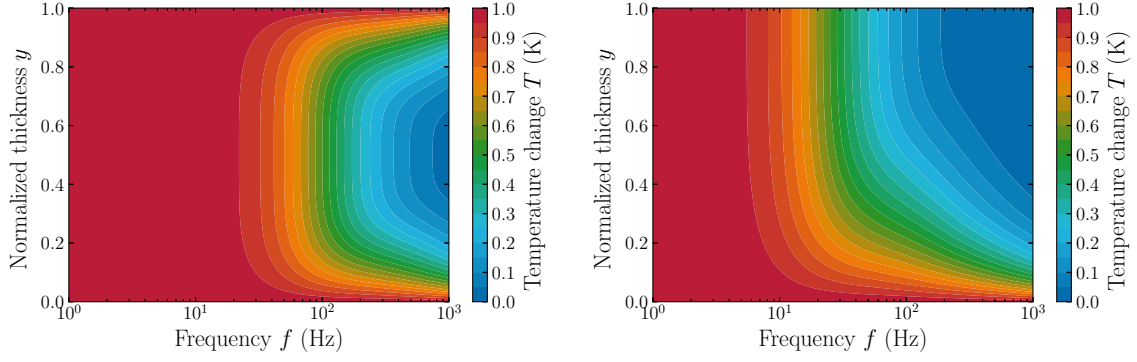\end{aligned} \tag{A.22}
$$

Amplitude and phase of the current signal with respect to the temperature are

$$|I_\omega| = \sqrt{2} \cdot pAT_0 \alpha z \cdot \frac{\sqrt{\sinh^2(2z) + \sin^2(2z)}}{\cosh(2z) + \cos(2z)}, \tag{A.23}$$

$$\arg(I_\omega) = 45° + \arctan\left(\frac{\sin(2z)}{\sinh(2z)}\right). \tag{A.24}$$
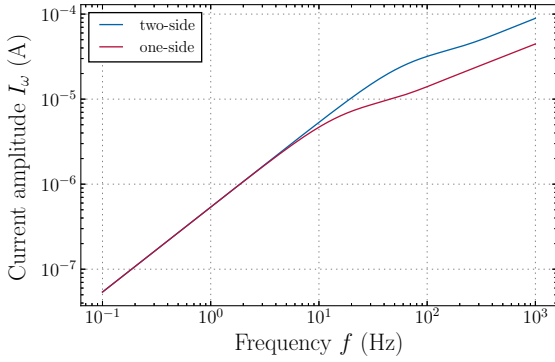
After a measurement, z has to be determined from $\arg(I_\omega) = \phi$ by

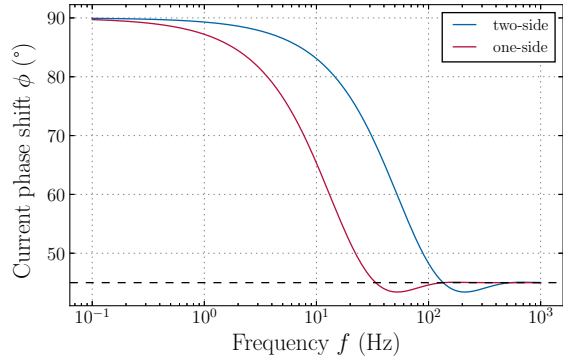$$\tan(\phi - 45°) = \frac{\sin(2z)}{\sinh(2z)}. \tag{A.25}$$

(a) Solution of the heat conduction equation for two-side heating.

(b) Solution of the heat conduction equation for one-side heating.

(c) Calculated pyroelectric current amplitude.

(d) Calculated current phase.

Fig. A.1.: Simulated temperature distribution, pyroelectric current amplitude and phase shift with respect to the excitation frequency f for two- and one-sided heating of LiTaO$_3$. Used parameters: $d = 0.1\,\mathrm{mm}$, $A = 4.9 \times 10^{-4}\,\mathrm{m}^2$, $a = 2.5 \times 10^{-7}\,\mathrm{m}^2\,\mathrm{s}^{-1}$, $T_0 = 1\,\mathrm{K}$ and $p = 176\,\mathrm{\mu C\,m}^{-2}\,\mathrm{K}^{-1}$.

Rearranging Eq. (A.23) gives the pyroelectric coefficient:

$$
\begin{aligned}
p &= \frac{|I_\omega|}{\sqrt{2} \cdot A T_0 \alpha z \cdot \frac{\sqrt{\sinh^2(2z)+\sin^2(2z)}}{\cosh(2z)+\cos(2z)}} \\
&= \frac{|I_\omega|}{\sqrt{2} \cdot A T_0 \frac{\omega_0}{2z} \frac{\sqrt{\sinh^2(2z)+\sin^2(2z)}}{\cosh(2z)+\cos(2z)}}.
\end{aligned}
\tag{A.26}
$$

A.3. Comparison and Maximum Excitation Frequency

A comparison between two-side and one-side heating is exemplified for a 0.1 mm thick LiTaO$_3$ single crystal as shown in Fig. A.1. The deviation of the phase shift ϕ towards 45° for growing frequencies is happening earlier in the case of one-side heating. According to DIAS *et al.* the estimation of the maximum frequency for a homogeneous heating is given by $\omega_0 \approx 2\alpha$, following from Eq. (A.4). Then, the maximum frequency is

$$
f_{\max} \ll \frac{\omega_0}{2\pi} = \frac{\alpha}{\pi} = \frac{a}{\pi d^2} = \frac{\lambda}{\pi \rho c_p d^2}.
\tag{A.27}
$$

Tab. A.1 gives thermodynamic parameters, which are necessary to estimate $f_{\max}$ for several ferro- and pyroelectric materials, as plotted in Fig. 3.1. Due to the attenuation of the heat

Tab. A.1.: Material parameters for the calculation of f_{max}, in which λ, ρ and c_p are the thermal conductivity, mass density and specific heat capacity, respectively.

Material	λ (W K^{-1} m^{-1})	ρ (g/cm^3)	c_p (J kg^{-1} K^{-1})	Reference
BaTiO$_3$	6.0	6.06	527.00	[333]
LiNbO$_3$	5.6	4.64	627.60	[7]
LiTaO$_3$	4.6	7.45	251.04	[7]
PbTiO$_3$	4.8	7.90	380.00	[284, 337]
Pb(Zr$_x$Ti$_{1-x}$)O$_3$	1.10	7.80	350.00	[256]
PVDF	0.2	1.76	1120.00	[92]
C$_6$H$_{17}$N$_3$O$_{10}$S	1.663	0.5192	1297.91	[183]
(Sr$_{1-x}$Ba$_x$)Nb$_2$O$_6$	1.15	5.33	480.00	[41]
GaN	130.0	6.15	490.00	[126]
AlN	285.0	3.23	600.0	[126]

wave, non-uniform heating appears for $\omega_0 \ll 2\alpha$, which can also be exploited, e.g. in LIMM based methods.

Unfortunately, this approximation does also apply for one-side heating, yielding the same expression as Eq. (A.27), because only ω is considered. Examining the dependency of ϕ on the frequency f gives a more reasonable determination of f_{max} for both cases. According to Eq. (A.10), f is contained within z in Eq. (A.17) and (A.25), which cannot be solved analytically. An approximate solution can be provided with the help of a TAYLOR series expansion aborted after the third order, given by

$$\tan(\phi - 45°) = \frac{\sin(z)}{\sinh(z)} \approx \frac{z - \frac{z^3}{3!}}{z + \frac{z^3}{3!}} = \frac{6 - z^2}{6 + z^2}, \tag{A.28}$$

for the two-side and

$$\tan(\phi - 45°) = \frac{\sin(2z)}{\sinh(2z)} \approx \frac{2z - \frac{8z^3}{3!}}{2z + \frac{8z^3}{3!}} = \frac{3 - 2z^2}{3 + 2z^2}, \tag{A.29}$$

for the one-side heating. Rearranging Eq. (A.28) and (A.29) for z yields an expression for f, again for two-side:

$$z = \sqrt{6 \cdot \frac{1 - \tan(\phi - 45°)}{1 + \tan(\phi - 45°)}} = \sqrt{6 \cdot \cot\phi} \quad \rightarrow \quad f = \frac{az^2}{\pi d^2} = \frac{6a}{\pi d^2} \cdot \cot\phi \tag{A.30}$$

and one-side heating:

$$z = \sqrt{\frac{3}{2} \cdot \frac{1 - \tan(\phi - 45°)}{1 + \tan(\phi - 45°)}} = \sqrt{\frac{3}{2} \cdot \cot\phi} \quad \rightarrow \quad f = \frac{az^2}{\pi d^2} = \frac{3a}{2\pi d^2} \cdot \cot\phi. \tag{A.31}$$

By comparing Eq. (A.30) and (A.31), it is apparent that the frequency for two-side heating is four times the frequency of a one-side heating, which is plausible from Fig. A.1(d). For the determination of f_{max} a minimal allowable phase ϕ has to be chosen, because the optimum of $\phi = 90°$ leads to $z = f = 0$. For $\phi = 89°$ the maximum frequency is given by

$$f_{\mathrm{max,two\text{-}side}} = 0.1046 \cdot \frac{a}{\pi d^2} \quad \text{and} \quad f_{\mathrm{max,one\text{-}side}} = 0.0262 \cdot \frac{a}{\pi d^2}. \tag{A.32}$$

Comparing these frequency limits with $f_{\mathrm{max}} = \frac{a}{\pi d^2}$, obtained by DIAS *et al.* (Ref. [62]), the actual maximum frequency is two orders of magnitude lower. This is in accordance with practical observations in the setup described in Chapter 4.

B. Loss Current Correction for Shunt Method

According to SCOTT the charge Q obtained from an electrical hysteresis measurement is composed of a polarization and an ohmic part [304]:

$$Q = \int I \; \mathrm{d}t = P \cdot A + \sigma \cdot E \cdot A \cdot t, \tag{B.1}$$

in which P is the material polarization, A the electrode area, σ the electrical conductivity, E the applied electric field and t the measurement time. The loss current I_{loss} is contained in the last term:

$$I_{\mathrm{loss}}(t) = \sigma \cdot E(t) \cdot A = \frac{V_{\mathrm{in}}(t)}{R_{\mathrm{S}}}, \tag{B.2}$$

in which V_{in} and R_{S} are the applied input voltage and the sample resistance of the ferroelectric. For AC signals with sample capacity C_{S} and sample resistance R_{S} in parallel, the dielectric loss is given from the real and imaginary part of the impedance Z:

$$\tan\delta = \frac{\mathrm{Im}(Z)}{\mathrm{Re}(Z)} = \frac{\mathrm{Im}(Z)}{R_{\mathrm{S}}} \tag{B.3}$$

For a single capacity the imaginary part is given by:

$$\mathrm{Im}(Z) = \frac{1}{\omega C_{\mathrm{S}}}, \tag{B.4}$$

where $\omega = 2\pi f$ is the angular frequency, which can be obtained from the driving frequency f of the input voltage signal $V_{\mathrm{in}}(t)$. Combining Eq. (B.2), (B.3), (B.4), and using that $\mathrm{Re}(Z) = R_{\mathrm{S}}$, the loss current is given by:

$$I_{\mathrm{loss}}(t) = V_{\mathrm{in}}(t) \cdot 2\pi f \cdot C_{\mathrm{S}} \cdot \tan\delta. \tag{B.5}$$

C. Conductivity Correction

This section provides a derivation of Eq. (3.4) in Sec. 3.3.5 for correcting the intrinsic electrical conduction ρ_S of the sample by previously measuring the sample resistance R_S and capacity C_S as shown by WHATMORE *et al.* [360, 362].

The pyroelectric material is modelled as a current source I_S in parallel with the sample resistance R_S and capacity C_S, as visualized in Fig. C.1. Applying KIRCHHOFF's circuit laws, i.e. the sum of all currents in a point and the sum of all voltages in a loop are zero, the total current I, measured with an electrometer (equivalent to an amperemeter with input resistance R_E) and the voltages at each element are given by:

$$I - I_S - I_{C_S} - I_{R_S} = 0, \tag{C.1}$$
$$U_{R_E} + U_{R_S} = 0, \tag{C.2}$$
$$U_{R_E} + U_{C_S} = 0. \tag{C.3}$$

The voltage drop U_{R_E} over the input resistance of the electrometer is given by

$$U_{R_E} = I \cdot R_E. \tag{C.4}$$

Following Eq. (C.1), the sample current I_S due to the pyroelectric effect can be written as:

$$I_S = I - I_{C_S} - I_{R_S} \tag{C.5}$$
$$= I - \frac{U_{C_S}}{Z_{C_S}} - \frac{U_{R_S}}{R_S}. \tag{C.6}$$

The voltages over the sample capacity and resistance can be replaced by combining Eq. (C.4) with Eq. (C.2) and (C.3). Furthermore, the impedance of the capacitor is given by $Z_{C_S} =$
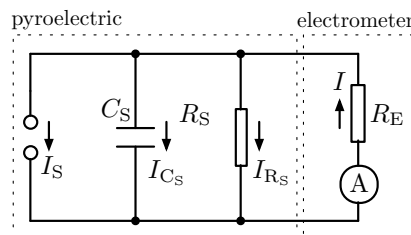

Fig. C.1.: Equivalent circuit of a pyroelectric material connected to an electrometer measuring current.

$-i/\omega C_{\mathrm{S}}$, in which ω is the circular frequency given from the measurement frequency, e.g. frequency of the temperature oscillation. Then, Eq. (C.6) can be written as:

$$I_{\mathrm{S}} = I + \frac{I \cdot R_{\mathrm{E}}}{Z_{C_{\mathrm{S}}}} + \frac{I \cdot R_{\mathrm{E}}}{R_{\mathrm{S}}} \tag{C.7}$$

$$= I - \frac{I \cdot R_{\mathrm{E}} \cdot \omega C_{\mathrm{S}}}{i} + \frac{I \cdot R_{\mathrm{E}}}{R_{\mathrm{S}}} \tag{C.8}$$

$$= I + iIR_{\mathrm{E}}\omega C_{\mathrm{S}} + \frac{IR_{\mathrm{E}}}{R_{\mathrm{S}}} \tag{C.9}$$

$$= I \left[\left(1 + \frac{R_{\mathrm{E}}}{R_{\mathrm{S}}} \right) + i\omega R_{\mathrm{E}} C_{\mathrm{S}} \right] \tag{C.10}$$

Thus, the absolute value of the sample current I_{S} is given by:

$$|I_{\mathrm{S}}| = |I| \cdot \sqrt{\left(1 + \frac{R_{\mathrm{E}}}{R_{\mathrm{S}}} \right)^2 + (\omega R_{\mathrm{E}} C_{\mathrm{S}})^2}. \tag{C.11}$$

Due to the capacity C_{S}, an additional phase shift ϕ_C may occur, which is given from the real and imaginary part by:

$$\tan(\phi_{I_{\mathrm{S}}} - \phi_I) = \tan \phi_C = \frac{\omega R_{\mathrm{E}} C_{\mathrm{S}}}{1 + \frac{R_{\mathrm{E}}}{R_{\mathrm{S}}}}, \tag{C.12}$$

which approaches zero in case of small R_{E}, ω or C_{S} or in the case of large R_{S}.

The square root expression for the pyroelectric current in Eq. (C.11) is translating directly to the pyroelectric coefficient p [360], using sample area A and temperature amplitude T_{Amp}:

$$p = \frac{|I_{\mathrm{S}}|}{\omega A T_{\mathrm{Amp}}} \tag{C.13}$$

$$= \frac{|I| \sin \phi}{\omega A T_{\mathrm{Amp}}} \sqrt{\left(1 + \frac{R_{\mathrm{E}}}{R_{\mathrm{S}}} \right)^2 + (\omega R_{\mathrm{E}} C_{\mathrm{S}})^2}, \tag{C.14}$$

$$= p_{\mathrm{meas}} \sqrt{\left(1 + \frac{R_{\mathrm{E}}}{R_{\mathrm{S}}} \right)^2 + (\omega R_{\mathrm{E}} C_{\mathrm{S}})^2} \approx p_{\mathrm{meas}} \left(1 + \frac{R_{\mathrm{E}}}{R_{\mathrm{S}}} \right). \tag{C.15}$$

In most practical cases, the second part of the correction depending on the sample capacity C_{S} can be neglected. The dependency of the measured pyroelectric coefficient p_{meas} on R_{S} is shown in Fig. C.2 for LiNbO$_3$. When the sample resistance R_{S} matches the input resistance of the electrometer R_{E}, only half of the actual pyroelectric coefficient can be measured ($p/2$ in Fig. C.2). For R_{S} below R_{E}, the measured pyroelectric coefficient tends to decreases linearly. Providing an electrometer with low input resistance allows low sample resistances, i.e. a difference of at least two orders of magnitude between R_{E} and R_{S} should be sufficient for accurate measurements of p without corrections. The input resistance R_{E} is often provided in terms of a voltage burden of the used electrometer [341], which further depends on the used measurement range.

WHATMORE *et al.* did not consider the phase shift ϕ between current and temperature due to thermally stimulated currents, which thus was added in Eq. (C.14). Finally, the total phase shift is a combination of ϕ and ϕ_C.
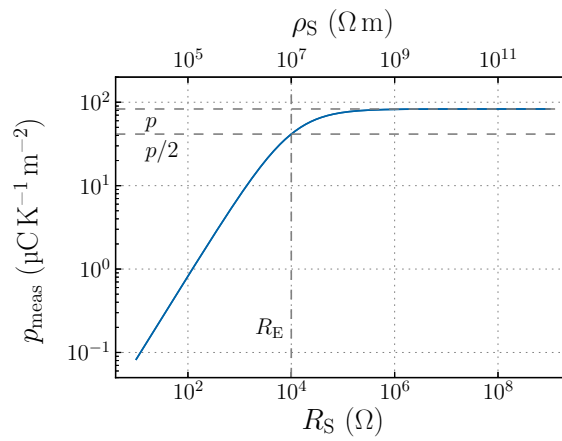
Fig. C.2.: Simulated measurement of the pyroelectric coefficient p_{meas} with respect to the sample resistance R_{S}. The simulated $\mathrm{LiNbO_3}$ thin film has an area of $1\,\mathrm{cm}^2$, a thickness of $100\,\mathrm{nm}$, an ideal pyroelectric coefficient of $p = 83\,\mathrm{\mu C\,K^{-1}\,m^{-2}}$ [160], a dielectric permittivity of $\varepsilon_{\mathrm{r}} = 29$, and is measured at a frequency of $10\,\mathrm{mHz}$. The input resistance $R_{\mathrm{E}} = 10^4\,\Omega$ is provided by the voltage burden [341] of the used electrometer.

D. Comparison of Pyroelectric Figures of Merit

Fig. D.1 and Tab. D.1 summarizes figures of merit of typical pyro- and ferroelectrics. The values are calculated from the given material parameters. In cases where no C_E was given (PMN-PT) it was calculated from the given F_I or F_V or from additional literature (GaN and AlN).
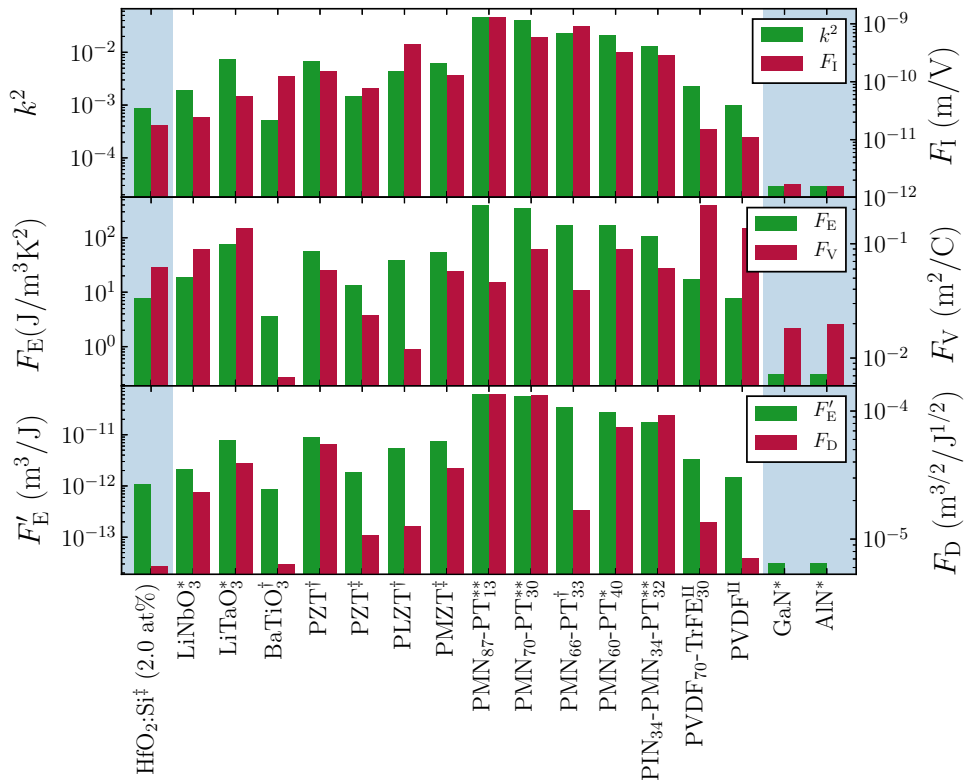
Fig. D.1.: Comparison of figures of merit of selected pyroelectric materials. The corresponding values and references can be found in Tab. D.1.

Tab. D.1.: Figures of merit of selected pyroelectric materials.

Material	C_E ×10^6 (J m^-3 K^-1)	$|p|$ ×10^-6 (C K^-1 m^-2)	ε_r	$\tan\delta$	k^2 ×10^-4	F_E (J m^-3 K^-2)	F_E' ×10^-13 (m^3 J^-1)	F_I ×10^-12 (m V^-1)	F_V ×10^-2 (m^2 C^-1)	F_D ×10^-6 (m^3/2 J^-1/2)	Ref.
AlN*	3.15	5.0	9.1	–	0.294	0.309	0.310	1.585	1.959	–	[44, 151, 311]
BaTiO$_3$†	2.06	260	2100	0.021	5.31	3.64	8.60	126.48	0.68	6.42	[58]
GaN*	3.15	5.3	10.4	–	0.290	0.305	0.307	1.680	1.825	–	[10, 56, 128]
HfO$_2$:Si‡ (2.0 mol%)	2.63	46.22	31.55	0.03	8.71	7.65	11.03	17.55	6.28	6.19	[130]
LiNbO$_3$*	2.92	72	31.4	0.004	19.14	18.65	21.82	24.63	8.86	23.36	[83, 366]
LiTaO$_3$*	3.20	180	47	0.005	72.99	77.86	76.03	56.25	13.52	39.00	[263]
PLZT† (8/40/60)	2.64	1200	4285	0.034	43.05	37.96	54.24	453.65	1.20	12.63	[37]
PMZT‡	2.70	352	255	0.006	60.98	54.88	75.28	130.37	5.77	35.42	[376]
PMN$_{70}$-PT$_{30}$**	2.49	1470	714	0.003	411.6	341.82	550.64	590.00	9.00	133.00	[340]
PMN$_{67}$-PT$_{33}$†	2.23	2007	2618	0.122	233.7	173.76	349.11	899.55	3.88	16.92	[71]
PVDF$_{70}$-TrFE$_{30}$ II	2.30	35	8.0	0.018	22.56	17.29	32.69	15.22	21.48	13.48	[148, 231]
PVDF II	2.30	25	9.0	0.030	10.23	7.84	14.83	10.87	13.64	7.03	[263]
PZT†	2.50	380	290	0.003	67.49	56.24	89.98	152.00	5.92	54.77	[263]
PZT‡	2.70	211	372	0.016	15.02	13.52	18.54	78.15	2.37	10.77	[376]

* single crystal with {001} or {0001} orientation
** single crystal with {111} orientation
† ceramic
‡ thin film
II polymer

Bibliography

[1] S. C. Abrahams. "Structurally based prediction of ferroelectricity in inorganic materials with point group 6*mm*". In: *Acta Crystallographica Section B* B44.6 (1988), pp. 585–595. DOI: 10.1107/S0108768188010110.

[2] S. C. Abrahams. "Structurally based predictions of ferroelectricity in seven inorganic materials with space group *Pba*2 and two experimental confirmations". In: *Acta Crystallographica Section B* B45 (1989), pp. 228–232. DOI: 10.1107/S0108768189001072.

[3] S. C. Abrahams, S. K. Kurtz, and P. B. Jamieson. "Atomic displacement relationship to Curie temperature and spontaneous polarization in displacive ferroelectrics". In: *Physical Review* 172 (1968), pp. 551–553. DOI: 10.1103/PhysRev.172.551.

[4] W. Ackermann. "Beobachtungen über Pyroelektrizität in ihrer Abhängigkeit von der Temperatur". In: *Annalen der Physik* 351.2 (1915), pp. 197–220. DOI: 10.1002/andp.19153510203.

[5] M. Acosta, N. Novak, V. Rojas, et al. "BaTiO$_3$-based piezoelectrics: Fundamentals, current status, and perspectives". In: *Applied Physics Reviews* 4.4, 041305 (2017). DOI: 10.1063/1.4990046.

[6] M. Alexe, C. Harnagea, D. Hesse, et al. "Polarization imprint and size effects in mesoscopic ferroelectric structures". In: *Applied Physics Letters* 79.2 (2001), pp. 242–244. DOI: 10.1063/1.1385184.

[7] AlmaOptics. *Crystals.* URL: http://www.almazoptics.com/material.htm (visited on 06/22/2018).

[8] H. Amano, M. Kito, K. Hiramatsu, et al. "P-Type Conduction in Mg-Doped GaN Treated with Low-Energy Electron Beam Irradiation (LEEBI)". In: *Japanese Journal of Applied Physics* 28.Part 2 (1989), pp. L2112–L2114. DOI: 10.1143/JJAP.28.L2112.

[9] M. Baldauf, T. Hammer, S. Kosse, et al. "Verfahren zur Spaltung von Wasser und Vorrichtung zum Spalten von Wasser". Pat. (DE). WO2012110354 A1. 2012.

[10] A. S. Barker and M. Ilegems. "Infrared Lattice Vibrations and Free-Electron Dispersion in GaN". In: *Physical Review B* 7 (1973), pp. 743–750. DOI: 10.1103/PhysRevB.7.743.

[11] A. T. Bartic, D. J. Wouters, H. E. Maes, et al. "Preisach model for the simulation of ferroelectric capacitors". In: *Journal of Applied Physics* 89.6 (2001), pp. 3420–3425. DOI: 10.1063/1.1335639.

[12] A. K. Batra and M. D. Aggarwal. *Pyroelectric Materials.* Vol. PM231. Infrared Detectors, Particle Accelerators, and Energy Harvesters. SPIE, 2013. ISBN: 9780819493316.

[13] S. Bauer and B. Ploss. "A heat wave method for the measurement of thermal and pyroelectric properties of pyroelectric films". In: *Ferroelectrics* 106 (1990), pp. 393–398. DOI: 10.1080/00150199008214615.

[14] S. Bauer and B. Ploss. "A method for the measurement of the thermal, dielectric, and pyroelectric properties of thin pyroelectric films and their application for integrated heat sensors". In: *Journal of Applied Physics* 68.12 (1990), pp. 6361–6367. DOI: 10.1063/1.346882.

[15] S. Bauer and B. Ploss. "Polarization distribution of thermally poled PVDF films, measured with a heat wave method (LIMM)". In: *Ferroelectrics* 118 (1991), pp. 363–378. DOI: 10.1080/00150199108014772.

[16] F. Bechstedt, U. Grossner, and J. Furthmüller. "Dynamics and polarization of group-III nitride lattices: A first-principles study". In: *Physical Review B* 62.12 (2000), pp. 8003–8011. DOI: 10.1103/PhysRevB.62.8003.

[17] H. P. Beerman. "Investigation of pyroelectric material characteristics for improved infrared detector performance". In: *Infrared Physics* 15 (1975), pp. 225–231. DOI: 10.1016/0020-0891(75)90036-6.

[18] A. Benke, E. Mehner, M. Rosenkranz, et al. "Pyroelectrically Driven OH Generation by Barium Titanate and Palladium Nanoparticles". In: *Journal of Physical Chemistry C* 119 (2015), 18278–18286. DOI: 10.1021/acs.jpcc.5b04589.

[19] F. Bernardini, V. Fiorentini, and D. Vanderbilt. "Accurate calculation of polarization-related quantities in semiconductors". In: *Physical Review B* 63.19, 193201 (2001). DOI: 10.1103/PhysRevB.63.193201.

[20] F. Bernardini, V. Fiorentini, and D. Vanderbilt. "Spontaneous polarization and piezo-electric constants of III-V nitrides". In: *Physical Review B* 56.16 (1997), R10024–R10027. DOI: 10.1103/PhysRevB.56.R10024.

[21] V. Bharti, T. Kaura, and R. Nath. "Ferroelectric hysteresis in simultaneously stretched and corona-poled PVDF films". In: *IEEE Transactions on Dielectrics and Electrical Insulation* 4.6 (1997), pp. 738–741. DOI: 10.1109/94.654689.

[22] B. Bhatia, J. Karthik, T. Tong, et al. "Pyroelectric current measurements on $PbZr_{0.2}Ti_{0.8}O_3$ epitaxial layers". In: *Journal of Applied Physics* 112.10, 104106 (2012). DOI: 10.1063/1.4766271.

[23] A. B. Bhattacharyya, S. Tuli, and S. Kataria. "An Automated Nondestructive Characterization System for Pyroelectric Materials". In: *IEEE Transactions on Instrumentation and Measurement* 43.1 (1994), pp. 215–218. DOI: 10.1109/19.286351.

[24] P. Bogusławski and J. Bernholc. "Doping properties of C, Si, and Ge impurities in GaN and AlN". In: *Physical Review B* 56.15 (1997), pp. 9496–9505. DOI: 10.1103/PhysRevB.56.9496.

[25] M. Bohr, R. Chau, T. Ghani, et al. "The High-k Solution". In: *IEEE Spectrum* 44.10 (2007), pp. 29–35. DOI: 10.1109/MSPEC.2007.4337663.

[26] M. Born. "On the Quantum Theory of Pyroelectricity". In: *Reviews of Modern Physics* 17.2-3 (1945), pp. 245–251. DOI: 10.1103/RevModPhys.17.245.

[27] T. S. Böscke, J. Müller, D. Bräuhaus, et al. "Ferroelectricity in hafnium oxide thin films". In: *Applied Physics Letters* 99.10, 102903 (2011). DOI: 10.1063/1.3634052.

[28] R. Bouregba and G. Poullain. "Numerical Extraction of the True Ferroelectric Polarization Due to Switching Domains from Hysteresis Loops Measured Using A Sawyer-Tower Circuit". In: *Ferroelectrics* 274.1 (2002), pp. 165–181. DOI: 10.1080/00150190213947.

[29] C. R. Bowen, J. Taylor, E. Le Boulbar, et al. "A modified figure of merit for pyroelectric energy harvesting". In: *Materials Letters* 138.C (2015), pp. 243–246. DOI: 10.1016/j.matlet.2014.10.004.

[30] C. R. Bowen, J. Taylor, E. LeBoulbar, et al. "Pyroelectric materials and devices for energy harvesting applications". In: *Energy & Environmental Science* 7.12 (2014), pp. 3836–3856. DOI: 10.1039/C4EE01759E.

[31]   J. D. Brownridge. "Pyroelectric X-ray generator". In: *Nature* 358 (1992), pp. 287–288. DOI: 10.1038/358287b0.

[32]   R. L. Byer and C. B. Roundy. "Pyroelecric coefficient direct measurement technique and application to a nsec response time detector". In: *Ferroelectrics* 3.1 (1972), pp. 333–338. DOI: 10.1080/00150197208235326.

[33]   A. D. Bykhovski, V. V. Kaminski, M. S. Shur, et al. "Pyroelectricity in gallium nitride thin films". In: *Applied Physics Letters* 69.21 (1996), pp. 3254–3256. DOI: 10.1063/1.118027.

[34]   T. Böscke. "Crystalline Hafnia and Zirconia based Dielectrics for Memory Applications". PhD thesis. Technische Universität Dresden, 2010. ISBN: 9783736933460.

[35]   G. Catalan, L. J. Sinnamon, and J. M. Gregg. "The effect of flexoelectricity on the dielectric properties of inhomogeneously strained ferroelectric thin films". In: *Journal of Physics: Condensed Matter* 16.1 (2004), pp. 2253–2264. DOI: 10.1088/0953-8984/16/13/006.

[36]   P. Chandra and P. B. Littlewood. "A Landau Primer for Ferroelectrics". English. In: *Physics of Ferroelectrics: A Modern Perspective*. Berlin, Heidelberg: Springer Berlin Heidelberg, 2007, pp. 69–116. ISBN: 978-3-540-34591-6. DOI: 10.1007/978-3-540-34591-6_3.

[37]   J.-G. Cheng, J. Tang, S.-L. Guo, et al. "Investigation of the Ferroelectric Properties of Lead-Modified $Sr_{0.5}Ba_{0.5}Nb_2O_6$ With Special Reference to Uncooled Infrared Detection". In: *Journal of Electronic Materials* 16.5 (1987), pp. 323–327. DOI: 10.1007/BF02657906.

[38]   J.-G. Cheng, J. Tang, S.-L. Guo, et al. "The properties of tantlum modified lithium niobate thin films prepared by a diol based sol-gel process". In: *European Physical Journal Applied Physics* 36 (2006), pp. 5–10. DOI: 10.1051/epjap:2006099.

[39]   A. G. Chernikova, D. S. Kuzmichev, D. V. Negrov, et al. "Ferroelectric properties of full plasma-enhanced ALD TiN/ La:HfO_2/TiN stacks". In: *Applied Physics Letters* 108.24, 242905 (2016). DOI: 10.1063/1.4953787.

[40]   J. H. Choi, Y. Mao, and J. P. Chang. "Development of hafnium based high-k materials – A review". In: *Materials Science & Engineering R* 72.6 (2011), pp. 97–136. DOI: 10.1016/j.mser.2010.12.001.

[41]   C. L. Choy, W. P. Leung, T. G. Xi, et al. "Specific heat and thermal diffusivity of strontium barium niobate ($Sr_{1-x}Ba_xNb_2O_6$) single crystals". In: *Journal of Applied Physics* 71.1 (1992), pp. 170–173. DOI: 10.1063/1.350732.

[42]   A. G. Chynoweth. "Dynamic Method for Measuring the Pyroelectric Effect with Special Reference to Barium Titanate". In: *Journal of Applied Physics* 27.1 (1956), pp. 78–84. DOI: 10.1063/1.1722201.

[43]   R. Clausius. *Die Mechanische Behandlung der Electricität*. Wiesbaden: Vieweg+Teubner Verlag, 1879. ISBN: 978-3-663-20232-5. DOI: 10.1007/978-3-663-20232-5_9.

[44]   A. T. Collins, E. C. Lightowlers, and P. J. Dean. "Lattice Vibration Spectra of Aluminum Nitride". In: *Physical Review* 158.3 (1967), pp. 833–838. DOI: 10.1103/PhysRev.158.833.

[45]   G. J. Coombs and R. A. Cowley. "Paraelectric, piezoelectric and pyroelectric crystals: I. Dielectric properties". In: *Journal of Physics C: Solid State Physics* 6.1 (1973), pp. 121–142. DOI: 10.1088/0022-3719/6/1/024.

[46] A. D. Corso, M. Posternak, R. Resta, et al. "*Ab initio* study of piezoelectricity and spontaneous polarization in ZnO". In: *Physical Review B* 50.15 (1994), pp. 10715–10721. DOI: `10.1103/PhysRevB.50.10715`.

[47] A. Costales, M. A. Blanco, Á. Martín Pendás, et al. "Chemical Bonding in Group III Nitrides". In: *Journal of the American Chemical Society* 124.15 (2002), pp. 4116–4123. DOI: `10.1021/ja017380o`.

[48] T. A. T. Cowell and J. Woods. "The evaluation of thermally stimulated current curves". In: *British Journal of Applied Physics* 18.8 (1967), pp. 1045–1051. DOI: `10.1088/0508-3443/18/8/302`.

[49] E. Crisman, J. S. Derov, A. J. Drehman, et al. "Large Pyroelectric Response from Reactively Sputtered Aluminum Nitride Thin Films". In: *Electrochemical and Solid-State Letters* 8.3 (2005), H31–H32. DOI: `10.1149/1.1857742`.

[50] E. Crisman, A. Drehman, R. Miller, et al. "Enhanced AlN nanostructures for pyroelectric sensors". In: *physica status solidi (c)* 11.3-4 (2014), pp. 517–520. DOI: `10.1002/pssc.201300513`.

[51] E. Crisman, V. Vasilyev, A. Drehman, et al. "Observation of Large, Anomalous Pyroelectric Response in AlN Thin Films". In: *MRS Online Proceedings Library* 1288 (2011). DOI: `10.1557/opl.2011.627`.

[52] L. Cross. "Flexoelectric effects: Charge separation in insulating solids subjected to elastic strain gradients". In: *Journal of Materials Science* 41 (2006), pp. 53–63. DOI: `10.1007/s10853-005-5916-6`.

[53] C. E. Curtis, L. M. Doney, and J. R. Johnson. "Some Properties of Hafnium Oxide, Hafnium Silicate, Calcium Hafnate, and Hafnium Carbide". In: *Journal of the American Ceramic Society* 37.10 (1954), pp. 458–465. DOI: `10.1111/j.1151-2916.1954.tb13977.x`.

[54] M. Daglish. "A dynamic method for determining the pyroelectric response of thin films". In: *Integrated Ferroelectrics* 22 (1998), pp. 473–488. DOI: `10.1080/10584589808208067`.

[55] D. Damjanovic. "Ferroelectric, dielectric and piezoelectric properties of ferroelectric thin films and ceramics)". In: *Reports on Progress in Physics* 61 (1998), pp. 1267–1324. DOI: `10.1088/0034-4885/61/9/002`.

[56] B. A. Danilchenko, T. Paszkiewicz, S Wolski, et al. "Heat capacity and phonon mean free path of wurtzite GaN". In: *Applied Physics Letters* 89.6, 061901 (2006). DOI: `10.1063/1.2335373`.

[57] M. Davis, D. Damjanovic, and N. Setter. "Pyroelectric properties of $(1-x)$Pb(Mg$_{1/3}$Nb$_{2/3}$)O$_3$-xPbTiO$_3$ and $(1-x)$Pb(Zn$_{1/3}$Nb$_{2/3}$)O$_3$-xPbTiO$_3$ single crystals measured using a dynamic method". In: *Journal of Applied Physics* 96.5 (2004), pp. 2811–2815. DOI: `10.1063/1.1775308`.

[58] K. K. Deb, M. D. Hill, and J. F. Kelly. "Pyroelectric characteristics of modified barium titanate ceramics". In: *Journal of Material Research* 7.12 (1992), pp. 3296–3305. DOI: `10.1557/JMR.1992.3296`.

[59] R. Deng. "AlN, ScN, and Al-Sc-N Ternary Alloys: Structural, Optical, and Electrical Properties". PhD thesis. Rensselaer Polytechnic Institute Troy, New York, 2013.

[60] A. F. Devonshire. "Theory of ferroelectrics". English. In: *Advances in Physics* 3.10 (1954), pp. 85–130. DOI: `10.1080/00018735400101173`.

[61] H. Diamant, K. Drenck, and R. Pepinsky. "Bridge for Accurate Measurement of Ferroelectric Hysteresis". In: *Review of Scientific Instruments* 28.30 (1957), pp. 30–33. DOI: 10.1063/1.1715701.

[62] C. Dias, M. Simon, R. Quad, et al. "Measurement of the pyroelectric coefficient in composites using a temperature-modulated excitation". In: *Journal of Physics D: Applied Physics* 26.1 (1993), pp. 106–110. DOI: 10.1088/0022-3727/26/1/017.

[63] A. E. Dubinov and A. A. Dubinova. "Exact integral-free expressions for the integral Debye functions". In: *Technical Physics Letters* 34.12 (2008), pp. 999–1001. DOI: 10.1134/S106378500812002X.

[64] M.-A. Dubois and P. Muralt. "Properties of aluminum nitride thin films for piezoelectric transducers and microwave filter applications". In: *Applied Physics Letters* 74.20 (1999), pp. 3032–3034. DOI: 10.1063/1.124055.

[65] S. Ducharme, M. Bai, M. Poulsen, et al. "Mesoscopic structures in two-dimensional ferroelectric polymers". In: *Ferroelectrics* 252 (2001), pp. 191–199. DOI: 10.1080/00150190108016256.

[66] D. Ehre and H. Cohen. "Contact-free pyroelectric measurements using x-ray photoelectron spectroscopy". In: *Applied Physics Letters* 103, 052901 (2013). DOI: 10.1063/1.4817010.

[67] D. Ehre, V. Lyahovitskaya, A. Tagentsev, et al. "Amorphous Piezo- and Pyroelectric Phases of $BaZrO_3$ and $SrTiO_3$". In: *Advanced Materials* 19.11 (2007), pp. 1515–1517. DOI: 10.1002/adma.200602149.

[68] D. Ehre, E. Mirzadeh, O. Stafsudd, et al. "Pyroelectric Measurement of Surface Layer: The Case of Thin Film on Dielectric Substrate". In: *Ferroelectrics* 472.1 (2014), pp. 41–49. DOI: 10.1080/00150193.2014.964125.

[69] L. M. Eng, M. B. C. Loppacher, M. G. R. Bennewitz, et al. "Ferroelectric Domain Characterisation and Manipulation: A Challenge for Scanning Probe Microscopy". In: *Physical Review Letters* 222.1 (1999), pp. 153–162. DOI: 10.1080/00150199908014811.

[70] E. V. Etzkorn and D. R. Clarke. "Cracking of GaN Films". In: *Journal of Applied Physics* 89.2 (2001), pp. 1025–1034. DOI: 10.1063/1.1330243.

[71] B. Fang, K. Qian, Z. Chen, et al. "Large strain and pyroelectric properties of $Pb(Mg_{1/3}Nb_{2/3})O_3$ - $PbTiO_3$ ceramics prepared by partial oxalate route". In: *Functional Materials Letters* 07.05, 1450059 (2014). DOI: 10.1142/S1793604714500593.

[72] S. N. Fedosov, A. V. Sergeeva, J. A. Giacometti, et al. "Corona poling of a ferroelectric polymer (PVDF)". In: *International Society for Optics and Photonics* (1999), pp. 53–58. DOI: 10.1117/12.373719.

[73] F. P. G. Fengler, R. Nigon, P. Muralt, et al. "Analysis of Performance Instabilities of Hafnia-Based Ferroelectrics Using Modulus Spectroscopy and Thermally Stimulated Depolarization Currents". In: *Advanced Electronic Materials* 4.3, 1700547 (2018). DOI: 10.1002/aelm.201700547.

[74] S. Flachowsky, T. Mikolajick, S. Müller, et al. "Doped Hafnium Oxide — An Enabler for Ferroelectric Field Effect Transistors". In: *6th Forum on New Materials - Part C*. Vol. 95. Advances in Science and Technology. Trans Tech Publications, 2014, pp. 136–145. DOI: 10.4028/www.scientific.net/AST.95.136.

[75] V. Fridkin and S. Ducharme. "Ferroelectricity and Ferroelectric Phase Transition". In: *Ferroelectricity at the Nanoscale*. Berlin, Heidelberg: Springer Berlin Heidelberg, 2013, pp. 1–9. ISBN: 978-3-642-41006-2. DOI: 10.1007/978-3-642-41007-9_1.

[76]   J. Frutos and B. Jimenéz. "Study of the spatial distribution of the polarization in ferroelectric ceramics by means of low frequency sinusoidal thermal waves". In: *Ferroelectrics* 109.1 (1990), pp. 101–106. DOI: 10.1080/00150199008211397.

[77]   V. Fuflyigin, E. Salley, A. Osinsky, et al. "Pyroelectric properties of AlN". In: *Applied Physics Letters* 77.19 (2000), pp. 3075–3077. DOI: 10.1063/1.1324726.

[78]   L. E. Garn and E. J. Sharp. "Use of low-frequency sinusoidal temperature waves to separate pyroelectric currents from nonpyroelectric currents. Part I. Theory". In: *Journal of Applied Physics* 53.12 (1982), pp. 8974–8979. DOI: 10.1063/1.330454.

[79]   L. E. Garn and E. J. Sharp. "Use of low-frequency sinusoidal temperature waves to separate pyroelectric currents from nonpyroelectric currents. Part II. Experiment". In: *Journal of Applied Physics* 53.12 (1982), pp. 8980–8987. DOI: 10.1063/1.330455.

[80]   C. Garrett. "Nonlinear optics, anharmonic oscillators, and pyroelectricity". In: *IEEE Journal of Quantum Electronics* 4.3 (1968), pp. 70–84. DOI: 10.1109/JQE.1968.1075030.

[81]   N. D. Gavrilova. "Study of the temperature dependence of the pyroelectric coefficients of crystals by the static method". In: *Soviet Physics-Crystallography* 10.3 (1965), pp. 278–281.

[82]   N. D. Gavrilova, E. G. Maksimov, V. K. Novik, et al. "The low-temperature behaviour of the pyroelectric coefficient". In: *Ferroelectrics* 100.1 (1989), pp. 223–240. DOI: 10.1080/00150198908007918.

[83]   T. Gebre, A. K. Batra, P. Guggilla, et al. "Pyroelectric Properties of Pure and Doped Lithium Niobate Crystals for Infrared Sensors". In: *Ferroelectrics Letters Section* 31.5-6 (2004), pp. 131–139. DOI: 10.1080/07315170490901436.

[84]   R. Ghane-Motlagh, M. Kroener, F. Goldschmidtboeing, et al. "A dynamic method for the measurement of pyroelectric properties of materials". In: *Smart Materials and Structures* 27.8, 084004 (2018). DOI: 10.1088/1361-665X/aac0b3.

[85]   J. A. Giacometti and J. S. C. Campos. "Constant current corona triode with grid voltage control. Application to polymer foil charging". In: *Review of Scientific Instruments* 61.3 (1990), pp. 1143–1150. DOI: 10.1063/1.1141438.

[86]   J. A. Giacometti and O. N. Oliveira. "Corona charging of polymers". In: *IEEE Transactions on Electrical Insulation* 27.5 (1992), pp. 924–943. DOI: 10.1109/14.256470.

[87]   B. Gil. *Physics of Wurtzite Nitrides and Oxides.* Vol. 197. Passport to Devices. Springer, 2014. ISBN: 3319068059. DOI: 10.1007/978-3-319-06805-3.

[88]   A. M. Glass. "Investigation of the Elctrical Properties of $Sr_{1-x}Ba_xNb_2O_6$ with Special Reference to Pyroelectric Detection". In: *Journal of Applied Physics* 40.12 (1969), pp. 4699–4713. DOI: 10.1063/1.1657277.

[89]   M. D. Glinchuk and P. I. Bykov. "The anomalies of the properties of nanomaterials related to the distribution of the grain sizes". In: *ArXiv* (2004). DOI: arXiv:cond-mat/0406032.

[90]   V. J. Gokhale and M. Rais-Zadeh. "Uncooled Infrared Detectors Using Gallium Nitride on Silicon Micromechanical Resonators". In: *Journal of Microelectromechanical Systems* 23.4 (2014), pp. 803–810. DOI: 10.1109/JMEMS.2013.2292368.

[91]   V. J. Gokhale, Y. Sui, and M. Rais-Zadeh. "Novel uncooled detector based on gallium nitride micromechanical resonators". In: *SPIE Defense, Security, and Sensing.* Ed. by B. F. Andresen, G. F. Fulop, and P. R. Norton. SPIE, 2012, 835319. DOI: 10.1117/12.920450.

[92]   Goodfellow. *Polyvinylidenefluoride (PVDF) Material Information*. URL: `http://www.goodfellow.com/E/Polyvinylidenefluoride.html` (visited on 06/22/2018).

[93]   I. Gorczyca and N. E. Christensen. "Band structure and high-pressure phase transition in GaN". In: *Solid State Communications* 80.5 (1991), pp. 335–338. DOI: `10.1016/0038-1098(91)90141-H`.

[94]   W. Götz, N. M. Johnson, C. Chen, et al. "Activation energies of Si donors in GaN". In: *Applied Physics Letters* 68.22 (1996), pp. 3144–3146. DOI: `http://dx.doi.org/10.1063/1.115805`.

[95]   E. D. Grimley, T. Schenk, X. Sang, et al. "Structural Changes Underlying Field-Cycling Phenomena in Ferroelectric HfO$_2$ Thin Films". In: *Advanced Electronic Materials* 2.9, 1600173 (2016). DOI: `10.1002/aelm.201600173`.

[96]   J. Grindley. *An Introduction to the Phenomenological Theory of Ferroelectricity*. Pergamon, 1970. ISBN: 9781483154596. DOI: `10.1016/C2013-0-01549-6`.

[97]   R. Gross and A. Marx. *Festkörperphysik*. De Gruyter Studium Series. Walter de Gruyter GmbH, 2014. ISBN: 978-3-110-35869-8.

[98]   J. Groten, M. Zirkl, G. Jakopic, et al. "Pyroelectric scanning probe microscopy: A method for local measurement of the pyroelectric effect in ferroelectric thin films". In: *Physical Review* 82.5, 054112 (2010). DOI: `10.1103/PhysRevB.82.054112`.

[99]   P. J. Grout and N. H. March. "Low-Temperature Behavior of Pyroelectricity". In: *Physical Review Letters* 37.12 (1976), pp. 791–792. DOI: `10.1103/PhysRevLett.37.791`.

[100]   A. Gruverman and O. Auciello. "Imaging and control of domain structures in ferroelectric thin films via scanning force microscopy". In: *Annual Review of Materials Research* 28.1 (1998), pp. 101–123. DOI: `10.1146/annurev.matsci.28.1.101`.

[101]   P. Guggilla, A. K. Batra, and M. E. Edwards. "Electrical characterization of LiTaO3: P(VDF-TrFE) composites". In: *Journal of Materials Science* 44.20 (2009), pp. 5469–5474. DOI: `10.1007/s10853-009-3753-8`.

[102]   W. Guo, J. Xie, C. Akouala, et al. "Comparative Study of Etching High Crystalline Quality AlN and GaN". In: *Journal of Crystal Growth* 366 (2013), pp. 20–25. DOI: `10.1016/j.jcrysgro.2012.12.141`.

[103]   E. Gutmann, A. Benke, K. Gerth, et al. "Pyroelectrocatalytic Disinfection Using the Pyroelectric Effect of Nano- and Microcrystalline LiNbO$_3$ and LiTaO$_3$ Particles". In: *Journal of Physical Chemistry C* 116 (2012), pp. 5383–5393. DOI: `10.1021/jp210686m`.

[104]   J Guyonnet. "Domain Walls in Ferroelectric Materials". In: *Ferroelectric Domain Walls*. Cham: Springer International Publishing, 2014, pp. 7–24. ISBN: 978-3-319-05749-1. DOI: `10.1007/978-3-319-05750-7_2`.

[105]   J. C. Hackley and T. Gougousi. "Properties of atomic layer deposited HfO$_2$ thin films". In: *Thin Solid Films* 517.24 (2009), pp. 6576–6583. DOI: `10.1016/j.tsf.2009.04.033`.

[106]   A. Hadni, J. M. Bassia, X. Gerbaux, et al. "Laser scanning microscope for pyroelectric display in real time". In: *Applied Optics* 15.9 (1976), pp. 2150–2158. DOI: `10.1364/AO.15.002150`.

[107]   G. Hansdah and B. K. Sahoo. "Pyroelectric effect and lattice thermal conductivity of InN/GaN heterostructures". In: *Journal of Physics and Chemistry of Solids* 117 (2018), pp. 111–116. DOI: `10.1016/j.jpcs.2018.02.018`.

[108] J. Hanzig*, E. Mehner*, S. Jachalke, et al. "Dielectric to pyroelectric phase transition induced by defect migration". In: *New Journal of Physics* 17, 023036 (2015). *These authors contributed equally to this work. DOI: 10.1088/1367-2630/17/2/023036.

[109] J. Hanzig, M. Zschornak, F. Hanzig, et al. "Migration-induced field-stabilized polar phase in strontium titanate single crystals at room temperature". In: *Physical Review B* 88.2, 024104 (2013). DOI: 10.1103/PhysRevB.88.024104.

[110] J. Hanzig, M. Zschornak, E. Mehner, et al. "The anisotropy of oxygen vacancy migration in SrTiO$_3$". In: *Journal of Physics: Condensed Matter* 28.22, 225001 (2016). DOI: 10.1088/0953-8984/28/22/225001.

[111] N. P. Hartley, P. T. Squire, and E. H. Putley. "A new method of measuring pyroelectric coefficients". In: *Journal of Physics E: Scientific Instruments* 5 (1972), pp. 787–789. DOI: 10.1088/0022-3735/5/8/022.

[112] C. Hartmann, A. Dittmar, J. Wollweber, et al. "Bulk AlN growth by physical vapour transport". In: *Semiconductor Science and Technology* 29.8, 084002 (2014). DOI: 10.1088/0268-1242/29/8/084002.

[113] M. Hirahara and Y. Umemura. "Fabrication of Three-Layer-Component Organoclay Habryd Films with Reverse Deposition Orders by a Modified Langmuir-Schaefer Technique and Their Pyroelectric Currents Measured by a Noncontact Method". In: *Langmuir* 31.30 (2015), pp. 8346–8353. DOI: 10.1021/acs.langmuir.5b01401.

[114] K. Hiramatsu, T. Detchprohm, and I. Akasaki. "Relaxation Mechanism of Thermal Stresses in the Heterostructure of GaN Grown on Sapphire by Vapor Phase Epitaxy". In: *Japanese Journal of Applied Physics* 32.4R (1993), pp. 1528–1533. DOI: 10.1143/JJAP.32.1528.

[115] M. Hoffmann, U. Schroeder, C. Künneth, et al. "Ferroelectric phase transitions in nanoscale HfO$_2$ films enable giant pyroelectric energy conversion and highly efficient supercapacitors". In: *Nano Energy* 18.C (2015), pp. 154–164. DOI: 10.1016/j.nanoen.2015.10.005.

[116] M. Hoffmann, T. Schenk, M. Pešić, et al. "Insights into antiferroelectrics from first-order reversal curves". In: *Applied Physics Letters* 111.18 (2017), p. 182902. DOI: 10.1063/1.5003612.

[117] P. Hofmann. "Investigation of correlations between HVPE growth, crystal properties and dopant incorporation in gallium nitride". PhD thesis. Technical University of Dresden / NaMLab gGmbH, 2018. ISBN: 9783752884920.

[118] P. Hofmann, M. Krupinski, F. Habel, et al. "Novel approach for n-type doping of HVPE gallium nitride with germanium". In: *Journal of Crystal Growth* 450.C (2016), pp. 61–65. DOI: 10.1016/j.jcrysgro.2016.06.019.

[119] P. Hofmann, G. Leibiger, M. Krupinski, et al. "Doping marker layers for ex situ growth characterisation of HVPE gallium nitride". In: *CrystEngComm* 19.5 (2017), pp. 788–794. DOI: 10.1039/C6CE02474B.

[120] S. T. Hughes and A. R. Piercy. "The simultaneous measurement of pyroelectric and relaxation currents in poly(vinylidene fluoride)". In: *Journal of Physics E: Scientific Instruments* 19.11 (1986), pp. 976–982. DOI: 0022-3735/19/11/021.

[121] H. Ibach and H. Lüth. *Solid-State Physics: An Introduction to Principles of Materials Science*. Springer Berlin Heidelberg, 2009. ISBN: 9783540938040.

[122] E. Iborra, J. Olivares, M. Clement, et al. "Piezoelectric properties and residual stress of sputtered AlN thin films for MEMS applications". In: *Sensors and Actuators A: Physical* 115.2-3 (2004), pp. 501–507. DOI: 10.1016/j.sna.2004.03.053.

[123] L. Ibos, A. Bernes, G. Teyssedre, et al. "Correlation between Pyroelectric Properties and Dielectric Behaviour in Ferroelectric Polymer". In: *Ferroelectrics* 238 (2000), pp. 163–170. DOI: 10.1080/00150190008008780.

[124] "IEEE Standard on Piezoelectricity". In: *ANSI/IEEE Std 176-1987* (1988), pp. 1–66. DOI: 10.1109/IEEESTD.1988.79638.

[125] Intel. *Intel's Fundamental Advance in Transistor Design Extends Moore's Law, Computing Performance*. URL: https://www.intel.com/pressroom/archive/releases/2007/20071111comp.htm (visited on 06/19/2018).

[126] Ioffe Institute. *Semiconductors on NSM*. URL: http://www.ioffe.ru/SVA/NSM/Semicond (visited on 06/22/2018).

[127] Y. Ivry, V. Lyahovitskaya, I. Zon, et al. "Enhanced pyroelectric effect in self-supported films of $BaTiO_3$ with polycrystalline macrodomains". In: *Applied Physics Letters* 90.17, 172905 (2007). DOI: 10.1063/1.2730749.

[128] S. Jachalke*, P. Hofmann*, G. Leibiger, et al. "The pyroelectric coefficient of free standing GaN grown by HVPE". In: *Applied Physics Letters* 109.14, 142906 (2016). *These authors contributed equally to this work. DOI: 10.1063/1.4964265.

[129] S. Jachalke, E. Mehner, H. Stöcker, et al. "How to measure the pyroelectric coefficient?" In: *Applied Physics Reviews* 4.2, 021303 (2017). DOI: 10.1063/1.4983118.

[130] S. Jachalke, T. Schenk, M. H. Park, et al. "Pyroelectricity of silicon-doped hafnium oxide thin films". In: *Applied Physics Letters* 112.14, 142901 (2018). DOI: 10.1063/1.5023390.

[131] S.-J. Jeong, Y. Gu, J. Heo, et al. "Thickness scaling of atomic-layer-deposited HfO_2 films and their application to wafer-scale graphene tunnelling transistors". In: *Scientific Reports* 6.20907 (2016), pp. 1–12. DOI: 10.1038/srep20907.

[132] R. Jiménez, T. Hungría, A. Castro, et al. "Phase transitions in $Na_{1-x}Li_xNbO_3$solid solution ceramics studied by a new pyroelectric current based method". In: *Journal of Physics D: Applied Physics* 41.6, 065408 (2008). DOI: 10.1088/0022-3727/41/6/065408.

[133] R. Jiménez and B. Jiménez. "Pyroelectricity in Polycrystalline Ferroelectrics". In: *Multifunctional Polycrystalline Ferroelectric Materials*. Dordrecht: Springer Netherlands, 2011, pp. 573–616. DOI: 10.1007/978-90-481-2875-4_12.

[134] R. Jiménez, P. Ramos, M. L. Calzada, et al. "Pyroelectricity in lead titanate thin films." In: *Boletin de la Sociedad Espanola de Ceramica y Vidrio* 37.2-3 (1998), pp. 117–121.

[135] A. Kakekhani and S. Ismail-Beigi. "Ferroelectric oxide surface chemistry: water splitting via pyroelectricity". In: *Journal of Materials Chemistry A* 4 (2016), pp. 5235–5246. DOI: 10.1039/C6TA00513F.

[136] J. Kamimura, P. Bogdanoff, J. Lähnemann, et al. "Photoelectrochemical Properties of (In,Ga)N Nanowires for Water Splitting Investigated by in Situ Electrochemical Mass Spectroscopy". In: *Journal of the American Chemical Society* 135.28 (2013), pp. 10242–10245. DOI: 10.1021/ja404043k.

[137] S. Kar-Narayan and N. D. Mathur. "Direct and indirect electrocaloric measurements using multilayer capacitors". In: *Journal of Physics D: Applied Physics* 43.3, 032002 (2010). DOI: 10.1088/0022-3727/43/3/032002.

[138] T. Kaura, R. Nath, and M. M. Perlman. "Simultaneous stretching and corona poling of PVDF films". In: *Journal of Physics D: Applied Physics* 24.10 (1991), pp. 1848–1852. DOI: 10.1088/0022-3727/24/10/020.

[139]   B. Kebede, R. A. Coutu Jr, and L. Starman. "Optimal microelectromechanical systems (MEMS) device for achieving high pyroelectric response of AlN". In: ed. by M. A. Maher and P. J. Resnick. SPIE, 2014, 89730I. DOI: 10.1117/12.2037386.

[140]   B. Khanbabaee, E. Mehner, C. Richter, et al. "Large piezoelectricity in electric-field modified single crystals of SrTiO$_3$". In: *Applied Physics Letters* 109.22, 222901 (2016). DOI: 10.1063/1.4966892.

[141]   R. D. King-Smith and D. Vanderbilt. "Theory of polarization of crystalline solids". In: *Physical Review B* 47.3 (1993), pp. 1651–1654. DOI: 10.1103/PhysRevB.47.1651.

[142]   E. H. Kisi, C. J. Howard, and R. J. Hill. "Crystal Structure of Orthorhombic Zirconia in Partially Stabilized Zirconia". In: *Journal of the American Ceramic Society* 72.9 (1989), pp. 1757–1760. DOI: 10.1111/j.1151-2916.1989.tb06322.x.

[143]   C. Kittel. "Theory of Antiferroelectric Crystals". In: *Physical Review* 82 (5 1951), pp. 729–732. DOI: 10.1103/PhysRev.82.729.

[144]   G. J. Klap, S. M. van Klooster, M. Wübbenhorst, et al. "Scanning pyroelectric microscopy of zeolite loaded with polar molecules". In: *MRS Conference Proceedings* 3 (1999), pp. 2117–2120.

[145]   W. Kleber, H.-J. Bautsch, and J. Bohm. *Einführung in die Kristallographie*. Ed. by J. Bohm and D. Klimm. Oldenbourg Verlag München, 2010.

[146]   M. Kneissl, T. Kolbe, C. Chua, et al. "Advances in group III-nitride-based deep UV light-emitting diode technology". In: *Semiconductor Science and Technology* 26.1, 014036 (2010). DOI: 10.1088/0268-1242/26/1/014036.

[147]   K. Köhler, R. Gutt, J. Wiegert, et al. "Diffusion of Mg Dopant in Metal-Organic Vapor-Phase Epitaxy grown GaN and Al$_x$Ga$_{1-x}$N". In: *Journal of Applied Physics* 113.7, 073514 (2013). DOI: 10.1063/1.4792662.

[148]   R. Köhler, N. Neumann, and G. Hofmann. "Pyroelectric single-element and linear-array sensors based on P(VDF/TrFE) thin films". In: *Sensors and Actuators A: Physical* 45.3 (1994), pp. 209–218. DOI: 10.1016/0924-4247(94)00842-6.

[149]   D. D. Koleske, A. E. Wickenden, R. L. Henry, et al. "GaN decomposition in H$_2$ and N$_2$ at MOVPE temperatures and pressures". In: *Journal of Crystal Growth* 223.4 (2001), pp. 466–483. DOI: 10.1016/S0022-0248(01)00617-0.

[150]   L. B. Kong, T. Li, H. H. Hng, et al. *Waste Energy Harvesting – Mechanical and Thermal Energies*. Springer Berlin Heidelberg, 2014.

[151]   V. I. Koshchenko, Y. K. Grinberg, and A. F. Demidenko. "Thermodynamic properties of AlN (5-2700 K), GaP (5-1500 K) and BP (5-800 K)". In: *Applied Physics Letters* 20.11 (1984), pp. 1787–1790.

[152]   L. Kouchachvili and M. Ikura. "Improving the efficiency of pyroelectric conversion". In: *International Journal of Energy Research* 32.4 (2008), pp. 328–335. DOI: 10.1002/er.1361.

[153]   M. G. Kozodaev, A. G. Chernikova, E. V. Korostylev, et al. "Ferroelectric properties of lightly doped La:HfO$_2$ thin films grown by plasma-assisted atomic layer deposition". In: *Applied Physics Letters* 111.13, 132903 (2017). DOI: 10.1063/1.4999291.

[154]   S. A. Kukushkin, A. V. Osipov, O. N. Sergeeva, et al. "Pyroelectric and piezoelectric responses of thin AlN films epitaxy-grown on a SiC/Si substrate". In: *Physics of the Solid State* 58.5 (2016), pp. 967–970. DOI: 10.1134/S1063783416050139.

[155] C. Künneth, R. Materlik, M. Falkowski, et al. "Impact of Four-Valent Doping on the Crystallographic Phase Formation for Ferroelectric HfO$_2$ from First-Principles: Implications for Ferroelectric Memory and Energy-Related Applications". In: *ACS Applied Nano Materials* 1.1 (2017), pp. 254–264. DOI: 10.1021/acsanm.7b00124.

[156] N. Kurz, Y. Lu, L. Kirste, et al. "Temperature Dependence of the Pyroelectric Coefficient of AlScN Thin Films". In: *Physica Status Solidi (a)* 95, 1700831 (2018). DOI: 10.1002/pssa.201700831.

[157] Z. Kutnjak and B. Rožič. "Indirect and Direct Measurements of the Electrocaloric Effect". In: *Electrocaloric Materials*. Ed. by T. Correia and Q. Zhang. Vol. 34. Berlin, Heidelberg: Springer Berlin Heidelberg, 2014. DOI: 10.1007/978-3-642-40264-7_7.

[158] Z. Kutnjak, B. Rožič, and R. Pirc. *Electrocaloric Effect: Theory, Measurements, and Applications*. Hoboken, NJ, USA: John Wiley & Sons, Inc., 2015. DOI: 10.1002/047134608X.W8244.

[159] J. Lähnemann, O. Brandt, U. Jahn, et al. "Direct experimental determination of the spontaneous polarization of GaN". In: *Physical Review B* 86.8, 081302 (2012). DOI: 10.1103/PhysRevB.86.081302.

[160] S. B. Lang. "Pyroelectricity: From ancient curiosity to modern imaging tool". In: *Physics Today* 58 (2005), pp. 31–36. DOI: 10.1063/1.2062916.

[161] S. B. Lang. *The Sourcebook of Pyroelectricity*. Gordon and Breach, Science Publishers, Inc., 1974.

[162] S. B. Lang and D. K. Das-Gupta. "Laser-intensity-modulation method: A technique for determination of spatial distributions of polarization and space charge in polymer electrets". In: *Journal of Applied Physics* 59.6 (1986), pp. 2151–2160. DOI: 10.1063/1.336352.

[163] S. B. Lang and S. Muesnit. "Review of some lesser-known applications of piezoelectric and pyroelectric polymers". In: *Applied Physics A: Materials Science and Processing* 85.2 (2006), pp. 125–134. DOI: 10.1007/s00339-006-3688-8.

[164] S. B. Lang and F. Steckel. "Method for the Measurement of the Pyroelectric Coefficient, dc Dielectric Constant, and Volume Resistivity of a Polar Material". In: *The Review of Scientific Instruments* 36.7 (1965), pp. 929–932. DOI: 10.1063/1.1719787.

[165] M. Lanza. "A Review on Resistive Switching in High-k Dielectrics: A Nanoscale Point of View Using Conductive Atomic Force Microscope". In: *Materials* 7.3 (2014), pp. 2155–2182. DOI: 10.3390/ma7032155.

[166] F. Y. Lee, A. Navid, and L. Pilon. "Pyroelectric waste heat energy harvesting using heat conduction". In: *Applied Thermal Engineering* 37 (2012), pp. 30–37. DOI: 10.1016/j.applthermaleng.2011.12.034.

[167] J. J. Lee, C. L. Thio, and S. B. Desu. "Retention and imprint properties of ferroelectric thin films". In: *physica status solidi (a)* 151.1 (1995), pp. 171–182. DOI: 10.1002/pssa.2211510120.

[168] D. Lehninger, D. Rafaja, J. Wünsche, et al. "Formation of orthorhombic (Zr,Ta)O$_2$ in thin Zr-Ta-O films". In: *Applied Physics Letters* 110.26, 262903 (2017). DOI: 10.1063/1.4990529.

[169] M. Leroux, N. Grandjean, M. Laügt, et al. "Quantum confined Stark effect due to built-in internal polarization fields in (Al,Ga)N/GaN quantum wells". In: *Physical Review B* 58.20 (1998). DOI: 10.1103/PhysRevB.58.R13371.

[170] M. Leszczynski, T. Suski, H. Teisseyre, et al. "Thermal Expansion of Gallium Nitride". In: *Journal of Applied Physics* 76.8 (1994), pp. 4909–4911. DOI: 10.1063/1.357273.

[171]   M. E. Levinshtein, S. L. Rumyantsev, and M. S. Shur. *Properties of Advanced Semiconductor Materials: GaN, AIN, InN, BN, SiC, SiGe*. 2001.

[172]   F. Li, T. Yang, Z. Xu, et al. "The origin of ultrahigh piezoelectricity in relaxor-ferroelectric solid solution crystals". In: *Nature Communications* 7 (2016), pp. 1–9. DOI: 10.1038/ncomms13807.

[173]   B.-T. Lin, Y.-W. Lu, J. Shieh, et al. "Induction of ferroelectricity in nanoscale ZrO_2 thin films on Pt electrode without post-annealing". In: *Journal of the European Ceramic Society* 37.3 (2017), pp. 1135–1139. DOI: 10.1016/j.jeurceramsoc.2016.10.028.

[174]   M. E. Lines and A. M. Glass. "Low-temperature behavior of spontaneous polarization in $LiNbO_3$ and $LiTaO_3$". In: *Physical Review B* 13.180 (1976), pp. 180–191. DOI: 10.1103/PhysRevB.13.180.

[175]   M. E. Lines and A. M. Glass. "Primary Pyroelectric Effect in $LiTaO_3$". In: *Physical Review Letters* 39.21 (1977), pp. 1362–1365. DOI: 10.1103/PhysRevLett.39.1362.

[176]   M. E. Lines and A. M. Glass. *Principles and Applications of Ferroelectrics and Related Materials*. Oxford University Press, 1977. ISBN: 9780198507789. DOI: 10.1093/acprof:oso/9780198507789.001.0001.

[177]   C. Liu, F. Yun, and H. Morkoç. "Ferromagnetism of ZnO and GaN: A Review". In: *Journal of Materials Science: Materials in Electronics* 16.9 (2005), pp. 555–597. DOI: 10.1007/s10854-005-3232-1.

[178]   G. Liu, S. Zhang, W. Jiang, et al. "Losses in ferroelectric materials". In: *Materials Science and Engineering: R: Reports* 89 (2015), pp. 1–48. DOI: 10.1016/j.mser.2015.01.002.

[179]   J. Liu, P. B. Allen, and M. V. Fernández-Serra. "Erratum: First-principles study of pyroelectricity in GaN and ZnO". In: *Physical Review B* 98.3, 039905 (2018). DOI: 10.1103/PhysRevB.98.039905.

[180]   J. Liu, M. V. Fernández-Serra, and P. B. Allen. "First-principles study of pyroelectricity in GaN and ZnO". In: *Physical Review B* 93.8, 081205 (2016). DOI: 10.1103/PhysRevB.93.081205.

[181]   J. Liu and S. T. Pantelides. "Mechanisms of Pyroelectricity in Three- and Two-Dimensional Materials". In: *Physical Review Letters* 120.20, 207602 (2018). DOI: 10.1103/PhysRevLett.120.207602.

[182]   S. T. Liu, J. D. Zook, and D. Long. "Relationships between pyroelectric and ferroelectric parameters". In: *Ferroelectrics* 9.1 (1975), pp. 39–43. DOI: 10.1080/00150197508240079.

[183]   G. M. Loiacono and G. Kostecky. "Thermal properties of Pure and Doped TGS, DTGS, TGFB and DTGFB single crystals". In: *Materials Research Bulletin* 16.1 (1981), pp. 53–58. DOI: 10.1016/0025-5408(81)90177-X.

[184]   P. D. Lomenzo, Q. Takmeel, C. Zhou, et al. "Mixed Al and Si doping in ferroelectric HfO_2 thin films". In: *Applied Physics Letters* 107.24, 242903 (2015). DOI: 10.1063/1.4937588.

[185]   P. D. Lomenzo, Q. Takmeel, C. Zhou, et al. "TaN interface properties and electric field cycling effects on ferroelectric Si-doped HfO_2 thin films". In: *Journal of Applied Physics* 117.13, 134105 (2015). DOI: 10.1063/1.4916715.

[186]   P. D. Lomenzo, Q. Takmeel, C. Zhou, et al. "The effects of layering in ferroelectric Si-doped HfO_2 thin films". In: *Applied Physics Letters* 105.7, 072906 (2014). DOI: 10.1063/1.4893738.

[187] P. D. Lomenzo, P. Zhao, Q. Takmeel, et al. "Ferroelectric phenomena in Si-doped HfO$_2$ thin films with TiN and Ir electrodes". In: *Journal of Vacuum Science & Technology B, Nanotechnology and Microelectronics: Materials, Processing, Measurement, and Phenomena* 32.3, 03D123 (2014). DOI: 10.1116/1.4873323.

[188] A. J. Lovinger. "Ferroelectric polymers". In: *Science* 220.4602 (1983), pp. 1115–1121. DOI: 10.1126/science.220.4602.1115.

[189] J. Lu, J. Lv, X. Liang, et al. "Improved approach to measure the direct flexoelectric coefficient of bulk polyvinylidene fluoride". In: *Journal of Applied Physics* 119, 094104 (2016). DOI: 10.1063/1.4943069.

[190] N. Lu and I. Ferguson. "III-nitrides for energy production: photovoltaic and thermo-electric applications". In: *Semiconductor Science and Technology* 28.7, 074023 (2013). DOI: 10.1088/0268-1242/28/7/074023.

[191] I. Lubomirsky and O. Stafsudd. "Invited Review Article: Parctical guide for pyro-electric measurements". In: *Review of Scientific Instruments* 82, 051101 (2012). DOI: 10.1063/1.4709621.

[192] M. Magnuson, M. Mattesini, C. Höglund, et al. "Electronic structure of GaN and Ga investigated by soft x-ray spectroscopy and first-principles methods". In: *Physical Review B* 81.8, 085125 (2010). DOI: 10.1103/PhysRevB.81.085125.

[193] E. Malguth, A. Hoffmann, W. Gehlhoff, et al. "Structural and Electronic Properties of Fe^{3+} and Fe^{2+} Centers in GaN from Optical and EPR Experiments". In: *Physical Review B* 74, 165202 (16 2006). DOI: 10.1103/PhysRevB.74.165202.

[194] C. Mart, T. Kämpfe, S. Zybell, et al. "Layer thickness scaling and wake-up effect of pyroelectric response in Si-doped HfO$_2$". In: *Applied Physics Letters* 112.5, 052905 (2018). DOI: 10.1063/1.5019308.

[195] C. Mart, W. Weinreich, M. Czernohorsky, et al. "CMOS Compatible Pyroelectric Applications Enabled by Doped HfO$_2$ Films on Deep-Trench Structures". In: *2018 48th European Solid-State Device Research Conference (ESSDERC)*. 2018, pp. 130–133. DOI: 10.1109/ESSDERC.2018.8486864.

[196] S. Martin, N. Baboux, D. Albertini, et al. "A new technique based on current mea-surement for nanoscale ferroelectricity assessment: Nano-positive up negative down". In: *Review of Scientific Instruments* 88.2, 023901 (2017). DOI: 10.1063/1.4974953.

[197] D. Marty-Dessus, L. Berquez, A. Petre, et al. "Space charge cartography by FLIMM: a three dimensional approach". In: *Journal of Physics D: Applied Physics* 35 (2002), pp. 3249–3256. DOI: 10.1088/0022-3727/35/24/316.

[198] R. Materlik, C. Künneth, and A. Kersch. "The origin of ferroelectricity in Hf$_{1-x}$Zr$_x$O$_2$: A computational investigation and a surface energy model". In: *Journal of Applied Physics* 117.13, 134109 (2015). DOI: 10.1063/1.4916707.

[199] R. Materlik, C. Künneth, T. Mikolajick, et al. "The impact of charge compensated and uncompensated strontium defects on the stabilization of the ferroelectric phase in HfO$_2$". In: *Applied Physics Letters* 111.8, 082902 (2017). DOI: 10.1063/1.4993110.

[200] S. C. Mathur, A. K. Batra, and H. Singh. "Dielectric and pyroelectric studies on TGS, TGFB and TGS-TGFB system". In: *Ferroelectrics* 39 (1981), pp. 1197–1200. DOI: 10.1080/00150198108219608.

[201] K. Matocha, T. P. Chow, and R. J. Gutmann. "Positive flatband voltage shift in MOS capacitors on n-type GaN". In: *IEEE Electron Device Letters* 23.2 (2002), pp. 79–81. DOI: 10.1109/55.981312.

[202]   K. Matocha, V. Tilak, and G. Dunne. "Comparison of metal-oxide-semiconductor ca-
        pacitors on c- and m-plane gallium nitride". In: *Applied Physics Letters* 90.12, 123511
        (2007). DOI: 10.1063/1.2716309.

[203]   T. Matsuoka, H. Okamoto, M. Nakao, et al. "Optical bandgap energy of wurtzite InN".
        In: *Applied Physics Letters* 81.7 (2002), pp. 1246–1248. DOI: 10.1063/1.1499753.

[204]   Matsusada Precision. *AMS / AMT Series*. 2018. URL: https://www.matsusada.com/
        pdf/ams_amt.pdf.

[205]   I. M. McKinley, F. Y. Lee, and L. Pilon. "A novel thermomechanical energy conversion
        cycle". In: *Applied Energy* 126 (2014), pp. 78–89. DOI: 10.1063/1.4846735.

[206]   H. D. Megaw. "Ferroelectricity and crystal structure. II". In: *Acta Cryst* 7 (1954),
        pp. 187–194. DOI: 10.1107/S0365110X54000527.

[207]   E. Mehner. "Pyroelektrische Materialien: elektrisch induzierte Phasenumwandlungen,
        thermisch stimulierte Radikalerzeugung". German. PhD thesis. TU Bergakademie
        Freiberg, 2017.

[208]   E. Mehner, S. Jachalke, J. Hanzig, et al. "Anomalous ferroelectricity in P(VDF$_{70}$-
        TrFE$_{30}$)". In: *Ferroelectrics* 510 (2017), pp. 1–20. DOI: 10.1080/00150193.2017.
        1328249.

[209]   A. Mellinger, R. Singh, M. Wegener, et al. "Three-dimensional mapping of the polar-
        ization profiles with thermal pulses". In: *Applied Physics Letters* 86 (2005), p. 082903.
        DOI: 10.1063/1.1870124.

[210]   N. Menou, C. Muller, I. S. Baturin, et al. "Polarization fatigue in PbZr$_{0.45}$Ti$_{0.55}$O$_3$-
        based capacitors studied from high resolution synchrotron x-ray diffraction". In: *Jour-
        nal of Applied Physics* 97.6, 064108 (2005). DOI: 10.1063/1.1870098.

[211]   D. A. B. Miller, D. S. Chemla, T. C. Damen, et al. "Band-Edge Electroabsorption in
        Quantum Well Structures: The Quantum-Confined Stark Effect". In: *Physical Review
        Letters* 53.22 (1984), pp. 2173–2176. DOI: 10.1103/PhysRevLett.53.2173.

[212]   S. L. Miller, R. D. Nasby, J. R. Schwank, et al. "Device modeling of ferroelectric
        capacitors". In: *Journal of Applied Physics* 68.12 (1990), pp. 6463–6471. DOI: 10.
        1063/1.346845.

[213]   T. Mizutani, T. Yamada, and M. Ieda. "Thermally stimulated currents in polyvinyli-
        dene fluoride: I. Unstretched α-form PVDF". In: *Journal of Physics D: Applied Physics*
        14.6 (2000), pp. 1139–1147. DOI: 10.1088/0022-3727/14/6/022.

[214]   T. Mizutani, T. Yamada, and M. Ieda. "Thermally stimulated currents in polyvinyli-
        dene fluoride: II. Effects of stretching". In: *Journal of Physics D: Applied Physics* 15.2
        (2000), pp. 289–297. DOI: 10.1088/0022-3727/15/2/014.

[215]   B. Monemar, P. P. Paskov, and A. Kasic. "Optical properties of InN—the bandgap
        question". In: *Superlattices and Microstructures* 38.1 (2005), pp. 38–56. DOI: 10.1016/
        j.spmi.2005.04.006.

[216]   W. J. Moore, J. A. Freitas Jr., G. C. B. Braga, et al. "Identification of Si and
        O donors in hydride-vapor-phase epitaxial GaN". In: *Applied Physics Letters* 79.16
        (2001), pp. 2570–2572. DOI: 10.1063/1.1411985.

[217]   M. A. Moram and S. Zhang. "ScGaN and ScAlN: emerging nitride materials". In: *Jour-
        nal of Materials Chemistry A* 2.17 (2014), pp. 6042–6050. DOI: 10.1039/c3ta14189f.

[218]   O. F. Mosotti. "Discussione analitica sull'influenza che l'azione di un mezzo dielettrico
        ha sulla distribuzione dell'elettricità alla superficie di più corpi elettrici disseminato
        in esso". In: *Memorie di Matematica e di Fisica della Società Italiana delle Scienze
        (Modena)* 24 (1850), pp. 49–74.

[219] S. Mueller, C. Adelmann, A. Singh, et al. "Ferroelectricity in Gd-Doped HfO$_2$ Thin Films". In: *ECS Journal of Solid State Science and Technology* 1.6 (2012), N123–N126. DOI: 10.1149/2.002301jss.

[220] S. Mueller, J. Mueller, A. Singh, et al. "Incipient Ferroelectricity in Al-Doped HfO$_2$ Thin Films". In: *Advanced Functional Materials* 22.11 (2012), pp. 2412–2417. DOI: 10.1002/adfm.201103119.

[221] S. Mueller, J. Mueller, A. Singh, et al. "Incipient Ferroelectricity in Al-Doped HfO$_2$ Thin Films". In: *Advanced Functional Materials* 22.11 (2012), pp. 2412–2417. DOI: 10.1002/adfm.201103119.

[222] J. Müller, T. S. Böscke, U. Schröder, et al. "Ferroelectricity in Simple Binary ZrO$_2$and HfO$_2$". In: *Nano Letters* 12.8 (2012), pp. 4318–4323. DOI: 10.1021/nl302049k.

[223] J. Müller, P. Polakowski, S. Mueller, et al. "Ferroelectric Hafnium Oxide Based Materials and Devices: Assessment of Current Status and Future Prospects". In: *ECS Journal of Solid State Science and Technology* 4.5 (2015), N30–N35. DOI: 10.1149/2.0081505jss.

[224] J. Müller, U. Schröder, T. S. Böscke, et al. "Ferroelectricity in yttrium-doped hafnium oxide". In: *Journal of Applied Physics* 110.11, 114113 (2011). DOI: 10.1063/1.3667205.

[225] A. Munkholm, G. B. Stephenson, J. A. Eastman, et al. "In situ Studies of the Effect of Silicon on GaN Growth Modes". In: *Journal of Crystal Growth* 221.1–4 (2000), pp. 98–105. ISSN: 0022-0248. DOI: 10.1016/S0022-0248(00)00656-4.

[226] S. Nakamura, N. Iwasa, M. Senoh, et al. "Hole Compensation Mechanism of P-Type GaN Films". In: *Japanese Journal of Applied Physics* 31.Part 1, No. 5A (1992), pp. 1258–1266. DOI: 10.1143/JJAP.31.1258.

[227] S. Nakamura, T. Mukai, and M. Senoh. "High-brightness InGaN/AlGaN double-hetero-structure blue-green-light-emitting diodes". In: *Journal of Applied Physics* 76.12 (1994), pp. 8189–8191. DOI: 10.1063/1.357872.

[228] S. Nakamura, T. Mukai, M. Senoh, et al. "Thermal Annealing Effects on P-Type Mg-Doped GaN Films". In: *Japanese Journal of Applied Physics* 31.Part 2, No. 2B (1992), pp. L139–L142. DOI: 10.1143/JJAP.31.L139.

[229] K. Nassau and H. J. Levinstein. "Ferroelectric Behavior of Lithium Niobate". In: *Applied Physics Letters* 7.3 (1965), pp. 69–70. DOI: 10.1063/1.1754304.

[230] A. Navid and L. Pilon. "Pyroelectric energy harvesting using Olsen cycles in purified and porous poly(vinylidene fluoride-trifluoroethylene)[P(VDF-TrFE)] thin films". In: *Smart Materials and Structures* 20.2 (2011), p. 025012. DOI: 10.1088/0964-1726/20/2/025012.

[231] N. Neumann, R. Köhler, and G. Hofmann. "Pyroelectric thin film sensors and arrays based on P(VDF/TrFE)". In: *Integrated Ferroelectrics* 6.1-4 (1995), pp. 213–230. DOI: doi:10.1080/10584589508019366.

[232] D. A. Neumayer and J. G. Ekerdt. "Growth of Group III Nitrides. A Review of Precursors and Techniques". In: *Chemistry of Materials* 8.1 (1996), pp. 9–25. DOI: 10.1021/cm950108r.

[233] R. E. Newnham. *Properties of Materials: Anisotropy, Symmetry, Structure.* Oxford University Press, 2004. ISBN: 9780198520757.

[234] R. E. Newnham, D. P. Skinner, and L. E. Cross. "Connectivity and piezoelectric-pyroelectric composites". In: *Materials Research Bulletin* 13.5 (1978), pp. 525–536. DOI: 10.1016/0025-5408(78)90161-7.

[235]   H. Nguyen, A. Navid, and L. Pilon. "Pyroelectric energy converter using co-polymer P(VDF-TrFE) and Olsen cycle for waste heat energy harvesting". In: *Applied Thermal Engineering* 30.14-15 (2010), pp. 2127–2137. DOI: `10.1016/j.applthermaleng.2010.05.022`.

[236]   Y. Ni, L. Li, L. He, et al. "Dependence of carbon doping concentration on the strain-state and properties of GaN grown on Si substrate". In: *Superlattices and Microstructures* 120 (2018), pp. 720–726. DOI: `10.1016/j.spmi.2018.06.012`.

[237]   D. Nilsson, E. Janzén, and A. Kakanakova-Georgieva. "Lattice parameters of AlN bulk, homoepitaxial and heteroepitaxial material". In: *Journal of Physics D: Applied Physics* 49.17, 175108 (2016). DOI: `10.1088/0022-3727/49/17/175108`.

[238]   O. Ohtaka, H. Fukui, T. Kunisada, et al. "Phase Relations and Volume Changes of Hafnia under High Pressure and High Temperature". In: *Journal of the American Ceramic Society* 84.6 (2004), pp. 1369–1373. DOI: `10.1111/j.1151-2916.2001.tb00843.x`.

[239]   M. B. Okatan and S. P. Alpay. "Imprint in ferroelectric materials due to space charges: A theoretical analysis". In: *Applied Physics Letters* 95.9, 092902 (2009). DOI: `10.1063/1.3222871`.

[240]   R. B. Olsen, J. M. Briscoe, D. A. Bruno, et al. "A pyroelectric energy converter which employs regeneration". In: *Ferroelectrics* 38.1 (1981), pp. 975–978. DOI: `10.1080/00150198108209595`.

[241]   T. Olsen, U. Schröder, S. Müller, et al. "Co-sputtering yttrium into hafnium oxide thin films to produce ferroelectric properties". In: *Applied Physics Letters* 101.8, 082905 (2012). DOI: `10.1063/1.4747209`.

[242]   Omega Engineering. *Very High Temperature Thermocouple Probes*. URL: `https://www.omega.co.uk/pptst/XTA-W5R26.html` (visited on 06/19/2018).

[243]   C. M. Othon and S. Ducharme. "Polarization patterning by laser-induced phase change in ferroelectric polymer films". In: *Applied Physics A* 104 (2011), pp. 727–731. DOI: `10.1007/s00339-011-6329-9`.

[244]   A. Pal, V. K. Narasimhan, S. Weeks, et al. "Enhancing ferroelectricity in dopant-free hafnium oxide". In: *Applied Physics Letters* 110.2, 022903 (2017). DOI: `10.1063/1.4973928`.

[245]   M. H. Park, C.-C. Chung, T. Schenk, et al. "Origin of Temperature-Dependent Ferroelectricity in Si-Doped HfO_2". In: *Advanced Electronic Materials* 4.4, 1700489 (2018). DOI: `10.1002/aelm.201700489`.

[246]   M. H. Park, H. J. Kim, Y. J. Kim, et al. "Evolution of phases and ferroelectric properties of thin $Hf_{0.5}Zr_{0.5}O_2$ films according to the thickness and annealing temperature". In: *Applied Physics Letters* 102.24, 242905 (2013). DOI: `10.1063/1.4811483`.

[247]   M. H. Park, H. J. Kim, Y. J. Kim, et al. "Toward a multifunctional monolithic device based on pyroelectricity and the electrocaloric effect of thin antiferroelectric $Hf_xZr_{1-x}O_2$ films". In: *Nano Energy* 12.C (2014), pp. 131–140. DOI: `10.1016/j.nanoen.2014.09.025`.

[248]   M. H. Park, Y. H. Lee, H. J. Kim, et al. "Ferroelectricity and Antiferroelectricity of Doped Thin HfO_2-Based Films". In: *Advanced Materials* 27.11 (2015), pp. 1811–1831. DOI: `10.1002/adma.201404531`.

[249]   M. H. Park, T. Schenk, C. M. Fancher, et al. "A comprehensive study on the structural evolution of HfO_2 thin films doped with various dopants". In: *Journal of Materials Chemistry C* 5.19 (2017), pp. 4677–4690. DOI: `10.1039/C7TC01200D`.

[250] M. R. Park, Y. Abbas, H. Abbas, et al. "Resistive switching characteristics in hafnium oxide, tantalum oxide and bilayer devices". In: *Microelectronic Engineering* 159.C (2016), pp. 190–197. DOI: 10.1016/j.mee.2016.03.043.

[251] J. Parravicini, J. Safioui, V. Degiorgio, et al. "All-optical technique to measure the pyroelectric coefficient in electro-optic crystals". In: *Journal of Applied Physics* 109.3, 033106 (2011). DOI: 10.1063/1.3544069.

[252] P. Paufler. *Physikalische Kristallographie.* Akademie-Verlag Berlin, 1986.

[253] Q. Peng and R. E. Cohen. "Origin of pyroelectricity in $LiNbO_3$". In: *Physical Review B* 83.22, 220103 (2011). DOI: 10.1103/PhysRevB.83.220103.

[254] M. Pešić, F. P. G. Fengler, L. Larcher, et al. "Physical Mechanisms behind the Field-Cycling Behavior of HfO_2-Based Ferroelectric Capacitors". In: *Advanced Functional Materials* 26.25 (2016), pp. 4601–4612. DOI: 10.1002/adfm.201600590.

[255] B. W. Peterson, S. Ducharme, V. M. Fridkin, et al. "Mapping surface polarization in thin films of the ferroelectric polymer P(VDF-TrFE)". In: *Ferroelectrics* 304 (2004), pp. 51–54. DOI: 10.1080/00150190490454495.

[256] PI Ceramics. *Piezoelektrische Materialien.* URL: https://www.piceramic.de/de/piezo-technologie/piezoelektrische-materialien (visited on 06/22/2018).

[257] G. Piazza, V. Felmetsger, P. Muralt, et al. "Piezoelectric aluminum nitride thin films for microelectromechanical systems". In: *MRS Bulletin* 37.11 (2012), pp. 1051–1061. DOI: 10.1557/mrs.2012.268.

[258] Y. Ping, J. Yadong, N. Neumann, et al. "Application of Single-crystalline PMN-PT and PIN-PMN-PT in High-Performance Pyroelectric Detectors". In: *Ultrasonics, Ferroelectrics and Frequency Control, IEEE Transactions on* 59.9 (2012), pp. 1983–1989. DOI: 10.1109/TUFFC.2012.2417.

[259] L. Pintilie and M. Alexe. "Ferroelectric-like hysteresis loop in nonferroelectric systems". In: *Applied Physics Letters* 87.11, 112903 (2005). DOI: 10.1063/1.2045543.

[260] B. Ploss, R. Emmerich, and S. Bauer. "Thermal wave probing of pyroelecric distributions in the surface region of ferroelectric materials: A new method for the analysis". In: *Journal of Applied Physics* 72.11 (1992), pp. 5363–5370. DOI: 10.1063/1.351975.

[261] B. Ploss, B. Ploss, and F. Shin. "A General Formula for the Effective Pyroelectric Coefficient of Composites". In: *IEEE Transactions on Dielectrics and Electrical Insulation* 13.5 (2006), pp. 1170–1176. DOI: 10.1109/TDEI.2006.247846.

[262] B. Ploss, B. Ploss, F. Shin, et al. "Pyroelectric Activity of Ferroelectric PT/PVDF-TrFE". In: *IEEE Transactions on Dielectrics and Electrical Insulation* 7.4 (2000), pp. 517–522. DOI: 10.1109/94.868071.

[263] B. Ploss and S. Bauer. "Characterization of materials for integrated pyroelectric sensors". In: *Sensors and Actuators A: Physical* 26.1-3 (1991), pp. 407–411. DOI: 10.1016/0924-4247(91)87023-V.

[264] P. Polakowski and J. Müller. "Ferroelectricity in undoped hafnium oxide". In: *Applied Physics Letters* 106.23, 232905 (2015). DOI: 10.1063/1.4922272.

[265] P. Polakowski, S. Riedel, W. Weinreich, et al. "Ferroelectric deep trench capacitors based on Al:HfO_2 for 3D nonvolatile memory applications". In: *2014 IEEE 6th International Memory Workshop (IMW).* IEEE, 2014. DOI: 10.1109/IMW.2014.6849367.

[266] A. Y. Polyakov, N. B. Smirnov, A. V. Govorkov, et al. "Properties of Fe-doped, thick, freestanding GaN Crystals grown by Hydride Vapor Phase Epitaxy". In: *Journal of Vacuum Science & Technology B* 25.3 (2007), pp. 686–690. DOI: http://dx.doi.org/10.1116/1.2718962.

[267]   S. T. Popescu, A. Petris, and I. Vlad. "Interferometric measurement of the pyroelectric coefficient in lithium niobate". In: *Journal of Applied Physics* 113.4, 043101 (2013). DOI: `10.1063/1.4788696`.

[268]   S. Porowski. "Growth and properties of single crystalline GaN substrates and homoepitaxial layers". In: *Materials Science and Engineering: B* 44.1-3 (1997), pp. 407–413. DOI: `10.1016/S0921-5107(96)01730-8`.

[269]   T. Putzeys and M. Wübbenhorst. "High Sensitivity Scanning Pyroelectric Microscope: Interdigitated Comb Electrodes and Advanced Image Processing". In: *IEEE Transactions on Dielectrics and Electrical Insulation* 19.4 (2012), pp. 1186–1190. DOI: `10.1109/TDEI.2012.6259988`.

[270]   A. Quintel, J. Hullinger, and M. Wübbenhorst. "Analysis of the Polarization Distribution in a Polar Perhydrotriphenylene Inclusion Compound by Scanning Pyroelectri Microscopy". In: *The Journal of Physical Chemistry B* 102.22 (1998), pp. 4277–4283. DOI: `10.1021/jp973350p`.

[271]   K. M. Rabe, M. Dawber, C. Lichtensteiger, et al. "Modern Physics of Ferroelectrics: Essential Background". English. In: *Physics of Ferroelectrics: A Modern Perspective*. Berlin, Heidelberg: Springer Berlin Heidelberg, 2007, pp. 1–30. ISBN: 978-3-540-34591-6. DOI: `10.1007/978-3-540-34591-6_1`.

[272]   K. M. Rabe and U. V. Waghmare. "Ferroelectric phase transitions from first principles". In: *Journal of Physics and Chemistry of Solids* 57.10 (1996), pp. 1397–1403. DOI: `10.1016/0022-3697(96)00004-2`.

[273]   R. Radebaugh. "Behavior of the pyroelectric coefficient at low temperatures". In: *Physical Review Letters* 9 (1978). DOI: `10.1007/b101200`.

[274]   R. Resta. "Quantum-Mechanical Position Operator in Extended Systems". In: *Physical Review Letters* 80.9 (1998), pp. 1800–1803. DOI: `10.1103/PhysRevLett.80.1800`.

[275]   R. Resta and D. Vanderbilt. "Theory of Polarization: A Modern Approach". English. In: *Physics of Ferroelectrics: A Modern Perspective*. Berlin, Heidelberg: Springer Berlin Heidelberg, 2007, pp. 31–68. ISBN: 978-3-540-34591-6. DOI: `10.1007/978-3-540-34591-6_2`.

[276]   C. Richter, T. Schenk, M. H. Park, et al. "Si Doped Hafnium Oxide-A "Fragile" Ferroelectric System". In: *Advanced Electronic Materials* 106, 1700131 (2017). DOI: `10.1002/aelm.201700131`.

[277]   C. Richter, M. Zschornak, D. Novikov, et al. "Picometer polar atomic displacements in strontium titanate determined by resonant X-ray diffraction". In: *Nature Communications* (2018). DOI: `10.1038/s41467-017-02599-6`.

[278]   E. Richter, E. Gridneva, M. Weyers, et al. "Fe-doping in hydride vapor-phase epitaxy for semi-insulating gallium nitride". In: *Journal of Crystal Growth* 456.C (2016), pp. 97–100. DOI: `10.1016/j.jcrysgro.2016.05.016`.

[279]   E. Richter, T. Stoica, U. Zeimer, et al. "Si Doping of GaN in Hydride Vapor-Phase Epitaxy". In: *Journal of Electronic Materials* 42.5 (2012), pp. 820–825. DOI: `10.1007/s11664-012-2373-2`.

[280]   D. Ricinschi and M. Okuyama. "A nucleation-growth model for ferroelectric hysteresis loops with complete and partial switching". In: *Journal of the European Ceramic Society* 25.12 (2005), pp. 2357–2361. DOI: `10.1016/j.jeurceramsoc.2005.03.056`.

[281]   Rigol Technologies. *MSO1000Z/DS1000Z Series Digital Oscilloscope – User Guide*. 2016. URL: `http://beyondmeasure.rigoltech.com/acton/attachment/1579/f-050a/1/-/-/-/-/MSO1000Z%26DS1000Z_UserGuide.pdf`.

[282] H. Roetschi. "New type of loop tracer for ferroelectrics". In: *Journal of Scientific Instruments* 39.4 (1962), pp. 152–153. DOI: 10.1088/0950-7671/39/4/304.

[283] L. T. Romano, C. G. Van de Walle, J. W. Ager, et al. "Effect of Si Doping on Strain, Cracking, and Microstructure in GaN thin Films grown by Metalorganic Chemical Vapor Deposition". In: *Journal of Applied Physics* 87.11 (2000), pp. 7745–7752. DOI: 10.1063/1.373529.

[284] G. A. Rossetti and N. Maffei. "Specific heat study and Landau analysis of the phase transition in $PbTiO_3$ single crystals". In: *Journal of Physics: Condensed Matter* 17.25 (2005), pp. 3953–3963. DOI: 10.1088/0953-8984/17/25/021.

[285] R. Ruh, H. J. Garrett, R. F. Domagala, et al. "The System Zirconia-Hafnia". In: *Journal of the American Ceramic Society* 51.1 (1968), pp. 23–28. DOI: 10.1111/j.1151-2916.1968.tb11822.x.

[286] W. Sakamoto, D. Kanda, and D. K. Das-Gupta. "Dielectric and pyroelectric properties of a composite of ferroelectric ceramic and polyurethane". In: *Materials Research Innovations* 5.6 (2002), pp. 257–260. DOI: 10.1007/s10019-002-0164-8.

[287] X. Sang, E. D. Grimley, T. Schenk, et al. "On the structural origins of ferroelectricity in HfO_2 thin films". In: *Applied Physics Letters* 106.16, 162905 (2015). DOI: 10.1063/1.4919135.

[288] C. B. Sawyer and C. H. Tower. "Rochelle salt as a dielectric". In: *Physical Review* 35.3 (1930), pp. 269–273. DOI: 10.1103/PhysRev.35.269.

[289] A. Saxena, M. Fhaim, V. Gupta, et al. "Pyroelectric properties of phosphoric acid-doped TGS single crystals". In: *Journal of Physics D: Applied Physics* 36 (2003), pp. 3168–3175. DOI: 10.1088/0022-3727/36/24/012.

[290] Y. Saya, S. Watanabe, M. Kawai, et al. "Investigation of Nonswitching Regions in Ferroelectric Thin Films Using Scanning Force Microscopy". In: *Japanese Journal of Applied Physics* 39.6S (2000), pp. 3799–3803. DOI: 10.1143/JJAP.39.3799.

[291] L. B. Schein, P. J. Cressman, and L. E. Cross. "Electrostatic measurements of tertiary pyroelectricity in partially clamped $LiNbO_3$". In: *Ferroelectrics* 22.1 (1979), pp. 945–948. DOI: 10.1080/00150197908239449.

[292] L. B. Schein, P. J. Cressman, and L. E. Cross. "Electrostatic measurements of unusually large secondary pyroelectricity in partially clamped $LiNbO_3$". In: *Ferroelectrics* 22.1 (1979), pp. 937–943. DOI: 10.1080/00150197908239448.

[293] L. B. Schein, P. J. Cressman, and F. M. Tesche. "Electrostatic observations of laser-induced optical damage in $LiNbO_3$". In: *Journal of Applied Physics* 48.11 (1977), p. 4844. DOI: 10.1063/1.323513.

[294] T. Schenk. "Formation of Ferroelectricity in Hafnium Oxide Based Thin Films ". PhD thesis. Technische Universtität Dresden, 2016.

[295] T. Schenk, M. Hoffmann, J. Ocker, et al. "Complex Internal Bias Fields in Ferroelectric Hafnium Oxide". In: *ACS Applied Materials & Interfaces* 7.36 (2015), pp. 20224–20233. DOI: 10.1021/acsami.5b05773.

[296] T. Schenk, S. Mueller, U. Schroeder, et al. "Strontium doped hafnium oxide thin films: Wide process window for ferroelectric memories". In: *2013 43rd European Solid-State Device Research Conference (ESSDERC)*. IEEE, pp. 260–263. DOI: 10.1109/ESSDERC.2013.6818868.

[297] T. Schenk, M. Pešić, M. H. Park, et al. "10 Years Fluorite-type Ferroelectrics – A Survey (Invited)". In: *Toward Oxide-based Electronics, Spring Meeting*. Presentation. Luxembourg, 2017. DOI: 10.13140/RG.2.2.28716.36481.

[298]   T. Schenk, U. Schroeder, M. Pešić, et al. "Electric Field Cycling Behavior of Ferroelectric Hafnium Oxide". In: *ACS Applied Materials & Interfaces* 6.22 (2014), pp. 19744–19751. DOI: `10.1021/am504837r`.

[299]   T. Schenk, E. Yurchuk, and S. Mueller. "About the deformation of ferroelectric hystereses". In: *Applied Physics Reviews* 1.4 (2014), p. 041103. DOI: `10.1063/1.4902396`.

[300]   T. Schenk, M. Hoffmann, C. Richter, et al. "Doped Hafnium Oxide for Ferroelectric Memories (Invited)". In: *MRS Fall Meeting*. Presentation, Symposium KK—Materials and Technology for Non-Volatile Memories, Ferroelectric Memory II, KK6.01. Bosten, MA, 2015, pp. 1–47. DOI: `10.13140/RG.2.1.3912.4567`.

[301]   U. Schroeder, C. Richter, M. H. Park, et al. "Lanthanum-Doped Hafnium Oxide: A Robust Ferroelectric Material". In: *Inorganic Chemistry* 57.5 (2018), pp. 2752–2765. DOI: `10.1021/acs.inorgchem.7b03149`.

[302]   F. Schubert, S. Wirth, F. Zimmermann, et al. "Growth condition dependence of unintentional oxygen incorporation in epitaxial GaN". In: *Science and Technology of Advanced Materials* 17.1 (2016), pp. 239–243. DOI: `10.1080/14686996.2016.1178565`.

[303]   J. F. Scott. "Applications of Modern Ferroelectrics". In: *Science* 315.5814 (2007), pp. 954–959. DOI: `10.1126/science.1129564`.

[304]   J. F. Scott. "Ferroelectrics go bananas". In: *Journal of Physics: Condensed Matter* 20.2, 021001–3 (2007). DOI: `10.1088/0953-8984/20/02/021001`.

[305]   C. H. Seager, A. F. Wright, J. Yu, et al. "Role of Carbon in GaN". In: *Journal of Applied Physics* 92.11 (2002), pp. 6553–6560. DOI: `http://dx.doi.org/10.1063/1.1518794`.

[306]   G. Sebald, L. Seveyrat, D. Guyomar, et al. "Electrocaloric and pyroelectric properties of $0.75Pb(Mg_{1/3}Nb_{2/3})O_3$-$0.25PbTiO_3$ single crystals". In: *Journal of Applied Physics* 100.12, 124112 (2006). DOI: `10.1063/1.2407271`.

[307]   O. N. Sergeeva, A. A. Bogomolov, A. V. Solnyshkin, et al. "SEM, Dielectric, Pyroelectric, and Piezoelectric Response of Thin Epitaxial AlN Films Grown on SiC/Si Substrate". In: *Ferroelectrics* 477.1 (2015), pp. 121–130. DOI: `10.1080/00150193.2015.1000144`.

[308]   G. M. Sessler. *Topics in Applied Physics: Electrets*. Ed. by G. Sessler. Vol. 33. Springer Verlag Berlin/Heidelberg/NewYork, 1980. DOI: `10.1002/actp.1980.010311010`.

[309]   N. Setter. "What is a ferroelectric - a materials designer perspective". In: *Ferroelectrics* 500.1 (2016), pp. 164–182. DOI: `10.1080/00150193.2016.1232104`.

[310]   Y. V. Shaldin, V. T. Gabriélyan, and S. Matyjasik. "Pyroelectric properties of real $LiNbO_3$ single crystals grown from a congruent melt". In: *Crystallography Reports* 53.5 (2008), pp. 847–852. DOI: `10.1134/S1063774508050209`.

[311]   Y. V. Shaldin and S. Matyjasik. "Pyroelectric properties of AlN wide-gap semiconductor in the temperature range of 4.2 - 300 K". In: *Semiconductors* 45.9 (2011), pp. 1117–1123. DOI: `10.1134/S106378261109017X`.

[312]   Y. V. Shaldin and S. Matyjasik. "Pyroelectric properties of AlN wide-gap semiconductor in the temperature range of 4.2–300 K". In: *Semiconductors* 45.9 (2011), pp. 1117–1123. DOI: `10.1134/S106378261109017X`.

[313]   Y. Sharma, D. Barrionuevo, R. Agarwal, et al. "Ferroelectricity in Rare-Earth Modified Hafnia Thin Films Deposited by Sequential Pulsed Laser Deposition". In: *ECS Solid State Letters* 4.11 (2015), N13–N16. DOI: `10.1149/2.0031511ssl`.

[314] A. Shikanaia, H. Fukahori, Y. Kawakami, et al. "Optical properties of Si-, Ge- and Sn-doped GaN". In: *physica status solidi (b)* 235.1 (2003), pp. 26–30. DOI: 10.1002/pssb.200301525.

[315] M. Simhony and A. Shaulov. "Measurement of the pyroelectric coefficient and permittivity from the pyroelectric response to step radiation signals in ferroelectrics". In: *Applied Physics Letters* 21.8 (1972), pp. 375–377. DOI: 10.1063/1.1654419.

[316] N. B. Singh, A. Berghmans, H. Zhang, et al. "Physical vapor transport growth of large AlN crystals". In: *Journal of Crystal Growth* 250.1-2 (2003), pp. 107–112. DOI: 10.1016/S0022-0248(02)02235-2.

[317] J. K. Sinha. "Modified Sawyer and Tower circuit for the investigation of ferroelectric samples". In: *Journal of Scientific Instruments* 42.9 (1965), p. 696. DOI: 10.1088/0950-7671/42/9/308.

[318] N. Sinha, G. E. Wabiszewski, R. Mahameed, et al. "Piezoelectric aluminum nitride nanoelectromechanical actuators". In: *Applied Physics Letters* 95.5, 053106 (2009). DOI: 10.1063/1.3194148.

[319] S. W. Smith, A. R. Kitahara, M. A. Rodriguez, et al. "Pyroelectric response in crystalline hafnium zirconium oxide ($Hf_{1-x}Zr_xO_2$) thin films". In: *Applied Physics Letters* 110.7, 072901 (2017). DOI: 10.1063/1.4976519.

[320] J. Song, H. Lu, A. Gruverman, et al. "Polarization imaging in ferroelectric polymer thin film capacitors by pyroelectric scanning microscopy". In: *Applied Physics Letters* 104.19, 192901 (2014). DOI: 10.1063/1.4875960.

[321] N. A. Spaldin. "A beginner's guide to the modern theory of polarization". In: *Journal of Solid State Chemistry* 195 (2012), pp. 2–10. DOI: 10.1016/j.jssc.2012.05.010.

[322] L Spieß, G. Teichert, R. Schwarzer, et al. *Moderne Röntgenbeugung*. Vieweg+Teubner Verlag, 2009. ISBN: 978-3-8349-9434-9. DOI: 10.1007/978-3-8349-9434-9.

[323] B. Stadlober, J. Groten, M. Zirkl, et al. "Scanning Pyroelectric Microscopy for Characterizing Large-Area Printed Ferroelectric Sensors on the Nanoscale". In: *Proceedings of SPIE* 8479, 847903 (2012). DOI: 10.1117/12.946213.

[324] G. E. Stan, M. Botea, G. A. Boni, et al. "Electric and pyroelectric properties of AlN thin films deposited by reactive magnetron sputtering on Si substrate". In: *Applied Surface Science* 353 (2015), pp. 1195–1202. DOI: 10.1016/j.apsusc.2015.07.059.

[325] L. A. Starman, V. S. Vasilyev, C. M. Holbrook, et al. "Pyroelectric AlN Thin Films Used as a MEMS IR Sensing Material". In: *MEMS and Nanotechnology, Volume 8*. Cham: Springer International Publishing, 2014, pp. 55–66. DOI: 10.1007/978-3-319-07004-9_7.

[326] S. Starschich and U. Boettger. "An extensive study of the influence of dopants on the ferroelectric properties of HfO_2". In: *Journal of Materials Chemistry C* 5.2 (2017), pp. 333–338. DOI: 10.1039/C6TC04807B.

[327] S. Starschich, D. Griesche, T. Schneller, et al. "Chemical solution deposition of ferroelectric yttrium-doped hafnium oxide films on platinum electrodes". In: *Applied Physics Letters* 104.20, 202903 (2014). DOI: 10.1063/1.4879283.

[328] S. Starschich, T. Schenk, U. Schroeder, et al. "Ferroelectric and piezoelectric properties of $Hf_{1-x}Zr_xO_2$ and pure ZrO_2 films". In: *Applied Physics Letters* 110.18, 182905 (2017). DOI: 10.1063/1.4983031.

[329] S. Starschicht and U. Böttger. "Doped ZrO_2 for Improved Piezoelectric Properties". In: *Journal of Applied Physics* 123.4, 044101 (2017). DOI: 10.1063/1.4997681.

[330]   M. Stewart and M. Cain. "Spatial Characterization of Piezoelectric Materials Using the Scanning Laser Intentisity Modulation Method (LIMM)". In: *Journal of the American Ceramic Society* 91.7 (2008), pp. 2176–2181. DOI: 10.1111/j.1551-2916.2008.02401.x.

[331]   M. Stewart and M. Cain. "Use of scanning LIMM (Laser Intensity Modulation Method) to characterise polarisation variability in dielectric material". In: *Journal of Physics: Conference Series* 183, 012001 (2009). DOI: 10.1088/1742-6596/183/1/012001.

[332]   H. Stöcker. "Pyroelektrische Röntgenstrahlerzeugung mit Lithiumniobat". German. Diploma Thesis. Dresden: Technische Universität Dresden, 2007.

[333]   SurfaceNet. *Crystals*. URL: http://www.surfacenet.de/crystals-281.html (visited on 06/22/2018).

[334]   H. Sussner, D. E. Horne, and D. Y. Yoon. "A new method for determining the pyroelectric coefficient of thin polymer films using dielectric heating". In: *Applied Physics Letters* 32.3 (1978), pp. 137–139. DOI: 10.1063/1.89974.

[335]   B. Szigeti. "Low-Temperature Behavior of Pyroelectricity—A Reply". In: *Physical Review Letters* 37.12 (1976), pp. 792–794. DOI: 10.1103/PhysRevLett.37.792.

[336]   B. Szigeti. "Temperature Dependence of Pyroelectricity". In: *Physical Review Letters* 35.22 (1975), pp. 1532–1534. DOI: 10.1103/PhysRevLett.35.1532.

[337]   M. Tachibana, T. Kolodiazhnyi, and E. Takayama-Muromachi. "Thermal conductivity of perovskite ferroelectrics". In: *Applied Physics Letters* 93.9, 092902 (2008). DOI: 10.1063/1.2978072.

[338]   T. Takeuchi, S. Sota, M. Katsuragawa, et al. "Quantum-Confined Stark Effect due to Piezoelectric Fields in GaInN Strained Quantum Wells". In: *Japanese Journal of Applied Physics* 36.Part 2, No. 4A (1997), pp. L382–L385. DOI: 10.1143/JJAP.36.L382.

[339]   T. Takeuchi, C. Wetzel, S. Yamaguchi, et al. "Determination of piezoelectric fields in strained GaInN quantum wells using the quantum-confined Stark effect". In: *Applied Physics Letters* 73.12 (1998), pp. 1691–1693. DOI: 10.1063/1.122247.

[340]   Y. Tang, X. Wan, X. Zhao, et al. "Large pyroelectric response in relaxor-based ferroelectric $(1-x)Pb(Mg_{1/3}Nb_{2/3})O_3$ - $xPbTiO_3$ single crystals". In: *Journal of Applied Physics* 98.8, 084104 (2005). DOI: 10.1063/1.2106014.

[341]   Tektronix. *Low Level Measurements Handbook: Precision DC Current, Voltage, and Resistance Measurements*. 7th ed. 2016.

[342]   C. Tholander, I. A. Abrikosov, L. Hultman, et al. "Volume matching condition to establish the enhanced piezoelectricity in ternary $(Sc,Y)_{0.5}(Al,Ga,In)_{0.5}N$ alloys". In: *Physical Review B* 87.9, 094107 (2013). DOI: 10.1103/PhysRevB.87.094107.

[343]   X. Tian and A. Toriumi. "New opportunity of ferroelectric tunnel junction memory with ultrathin HfO_2-based oxides". In: *2017 IEEE Electron Devices Technology and Manufacturing Conference (EDTM)*. IEEE, 2017, pp. 36–64. DOI: 10.1109/EDTM.2017.7947507.

[344]   S. Tiedke and T. Schmitz. "Electrical Characterization of Nanoscale Ferroelectric Structures". In: *Nanoscale Characterisation of Ferroelectric Materials: Scanning Probe Microscopy Approach*. Ed. by M. Alexe and A. Gruverman. Springer Berlin Heidelberg, 2004. ISBN: 978-3-662-08901-9. DOI: 10.1007/978-3-662-08901-9_3.

[345] K. Tonisch, V. Cimalla, C. Foerster, et al. "Piezoelectric properties of polycrystalline AlN thin films for MEMS application". In: *Sensors and Actuators A: Physical* 132.2 (2006), pp. 658–663. DOI: 10.1016/j.sna.2006.03.001.

[346] T. C. U. Tromm, J. Zhang, J. Schubert, et al. "Ferroelectricity in Lu doped HfO_2 layers". In: *Applied Physics Letters* 111.14, 142904 (2017). DOI: 10.1063/1.4998336.

[347] A. Usikov, V. Soukhoveev, O. Kovalenkov, et al. "Accumulation of Background Impurities in Hydride Vapor Phase Epitaxy Grown GaN Layers". In: *Japanese Journal of Applied Physics* 52.8S (2013), 08JB22. DOI: 10.7567/JJAP.52.08JB22.

[348] W. Utsumi, H. Saitoh, H. Kaneko, et al. "Congruent melting of gallium nitride at 6 GPa and its application to single-crystal growth". In: *Nature Materials* 2.11 (2003), pp. 735–738. DOI: 10.1038/nmat1003.

[349] J. Van Houdt. "3D Memories and Ferroelectrics". In: *2017 IEEE International Memory Workshop (IMW)*. IEEE, 2017. DOI: 10.1109/IMW.2017.7939066.

[350] D. Vanderbilt and M. Cohen. "Monoclinic and triclinic phases in higher-order Devonshire theory". In: *Physical Review B* 63, 094108 (9 2001). DOI: 10.1103/PhysRevB.63.094108.

[351] V. V. Voronenkov, N. I. Bochkareva, R. I. Gorbunov, et al. "Two Modes of HVPE Growth of GaN and Related Macrodefects". In: *Physica Status Solidi (c)* 10.3 (2013), pp. 468–471. ISSN: 1610-1642. DOI: 10.1002/pssc.201200701.

[352] C.-M. Wang, K. Lau, and Q. Wang. "Dynamic hysteresis and scaling behaviours of lead-free $0.94Bi_{0.5}Na_{0.5}TiO_3$-$0.06BaTiO_3$ bulk ceramics". In: *RSC Advances* 6 (2016), pp. 30148–30153. DOI: 10.1039/C5RA27994A.

[353] H. Wang and A. B. Chen. "Calculation of shallow donor levels in GaN". In: *Journal of Applied Physics* 87.11 (2000), pp. 7859–7863. DOI: 10.1063/1.373467.

[354] J. Wang, H. P. Li, and R. Stevens. "Hafnia and hafnia-toughened ceramics". In: *Journal of Materials Science* 27 (1992), pp. 5397–5430. DOI: 10.1007/BF00541601.

[355] W. L. Warren, B. A. Tuttle, D. Dimos, et al. "Imprint in Ferroelectric Capacitors". In: *Japanese Journal of Applied Physics* 35.Part 1, No. 2B (1996), pp. 1521–1524. DOI: 10.1143/JJAP.35.1521.

[356] H. Wei and Y. Chen. "Synthesis and properties of $Pb(Zn_{1/3}Nb_{2/3})O_3$ modified $Pb(Zr_{0.95}Ti_{0.05})O_3$ pyroelectric ceramics". In: *Ceramics International* 40 (2014), pp. 8637–8643. DOI: 10.1016/j.ceramint.2014.01.081.

[357] T. Weigel. "Elektronendichteanalyse von pyroelektrischem $LiMO_3$-Röntgeneinkristalldiffraktometrie und ab-*initio* Modellierung". MA thesis. Leipziger Str. 23, 09599 Freiberg: Institut of Experimental Physics, TU Bergakademie Freiberg, 2017.

[358] T. Weigel, T. Leisegang, and D. C. Meyer. "Elektronendichteanalyse von pyroelektrischem $LiMO_3$- Röntgeneinkristalldiffraktometrie und ab-*initio* Modellierung". In: (2019). In preparation.

[359] C. Weißmantel and C. Hamann. *Grundlagen der Festkörperphysik*. Springer-Verlag Berlin Heidelberg, 1979. ISBN: 978-3-642-67116-6.

[360] R. W. Whatmore, O Molter, and C. P. Shaw. "Electrical properties of Sb and Cr-doped $PbZrO_3$-$PbTiO_3$-$PbMg_{1/3}Nb_{2/3}O_3$ ceramics". In: *Journal of the European Ceramic Society* 23 (2003), pp. 721–728. DOI: 10.1016/S0955-2219(02)00162-0.

[361] R. W. Whatmore, A. Patel, N. M. Shorrocks, et al. "Ferroelectric materials for thermal ir sensors state-of-the-art and perspectives". In: *Ferroelectrics* 104.1 (1990), pp. 269–283. DOI: 10.1080/00150199008223829.

[362] R. Whatmore. "Characterization of Pyroelectric Materials". In: *Characterization of Ferroelectric Bulk Materials and Thin Films*. Ed. by M. G. Cain, J. Tesar, and M. Veghel. Springer, 2014. ISBN: 978-1-4020-9310-4. DOI: `10.1007/978-1-4020-9311-1`.

[363] G. G. Wiseman. *Investigation of Electrocaloric Effects in Ferroelectric Substances*. National Aeronautics and Space Administration, 1968, pp. 1–77.

[364] G. G. Wiseman and J. K. Kuebler. "Electrocaloric Effectin Ferroelectric Rochelle Salt)". In: *Physical Review* 131.5 (1963), pp. 2023–2027. DOI: `10.1103/PhysRev.131.2023`.

[365] A. Wolos, M. Palczewska, M. Zajac, et al. "Optical and Magnetic Properties of Mn in Bulk GaN". In: *Physical Review B* 69, 115210 (11 2004). DOI: `10.1103/PhysRevB.69.115210`.

[366] K. K. Wong, I. o. E. Engineers, and I. Information service. *Properties of Lithium Niobate*. EMIS datareviews series. INSPEC/Institution of Electrical Engineers, 2002. ISBN: 9780852967997.

[367] X. Xu, R. P. Vaudo, and G. R. Brandes. "Fabrication of GaN wafers for electronic and optoelectronic devices". In: *Optical Materials* 23.1–2 (2003). Proceedings of the 8th International Conference on Electronic Materials, IUMRS-ICEM 2002. DOI: `10.1016/S0925-3467(03)00051-X`.

[368] K. Yamamoto, F. Goericke, A. Guedes, et al. "Pyroelectric aluminum nitride micro electromechanical systems infrared sensor with wavelength-selective infrared absorber". In: *Applied Physics Letters* 104.1, 111111 (2014). DOI: `10.1063/1.4869442`.

[369] W. S. Yan, R. Zhang, Z. L. Xie, et al. "A thermodynamic model and estimation of the experimental value of spontaneous polarization in a wurtzite GaN". In: *Applied Physics Letters* 94.4 (2009), pp. 042106–4. DOI: `10.1063/1.3072597`.

[370] W. S. Yan, R. Zhang, Z. L. Xie, et al. "The contributions of the acoustic modes and optical modes to the primary pyroelectric coefficient of GaN". In: *Applied Physics Letters* 94.24, 242111 (2009). DOI: `10.1063/1.3157839`.

[371] W. S. Yan, R. Zhang, X. Q. Xiu, et al. "Temperature dependence of the pyroelectric coefficient and the spontaneous polarization of AlN". In: *Applied Physics Letters* 90.21, 212102 (2007). DOI: `10.1063/1.2741600`.

[372] S. Yao, W. Ren, H. Ji, et al. "High pyroelectricity in lead-free $0.5Ba(Zr_{0.2}Ti_{0.8})O_3$-$0.5(Ba_{0.7}Ca_{0.3}TiO_3)$ ceramics". In: *Journal of Physics D: Applied Physics* 45, 195301 (2012). DOI: `10.1088/0022-3727/45/19/195301`.

[373] P. Yu, Y. Ji, N. Neumann, et al. "Application of Single-crystalline PMN-PT and PIN-PMN-PT in High-Performance Pyroelectric Detectors". In: *IEEE Transactions on Ultrasonics, Ferroelectrics and Frequency Control* 59.9 (2012), pp. 1983–1989. DOI: `10.1109/TUFFC.2012.2417`.

[374] H. J. Zajosz. "The harmonics of the nonlinear pyroelectric current and the simultaneous measurement of thermal diffusivity, pyroelectric coefficient and spontaneous polarization". In: *Ferroelectrics* 67.2 (1986), pp. 187–190. DOI: `10.1080/00150198608245021`.

[375] S. Zarubin, E. Suvorova, M. Spiridonov, et al. "Fully ALD-grown $TiN/Hf_{0.5}Zr_{0.5}O_2/TiN$ stacks: Ferroelectric and structural properties". In: *Applied Physics Letters* 109.19, 192903 (2016). DOI: `10.1063/1.4966219`.

[376] Q. Zhang and R. W. Whatmore. "Improved ferroelectric and pyroelectric properties in Mn-doped lead zirconate titanate thin films". In: *Journal of Applied Physics* 94.8 (2003), pp. 5228–5233. DOI: `10.1063/1.1613370`.

[377] Q. Q. Zhang, H. L. W. Chan, and C. L. Choy. "Dielectric and pyroelectric properties of P(VDF-TrFE) and PCLT–P(VDF-TrFE)0–3 nanocomposite films". In: *Composites Part A: Applied Science and Manufacturing* 30.2 (1999), pp. 163–167. DOI: 10.1016/S1359-835X(98)00113-4.

[378] C. Zhou, A. Ghods, V. G. Saravade, et al. "Review—The Current and Emerging Applications of the III-Nitrides". In: *ECS Journal of Solid State Science and Technology* 6.12 (2017), Q149–Q156. DOI: 10.1149/2.0101712jss.

[379] D. Zhou, J. Xu, Q. Li, et al. "Wake-up effects in Si-doped hafnium oxide ferroelectric thin films". In: *Applied Physics Letters* 103.19, 192904 (2013). DOI: 10.1063/1.4829064.

[380] W. Zhou, Q. Shi, B. F. Woodfield, et al. "Heat capacity of hafnia at low temperature". In: *The Journal of Chemical Thermodynamics* 43.6 (2011), pp. 970–973. DOI: 10.1016/j.jct.2011.02.002.

[381] D. Zhuang, Z. G. Herro, R. Schlesser, et al. "Seeded growth of AlN single crystals by physical vapor transport". In: *Journal of Crystal Growth* 287.2 (2006), pp. 372–375. DOI: 10.1016/j.jcrysgro.2005.11.047.

[382] F. Zimmermann, F. C. Beyer, G. Gärtner, et al. "Origin of orange color in nominally undoped HVPE GaN crystals". In: *Optical Materials* 70 (2017), pp. 127–130. DOI: 10.1016/j.optmat.2017.05.020.

[383] J. Zúñiga-Pérez, V. Consonni, L. Lymperakis, et al. "Polarity in GaN and ZnO: Theory, measurement, growth, and devices". In: *Applied Physics Reviews* 3.4, 041303 (2016). DOI: 10.1063/1.4963919.

Publication List

First Author Publications

1. S. Jachalke*, P. Hofmann*, G. Leibiger, F. S. Habel, E. Mehner, T. Leisegang, D. C. Meyer, T. Mikolajick. "The pyroelectric coefficient of free standing GaN grown by HVPE". in: *Applied Physics Letters* 109.14, 142906 (2016). *These authors contributed equally to this work. DOI: `10.1063/1.4964265`

2. S. Jachalke, E. Mehner, H. Stöcker, J. Hanzig, M. Sonntag, T. Weigel, T. Leisegang, D. C. Meyer. "How to measure the pyroelectric coefficient?" In: *Applied Physics Reviews* 4.2, 021303 (2017). DOI: `10.1063/1.4983118`

3. S. Jachalke, T. Schenk, M. H. Park, U. Schroeder, T. Mikolajick, H. Stöcker, E. Mehner, D. C. Meyer. "Pyroelectricity of silicon-doped hafnium oxide thin films". In: *Applied Physics Letters* 112.14, 142901 (2018). DOI: `10.1063/1.5023390`

Coauthor Contributions

1. R. Belitz, P. Meisner, M. Coeler, U. Wunderwald, J. Friedrich, J. Zosel, M. Schelter, S. Jachalke, E. Mehner. "Waste Heat Energy Harvesting by use of $BaTiO_3$ for Pyroelectric Hydrogen Generation". In: *Energy Harvesting and Systems* 4.3 (2017), pp. 107–113. DOI: `10.1515/ehs-2016-0009`

2. E. Mehner, S. Jachalke, J. Hanzig, T. Leisegang, H. Stöcker, D. C. Meyer. "Anomalous ferroelectricity in $P(VDF_{70}\text{-}TrFE_{30})$". In: *Ferroelectrics* 510 (2017), pp. 1–20. DOI: `10.1080/00150193.2017.1328249`

3. H. Stöcker, J. Hanzig, M. Zschornak, E. Mehner, S. Jachalke, C. Richter, F. Hanzig, F. Meutzner, T. Leisegang, D. C. Meyer. "Strontium titanate: From symmetry changes to functionality". In: *Crystal Research and Technology* 52 (2016), pp. 1–10. DOI: `10.1002/crat.201600222`

4. H. Stöcker, S. Rentrop, B. Abendroth, E. Mehner, S. Jachalke, J. Hanzig, T. Nestler, F. Meutzner, W. Münchgesang, T. Leisegang, D. C. Meyer. "Übergangsmetalloxide – Symmetrie trifft Funktion". In: *Glanzlichter der Forschung an der TU Bergakademie Freiberg 250 Jahre nach ihrer Gründung.* Ed. by U. Groß. Freiberg: Chemnitz Verlag, 2016, pp. 176–185. ISBN: 978-3-944509-26-6

5. H. Stöcker, J. Hanzig, F. Hanzig, M. Zschornak, E. Mehner, S. Jachalke, D. C. Meyer. "Strontium Titanate – Breaking the symmetry". In: *Functional structure design of new high-performance materials via atomic design and defect engineering (ADDE)*. ed. by D. Rafaja. Freiberg: SAXONIA Standortentwicklungs- und Verwaltungsgesellschaft mbH, 2015, pp. 100–113. ISBN: 978-3-934409-68-2

6. J. Hanzig⋆, E. Mehner⋆, S. Jachalke, F. Hanzig, M. Zschornak, C. Richter, T. Leisegang, H. Stöcker, D. C. Meyer. "Dielectric to pyroelectric phase transition induced by defect migration". In: *New Journal of Physics* 17, 023036 (2015). ⋆These authors contributed equally to this work. DOI: 10.1088/1367−2630/17/2/023036

Conference Contributions

Talks

1. S. Jachalke, H. Stöcker, E. Mehner, T. Leisegang, D. C. Meyer. *Neue Pyroelektrika aus der Halbleiterindustrie.* 69. BHT – Freiberger Universitätsforum, FK6, Freiberg, Germany. 07.06.2018

2. S. Jachalke, T. Schenk, M. H. Park, U. Schroeder, T. Mikolajick, H. Stöcker, E. Mehner, D. C. Meyer. *Pyroelectricity of silicon-doped hafnium oxide thin films (invited).* Conference „High-k oxides by ALD", Wroclaw, Poland. 07.–09.03.2018

3. S. Jachalke, P. Hofmann, G. Leibiger, F. S. Habel, E. Mehner, T. Leisegang, D. C. Meyer, T. Mikolajick. *The pyroelectric coefficient of free standing GaN grown by HVPE.* Deutsche Gesellschaft für Kristallzüchtung und Kristallwachstum e.V. – Arbeitskreis Massive Halbleiter, Freiberg, Germany. 11.–12.10.2017

4. S. Jachalke, E. Mehner, H. Stöcker, J. Hanzig, B. Abendroth, T. Leisegang, D. C. Meyer. *Stöchiometriebestimmung in polaren Dielektrika mittels RFA.* XRF-Anwendertreffen Bruker AXS, Essen, Germany. 27.–28.04.2017

5. S. Jachalke, P. Hofmann, G. Leibiger, F. S. Habel, E. Mehner, T. Leisegang, D. C. Meyer, T. Mikolajick. *The pyroelectric coefficient of free standing GaN grown by HVPE.* Frühjahrstagung der Deutschen Physikalischen Gesellschaft, Dresden, Germany, Talk DF 2.7. 19.–24.03.2017

6. S. Jachalke, P. Hofmann, G. Leibiger, F. S. Habel, E. Mehner, T. Leisegang, D. C. Meyer, T. Mikolajick. *The pyroelectric coefficient of free standing GaN grown by HVPE.* Joint ISAF/ECAPD/PFM Conference, Darmstadt, Germany, Talk Session 6a. 21.–25.08.2016

7. S. Jachalke, E. Mehner, J. Hanzig, F. Hanzig, M. Zschornak, H. Stöcker, D. C. Meyer. *Pyroelectricity in the model perovskite SrTiO₃?* E-MRS Spring Meeting, Lille, France, Talk W2.4. 26.–30.05.2015

Authored Posters

1. S. Jachalke, T. Schenk, M. H. Park, U. Schroeder, T. Mikolajick, H. Stöcker, E. Mehner, D. C. Meyer. *Pyroelectricity of silicon-doped hafnium oxide thin films.* IFAAP Jount Conference, Hiroshima, Japan, Poster. 27.05 – 01.06.2018

2. S. Jachalke, E. Mehner, H. Stöcker, E. Schleicher, T. Leisegang, D. C. Meyer. *Compositional influence on the pyroelectric coefficient of $(1-x)PMN-xPT$.* 80. Jahrestagung der DPG und DPG-Frühjahrstagung, Regensburg, Germany, Poster KR 1.2. 6.–11.03.2016

3. S. Jachalke, E. Mehner, H. Stöcker, D. C. Meyer. *Automated set-up for measurement and evaluation of pyroelectric properties.* 22. Jahrestagung der Deutschen Gesellschaft für Kristallographie, Berlin, Germany, Poster MS02-P01. 17.–20.03.2015

4. S. Jachalke, E. Mehner, H. Stöcker, T. Leisegang, D. C. Meyer. *Evaluation of structural phase transition by pyroelectric measurements.* 23rd Congress and General Assembly of the International Union of Crystallography, Montreal, Canada, Poster MS01.P13.A13. 05.–12.08.2015

5. S. Jachalke, E. Mehner, H. Stöcker, D. C. Meyer. *Measurement of pyroelectric properties and ferroelectric to paraelectric phase transition of semicrystalline PVDF and P(VDF-TrFE).* 21. Jahrestagung der Deutschen Gesellschaft für Kristallographie, Freiberg, Germany, Poster. 19.–22.03.2013

Coauthored Talks and Posters

1. T. Weigel, M. Zschornak, T. Behm, C. Funke, S. Jachalke, H. Stöcker, T. Leisegang, D. C. Meyer. *Determination of structure-property-relations from single crystal x-ray difraction data.* 26. Jahrestagung der Deutschen Gesellschaft für Kristallographie, Essen, Germany, Poster P087. 05.–08.03.2018

2. E. Mehner, S. Jachalke, J. Hanzig, S. H., C. Richter, M. Zschornak, D. C. Meyer. *Combining X-ray diffraction and pyroelectric measurements for phase transition investigations.* 29th European Crystallographic Meeting, Rovinj, Croatia, Poster MS15-P12. 23.–28.08.2015

3. M. Zschornak, J. Hanzig, H. Stöcker, C. Richter, M. Nentwich, E. Mehner, F. Hanzig, S. Jachalke, S. Gorfman, B. Khanbabaee, T. Leisegang, D. Novikov, S. Gemming, D. C. Meyer. *Dynamics of oxygen vacancies in strontium titanate.* 29th European Crystallographic Meeting, Rovinj, Croatia, Talk MS16-O3. 23.–28.08.2015

4. E. Mehner, J. Hanzig, S. Jachalke, F. Hanzig, M. Zschornak, H. Stöcker, D. C. Meyer. *Pyroelectricity in strontium titanate single crystals?* 22. Jahrestagung der Deutschen Gesellschaft für Kristallographie, Berlin, Germany, Talk MS06-T5. 17.–20.03.2015

5. B. Störr, R. Schmid, H. Stöcker, E. Mehner, S. Jachalke, J. Hanzig, M. Sonntag, T. Leisegang, D. C. Meyer. *Comprehensive collection of pyroelectric properties of organic and inorganic materials – database and categorization.* 22. Jahrestagung der Deutschen Gesellschaft für Kristallographie, Berlin, Germany, Poster MS02-P07. 17.–20.03.2015

6. H. Stöcker, B. Störr, S. Jachalke, E. Mehner, J. Hanzig, M. Sonntag, R. Schmid, T. Leisegang, M. D. C. *Do we know the Pyroelectric Coefficient of Barium Titanate?* 23. Jahrestagung der Deutschen Gesellschaft für Kristallographie, Göttingen, Germany, Poster LIG-P08. 16.–19.03.2015

7. M. Ureña de Vivanco, M. Sonntag, C. Forman, M. Gootz, E. Mehner, S. Jachalke, H. Stöcker, R. Strohmeyer, D. Scheithauer, I. Muritala, B. Störr, M. Zschornak, J. Hanzig, M. Herrmann, M. Koitsch, R. Pardemann, T. Leisegang, B. Meyer, D. C. Meyer. *Crystals as the heart of thermal-into-chemical-energy conversion devices.* 22. Jahrestagung der Deutschen Gesellschaft für Kristallographie, Berlin, Germany, Poster MS02-P06. 17.–20.03.2015

8. E. Mehner, J. Hanzig, S. Jachalke, F. Hanzig, M. Zschornak, H. Stöcker, D. C. Meyer. *Electric field induced pyroelectricity in strontium titanate.* 23rd Congress and General Assembly of the International Union of Crystallography, Montreal, Canada, Talk MS01.O03. 05.–12.08.2014

9. J. Hanzig, M. Zschornak, E. Mehner, F. Hanzig, S. Jachalke, M. Nentwich, H. Stöcker, T. Leisegang, C. Röder, D. C. Meyer. *Defect separation in strontium titanate: Formation of a polar phase.* 23rd Congress and General Assembly of the International Union of Crystallography, Montreal, Canada, Poster MS15.P02.A132. 05.–12.08.2014

10. T. Leisegang, B. Störr, E. Mehner, S. Jachalke, C. Cherkouk, M. Zschornak, H. Stöcker, M. Urena, U. Wunderwald, D. C. Meyer. *Pyroelectric Crystals: Structure, Properties and Applications.* 23rd Congress and General Assembly of the International Union of Crystallography, Montreal, Canada, Poster MS23.P04.A230. 05.–12.08.2014

Patents

1. C. Forman, M. Gootz, F. Hanzig, J. Hanzig, S. Jachalke, T. Leisegang, E. Mehner, B. Meyer, D. C. Meyer, C. Richter, H. Stöcker, M. E. Zschornak, T. (Anmelder). *Verfahren und Vorrichtung zur Umwandlung von thermischer Energie in elektrische Energie.* Anmeldetag: 18.07.2014, Deutsche Patentanmeldung, DE102014010885.6. 2014

Acknowledgments

The biggest thank is devoted to the most important persons in my life, my wife Anne and my two boys Ben and Ian. You are the ones, who encourage me every single day to give my best and I am truly thankful to have you in my life. Thanks for the continuing support in everything I do, such as the long evenings at the computer to finish my stuff, the guitar noise on and beyond the stage and the delays, when I have to take one or two more photos. You all and all of these things are the reason, why I feel like the happiest man on earth and I hope our lifetime will offer us much more happy and satisfying moments. Finally I want to thank the rest of my family for continuing support in every aspect. You encouraged me in this PhD, although it was not always clear to you, what I am actually doing there.

Versicherung

Hiermit versichere ich, dass ich die vorliegende Arbeit ohne unzulässige Hilfe Dritter und ohne Benutzung anderer als der angegebenen Hilfsmittel angefertigt habe; die aus fremden Quellen direkt oder indirekt übernommenen Gedanken sind als solche kenntlich gemacht.

Die Hilfe eines Promotionsberaters habe ich nicht in Anspruch genommen. Weitere Personen haben von mir keine geldwerten Leistungen für Arbeiten erhalten, die nicht als solche kenntlich gemacht worden sind. Die Arbeit wurde bisher weder im Inland noch im Ausland in gleicher oder ähnlicher Form einer anderen Prüfungsbehörde vorgelegt.

6. Mai 2019   M. Sc. Sven Jachalke

Declaration

I hereby declare that I completed this work without any improper help from a third party and without using any aids other than those cited. All ideas derived directly or indirectly from other sources are identified as such.

I did not seek the help of a professional doctorate-consultant. Only those persons identified as having done so received any financial payment from me for any work done for me. This thesis has not previously been published in the same or a similar form in Germany or abroad.

May 6, 2019   M. Sc. Sven Jachalke